Stator Fault Analysis of Synchronous Machines

by

Prabhakar Neti
B.Tech., Sri Venkateswra University, India1994
M.Tech., Jawaharlal Nehru Technological University, India1996

A Dissertation Submitted in Partial Fulfilment of the Requirements for the Degree of

DOCTOR OF PHILOSOPHY

in the Department of Electrical and Computer Engineering

Stator Fault Analysis of Synchronous Machines

by

Prabhakar Neti
B.Tech., Sri Venkateswra University, India1994
M.Tech., Jawaharlal Nehru Technological University, India1996

Supervisory Committee

Dr. Subhasis Nandi

Supervisor (Department of Electrical and Computer Engineering)

Dr. A.K.S. Bhat

Department Member (Department of Electrical and Computer Engineering)

Dr. H.H.L. Kwok

Department Member (Department of Electrical and Computer Engineering)

Dr. Afzal Suleman

Outside Member (Department of Mechanical Engineering)

Dr. Sang Bin Lee

External Examiner (Department of Electrical Engineering, Korea University)

Supervisory Committee

Dr. Subhasis Nandi

Supervisor (Department of Electrical and Computer Engineering)

Dr. A.K.S. Bhat

Department Member (Department of Electrical and Computer Engineering)

Dr. H.H.L. Kwok

Department Member (Department of Electrical and Computer Engineering)

Dr. Afzal Suleman

Outside Member (Department of Mechanical Engineering)

Dr. Sang Bin Lee

External Examiner (Department of Electrical Engineering, Korea University)

ABSTRACT

The stator inter-turn faults can result in catastrophic failure of the electric machines leading to extended downtime of the equipment, increased cost of repair and heavy financial losses in the industries. In the recent trends, online fault diagnosis of the electric machines that are employed in critical applications has been considered very important since frequent outage of the machines for the purpose of testing cannot be recommended. In this work, diagnostic tools have been developed to unambiguously detect the early stages of these faults in the salient-pole synchronous machines, both reluctance synchronous machine and synchronous machine with DC excitation. Motor current signature analysis, a very useful tool in the condition monitoring of electrical machines, has been primarily used for this purpose.

This study mainly consists of development of theoretical background for the diagnostic schemes followed by the implementation of these schemes on both simulated and experimental machines. For this purpose, detailed mathematical models of the synchronous machines have been developed that can include stator inter-turn faults with desired fault severity. The developed models can also accommodate some structural asymmetries of the machines. These models have been instrumental in testing the proposed diagnostic schemes under ideal conditions. Also, reversible stator inter-turn faults have been carefully created in the experimental machines to test the feasibility of the diagnostic schemes under practical conditions. In order to ensure unambiguous fault detection, a detailed analysis has been performed under various possible abnormal operating conditions of the machines such as supply unbalance, time harmonics and internal asymmetries of the machines.

Initially, certain drawbacks have been identified in a diagnostic scheme based on negative sequence quantities of the machine and critical improvements have been suggested to enhance its sensitivity. However, the modified method fails to detect faults involving one turn short. Hence a frequency domain approach has been considered to detect these faults. As a first step in this direction, it has been demonstrated that the triplen harmonics in the line current of synchronous machines cannot detect these faults unambiguously. Subsequently, owing to the stored magnetic energy in the machine after supply disconnection, it has been observed that the triplen harmonics in the terminal voltages of RSM can be useful for unambiguous detection of stator inter-turn faults. A new and very effective technique of online fault detection, based on the monitoring of some specific frequency components in the field current, has been developed for the synchronous machines with DC excitation. This scheme uses the structural asymmetries of the field winding. Similar results have also been realized using a rotor-mounted search-coil with very high sensitivity. In this work, an instrument has also been devised to implement fault diagnosis on machines using the computational capabilities of digital signal processors.

Table of Contents

List of Tables

List of Figures

List of Abbreviations

AC	Alternating current
DC	Direct current
DSP	Digital signal processor
DTC	Direct torque control
DFT	Discrete Fourier transform
EPVA	Extended Park's vector approach
FEM	Finite element method
FFT	Fast Fourier transform
FIR	Finite impulse response
HB	Healthy machine under balanced supply
HU	Healthy machine under unbalanced supply
IPMSM	Interior permanent magnet synchronous machine
MCSA	Motor current signature analysis
MMF	Magneto motive force
MUSIC	Multiple signal classification estimator
MWFA	Modified winding function approach
PD	Partial discharge
PF	Power factor
PSD	Power spectral density
RSM	Reluctance synchronous machine
SM	Synchronous machine
SOFM	Self-organizing feature map
T1	Machine with 1-turn fault under balanced supply
T2	Machine with 2-turn fault under balanced supply
T3	Machine with 3-turn fault under balanced supply
T4	Machine with 4-turn fault under balanced supply

T5	Machine with 5-turn fault under balanced supply
WFA	Winding function approach
UPF	Unity power factor

List of Symbols

A	Stator phase-A
B	Stator phase-B
C	Stator phase-C
C_P	Number of conductors / phase / pole
D	1/Effective air-gap length along the direct-axis
$\tilde{I}_A$	Phase-A current vector
$\tilde{I}_B$	Phase-B current vector
$\tilde{I}_C$	Phase-C current vector
$\mathrm{I_L}$	Line current
$\mathrm{I_{anL}}$	Stator current under no-load
$\mathrm{I_{afL}}$	Stator current under full-load
$\tilde{I}_0$	Zero sequence current per phase
$\tilde{I}_1$	Positive sequence current per phase
$\tilde{I}_2$	Negative sequence current per phase
J	Moment of inertia of the rotor
$\tilde{K}_0, \tilde{K}_1, \tilde{K}_2$	Complex constants of the machine
L	Self inductance of stator phase winding
L_d	Direct axis inductance
L_l	Leakage inductance of stator winding per phase
L_n	Net axial length of the stator iron
L_q	Quadrature axis inductance
L_{uv}	Mutual inductance between any two stator phases, u and v
L_2	Mean length of the end winding
N	Number of conductor per phase per stator slot
N_s	Number of shorted turns

$N_v(\phi)$	Winding function of any stator phase-v
P_P	Real power
P_1, P_2, P_3	Real powers per phase at three different operating points
Q	1/Effective air-gap length along the quadrature-axis
Q_P	Reactive power
Q_1, Q_2, Q_3	Reactive powers per phase at three different operating points
R	Radius of the reactance circle
S_p	Apparent power
S_1, S_2, S_3	Apparent powers per phase at three different operating points
T_e	Electromagnetic torque
T_l	Load torque
$\tilde{V}_A$	Phase-A voltage vector
$\tilde{V}_B$	Phase-B voltage vector
$\tilde{V}_C$	Phase-C voltage vector
V_{ph}	Stator voltage per phase
V_{tnL}	Stator voltage no-load
V_{tfL}	Stator voltage under full-load
$\tilde{V}_0$	Zero sequence voltage per phase
$\tilde{V}_1$	Positive sequence voltage per phase
$\tilde{V}_2$	Negative sequence voltage per phase
X_d	Direct axis reactance
X_q	Quadrature axis reactance
W_{co}	Magnetic co-energy of the machine
a	Angle subtended by one rotor slot at the centre of the rotor
b	Half of the angle subtended by the rotor bars on either side of inter polar gap
c	Any positive integer
d	Effective air-gap length along the direct-axis

f	Supply frequency
$g^{-1}(\phi, \theta)$	Inverse air-gap function
h	Any positive integer
i_e	Instantaneous end ring current
i_{sA}	Instantaneous phase-A current
i_{sB}	Instantaneous phase-B current
i_{sC}	Instantaneous phase-C current
i_{rf}	Instantaneous field current
i_{r1}	Instantaneous rotor loop-1 current
i_{sAf}	Instantaneous fault current
k	Order of permeance related harmonic
l	Stack length
m	Order of the stator winding space harmonic
m_p	Number of paths
$n_A(\phi)$	Turns function of phase-A
$n_B(\phi)$	Turns function of phase-B
$n_C(\phi)$	Turns function of phase-C
$<n_C(\phi)>$	Average value of the turns function of phase-C
$n_{Aa}(\phi)$	Turns function of asymmetric phase-A
$n_{Af}(\phi)$	Turns function of faulty part of phase-A
$n_{Ah}(\phi)$	Turns function of healthy part of phase-A
$n_a(\phi)$	Turns function of a part of phase-A removed to create asymmetry
$n_{rf1}(\phi)$	Turns function of standard field winding
$n_{rf2}(\phi)$	Turns function of two-coil field winding
$n_{rfa}(\phi)$	Turns function of asymmetric field winding
$n_r(\phi)$	Turns function of a typical rotor loop
n_p	Number of layers of stator winding

p	Number of fundamental pole-pairs
p_c	'x' co-ordinate of the centre of the reactance circle
q	Effective air-gap length along the quadrature-axis
q_c	'y' co-ordinate of the centre of the reactance circle
r	Radius of the rotor
x	$2\pi/3$
u	Any phase of stator winding
v	Any phase of stator winding
v_e	Instantaneous end ring voltage
v_{sA}	Instantaneous phase-A voltage
v_{sB}	Instantaneous phase-B voltage
v_{sC}	Instantaneous phase-C voltage
v_{rf}	Instantaneous field voltage
v_{r1}	Instantaneous rotor loop-1 voltage
w	Any positive integer
δ_{nL}	Load angle under no-load condition
δ_{fL}	Load angle under full-load condition
θ	Rotor position (mechanical radian)
θ_d	Angle subtended by the polar arc at the centre of the rotor
θ_q	Angle subtended by the inter-polar arc at the centre of the rotor
ϕ	Space angle (mechanical radian) with respect to stator frame of reference
ϕ_e	Number of flux lines per ampere-turn per inch
μ_o	Permeability of the free space
ω	Angular frequency

Acknowledgments

I take it as a profound privilege to express my deep sense of gratitude to my supervisor, Dr. Subhasis Nandi, for his valuable time, constant guidance and suggestions during this program. He has always encouraged for meeting high standards of quality and timely completion of this thesis, hence I am highly indebted to him. I would also like to thank Dr. Nandi for providing me with financial support and adequate research facilities during this program.

I would like to sincerely thank all the members of my supervisory committee, Dr. A.K.S. Bhat, Dr. H.H.L. Kwok and Dr. A. Suleman for their valuable time, constructive comments and constant encouragement in my thesis preparation and career guidance. I am also thankful to them for their timely appreciation and very friendly interaction.

I would like to thank University of Victoria for awarding graduate fellowship and several travel grants. I would also like to thank the Department of ECE for providing a continuous opportunity to work as a Teaching Assistant during this program that gave an exciting opportunity to interact with the undergraduate students of the department and keep my passion to teach intact.

My special thanks go to Mr. Rob Fichtner, Mr. Eric Laxdal and Mr. Duncan Hogg from the Department of ECE; and Mr. Rodney Katz from the Department of Mechanical Engineering for their kind cooperation and help to setup arrangements to conduct many critical experiments. Further, I cannot forget to thank all my fellow graduate students, friends and well wishers for their encouragement.

How would I be here without my family? I am highly indebted to my beloved parents, Sri Suryanarayana Neti and Smt. Lakshmi Annapurna Neti, who sacrificed

their every best to put me here. I wish to thank my wife, Sangeeta, for her love and stubborn confidence in me that made my targets very easy. My adorable daughter, Medha, has been a very cooperative kid because of which I could allocate sufficient time to accomplish this project. My elder sister and brother-in-law deserve a special mention for their selfless help and strong support. I would like to thank my parent-in-laws who came to Victoria and helped at the time of my daughter's birth. Also, I cannot forget the love and affection extended by all other members of my family.

Dedication

Dedicated to my beloved parents

Chapter 1

Overview of Stator Inter-turn Fault Analysis

1.1 Introduction to Condition Monitoring of Electric Machines

For any engineering application, safety and reliability are of paramount importance. These two features can be assured by a superior design of the system followed by its thorough protection during the operation. The process of continuous observation and protection of the electric machines against various faults is known as condition monitoring. In operating electric machines, several types of faults can develop. The following are the principal faults that can occur in these machines [1]:

- Bearing faults (40-50%)
- Stator insulation faults (30-40%)
- Rotor cage faults (5-10%) and
- Eccentricity & other types too scattered to classify.

Further, turn faults in the rotor windings, eccentricity and brush related faults can also take place in case of DC machines, slip ring induction machines and synchronous machines with DC excitation. As an example, the eccentricity related faults in DC and PM machines have been addressed in [2] and [3] respectively.

A faulty state may cause different types of abnormalities in the machine such as over current, excessive heating and vibrations. However, the incipient stage of a fault may not bring visible changes in the performance of the machine. If not detected and

eliminated in the incipient stages, such faults can eventually grow and cause a catastrophic failure of the machine. An early detection of a fault followed by disconnection of the machine from the service can save a great deal of maintenance cost and downtime of the equipment.

Ideally, a diagnostic tool is expected to unambiguously detect the faulty state of the machine as quickly as possible i.e., well before the fault grows to a dangerous level. It is also expected to generate a trip signal to disconnect the machine from the service, if required. Various currents, voltages, temperature, vibrations, speed, torque and other relevant signals of the machines can be used for this purpose. In general, to implement condition monitoring, the magnitude of one or more relevant signals is continuously measured and compared with the reference value obtained under a healthy condition of the machine. However, it is quite a challenge to identify a signal that can show clear and unambiguous variations under incipient stage of a fault. Ambiguity may arise because of the fact that several other abnormal operating conditions of the machine, within their allowed limits, can also cause very similar variations. These abnormal conditions can occur as a result of unavoidable supply unbalance, time harmonics and manufacturing imperfections of the machine.

Manufacturers as well as the users of the electric machines have recently started showing great concerns about the protection of these machines against various types of faults. Hence, research has picked up fervent pace in both industry and academia. Such research work has resulted in the development of several useful condition monitoring tools against different types of faults. An excellent review of these contributions has been provided in [4-6], which also revealed the fact that detection of stator inter-turn faults is still a challenge particularly in their incipient stages. A detailed survey of the fault diagnosis against stator inter-turn faults in electric machines has been presented in the subsequent sections.

1.2 Stator Inter-turn Faults in Electric Machines

The stator or the armature of an electric machine consists of several windings that are made up of copper conductors. These conductors are covered with a thin layer of insulation and are placed in the stator slots in a systematic manner. As an example, the stator windings of the reluctance synchronous machine (RSM) have been shown in Figure 1.1. Several conductors have been tightly placed in each of the stator slots as well in the end windings. The insulation layer on these conductors prevents internal short circuit of different turns. The failure of insulation of these turns, due to the reasons as described below, leads to an internal short circuit known as stator inter-turn fault as shown in Figure 1.2. The inter-turn faults can occur as a result of the following reasons [7]:

- High stator core or winding temperatures
- Slack core lamination, slot wedges, and joints
- Loose bracing for end winding
- Contamination due to oil, moisture, and dirt
- Short circuit or starting stresses
- Electrical discharges
- Leakage in cooling systems.

Due to the above mentioned reasons, inter-turn faults in an electric machine are very likely inspite of good insulation quality. Further, in the case of inverter driven small and medium power machines, winding insulation will be stressed to a greater extent due to very frequent and high rate of rise of voltages [8].

A state of fault involving few turns, typically one-turn, can be called as an incipient stage of the fault. The time elapsed in the growth of an incipient fault leading to a catastrophic failure of the machine varies from a third of a second to

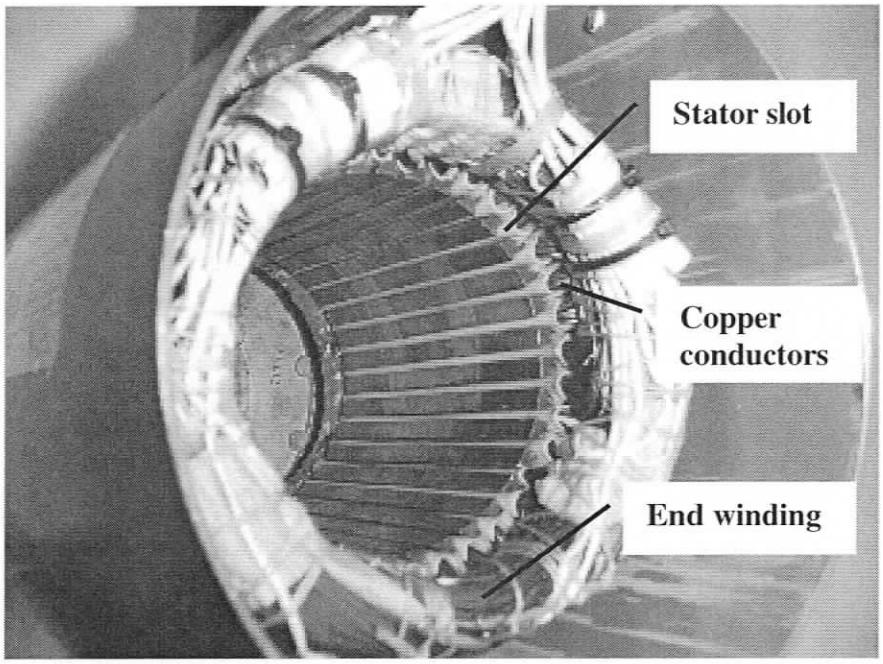

Figure 1.1 Stator windings of reluctance synchronous motor

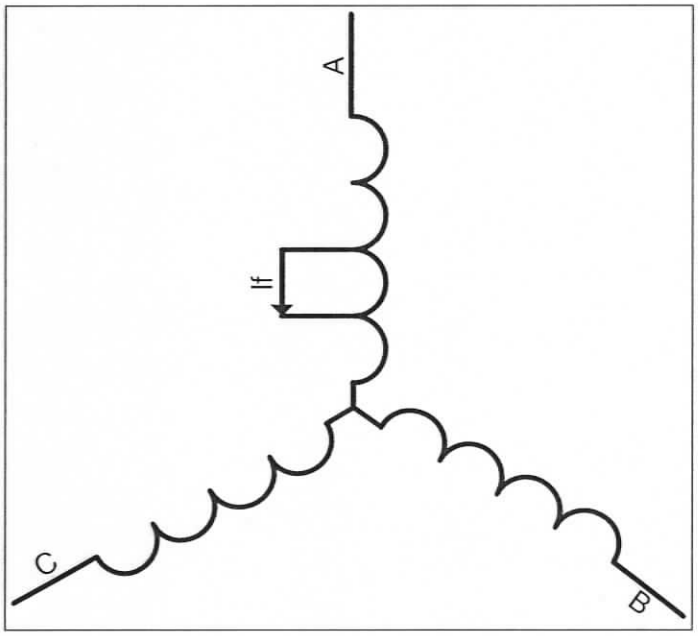

Figure 1.2 Inter-turn short in phase-A of stator winding

several minutes in the case of random-wound machines and can even be much longer in the case of form-wound machines [1]. If not detected and eliminated, such a fault can grow to a dangerous level and can even damage the core of the machine. Such damage can lead to drastically increased maintenance cost and downtime of the equipment, which is very much undesirable.

Offline surge tests are available to test the insulation strength of stator windings of large electric machines [9]. As per the recommendations (IEEE Standard 522-2004), the surge test can be conducted to test the winding insulation of form wound machines which lie in the range of 200kW to 100MW. This test can be applied to:

- Individual stator coils after manufacture
- Coils in completely wound stators of original manufacture
- Coils and windings for rewinds of used machinery
- Windings of machines in service to determine their suitability to further continue in service.

The suggested arrangement of surge test equipment has been shown in Figure 1.3. After placing the winding under test as shown in Figure 1.3, a steeply raising impulse has to be applied to the surge inducing coil. Its response can be observed with the help of a cathode ray oscilloscope, a one-turn search-coil and resistor type voltage divider. Presence of high frequency oscillations and typical reduction in the amplitude of voltage induced in the one-turn search-coil can be indicative of presence of shorted turn in the winding under test.

However, this test does not evaluate the ability of winding insulation to withstand abnormal voltage surges and repetitive voltage spikes in adjustable frequency drives. Moreover, condition monitoring of electric machines needs online monitoring. A good protective system need to detect stator inter-turn fault in the incipient stage itself and generate a trip signal to remove the motor from the service, if required.

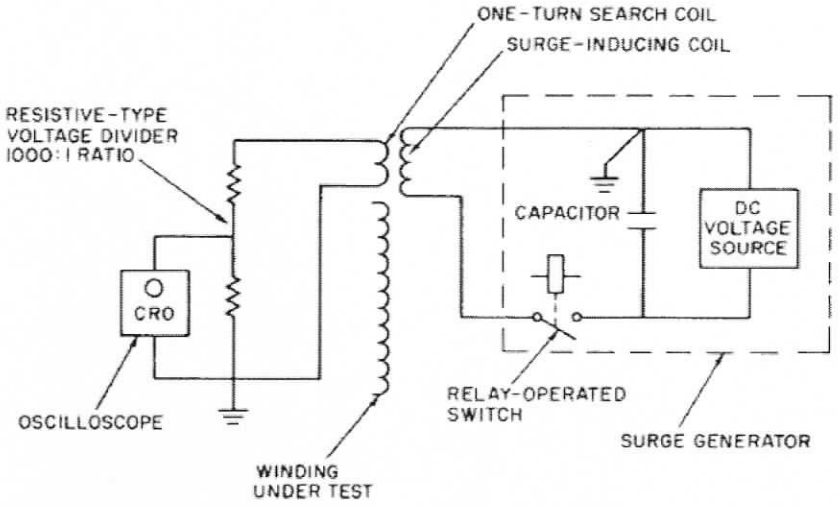

Figure 1.3 Arrangement of surge test equipment

1.3 Literature Survey on Stator Inter-turn Fault Analysis

The condition monitoring of the electric machines is as archaic as the history of the electric machines. In the beginning, some basic protective schemes have been incorporated against over current, over voltage, over heating and other such abnormalities to safeguard the electric machines and ensure reliability. In the modern era, electric machines drive many critical loads where safety and reliability are extremely important. Hence more attention is being paid to protect these machines.

For over 40 years, it has been demonstrated that periodic measurement of the PD (partial discharge) activity can detect deterioration of winding insulation well before failure occurred in high voltage motors and generators [10]. The deterioration of stator insulation in these machines exhibits a partial discharge activity almost 30 times higher than that of a normal motor. Such a clear and early warning of a fault facilitates to plan for corrective actions. The instrument called TGA-B can perform the partial discharge test on the high voltage machines on-line as well as off-line.

Thus using this scheme, the high voltage motors can be very well protected against deterioration of stator insulation.

In the case of low voltage motors, the diagnosis methods are yet to be standardised. Hence, in the recent times, many researchers have been focussing on the fault analysis of low voltage induction and salient-pole synchronous machines (SM). Different researchers have proposed different techniques. Each technique has its own advantages and disadvantages. A detailed account of various techniques has been given in the following paragraphs.

In the AC machines, a major breakthrough in the detection of stator inter-turn faults has been achieved by utilizing the effective negative sequence impedance as an indicator of these faults [11, 12]. This method can give very good results but may fail under extremely low-level of fault, particularly under supply unbalance. This issue was solved to certain extent by developing the voltage mismatch detectors [13].

Subsequently, a modified method has been proposed to compensate for the effects of internal asymmetry and supply voltage unbalances [1]. Here, the negative sequence current caused by the internal asymmetry of the machine and the supply unbalance were estimated and subtracted from the measured value of negative sequence current. This method was reported to be capable of detecting even a 1-turn fault very clearly. Since the residual current is load dependent, the method needed the storage of residual negative sequence current of the motor under different operating points. This method was further refined to easily obtain the complex constants of the machine by making use of least square approximation technique [14]. However, these constants were not shown to be obtained using supply unbalance in both [1] and [14]; leading one to conclude that the authors were under the impression that the negative sequence impedance of the motor was not sensitive to the changing supply unbalance. However, the results furnished later in this thesis clearly established that, in the case

of synchronous machines, the effective negative sequence impedance could be sensitive to the changing supply unbalance. This phenomenon can cause a serious ambiguity in the detection of faults involving few turns.

An effort was also made to solve this issue by making use of power decomposition technique [15]. The temperature effects and slip dependent variations of negative sequence resistance have been minimized. However, this method needs a set of three phase reference voltages along with the three-phase voltages and currents. It is also stated in the paper that this method caused ambiguity in detecting faults involving few turns with supply unbalance in other phases. In spite of increased computational complexity, unambiguous detection of a 1-turn fault was not possible.

A new method for the detection of stator inter-turn faults in induction motors has been proposed that uses the off-diagonal terms of the impedance matrix [16]. This method can be relatively simple and robust. It has been claimed that the scheme has better immunity to the varying supply unbalance, measurement errors and the slip-dependent variations of machine's internal asymmetry. However, the test results under changing supply unbalance have not been reported. Further, the changes in the off-diagonal terms are load-dependent.

In another attempt based on frequency domain analysis, a method of detection of stator inter-turn faults in three-phase induction motors has been demonstrated based on MCSA (motor current signature analysis) [17]. The test results have been presented with 8% of shorted turns in one phase of stator winding of a 3kW motor. Winding function approach (WFA) has been used to model induction motor with stator inter-turn faults. A large increase of third harmonic component has been projected as an indicator of a stator inter-turn fault in induction motors. Results were validated using both simulation and experimental studies. However, it has also been stated in the paper that the third harmonic component can be sensitive to saturation,

supply unbalance and internal asymmetries of the machine. This leads to a serious confusion between the faulty and other abnormal operating conditions of the motor.

In the fault diagnosis of induction motors, advanced signal processing techniques have been used to reduce the influence of noise and extract useful information [18]. These techniques make use of computationally intense algorithms called MUSIC (multiple signal classification estimator) and ROOT-MUSIC. The approximate relative computational complexity (number of computations involved) of these special algorithms is N^3 whereas the computational complexity of the classical spectral analysis is $N*\log_2(N)$. Here, N represents the number of samples of the data.

In a separate study, using extended Park's vector approach (EPVA), the detection of stator inter-turn faults in both synchronous and asynchronous machines has been carried out [19]. Experimental results were obtained in an industrial environment. In EPVA spectrum, the component at twice the supply frequency has been demonstrated to be highly sensitive to such faults. However, results under supply unbalance were not provided.

A novel scheme, based on neural networks, has been developed for detecting the stator inter-turn faults in induction machines [20]. A feed-forward neural network combined with the self-organizing feature map (SOFM) learns the model of a healthy machine and visually displays the operating condition of the machine. The drift of operating point of the machine to a specific region on this map has been shown as an indication of initiation of a fault. Experimental results establish that this method is immune to supply unbalance or internal asymmetries in the machine. This method needs additional feed-forward neural network followed by its learning process.

An attempt has been made to detect the stator inter-turn faults in induction motor using wavelet packet analysis [21]. This method makes use of the sensitivity of machine's electromagnetic torque to asymmetrical faults. The sampled voltage and

current signals have been utilized to compute the electromagnetic torque. The torque signal has been then decomposed into independent frequency bands using wavelet packet analysis. It has been claimed that the method is independent of the load variations and supply unbalance.

Penman et al [22] have proposed the measurement of the axial leakage flux resulting from an inter-turn fault in a large wound-rotor induction motor. The motor under test consists of form-wound stator coils with a provision to create inter-turn shorts. An algorithm has also been developed to locate the position of the fault in the stator winding. The theoretical predictions have been validated using experimental results. In this paper, the authors claimed that a further refinement of the fault detector is underway. Also, fault analysis of induction machines fed by both sinusoidal supply and voltage source inverter has also been carried out using the stray flux [23]. The method has been proven to give clear indication of the fault. However, the test results under changing supply unbalance have not been reported.

A novel technique to detect the stator insulation failure of a star-connected induction motor has been proposed whose neutral point is accessible [24]. The sum of all the three line to neutral voltages was utilized to detect turn faults. Immunity of this scheme to changes in the operating point of the machine, temperature, and supply voltage has been claimed. Theoretical findings have been validated using experimental results. The sensitivity of this scheme can be seriously affected since this voltage has many undesirable frequency components. However, optimization of sensitivity using a band-pass filter has been proposed.

A new method to detect the stator inter-turn faults in the induction motor has been proposed that substantially eliminates the influence of supply unbalance and time harmonics [25]. An excellent immunity to the supply unbalance and time harmonics has been achieved by analyzing the terminal voltages of the motor after

disconnecting it from the supply. Increase in the magnitude of some characteristic harmonic components has been projected as an indicator of turn-to-turn faults in the stator winding of the machine. The scheme is also capable of detecting the faulty phase of the stator winding. This method can be very good for some typical applications where motors are frequently operated in the transient condition, such as hoists, elevators or automobiles. However, strictly speaking, it is an effective method that can be only used to validate the on-line schemes used for the continuous duty motors.

Different schemes have been proposed for the detection of both rotor and stator inter-turn faults in the synchronous machines with DC excitation [26-33]. But, so far, sufficient research has not been carried out on the stator inter-turn faults of reluctance synchronous motors or synchronous motors with DC excitation.

Many researchers have analyzed the field current of synchronous machines against stator and rotor inter-turn faults [29-32]. Preliminary results of both transient and steady state behaviour of synchronous machine with stator inter-turn faults have been presented using simulations and experiments [30].

In a separate study, a detailed analysis has been presented on brushless synchronous generators using the 180 Hz positive-sequence stator voltage as an indicator of stator fault, the 30, 90, and 150 Hz armature circulating currents as indicators of field winding deterioration, and the 120 Hz exciter field current as an indicator of rotating rectifier diode shorts [31].

Also, an increase of 8^{th} harmonic in the field current of a 4-pole synchronous generator with a stator fault was highlighted in [32]. However, in this thesis, the 8^{th} harmonic has been shown to be sensitive to the supply unbalance and time harmonics.

In another study, the feasibility of using the mechanical vibrations of the synchronous machines to detect the winding deterioration has also been indicated [33]. Also, using a high frequency carrier signal injection, stator fault analysis has been presented in the inverter fed machines [34]. The method is shown to be sensitive to detect even one-turn fault. However, this method needs additional arrangements for the injection of carrier signal. Also, an initial simulated study has been presented on the performance of interior permanent magnet synchronous machine (IPMSM) drives under stator inter-turn fault condition [35]. The authors claimed that the proposed model can not only describe the behaviour of an IPMSM drive under stator turn fault conditions but also has flexibility in modifying control tasks. Additionally, by just inserting the motor parameters, obtained using finite element method into the proposed model, more accurate information of the behaviour of an IPMSM drive under stator turn fault conditions is achievable.

In one of the recent attempts, fault diagnosis has also been carried out on the direct torque control (DTC) induction drives using two different methods, one based on third harmonic component in the line currents and the other based on the multiple reference frames technique [36]. The scheme based on multiple reference frames technique has been claimed to take care of inherent asymmetry of the machine. Subsequently, the diagnostic scheme based on the multiple reference frames technique for DTC induction drives has been integrated into the DSP board itself [37] that utilizes the computational capabilities of the inbuilt processor. Also, a new strategy for the detection of these faults in induction motor drives has been proposed that can increase the availability of the machine in service in the presence of a fault [38]. This has been achieved by minimizing the adverse effects of stator inter-turn faults on the performance of these machines. Such a strategy can be helpful to avoid abrupt disconnection of the machine from service that can lead to a serious disaster in some applications.

1.4 Motivation and Objectives of Present Work

A detailed literature survey revealed many important aspects of condition monitoring of electric machines in the presence of stator faults. Following are the facts that motivated to conduct a research on the detection of stator inter-turn faults in salient-pole synchronous machines.

With the existing techniques, the high-voltage machines can be properly protected against the deterioration of winding insulation but not the low-voltage machines. Further, the problem of stator inter-turn faults is very severe in the case of random-wound machines. So far most of the research work has been conducted for the protection of induction machines against stator inter-turn faults but not much has been reported on salient-pole synchronous machines. Particularly, though the reluctance synchronous machines have been projected as a new alternative to AC drives [39], so far, only few publications have been found on the stator inter-turn fault analysis of these machines.

In addition, most of the methods introduced so far fail to perform unambiguous detection of stator inter-turn faults in the incipient stages. This is because of the fact that one or more of the supply unbalance, time harmonics, internal asymmetry and changes in operating point of the machines could cause the ambiguity. Some of the good methods needed some special equipment to unambiguously detect the turn-to-turn faults or were limited due to other factors.

From the above facts, it can be clearly felt that the existing techniques of condition monitoring cannot protect the low-voltage, random-wound salient-pole synchronous machines against the stator inter-turn faults. Hence this research area needs special attention.

In this work, an attempt has been made to develop diagnostic tools that are capable of detecting the incipient stages of stator inter-turn faults in low voltage, random-wound salient-pole synchronous machines, both RSM and SM with DC excitation. Also it has been aimed to minimize the influence of supply unbalance, time harmonics and internal asymmetry of the machines on the diagnosis results.

Finally, it has been intended to devise a simple and fast diagnostic tool by making use of the computational capabilities of a DSP to generate a trip signal in the event of a fault.

1.5 Thesis Outline

In Chapter 2, detection of stator inter-turn faults in RSM and SM against has been discussed that uses the negative-sequence currents of the machines. A major drawback of the existing method has been identified and a critical refinement has been suggested for the improved detection of incipient stages of fault, particularly under changing supply unbalance. However, the modified method still fails to detect the stator inter-turn fault in their incipient stages, particularly involving one shorted turn.

To rectify the above shortcoming, the frequency domains of voltages and currents of the machines have been explored next. This analysis comprises of both simulation and experimental study. In order to conduct simulation study in frequency domain, detailed models of these machines have been obtained. In Chapter 3, various aspects of modeling of the healthy RSM and SM with DC excitation have been discussed in detail. First, determination of the effective air-gaps along the direct and quadrature axes has been presented followed by the state space modeling of these machines. Further, stabilization of the machine models under full-load condition has been achieved by pole-arc reduction. Finally, in order to validate these models, a

comparison of the performance has been put forward with that of the corresponding experimental motors.

Chapter 4 deals with the modeling and performance analysis of RSM and SM with DC excitation under stator inter-turn fault and other abnormal operating conditions. Further, this chapter establishes the fact that triplen harmonics in the line current cannot be good indicators of the stator inter-turn faults; since supply unbalance, internal asymmetry and time harmonics can also predominantly increase these harmonics. Both simulation and experimental results have been presented for this purpose. Detailed mathematical proofs have also been furnished for supporting these results.

Chapter 5 discusses about a fault detection scheme for RSM that uses the stored magnetic energy of the machine after supply disconnection. Transient models of RSM, after supply disconnection, have been obtained under both healthy and faulty conditions. Detection of stator inter-turn faults has been demonstrated by analyzing the terminal voltages of the machine after supply disconnection. Both simulation and experimental results have been presented along with the mathematical proofs for supporting these results.

In chapter 6, a feasibility analysis has been put forward that suggests monitoring of some specific frequency components in the field current to detect the faults in the synchronous machines. Using suitable theory, simulations and experiments, it has been shown that the supply unbalance and time harmonics have minimal influence on these frequency components.

A novel scheme for the online detection of stator inter-turn faults in SM with DC excitation, as proposed in chapter 6, has been implemented in Chapter 7. First, detailed mathematical proofs have been furnished to show the sensitivity of the specific frequency components to the stator inter-turn faults. Next, experimental

results have been presented to validate the claims by testing the synchronous machines having two different types of field windings. The scheme has also been validated using a rotor-mounted search-coil that itself can act as a very good indicator of these faults.

The detection of inter-turn faults by using the computational capabilities of a digital signal processor (DSP) board has been discussed in Chapter 8. An algorithm has been developed to compute the Discrete Fourier Transform of the time domain signal to track the harmonic components of interest with minimum computational efforts. An instrument has been built to detect the stator inter-turn faults in SM with DC excitation used in a variable speed drive system.

Conclusions and future scope of this work follows in Chapter 9. A detailed comparison of various fault diagnostic schemes has also been presented by considering several qualitative factors of the fault diagnosis.

Chapter 2

Fault Analysis of Synchronous Machines using Negative Sequence Quantities

Many researchers have attempted to detect the stator inter-turn faults in AC machines using negative sequence quantities. A very high sensitivity of the scheme has been claimed to detect these faults involving even one turn. In this work, a major drawback of this method has been identified and a critical modification has also been suggested for improved detection of stator inter-turn faults in synchronous machines.

2.1 Description of Machines

In this thesis, the following synchronous machines have been considered for study:

- Reluctance synchronous machine (RSM)
- Synchronous machine (SM) with DC excitation
    - With standard field winding
    - With two-coil field winding

2.1.1 Description of RSM

The RSM under consideration is a 3-phase, 1.5 hp, 1800 rpm, 60 Hz, 4-pole random-wound machine with 36 stator slots and 24 damper bars having a continuous end ring construction. Its stator has a 3-phase, single layer concentric winding with 282 turns in each phase. Several taps have been brought out from the stator winding (phase-A) to physically create the inter-turn faults. Other relevant data pertaining to this

machine has been given in Appendix-A. The rotor lamination of the RSM is as shown in Figure 2.1. The complete rotor of the RSM has been shown in Figure 2.2.

2.1.2 Description of SM with DC Excitation

The other salient-pole synchronous machine under consideration is a 3-phase, 2 kW, 208V, 1800 rpm, 60 Hz, 4-pole random-wound machine having 36 stator slots. The stator has a 3-phase, double layer lap winding with 312 turns in each phase and the rotor has 20 damper bars. The damper bars have been shorted with the help of two copper laminations on either end of the rotor. The rotor lamination of the synchronous machine with DC excitation is as shown in Figure 2.3.

In this thesis, synchronous machines with two different types of field windings have been considered. The standard field winding has four-coils, one coil on each rotor pole. The two-coil field winding of the machine comprises of two series-connected coils, each placed on the diagonally opposite rotor poles. This structure can be adopted for the ease of construction. Each coil side occupies each of the inter-polar gaps. Ideally, though the flux pattern produced by the two-coil field winding will be similar to that produced by a standard four-coil field winding, their turns functions will be different as mentioned in the subsequent sections. Hence, the space harmonics of these two winding structures will be different. The rotors of the synchronous machines with standard and two-coil field winding have been shown in Figure 2.4 and Figure 2.5 respectively. The two-coil structure has been used for a specific scheme that involves analysis of field current for the detection of stator inter-turn faults in the machine. In an attempt to thoroughly test this scheme, the other type of field winding has also been considered since the results of this scheme depend on the space harmonics of the field winding. A search-coil is also mounted on one of the pole faces of the rotor. Several taps have been brought out from the stator winding (phase-A) to physically create the inter-turn faults. Other relevant data pertaining to this machine has been given in Appendix-A.

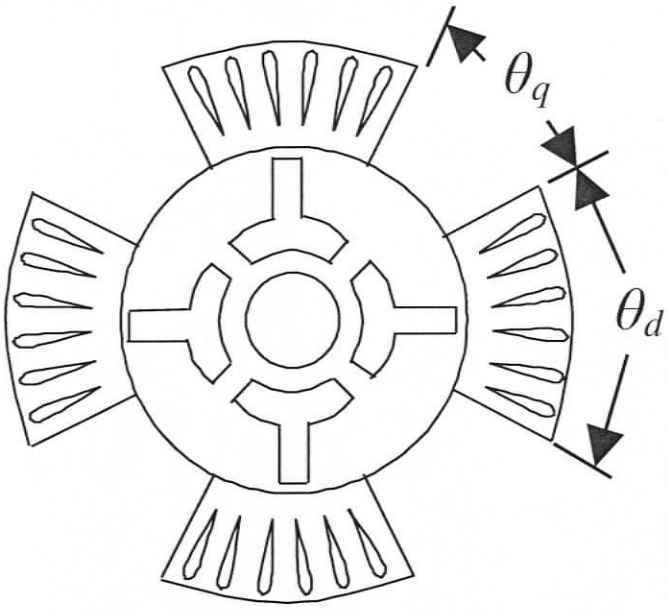

Figure 2.1 Rotor lamination of the RSM

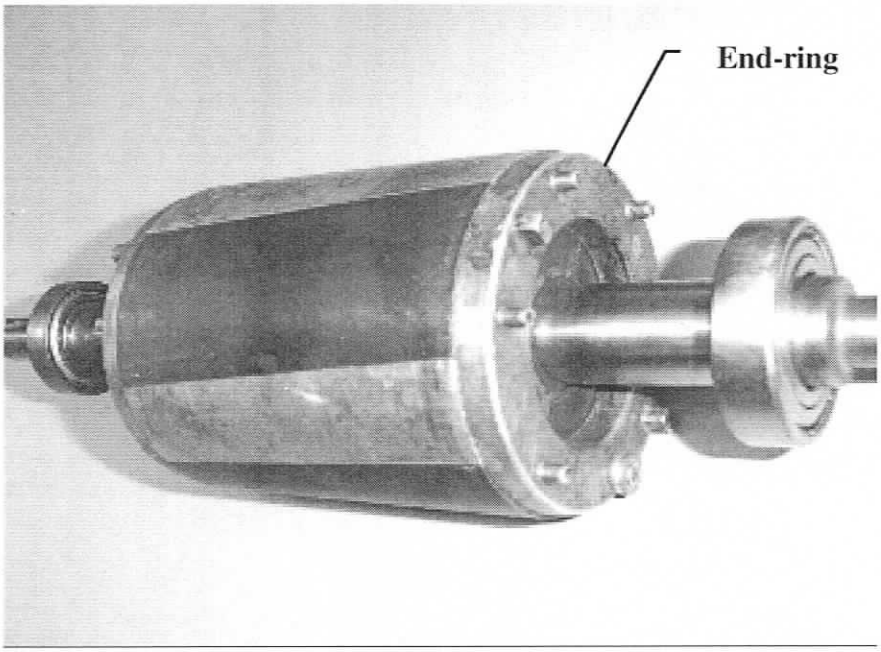

Figure 2.2 Rotor of the RSM

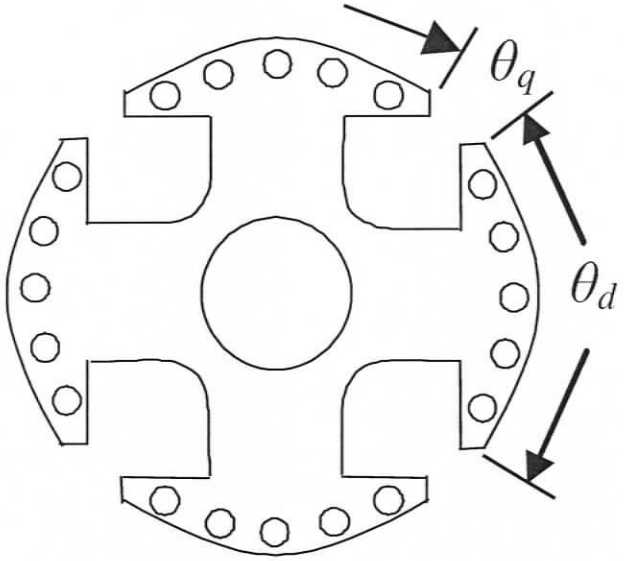

Figure 2.3 Rotor lamination of SM with DC excitation

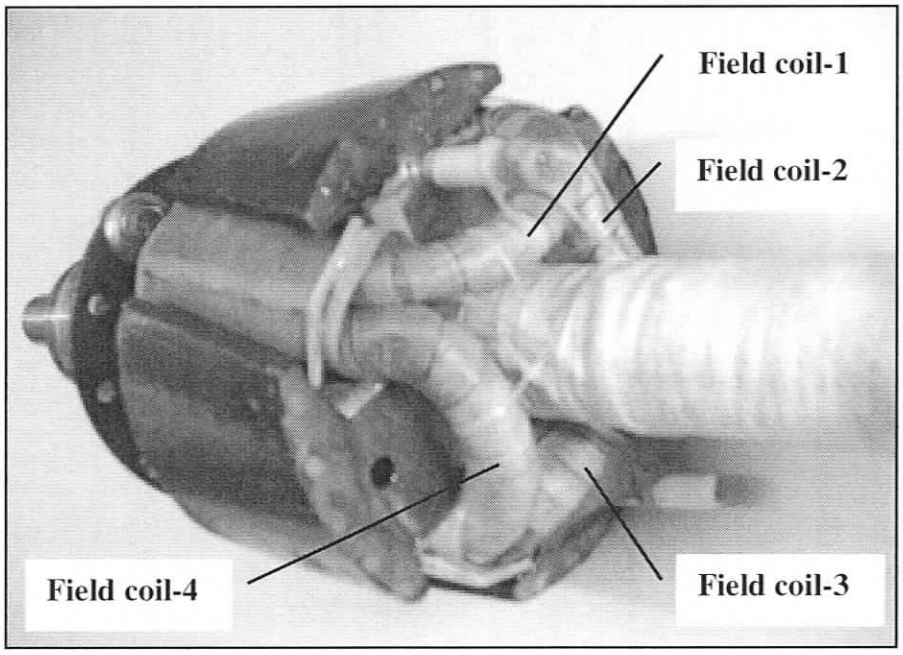

Figure 2.4 Rotor of SM with standard field winding

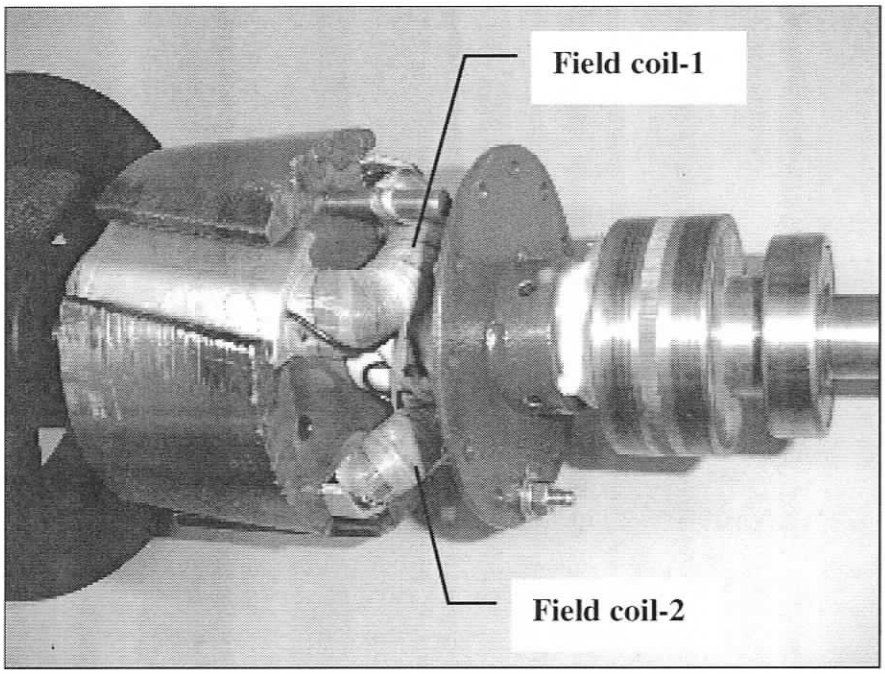

Figure 2.5 Rotor of SM with two-coil field winding

2.2 Theory of Negative Sequence Quantities and Detection of Stator Inter-turn Faults

The unbalanced 3-phase quantities can be represented as a vector sum of the positive, negative and zero sequence components. The positive sequence components can form a set of balanced 3-phase system that has the same phase-sequence as that of the original 3-phase quantities. The negative sequence components can form another set of balanced 3-phase system that has the opposite phase-sequence as that of the original 3-phase quantities. The zero sequence quantities do not have any rotation.

The sequence components of a 3-phase voltage system can be computed using a well-known transformation matrix [40] as given in (2.1). Here, $\tilde{V}_A$, $\tilde{V}_B$ and $\tilde{V}_C$ represent the three voltage phasors whereas $\tilde{V}_0$, $\tilde{V}_1$ and $\tilde{V}_2$ represent the zero, positive and negative sequence voltages per phase respectively. Similar relations can also be

given for the 3-phase currents as given in (2.2). Here, $\tilde{I}_A$, $\tilde{I}_B$ and $\tilde{I}_C$ represent the three current phasors whereas $\tilde{I}_0$, $\tilde{I}_1$ and $\tilde{I}_2$ represent the zero, positive and negative sequence currents per phase respectively.

$$\begin{bmatrix} \tilde{V}_0 \\ \tilde{V}_1 \\ \tilde{V}_2 \end{bmatrix} = \left(\frac{1}{3}\right) \begin{bmatrix} 1 & 1 & 1 \\ 1 & \alpha & \alpha^2 \\ 1 & \alpha^2 & \alpha \end{bmatrix} \begin{bmatrix} \tilde{V}_A \\ \tilde{V}_B \\ \tilde{V}_C \end{bmatrix} \tag{2.1}$$

$$\alpha = e^{j2\pi/3} \quad and \quad j = \sqrt{-1}$$

$$\begin{bmatrix} \tilde{I}_0 \\ \tilde{I}_1 \\ \tilde{I}_2 \end{bmatrix} = \left(\frac{1}{3}\right) \begin{bmatrix} 1 & 1 & 1 \\ 1 & \alpha & \alpha^2 \\ 1 & \alpha^2 & \alpha \end{bmatrix} \begin{bmatrix} \tilde{I}_A \\ \tilde{I}_B \\ \tilde{I}_C \end{bmatrix} \tag{2.2}$$

In an AC machine, the negative sequence current can flow due to the following reasons [1]:

- Unbalance in the supply voltage
- Internal asymmetry of the machine and/or
- A fault in the machine.

The terminals of an ideal symmetric 3-phase machine do not carry any negative sequence current when fed by an ideal balanced 3-phase supply. An inter-turn fault in the stator winding of the machine disturbs this symmetry and results in the flow of negative sequence current in the machine terminals.

Using the negative sequence currents, many researchers have attempted to detect the stator inter-turn faults in AC machines. Detection of even a one-turn fault in the stator winding has been claimed. A detailed review of these contributions has been

given in the first chapter of this thesis. In a healthy 3-phase AC machine, the negative sequence current can also be expressed as follows [14]:

$$\tilde{I}_2 = \tilde{K}_1 \tilde{V}_1 + \tilde{K}_2 \tilde{V}_2 \tag{2.3}$$

Here $\tilde{K}_1$ and $\tilde{K}_2$ are the load-dependent complex constants of the machine. The first term, $\tilde{K}_1 \tilde{V}_1$, in (2.3) represents the component of negative sequence current due to the internal asymmetry of the machine whereas the second term, $\tilde{K}_2 \tilde{V}_2$, represents the component due to the supply unbalance. By using $\tilde{K}_1$, $\tilde{K}_2$ and measured voltages, the component of negative sequence current due to supply unbalance and internal asymmetry of the machine can be estimated. The precision of computation offered by MATLAB (10e-15) and DSP (10e-09) can easily achieve the accuracy to compute these complex constants. In the earlier practices, the negative sequence current resulting from the supply unbalance and the internal asymmetry of the machine were estimated and subtracted from the measured value of the negative sequence current to obtain the fault-signature [1], [14]. This has been estimated based on the assumption that the parameters of the machine, $\tilde{K}_1$ and $\tilde{K}_2$, remain constant under changing supply unbalance.

However in this study, it has been observed that these parameters can be sensitive to the changing supply unbalance that can cause serious ambiguity in detecting stator inter-turn faults. In the related work [1], [14], the results under changing supply unbalance have not been furnished. Further, in [14], it is not clear if least-square method has been used to determine the parameters of the machine by considering the data under balanced condition only or both balanced and unbalanced supply conditions. In this case, erroneous determination of these parameters can be possible since the least-square method might return a solution that best fits the chosen data samples rather than exactly representing the machine parameters. Even if the constants determined using the data under balanced condition represent the machine

parameters correctly, it will be shown that these constants will fail to accommodate the effects of changing unbalance in the supply. Hence to minimize the influence of these factors on the determination of machine parameters, in this work, it has been proposed to determine the parameters of the synchronous machines considering the data under balanced as well as unbalanced conditions.

2.3 Variation of Effective Negative Sequence Impedance of Synchronous Machines under Changing Supply Unbalance

The effective negative sequence impedance is a characteristic parameter of a synchronous machine. However in the case of actual machines, a variation in the supply unbalance can vary the saturation of the machine and thus can vary the effective negative sequence impedance.

In order to study this effect, the negative sequence impedances of the synchronous machines have been determined by conducting an experiment [41]. From this experiment, the negative sequence impedance can be determined by applying a small voltage to the synchronous machine driven by a DC motor in such a way that the direction of rotation is opposite to the rotating magnetic field in the stator of the synchronous machine. The negative sequence impedance is then given by the ratio of the phase voltage to the phase current. These results for RSM and SM with DC excitation have been given in Table 2.1 and Table 2.2 respectively. In both of these machines, a clear variation of the effective negative sequence impedance has been observed with different negative sequence voltages applied.

Further, to verify these results, the parameters $\tilde{K}_1$ and $\tilde{K}_2$ pertaining to these machines have been determined using least-square method [14]. In the case of RSM, the variation of $\tilde{K}_1$ and $\tilde{K}_2$ under changing supply unbalance has been shown in Figure

2.6 and Figure 2.7 respectively. The corresponding variations in the case of SM with DC excitation have been shown in Figure 2.8 and Figure 2.9 respectively. Here, HB represents the healthy machine fed by a balanced supply whereas HU' and HU represent the healthy machine fed by unbalance (with a maximum of 2.5% unbalance) in phase-A respectively. In the case of RSM, HU' and HU represent 1.01% and 1.85% supply unbalance respectively. In the case of SM with DC excitation, HU' and HU represent 1.55% and 2.12% supply unbalance respectively. From this study, it can be clearly seen that the values of $\tilde{K}_1$ and $\tilde{K}_2$ will not remain constant under changing supply unbalance.

Table 2.1 Variation of Negative sequence impedance of RSM

V_{2Line} (V)	17	28	37	47	55	63	69
I_2 (A)	0.52	1.03	1.52	2.05	2.52	3.0	3.3
Z_2 / phase (Ω)	18.8	15.69	14.05	13.1	12.60	12.12	12.07
$Y_2=1/Z_2$	0.05	0.06	0.07	0.08	0.08	0.08	0.08

Table 2.2 Variation of Negative sequence impedance of SM with DC excitation

V_{2Line} (V)	10	15	20	25	30	35	40
I_2 (A)	1.24	2.05	2.94	3.86	5.03	6.3	7.5
Z_2 / phase (Ω)	4.65	4.22	3.93	3.74	3.44	3.21	3.07
$Y_2=1/Z_2$	0.22	0.24	0.26	0.27	0.29	0.31	0.32

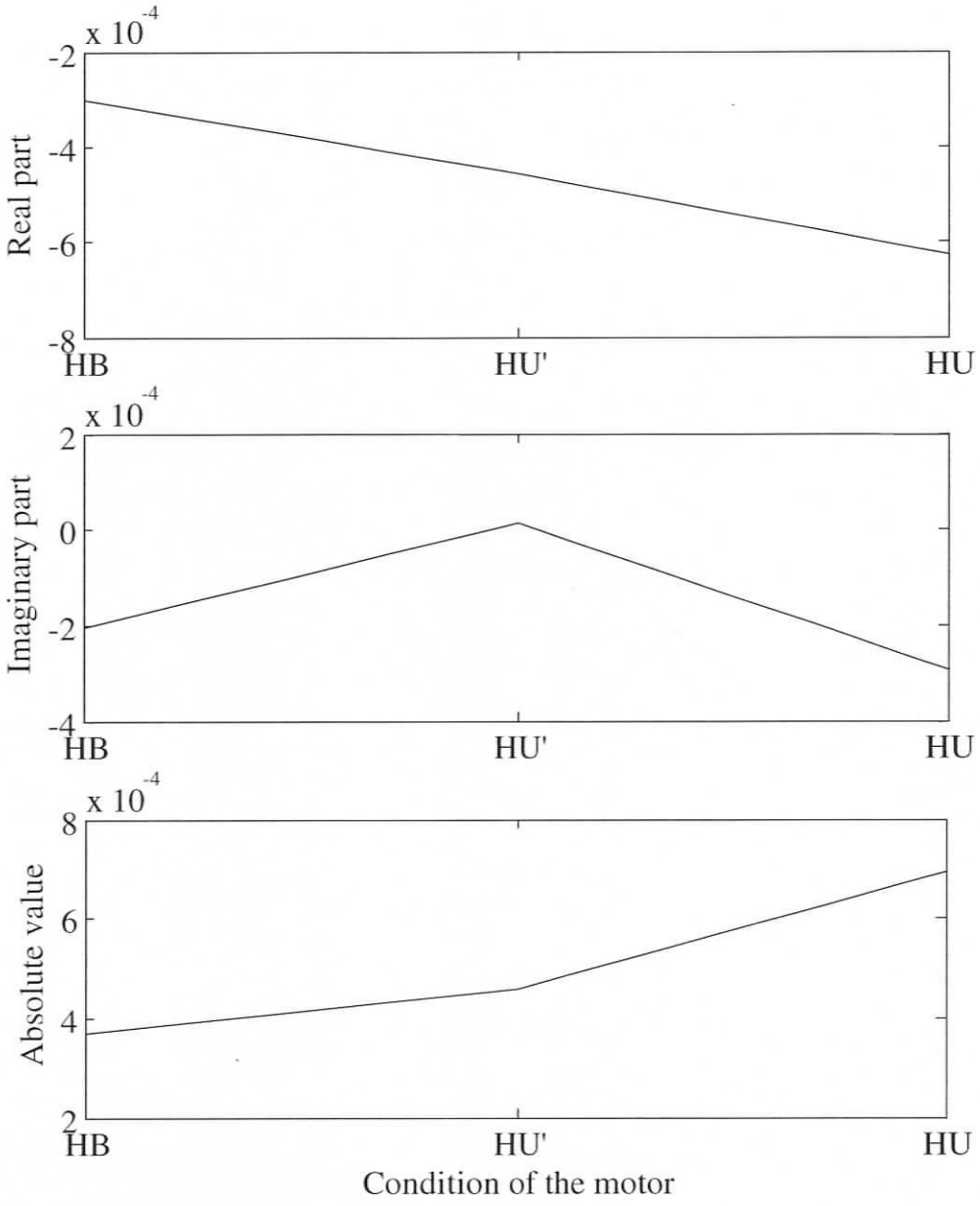

Figure 2.6 Variation of the parameter $\tilde{K}_I$ of RSM under full-load

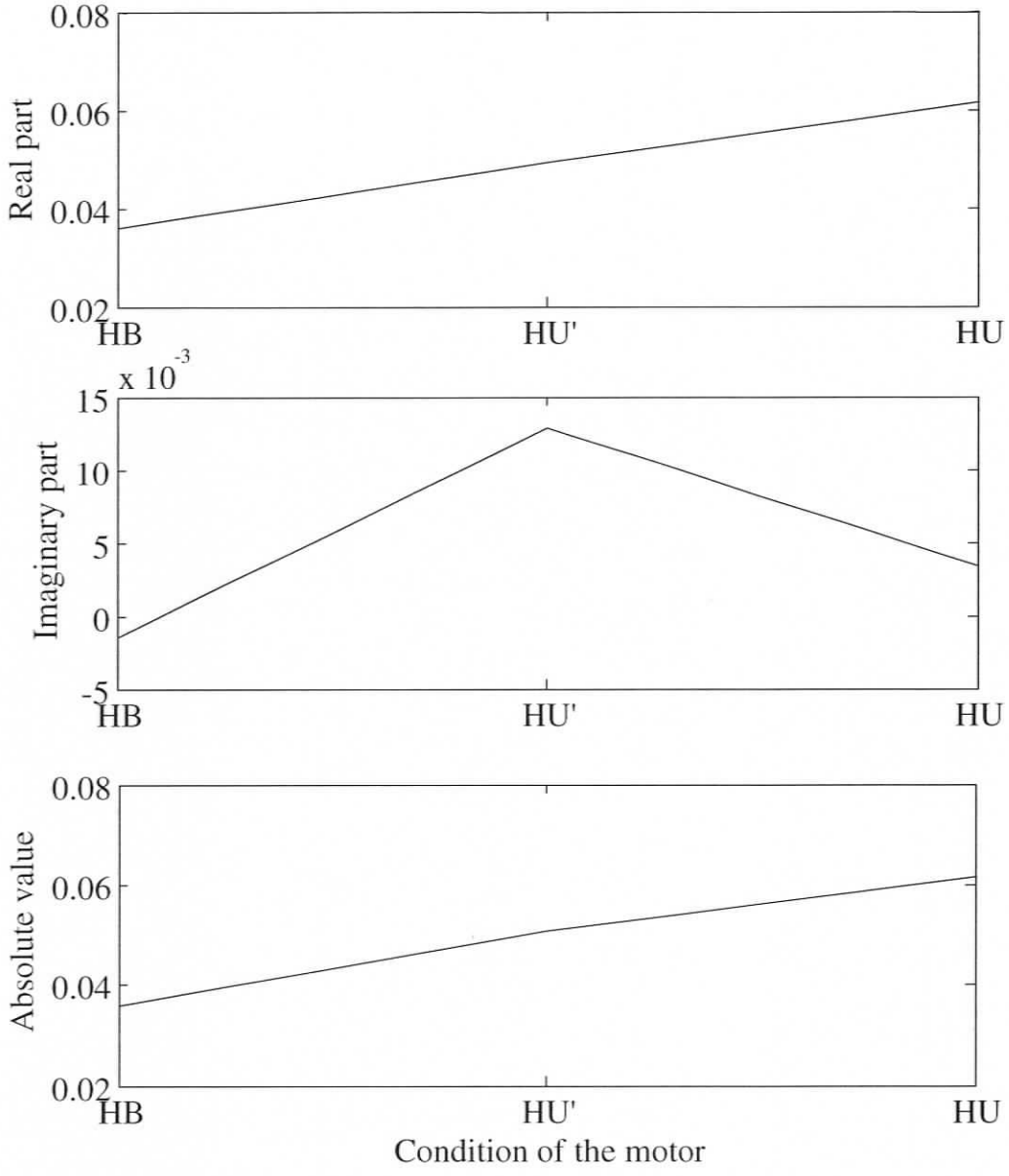

Figure 2.7 Variation of the parameter $\tilde{K}_2$ of RSM under full-load

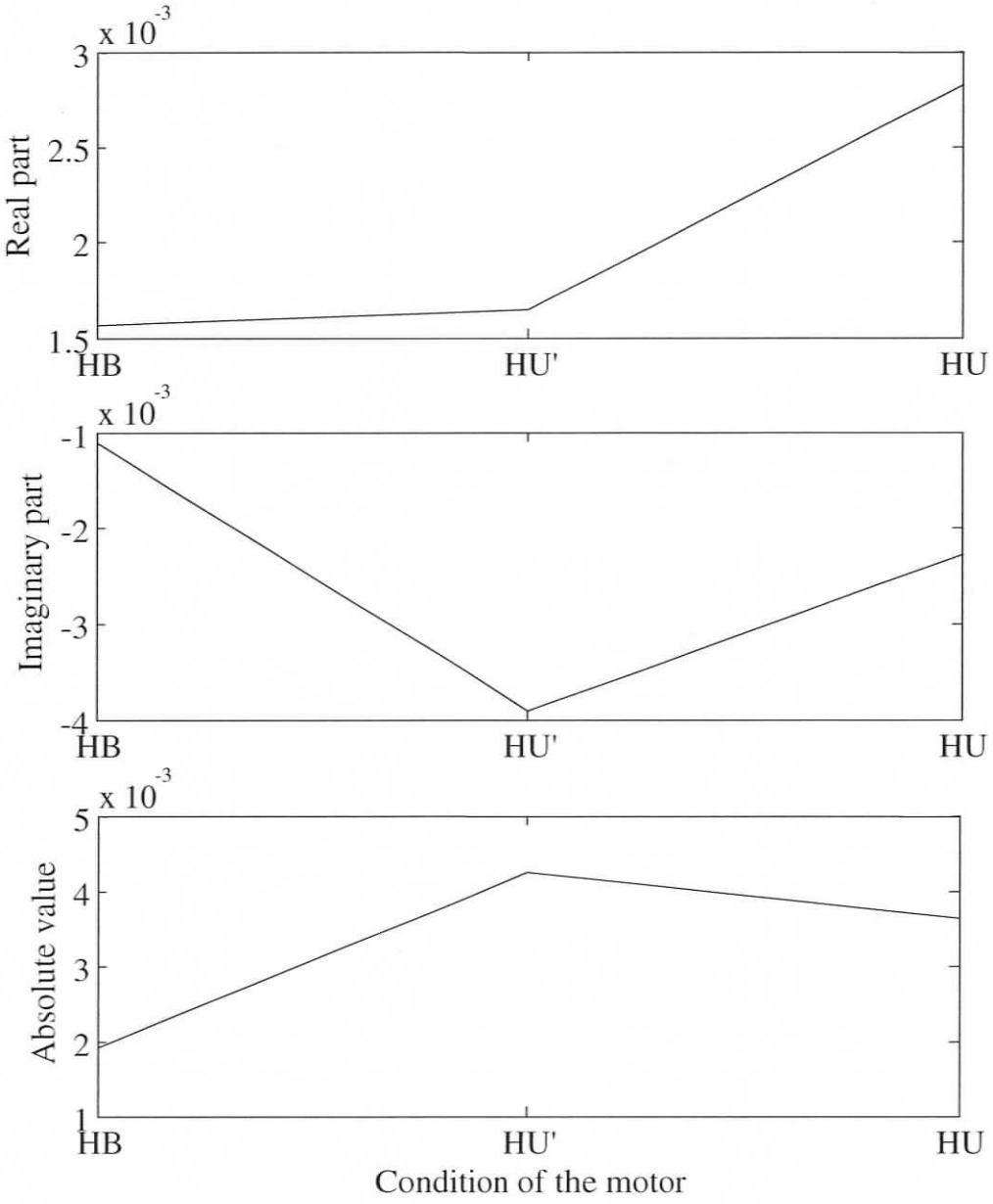

Figure 2.8 Variation of the parameter $\tilde{K}_1$ of SM with DC excitation under full-load, 0.8 lagging PF

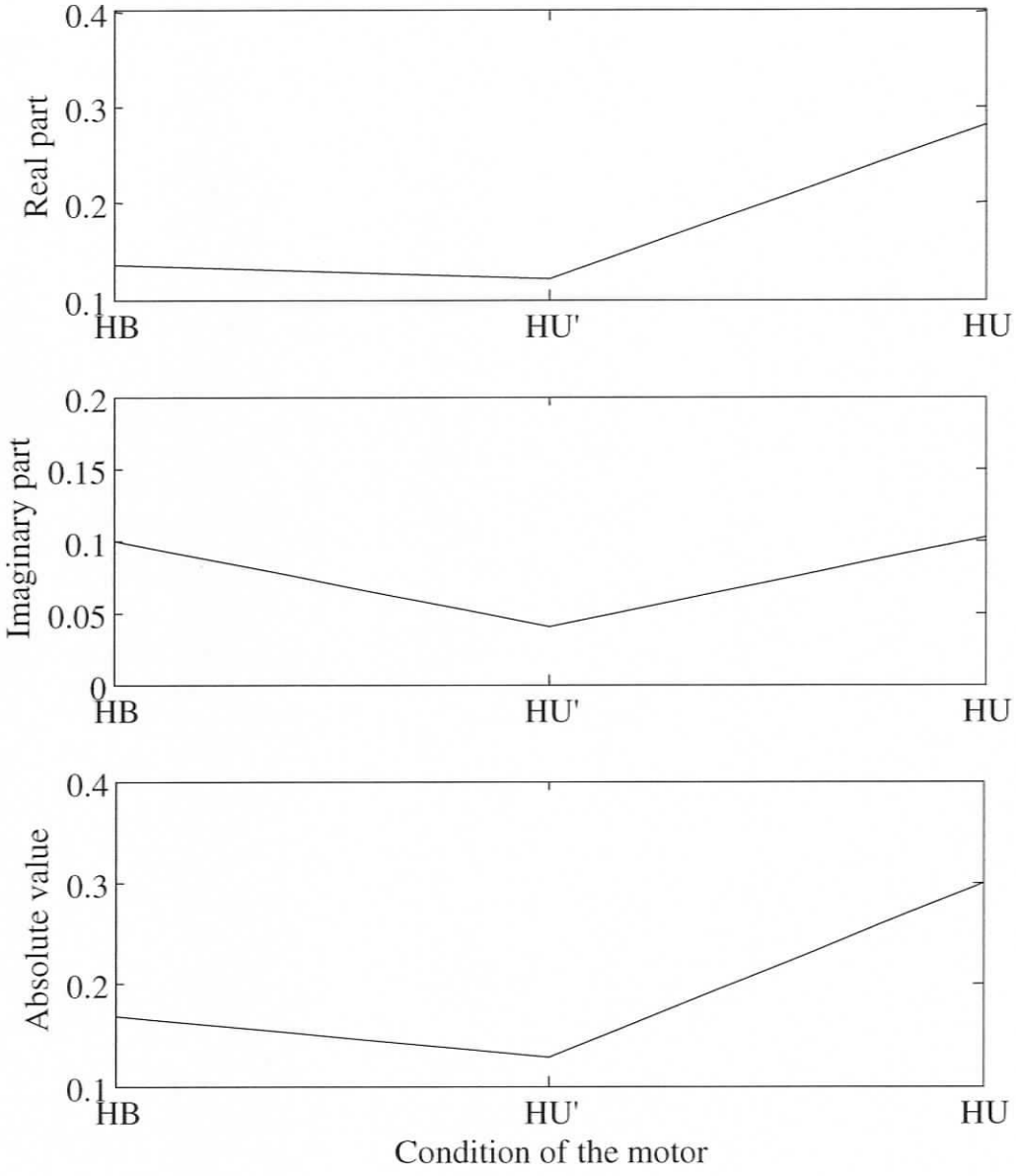

Figure 2.9 Variation of the parameter $\tilde{K}_2$ of SM with DC excitation under full-load, 0.8 lagging PF

2.4 Detection of Stator Inter-turn Faults Using Negative Sequence Quantities

In the previous section, it has been established that the parameters of the synchronous machines show considerable variation under changing supply unbalance. In this section, first the influence of these variations on the fault diagnosis of the machines has been presented. Subsequently, it is shown that improved detection of stator inter-turn faults can be obtained by mapping the effects of changing supply unbalance on the parameters $\tilde{K}_1$ and $\tilde{K}_2$.

2.4.1 Fault Analysis by Assuming the Machine Parameters to be Invariant under Changing Supply Unbalance

The complex constants $\tilde{K}_1$ and $\tilde{K}_2$ have been determined first by using the data of machine under balanced supply condition. The fault-signature of the machine can be obtained using the following formula:

$$\text{Fault-signature} = |\tilde{I}_{2\,(measured)} - \tilde{I}_{2\,(estimated)}| \tag{2.4}$$

Here, $\tilde{I}_{2\,(Measured)}$ has been obtained using (2.2) and $\tilde{I}_{2\,(Estimated)}$ has been obtained using (2.3). A fault in the machine increases the difference between $\tilde{I}_{2\,(Measured)}$ and $\tilde{I}_{2\,(Estimated)}$ thus increases the fault-signature. Both RSM and SM with DC excitation have been tested under healthy, stator inter-turn fault and supply unbalance conditions. The fault-signature thus obtained for RSM under full-load condition has been shown in Figure 2.10. Similarly, the fault-signature of SM with DC excitation under full-load condition, 0.8 lagging PF has been shown in Figure 2.11. Here, HB represents the healthy machine fed by a balanced supply whereas HU represents the healthy machine fed by unbalanced supply (1.85% for RSM and 2.12% for SM). T1 to T5 represent faults involving 1 to 5 turns in the stator windings. A large increase in the fault-signature under supply unbalance clearly indicated the ambiguity.

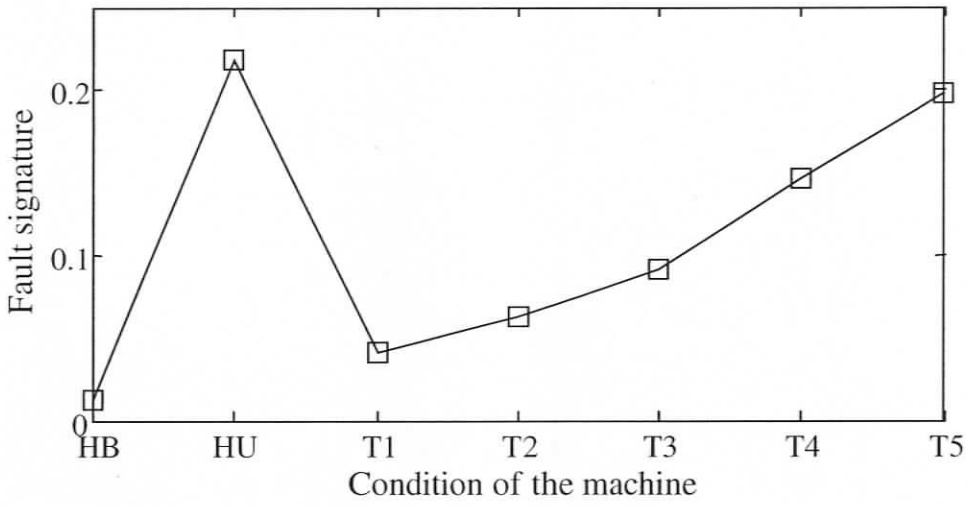

Figure 2.10 Fault-signature of RSM under full-load condition ($\tilde{K}_1$ & $\tilde{K}_2$ determined using balanced supply data)

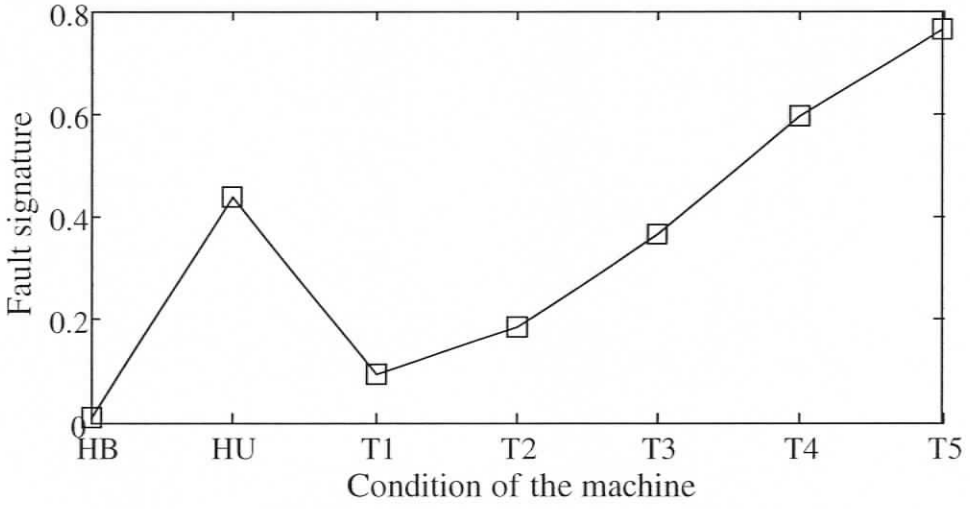

Figure 2.11 Fault-signature of SM with DC excitation under full-load, 0.8 lagging PF ($\tilde{K}_1$ & $\tilde{K}_2$ determined using balanced supply data)

The machine parameters determined using the data pertaining to the balanced supply condition failed to properly estimate the negative sequence current flowing under unbalanced supply conditions.

2.4.2 Fault Analysis by Mapping the Trend of Changing Supply Unbalance on the Machine Parameters

In an attempt to obtain improved results using this scheme, $\tilde{K}_1$ and $\tilde{K}_2$ have been determined using the machine data under balanced as well as unbalanced supply conditions. Theoretically the supply unbalance can occur in many possible ways [42]. It would be impractical to use the data under all the unbalanced conditions to determine the parameters of the machines. Hence, in this work, the machine data has been collected under six different supply unbalances (with a maximum of 2.5%) along with the balanced supply condition. The parameters of the machines have been determined using the data with five different unbalances along with the data under balanced supply condition. Both RSM and SM with DC excitation have been tested under healthy, stator inter-turn fault and supply unbalance conditions. The fault-signature thus obtained for RSM under full-load condition has been shown in Figure 2.12. Similarly, the fault-signature of SM with DC excitation under full-load condition, 0.8 lagging PF has been shown in Figure 2.13. The parameters, $\tilde{K}_1$ and $\tilde{K}_2$, have been calculated using the data of the machine obtained under HB and five different unbalances (HU1 to HU5). The data at HU has been used to check the performance of the scheme under an unbalanced supply condition that has not been used to determine the machine parameters. The various supply unbalances used for testing RSM and SM with DC excitation have been given in Table 2.3 and Table 2.4 respectively. Improved fault-signature has been obtained with the parameters of the machines computed using both balanced and unbalanced data.

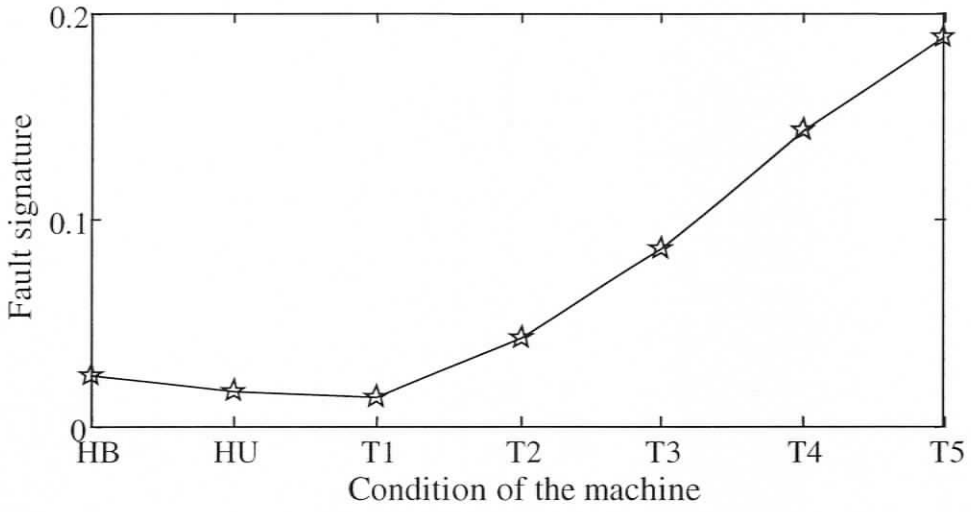

Figure 2.12 Fault-signature of RSM under full-load condition, (considering $\tilde{K}_1$ & $\tilde{K}_2$ determined using balanced as well as unbalanced supply data)

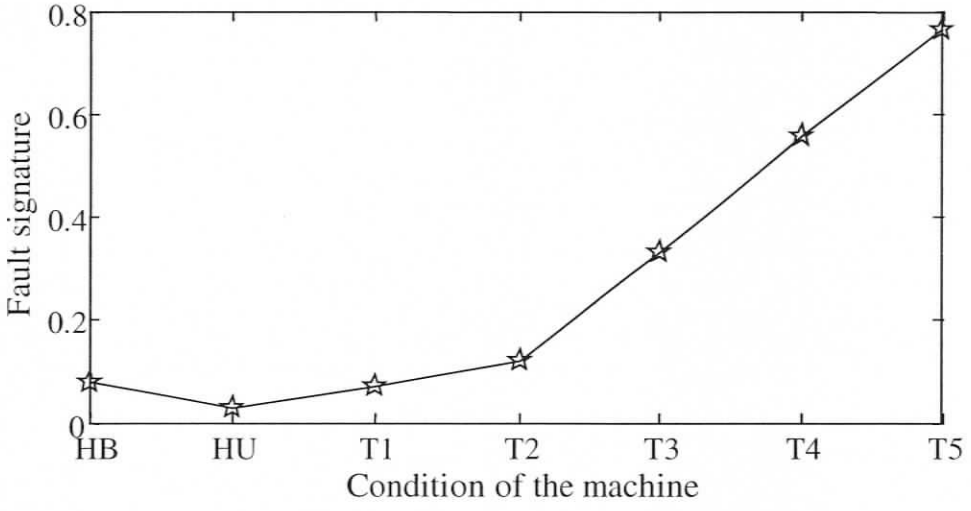

Figure 2.13 Fault-signature of SM with DC excitation under full-load, 0.8 lagging PF (considering $\tilde{K}_1$ & $\tilde{K}_2$ determined using balanced as well as unbalanced supply data)

Table 2.3 Percentage supply unbalances in the case of RSM

	No-load	Full-load
HU1	1.07	1.01
HU2	1.83	1.82
HU3	1.70	1.42
HU4	0.97	1.32
HU5	2.27	2.17
HU	1.96	1.85

Table 2.4 Percentage supply unbalances in the case of SM with DC excitation

	No-load			Half full-load			Full-load		
	0.8 Lag	0.8 Lead	UPF	0.8 Lag	0.8 Lead	UPF	0.8 Lag	0.8 Lead	UPF
HU1	1.15	1.05	1.20	0.99	1.07	1.25	1.08	1.13	1.30
HU2	1.41	1.68	1.39	1.42	1.49	1.54	1.50	1.57	1.54
HU3	1.50	1.40	1.55	1.50	1.51	1.64	1.56	1.49	1.59
HU4	1.41	1.47	1.28	1.25	1.08	1.23	1.39	1.16	1.39
HU5	1.89	2.06	2.24	2.01	2.06	2.29	1.99	2.07	2.21
HU	2.19	1.93	2.20	2.09	2.00	2.23	2.12	1.99	2.15

In order to check the dependability of this scheme, both machines have been rigorously tested under different operating points. Five different samples have been obtained for each condition of the machine at each operating point. In the case of RSM, the average fault-signatures under various supply unbalances (used for obtaining $\tilde{K}_1$ and $\tilde{K}_2$) have been given in Table 2.5.

The average fault signatures under HB, HU and T1 to T5 have been shown in Table 2.6. In each case, the sample standard deviations have been given in brackets below the corresponding average values. In the case of SM with DC excitation, the average fault-signatures and their corresponding sample standard deviations have been given in Table 2.7 and Table 2.8 respectively. The scheme could show improved detection of inter-turn faults after mapping the effects of supply unbalance on $\tilde{K}_1$ and $\tilde{K}_2$. In the case of RSM under full-load condition, at least a two-turn fault has been detected unambiguously whereas under no-load condition, at least a three-turn fault. In the case of SM with DC excitation, under full-load and half full-load conditions, at least a three-turn fault has been detected unambiguously whereas under no-load condition, at least a five-turn fault. The reason for poor detection of faults under no-load condition of SM with DC excitation could be as a result of very low magnitudes of the stator current under this condition. The distortion in current under no-load is possibly due to nonlinearities in magnetic circuit accentuated by the saliency of the machine. As an example, all the three stator currents of SM with DC excitation at no-load, UPF and full-load, UPF conditions have been shown in Figure 2.14.

Further, it is also a well known the fact that the least-square method can better describe the chosen data samples with more parameters considered for this purpose. So far, only $\tilde{K}_1$ and $\tilde{K}_2$ have been used to describe the data samples. In the case of SM with DC excitation, the neutral point of the machine was also accessible. Hence zero sequence voltage has also been considered to describe the negative sequence current as given in (2.5). The average values and the corresponding sample standard

deviations of the fault-signatures obtained with three machine parameters ($\tilde{K}_0$, $\tilde{K}_1$ and $\tilde{K}_2$) of SM with DC excitation at different operating points have been given in Table 2.9 and Table 2.10 respectively. With three constants describing the data, further improvement of fault detection can be achieved. Now, under full-load and half full-load conditions with any power factor, even a two-turn fault has been detected unambiguously whereas under no-load condition with any power factor, at least a four-turn fault. The sample calculations of $\tilde{K}_1$, $\tilde{K}_2$ and $\tilde{K}_0$, $\tilde{K}_1$ and $\tilde{K}_2$ have been given in Appendix-B.

$$\tilde{I}_2 = \tilde{K}_0\tilde{V}_0 + \tilde{K}_1\tilde{V}_1 + \tilde{K}_2\tilde{V}_2 \tag{2.5}$$

2.5 Discussions on Results and Contributions

In this work, a major drawback of fault detection scheme, based on negative sequence quantities, has been identified and a critical modification has also been suggested for improved detection of stator inter-turn faults in synchronous machines. It has been established that the effective negative sequence impedance and hence the negative sequence current of the synchronous machines changes with changing supply unbalance. Hence to achieve an improved detection of stator inter-turn faults, the data of the machine under balanced as well as unbalanced supply conditions have been used to determine the parameters of these machines. Further improvement has been achieved by considering zero sequence voltages. However, the modified scheme failed to detect a 1-turn fault. Further improvements may be achieved at the cost of more measurement and complexity [15]. Also, the values of $\tilde{K}_0$, $\tilde{K}_1$ and $\tilde{K}_2$ can change due to change in the ambient temperature and aging of the machine. Hence, in order to unambiguously detect a 1-turn stator fault in synchronous machines with less measurement, a frequency domain analysis has been carried out in the subsequent chapters.

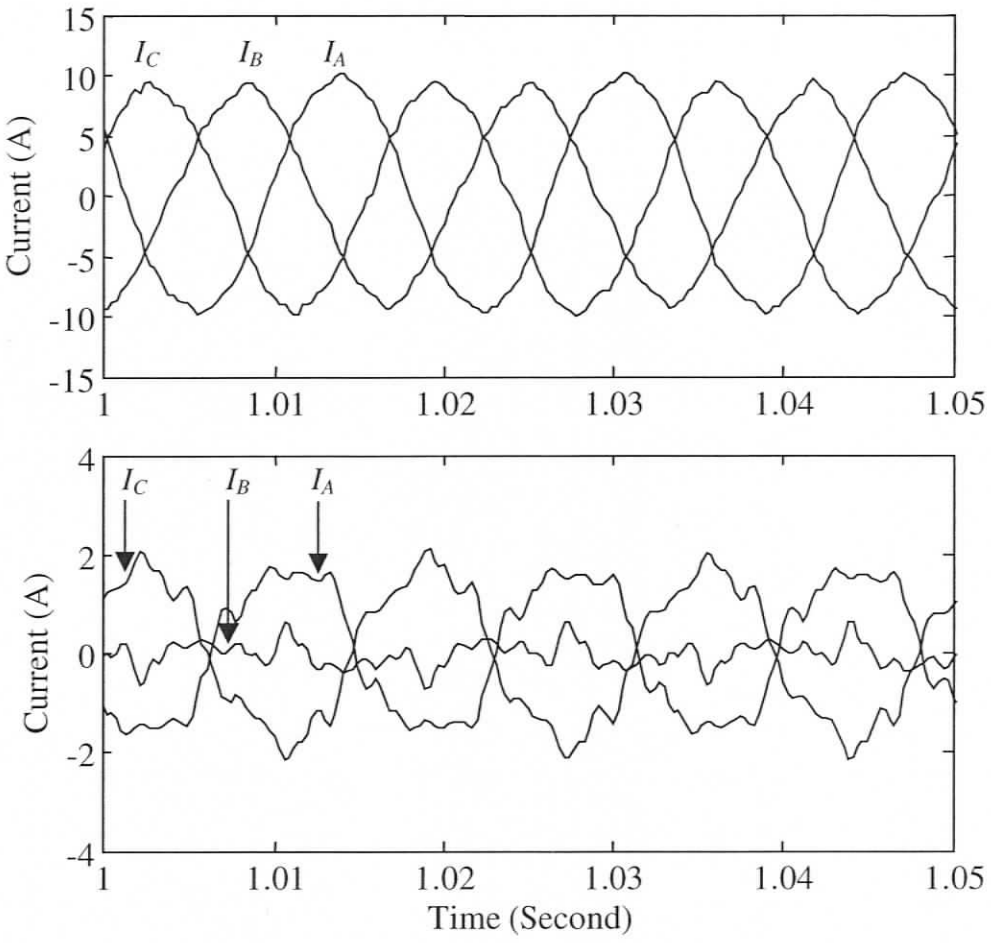

Figure 2.14 Stator currents of SM with standard field winding under full-load, UPF (top) and no-load, UPF (bottom)

Table 2.5 Experimental fault-signature of RSM using $\tilde{K}_1$ & $\tilde{K}_2$ (Under various unbalanced supplies used for obtaining $\tilde{K}_1$ & $\tilde{K}_2$)

	No-load	Full-load
HU1	0.023 (0.003)	0.008 (0.004)
HU2	0.020 (0.002)	0.011 (0.002)
HU3	0.045 (0.003)	0.024 (0.003)
HU4	0.054 (0.004)	0.036 (0.002)
HU5	0.053 (0.009)	0.035 (0.002)

Table 2.6 Experimental fault-signature of RSM using $\tilde{K}_1$ & $\tilde{K}_2$ (Under balanced, unbalanced and stator inter-turn faults)

	No-load	Full-load
HB	0.025 (0.005)	0.025 (0.008)
HU	0.027 (0.004)	0.020 (0.002)
T1	0.026 (0.010)	0.023 (0.010)
T2	0.048 (0.005)	0.054 (0.008)
T3	0.085 (0.008)	0.092 (0.009)
T4	0.118 (0.003)	0.140 (0.005)
T5	0.164 (0.002)	0.194 (0.008)

Table 2.7 Experimental fault-signature of SM with DC excitation using $\tilde{K}_1$ & $\tilde{K}_2$ (Under various unbalanced supplies used for obtaining $\tilde{K}_1$ & $\tilde{K}_2$)

	No-load			Half full-load			Full-load		
	0.8 Lag	0.8 Lead	UPF	0.8 Lag	0.8 Lead	UPF	0.8 Lag	0.8 Lead	UPF
HU1	0.020 (0.003)	0.172 (0.006)	0.063 (0.010)	0.037 (0.004)	0.132 (0.012)	0.010 (0.004)	0.022 (0.007)	0.098 (0.011)	0.039 (0.009)
HU2	0.050 (0.008)	0.036 (0.002)	0.027 (0.002)	0.053 (0.009)	0.100 (0.007)	0.052 (0.004)	0.097 (0.007)	0.030 (0.008)	0.013 (0.006)
HU3	0.178 (0.007)	0.108 (0.010)	0.203 (0.007)	0.121 (0.010)	0.184 (0.009)	0.166 (0.011)	0.096 (0.003)	0.063 (0.012)	0.132 (0.006)
HU4	0.203 (0.004)	0.301 (0.005)	0.265 (0.004)	0.127 (0.008)	0.034 (0.011)	0.152 (0.006)	0.130 (0.008)	0.078 (0.005)	0.043 (0.008)
HU5	0.153 (0.004)	0.205 (0.012)	0.244 (0.008)	0.167 (0.004)	0.058 (0.005)	0.126 (0.002)	0.166 (0.008)	0.071 (0.011)	0.105 (0.011)

Table 2.8 Experimental fault-signature of SM with DC excitation using $\tilde{K}_1$ & $\tilde{K}_2$ (Under balanced, unbalanced and stator inter-turn faults)

	No-load			Half full-load			Full-load		
	0.8 Lag	0.8 Lead	UPF	0.8 Lag	0.8 Lead	UPF	0.8 Lag	0.8 Lead	UPF
HB	0.044 (0.004)	0.053 (0.010)	0.067 (0.004)	0.064 (0.004)	0.080 (0.012)	0.070 (0.007)	0.088 (0.009)	0.066 (0.011)	0.070 (0.010)
HU 2.1	0.039 (0.006)	0.158 (0.003)	0.108 (0.009)	0.057 (0.004)	0.235 (0.008)	0.095 (0.005)	0.050 (0.015)	0.162 (0.029)	0.115 (0.006)
T1	0.045 (0.003)	0.018 (0.004)	0.028 (0.006)	0.096 (0.004)	0.156 (0.002)	0.081 (0.008)	0.064 (0.007)	0.113 (0.011)	0.113 (0.011)
T2	0.136 (0.005)	0.045 (0.004)	0.074 (0.004)	0.179 (0.006)	0.245 (0.007)	0.167 (0.004)	0.130 (0.006)	0.198 (0.007)	0.189 (0.003)
T3	0.303 (0.005)	0.159 (0.006)	0.225 (0.004)	0.352 (0.004)	0.408 (0.010)	0.355 (0.004)	0.333 (0.008)	0.390 (0.010)	0.380 (0.008)
T4	0.482 (0.006)	0.288 (0.007)	0.393 (0.006)	0.558 (0.007)	0.587 (0.006)	0.552 (0.010)	0.565 (0.010)	0.604 (0.006)	0.616 (0.017)
T5	0.681 (0.012)	0.433 (0.011)	0.563 (0.006)	0.737 (0.020)	0.758 (0.009)	0.747 (0.004)	0.802 (0.039)	0.819 (0.005)	0.834 (0.015)

Table 2.9 Experimental fault-signature of SM with DC excitation using $\tilde{K}_0$, $\tilde{K}_1$ & $\tilde{K}_2$ (Under various unbalanced supplies used for obtaining $\tilde{K}_0$, $\tilde{K}_1$ & $\tilde{K}_2$)

	No-load			Half full-load			Full-load		
	0.8 Lag	0.8 Lead	UPF	0.8 Lag	0.8 Lead	UPF	0.8 Lag	0.8 Lead	UPF
HU1	0.085 (0.003)	0.216 (0.006)	0.136 (0.002)	0.085 (0.009)	0.075 (0.012)	0.079 (0.006)	0.023 (0.011)	0.058 (0.006)	0.063 (0.008)
HU2	0.123 (0.006)	0.078 (0.003)	0.149 (0.003)	0.109 (0.012)	0.049 (0.006)	0.092 (0.009)	0.157 (0.012)	0.031 (0.018)	0.046 (0.012)
HU3	0.055 (0.005)	0.101 (0.007)	0.075 (0.004)	0.060 (0.008)	0.097 (0.006)	0.082 (0.018)	0.038 (0.005)	0.054 (0.008)	0.072 (0.008)
HU4	0.096 (0.005)	0.187 (0.009)	0.141 (0.006)	0.058 (0.010)	0.067 (0.008)	0.067 (0.008)	0.095 (0.012)	0.080 (0.007)	0.027 (0.012)
HU5	0.085 (0.004)	0.080 (0.013)	0.127 (0.005)	0.099 (0.004)	0.040 (0.008)	0.058 (0.005)	0.131 (0.007)	0.033 (0.008)	0.068 (0.009)

Table 2.10 Experimental fault-signature of SM with DC excitation using $\tilde{K}_0$, $\tilde{K}_1$ & $\tilde{K}_2$ (Under balanced, unbalanced and stator inter-turn faults)

	No-load			Half full-load			Full-load		
	0.8 Lag	0.8 Lead	UPF	0.8 Lag	0.8 Lead	UPF	0.8 Lag	0.8 Lead	UPF
HB	0.051 (0.003)	0.053 (0.009)	0.067 (0.004)	0.076 (0.005)	0.090 (0.015)	0.081 (0.007)	0.097 (0.008)	0.066 (0.013)	0.078 (0.012)
HU	0.128 (0.004)	0.244 (0.005)	0.296 (0.006)	0.105 (0.001)	0.142 (0.007)	0.100 (0.007)	0.063 (0.012)	0.104 (0.028)	0.104 (0.007)
T1	0.055 (0.004)	0.031 (0.004)	0.035 (0.005)	0.116 (0.004)	0.191 (0.002)	0.121 (0.009)	0.103 (0.010)	0.144 (0.014)	0.133 (0.013)
T2	0.145 (0.005)	0.044 (0.005)	0.071 (0.004)	0.205 (0.005)	0.288 (0.008)	0.208 (0.005)	0.178 (0.006)	0.236 (0.010)	0.217 (0.005)
T3	0.321 (0.006)	0.159 (0.008)	0.221 (0.003)	0.401 (0.008)	0.486 (0.011)	0.415 (0.004)	0.417 (0.012)	0.473 (0.007)	0.449 (0.011)
T4	0.512 (0.007)	0.289 (0.007)	0.390 (0.006)	0.639 (0.007)	0.703 (0.007)	0.643 (0.011)	0.696 (0.012)	0.740 (0.006)	0.724 (0.015)
T5	0.727 (0.014)	0.440 (0.011)	0.564 (0.006)	0.859 (0.022)	0.921 (0.011)	0.870 (0.005)	0.981 (0.046)	1.008 (0.009)	0.990 (0.011)

Chapter 3

Modeling of Synchronous Machines under Healthy Condition

Based on the findings of the previous chapter, it can be safely concluded that traditional negative sequence current based estimation failed to detect stator faults involving very few turns in RSM and SM. Hence frequency domain based approaches are attempted next. In the condition monitoring of electric machines, the fault is diagnosed based on their deviation in performance from that of the healthy machines, which are considered reference conditions. Hence, as a first step to conduct a frequency domain analysis, a study has been conducted on the performance of the healthy synchronous machines. For this purpose, initially a simulation analysis has been proposed. The simulated models play a vital role in conducting theoretical study with greater flexibility. Some of the signals that cannot be directly accessed in the practical motors, such as the currents in the damper bars, can be easily modeled and analyzed with the help of the simulated models. Also these models allow studying the behaviour of the machines under ideal operating conditions and then the deviation of actual signals from the ideal. Hence, a detailed modeling of synchronous machines has been presented. In the following sections, several finer aspects of the modeling have been discussed in detail. Finally, these models have been validated using suitable experiments.

3.1 Turns Functions and Modeling Approach

In this section, the turns functions of stator windings, rotor loops and the field windings the synchronous machines, described in section 2.1, have been described in

detail. Also, using these turns functions, a detailed description of the modeling approach of the synchronous machines has been presented.

3.1.1 Turns Functions of the Stator Windings of Synchronous Machines

The turns functions of the stator phase-A of the RSM and SM with DC excitation are as shown in Figure 3.1 and Figure 3.2 respectively. The turns functions of the phase-B and phase-C of these motors will be similar to that of their phase-A, but will be displaced by 60° and 120° (mechanical) respectively. The turns functions of phase-A, phase-B and phase-C of both RSM and SM with DC excitation can be expressed using Fourier series expansions as given in (3.1)-(3.3) with different coefficients for each of the motors as mentioned.

$$n_A(\phi) = a_{os} + \sum_{m=1,3,5,\ldots}^{\infty} a_{ms} \cos\left(pm\,\phi\right) \tag{3.1}$$

$$n_B(\phi) = a_{os} + \sum_{m=1,3,5,\ldots}^{\infty} a_{ms} \cos\left[pm\left(\phi - \frac{x}{p}\right)\right] \tag{3.2}$$

$$n_C(\phi) = a_{os} + \sum_{m=1,3,5,\ldots}^{\infty} a_{ms} \cos\left[pm\left(\phi - \frac{2x}{p}\right)\right] \tag{3.3}$$

Here, $x = \frac{2\pi}{3}$ and p = number of fundamental pole pairs = 2. In the case of RSM,

$$a_{os} = \frac{3N}{2},\ N = 47, a_{ms} = \frac{2N}{\pi m}(-1)^{(m-1)/2}\left\{1 + 2\cos\left(\frac{\pi m}{9}\right)\right\}$$

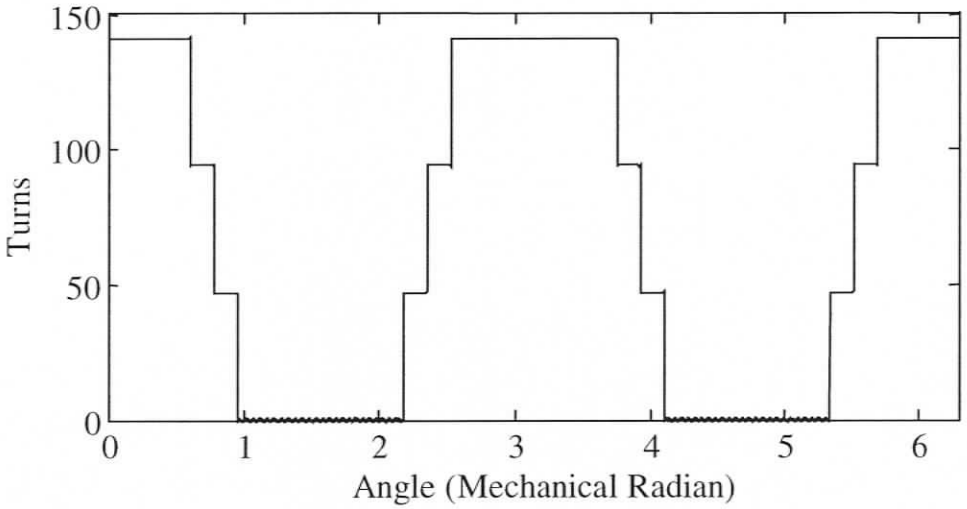

Figure 3.1 Turns function of stator phase-A of RSM

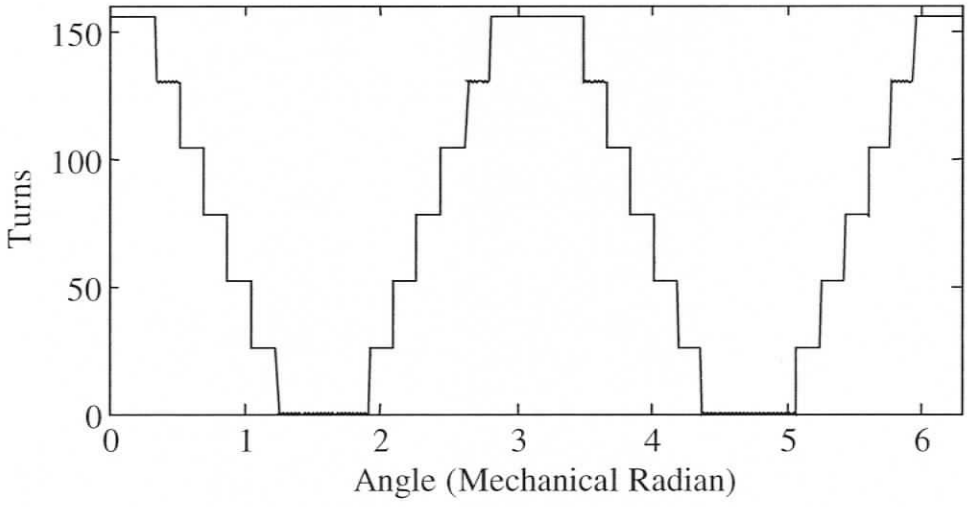

Figure 3.2 Turns function of stator phase-A of the SM with DC excitation

In the case of a SM with DC excitation,

$$a_{os} = \frac{3N}{2},\ N = 26,\ a_{ms} = \frac{2N}{\pi m}\sin\left(\frac{\pi m}{3}\right)\left\{1 + 2\cos\left(\frac{\pi m}{9}\right)\right\}$$

3.1.2 Turns Functions of the Rotor Loops of Synchronous Machines

The synchronous machines have damper bars, six on each rotor-pole of RSM whereas five on each rotor-pole of SM with DC excitation. These bars have a skew of one rotor slot pitch. They form several loops since they are shorted on either end of the rotor. The turns function of a typical rotor loop lying in the inter-polar gap is as shown in Figure 3.3. The Fourier expansion of this function is given by (3.4).

$$\begin{aligned} n_r(\phi,\theta) &= a_{or} + \sum_{w=1,2,3,..}^{\infty} a_{wr}\cos\left[w(\phi-\theta)\right] \\ a_{or} &= \frac{a+2b}{2\pi} \\ a_{wr} &= \frac{2}{a\pi w^2}\left[\cos(wb) - \cos\{w(a+b)\}\right] \end{aligned} \tag{3.4}$$

Here 'a' is the angle subtended by one rotor slot at the centre of the rotor and 'b' is half of the angle subtended by the rotor bars on either side of inter polar gap. The values of 'a' and 'b' will be different for RSM and the SM with DC excitation.

3.1.3 Turns Functions of the Field Windings of Synchronous Machines

The turns functions of the standard and the two-coil field windings have been shown in Figure 3.4 and Figure 3.5 respectively whereas their corresponding Fourier expansions have been given in (3.5) and (3.6).

$$n_{rf1}(\phi,\theta) = a_{orf1} + \sum_{m=1,3,5,\ldots}^{\infty} a_{mrf1} \cos\left[pm(\phi-\theta)\right]$$
$$a_{orf1} = \frac{N_{rf}}{2},\ N_{rf} = 1260,\ a_{mrf1} = \frac{2N_{rf}}{\pi m}\sin(m\theta_d) \tag{3.5}$$

$$n_{rf2}(\phi,\theta) = a_{orf2} + \sum_{w=1,2,3,\ldots}^{\infty} a_{wrf2} \cos\left[pw(\phi-\theta)\right]$$
$$a_{orf2} = \frac{N_{rf}\theta_d}{\pi},\ N_{rf} = 1260,\ a_{wrf2} = \frac{2N_{rf}}{\pi w}\sin(w\theta_d) \tag{3.6}$$

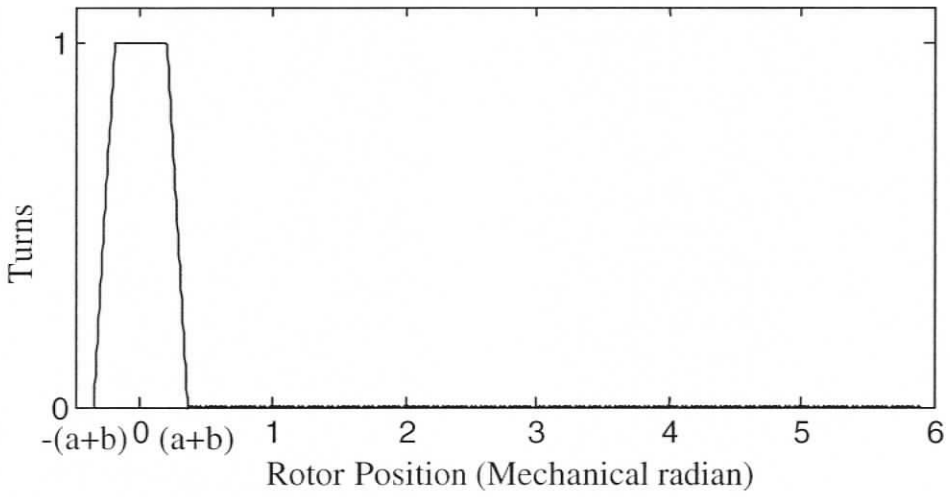

Figure 3.3 Turns function of a rotor loop of the synchronous machines (lying on the inter-polar gap)

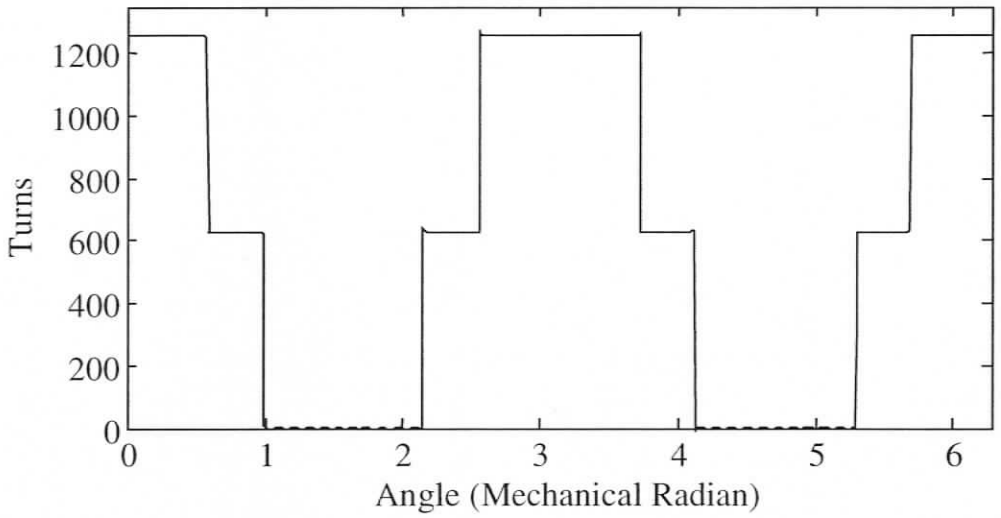

Figure 3.4 Turns function of standard field winding of SM

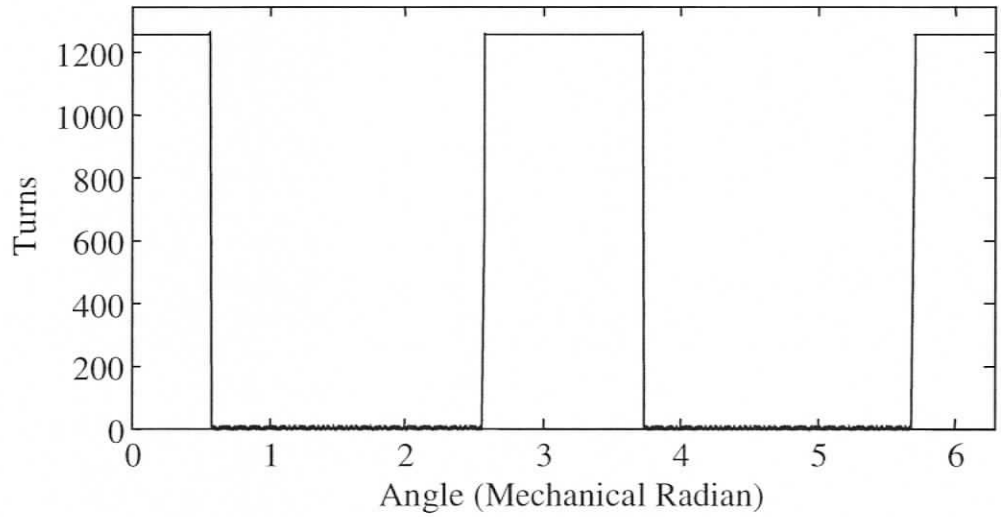

Figure 3.5 Turns function of two-coil field winding of SM

3.1.4 Inverse Air-gap Function of Synchronous Machines

The inverse air-gap function of both RSM and SM with DC excitation can be as shown in Figure 3.6. Here D, Q, θ_d and θ_q will have different values for each machine. The Fourier series expansion of the inverse air-gap function of these machines, $g^{-1}(\phi, \theta)$, can be expressed as given in (3.7).

$$
\begin{aligned}
g^{-1}(\phi,\theta) &= a_{og} + \sum_{k=2,4,6,..}^{\infty} a_{kg} \cos\{pk(\phi-\theta)\} \\
a_{og} &= \frac{2}{\pi}\left(D\,\theta_d + Q\,\theta_q\right) \\
a_{kg} &= \frac{4(Q-D)}{\pi k}(-1)^{(k+4)/2}\sin(k\theta_q)
\end{aligned}
\tag{3.7}
$$

Here,

D = 1/Effective air-gap length along the direct-axis

Q = 1/Effective air-gap length along the quadrature-axis

θ_d = Angle subtended by the polar arc at the centre of the rotor

θ_q = Angle subtended by the inter-polar arc at the centre of the rotor

ϕ = Space angle (mechanical radian) with respect to stator frame of reference and

θ = Rotor position (mechanical radian).

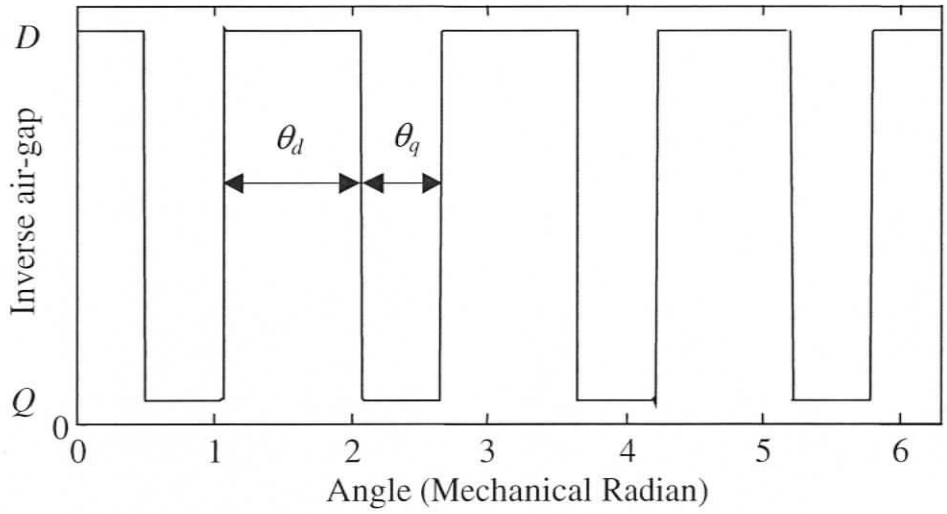

Figure 3.6 Inverse air-gap function of synchronous machines

3.1.5 Leakage Inductance of Stator Winding of Synchronous Machines

The leakage inductance of the stator winding also plays a very important role in the modeling of the machines. A method proposed by Hobart and Canfield [43] has been applied to determine the leakage inductance of the stator winding/phase. This method, though not very accurate, gives reasonably good results with less computational efforts compared to the method proposed by Alger [44]. The present method takes slot leakage and end winding leakage into account. The expression for the leakage inductance/phase (L_l) can be given as shown in (3.8).

$$L_l = \left(\frac{2pC_p^{\,2}}{10^8 m_p^{\,2}} \right) \left(\phi_e L_n + \frac{L_2}{n_p} \right) \tag{3.8}$$

In the case of RSM,

C_P = Number of conductors / phase / pole = 141

m_p = Number of paths = 1

n_p = Number of layers of stator winding = 1

L_n = Net axial length of the stator iron = 4.49 inch

L_2 = Mean length of the end winding = 10 inch

ϕ_e = Number of flux lines per ampere-turn per inch = 11.

By substituting the above quantities in (3.8), the value of leakage inductance of RSM has been obtained as

$$L_l = 0.0472 \text{ H/phase}$$

The leakage inductance of SM with DC excitation has been obtained by extrapolating the results of a similar machine from a standard textbook [45] and has been calculated to be

$$L_l = 0.0076 \text{ H/phase}$$

3.1.6 Modeling Approach of Synchronous Machines

In this work, the modeling of the synchronous machines has been carried out using the coupled circuit approach that requires various magnetizing and mutual inductances of the machine. In order to compute these inductances, winding function approach (WFA) and modified winding function approach (MWFA) have been used [46-50]. Based on WFA and MWFA, the inductance between any two windings can be computed using (3.9) and (3.10) respectively.

$$L_{12} = \mu_0 rl \int_0^{2\pi} \left[n_1(\phi) N_2(\phi) g^{-1}(\phi,\theta) \right] d\phi$$
$$N_2(\phi) = n_2(\phi) - \left\langle n_2(\phi) \right\rangle \tag{3.9}$$

$$L_{12} = \mu_o rl \left[\int_0^{2\pi} n_1(\phi,\theta) n_2(\phi,\theta) g^{-1}(\phi,\theta) d\phi - 2\pi a_{og} < M_1(\theta) >< M_2(\theta) > \right] \tag{3.10}$$
$$where \ , \ < M_x(\theta) > = \frac{1}{2\pi a_{og}} \int_0^{2\pi} n_x(\phi,\theta) g^{-1}(\phi,\theta) d\phi$$

Here,

μ_o = Permeability of the free space

r = Radius of the rotor and

l = Stack length.

In order to compute these inductances using WFA and MWFA, machine data are required. Most of this data can be obtained from the information furnished by the manufacturers. However, the manufacturer do not supply some information such as the effective air-gap lengths along the direct and quadrature axes that plays very important role in the performance of these machines. Usually, these effective air-gap lengths were obtained on a trial and error basis. Since the saturation levels are different along the direct and quadrature axes, it is difficult to predict the values of the effective air-gaps accurately. Hence, in the present work, the effective air-gaps of the machines have been determined in a more systematic manner that uses experimentally determined values of the direct and quadrature axes reactances.

Also, it is very important to note that the effective air-gaps play a vital role in the performance of RSM in particular. The principle of operation of RSM indicates that its operating torque is critically dependent on the difference between the direct axis

and the quadrature axis reactances, X_d and X_q, respectively [51]. To maximize the difference between X_d and X_q, special types of rotor constructions have been employed [52]. Since these reactances are directly related to the effective air-gap lengths, it became essential to determine them.

In the subsequent sections, various critical aspects of modeling of both RSM and SM with DC excitation have been discussed in depth. The developed models have also been experimentally validated.

3.1.7 Experimental Determination of Direct and the Quadrature Axes Reactances of the Synchronous Machines

The direct and the quadrature axes reactances are operating point dependent. Hence, a new method based on the P-Q diagram of the machine [53, 54] has been adopted to determine them. This method seems to be much superior compared to the conventional slip test. This method makes use of the data pertaining to different operating points of the machine. The load-test readings of both RSM and SM (run without DC excitation) are as shown in Table 3.1 and Table 3.2 respectively.

In the case of RSM, readings near no-load have been considered to avoid the effect of flux barriers. The attributes of the reactance circle can be obtained by solving (3.11) for p_c, q_c and $(p_c^2+q_c^2-R^2)$, where (p_c, q_c) are the co-ordinates of the centre and R is radius of the circle. P_1, P_2 & P_3 are the real powers per phase; Q_1, Q_2 & Q_3 are the reactive powers per phase whereas S_1, S_2 & S_3 are the apparent powers per phase at three different operating points.

$$\begin{bmatrix} q_c \\ p_c \\ p_c^{\,2} + q_c^{\,2} - R^2 \end{bmatrix} = \begin{bmatrix} -2Q_1 & -2P_1 & 1 \\ -2Q_2 & -2P_2 & 1 \\ -2Q_3 & -2P_3 & 1 \end{bmatrix}^{-1} \begin{bmatrix} -S_1^{\,2} \\ -S_2^{\,2} \\ -S_3^{\,2} \end{bmatrix} \qquad (3.11)$$

Using data from Table 3.1 and solving (3.11) leads to the following results:

p_c = -74.6610,

q_c = -656.7440 and

R = 183.1929.

Table 3.1 Load test data of RSM

SL. No.	Line Current I_L (A)	Real Power P_P (Watt)	Reactive Power Q_P (VAR)	Apparent Power S_P (VA)
1	1.8	137.68	1427.50	1434.14
2	1.9	416.29	1455.45	1513.81
3	2.0	519.00	1506.59	1593.49

Table 3.2 Load test data of SM run without DC excitation

SL. No.	Line Current I_L (A)	Real Power P_P (Watt)	Reactive Power Q_P (VAR)	Apparent Power S_P (VA)
1	5.83	389	4628.6	4644.9
2	6.16	570	4874.6	4907.8
3	6.72	741	5302.4	5354.0

The direct and quadrature axes reactances of the machine can then be obtained by solving (3.12)-(3.14) as given in (3.15).

$$\frac{r}{X_q} = 0.5\left[\frac{|p_c - R| - |p_c + R|}{|q_c + R|}\right] \tag{3.12}$$

$$\frac{X_d}{X_q} = 1 + \left[\frac{|p_c - R| + |p_c + R|}{|q_c + R|} \right] \tag{3.13}$$

$$X_d = \frac{V_{ph}{}^2 X_d X_q}{|q_c + R|\left(X_d X_q + r^2\right)} \tag{3.14}$$

$$\begin{aligned} X_d &= 146.887\,\Omega, \quad L_d = 0.3896\,H \\ X_q &= 82.8084\,\Omega, \quad L_q = 0.2197\,H \end{aligned} \tag{3.15}$$

Following a similar procedure, the direct and the quadrature axes reactances of the SM having DC excitation have been obtained as given in (3.16).

$$\begin{aligned} X_d &= 50.3112\,\Omega, \quad L_d = 0.13345\,H \\ X_q &= 29.0436\,\Omega, \quad L_q = 0.07704\,H \end{aligned} \tag{3.16}$$

3.2 Determination of Effective Air-Gaps

The air-gap lengths have been computed by comparing the theoretically obtained coefficients of the direct and quadrature axes inductances with the corresponding experimentally determined values as discussed in the next sections.

3.2.1 Derivation of Stator Inductances of Synchronous Machines using WFA

Since the turns functions of the stator windings and the inverse air-gap function of the machines are known, by using WFA, the inductance between any two phases, phase '*u*' and phase '*v*' of stator winding can be obtained.

Substituting for $n_1(\phi)$, $N_2(\phi)$ from (3.1)-(3.3) and $g^{-1}(\phi, \theta)$ from (3.7) in (3.9), the

general expression for the inductance between any two phases with any number of winding space harmonics (m) and permeance related harmonics (k) can be obtained as given in (3.17).

$$L_{uv} = \left[Z_0 + \sum_{k = 2,4,6,..}^{\infty} Z_k \cos\left[pk\theta - \frac{k\{(u-1)+(v-1)\}x}{p} \right] \right] \quad (3.17)$$

$$Z_0 = \frac{2\pi\mu_o rl\ a_{og}}{2} \left[\sum_{m = 1,3,5,..}^{\infty} (a_{ms})^2 \cos\left[m(v-u)x\right] \right],$$

$$Z_k = 2\pi\ \mu_o rl\,(A_r + A_f)a_{kg}$$

$$A_f = \sum_{m=1,3,..}^{\infty} \frac{a_{ms}\,a_{(k+m)s}}{2} \cos\left[\left(\frac{k}{2} + m \right)(v-u)x \right],$$

$$A_r = \sum_{\substack{m=1,3,... \\ (k-m)>0}}^{\infty} A_{ar}, \quad A_{ar} = \frac{a_{ms}\,a_{(k-m)s}}{4}, \ for \ \ k = 2m,$$

$$A_{ar} = \frac{a_{ms}\,a_{(k-m)s}}{2} \cos\left[\left(\frac{k}{2} - m \right)(v-u)x \right], \ \ for\ k \neq 2m$$

For a 3-phase machine, the values of u & v to be used for computations are as follows:

$u = v = A = 1; \quad u = v = B = 2; \quad u = v = C = 3$

Also, if $u = v$ then $Z_0 = L_0$ & $Z_k = L_k$

Otherwise, $Z_0 = M_0$ & $Z_k = M_k$

By choosing the values of u and v according to the phases, various magnetizing and mutual inductances can be obtained whereas by varying m and k the winding harmonics and air-gap harmonics can be varied. A sample computation for L_{uv} for u =

A and $v = B$ is shown in Appendix-C. In order to compute any stator inductance using equation (3.17), all the parameters are known except the effective air-gap lengths of the machines along its direct and quadrature axes, D and Q respectively.

3.2.2 Determination of Effective Air-gap Lengths along Direct and Quadrature Axes of the Synchronous Machines

It is known that the saliency of the machine and non-sinusoidal distribution of the windings have a direct influence on machine inductances [55, 56]. Suitably using this concept, the effective air-gap lengths along the direct and quadrature axes can be found by comparing the coefficients of stator inductances with the experimentally determined values of direct and quadrature axis inductances. The relation between the coefficients of stator inductances and L_d & L_q can be established for any higher number of space and permeance related harmonics by using the definition of L_d and L_q [57], i.e., the net flux linkage per unit phase current when the magneto motive force (MMF) axis coincides with the direct and the quadrature axis respectively. The net flux linkage per unit phase current at any rotor position can then be obtained based on the definition provided in [57] as,

$$L = L_{AA} - 0.5(L_{AB} + L_{AC}) + L_l \tag{3.18}$$

According to [57] this function will have maxima and minima when the MMF axis coincides with the direct and quadrature axes respectively and corresponding values of the function are L_d and L_q. Two simultaneous equations with two variables (D & Q) can be obtained at the maxima and the minima of (3.18). The solution of these simultaneous equations gives rise to the required air-gap lengths. In fact, the position of the maxima and minima of the function L, as given by (3.18), depend on the number of fundamental pole pairs of the machine. For the machines under consideration, with 2 fundamental pole pairs, the maxima and minima can occur at $\theta = 0$ & $\theta = \pi/4$ mechanical radian respectively. Upon substituting for L_{AA}, L_{AB} and L_{AC}

in (3.18) from (3.17) and computing maxima and minima gives rise to the following general expressions of L_d and L_q for any number of higher space and permeance related harmonics as given by (3.19)-(3.20) (derivation shown in Appendix-C).

$$L_d = \sum_{n=0,1,2,3,\ldots} L_{2n} - \sum_{m=0,1,2,3,\ldots} M_{6m} + 0.5 \sum_{p=1,3,5,\ldots} M_{(3p\pm1)} + L_l \tag{3.19}$$

$$L_q = \sum_{n=0,1,2,3,\ldots} (-1)^n (L_{2n}) - \sum_{m=0,1,2,3,\ldots} (-1)^m (M_{6m}) + 0.5 \sum_{p=0,1,2,3,\ldots} (M_{(12p\pm4)} - M_{(12p\pm2)}) + L_l \tag{3.20}$$

(only for the positive subscripts of M)

However, one does not have to use (3.19) and (3.20) to compute *Ld* and *Lq* in practice. MATLAB built-in functions "MAX" and "MIN" can be used for this purpose on an array of values of L at different rotor positions. The array can be formed using (3.18).

Presently, the following three different cases have been considered with different space harmonics (m) and permeance harmonics (k):

(i) $k = 2$ & $m = 1$

(ii) $k = 2$ & $m = 21$ and

(iii) $k = 4$ & $m = 21$.

The comparison of the results for above cases along with the physical measurements of the air-gap lengths of the RSM has been shown in Table 3.3.

It can be clearly seen that the d-axis length does not vary much but the q-axis length varies widely. However, for the simulation purpose, better accuracy of d-axis length mattered more for a stable model. The readings near no-load have been considered as the effects of flux barriers are minimal at no-load and will then match with the model which did not include the flux barrier effects. This can be explained using stator voltages and currents under no-load (V_{tnL} & I_{anL}) and full-load (V_{tfL} & I_{afL}) as shown in Figure 3.7. For a synchronous machine under no-load condition the load-angle, δ_{nL}, is low. With the polarized section of the rotor lying almost right below the poles of the rotating magnetic field, the influence of flux barriers is minimal. This has also been verified using finite element analysis given later in this chapter as shown in Figure 3.21 and Figure 3.22). In the case of the RSM, the sample calculations of case (i) $k = 2$ & $m = 1$ are as follows. L_0 and L_2 can be obtained by considering fundamental space harmonic. Using (3.19) and (3.20)

Table 3.3 Comparison of air-gaps of RSM

Air-gap	Physical	Effective (With $k = 2$ & $m = 1$)	Effective (With $k = 2$ & $m = 1, 3,.., 21$)	Effective (With $k = 2, 4$ & $m = 1, 3,.., 21$)
Along d-axis (mm)	0.392	0.6418	0.5821	0.5912
Along q-axis (mm)	11.56	3.0724	18.8679	37.3134

$$L_d = L_l + 1.5\ [L_0 + L_2]$$
$$L_q = L_l + 1.5\ [L_0 - L_2] \tag{3.21}$$

Here,

$$L_0 = 2\pi\ \mu_o rl\ a_{og}\ \frac{a_{1s}^{\ 2}}{2}\ and\quad L_2 = 2\pi\ \mu_o rl\ a_{2g}\ \frac{a_{1s}^{\ 2}}{4}$$

Substituting the values of various quantities, (3.21) can be written as

$$\begin{bmatrix} 0.2158 & 0.0188 \\ 0.0779 & 0.1566 \end{bmatrix} \begin{bmatrix} D \\ Q \end{bmatrix} = \begin{bmatrix} 342.4 \\ 172.5 \end{bmatrix} \tag{3.22}$$

Solving (3.22), the effective air-gap lengths can be calculated as

$$d = 1/D = 0.6418\ \ mm$$
$$q = 1/Q = 3.0724\ \ mm \tag{3.23}$$

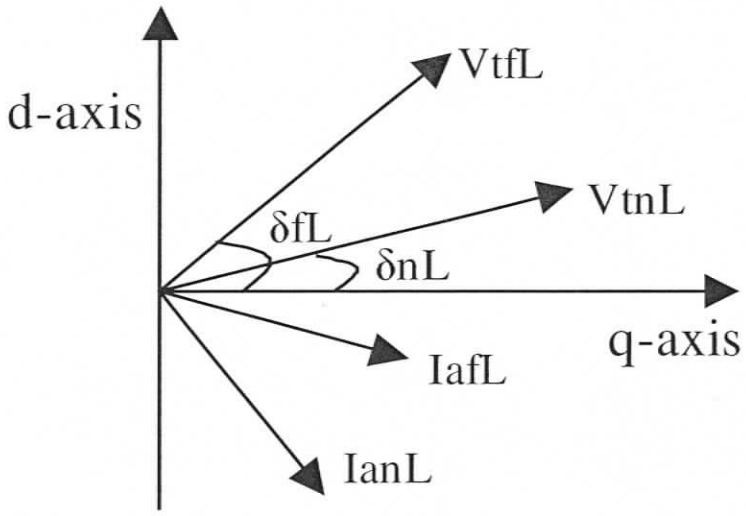

Figure 3.7 Vector diagram of no-load and full-load quantities

A similar procedure has been adopted to compute the effective air-gaps of the SM with DC excitation when run as a RSM (i.e., without field excitation). The comparison of the results for the cases, (i) $k = 2$ & $m = 1$, (ii) $k = 2$ & $m = 21$ and (iii) $k = 4$ & $m = 21$, with the physical measurements of the air-gaps of synchronous machine has been shown in Table 3.4. Even in the case of synchronous motor, it can be clearly seen that the computed values of q-axis air-gap lengths are sensitive to the permeance and winding space harmonics. The effective air-gap along the d-axis is nearly three times the physical air-gap. This is due to the fact that its pole-arc is not circular as shown in Figure 3.8. The minimum value of the physical air-gap at the pole tip is 0.6mm whereas the maximum value of physical air-gap at the pole edge is 1.35mm. Because of the absence of flux barriers the results seem to be more accurate.

Table 3.4 Comparison of air-gaps of SM with DC excitation

Air-gap	Physical	Effective (With $k = 2$ & $m = 1$)	Effective (With $k = 2$ & $m = 1, 3,.., 21$)	Effective (With $k = 2, 4$ & $m = 1, 3,.., 21$)
Along d-axis (mm)	0.6	1.7411	1.7516	1.7769
Along q-axis (mm)	40.27	32.2552	39.9151	59.1058

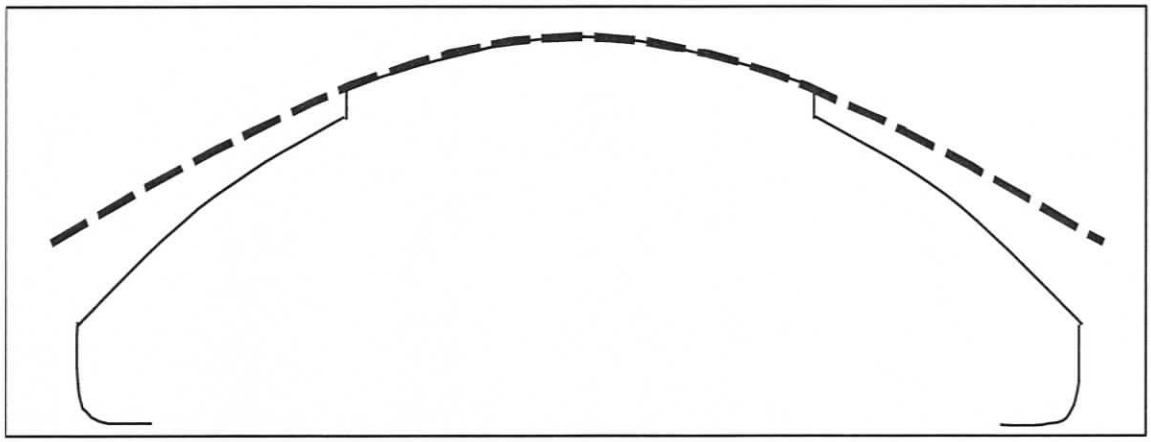

Figure 3.8 Pole-arc of SM with DC excitation

3.3 Computation of Stator Inductances of Synchronous Machines using WFA

Various magnetizing inductances of both RSM and SM with DC excitation have been computed using WFA as discussed in the following sections. The computed inductances have been verified by using finite element analysis as given in Appendix-D.

3.3.1 Stator Inductances of RSM

From the computed values of the effective air-gap lengths of the synchronous machines, various stator inductances can be now obtained using (3.17). The variation of stator magnetizing and mutual inductances of the RSM with respect to the rotor position are as shown in Figure 3.9 and Figure 3.10 respectively.

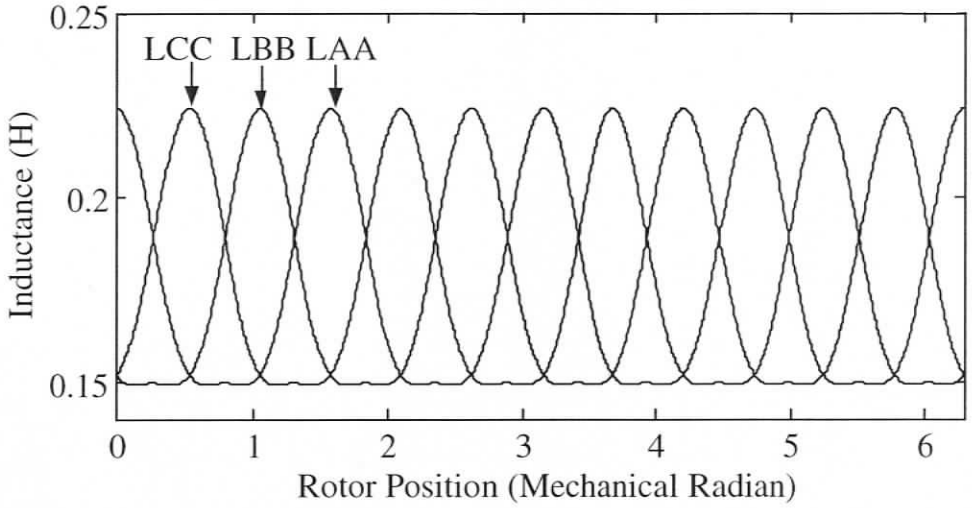

Figure 3.9 Stator magnetizing inductances of RSM

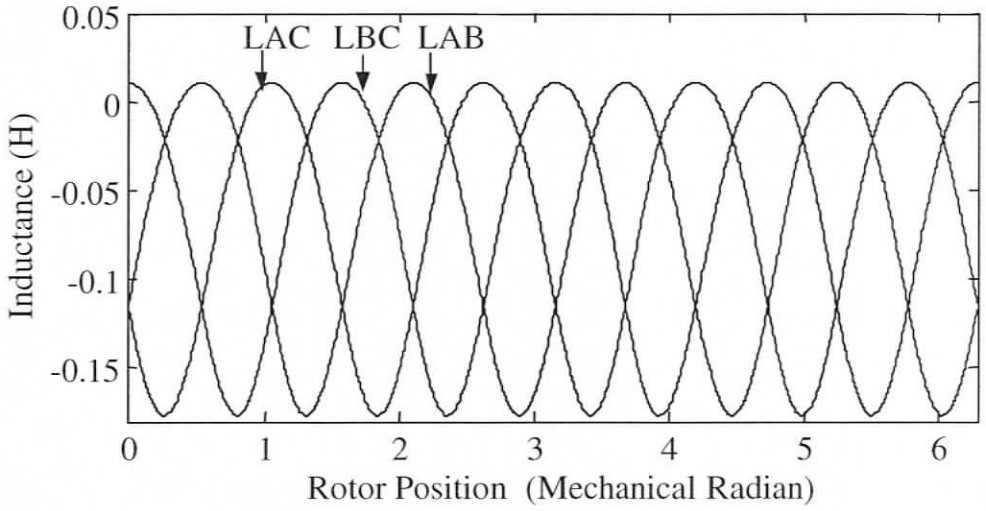

Figure 3.10 Stator mutual inductances of RSM

3.3.2 Stator Inductances of SM with DC Excitation

The variation of stator magnetizing and mutual inductances of the SM with DC excitation with respect to the rotor position are as shown in Figure 3.11 and Figure 3.12 respectively.

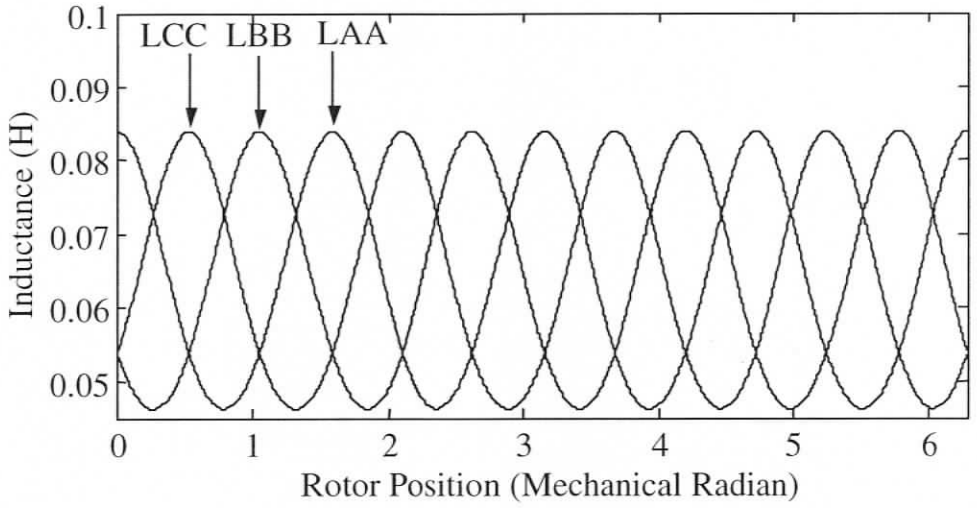

Figure 3.11 Stator magnetizing inductances of SM with DC excitation

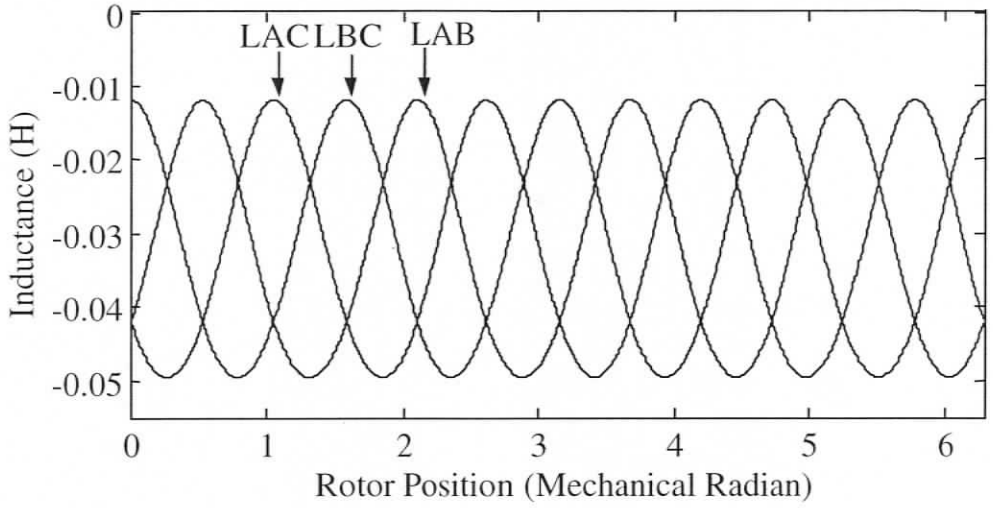

Figure 3.12 Stator mutual inductances of SM with DC excitation

3.4 Computation of Mutual Inductances between Stator and Rotor Circuits Using MWFA

Various mutual inductances of both RSM and SM with DC excitation have been computed using MWFA as discussed in the following sections. The computed inductances have been verified by using finite element analysis as given in Appendix-D.

3.4.1 Mutual Inductances between Stator Winding and Rotor Loops of RSM

The inductance between any stator phase 'u' and rotor loop (L_{ur}) can be obtained by using MWFA. In the case of a RSM, the variation of L_{Ar} with respect to the rotor position has been plotted as shown in Figure 3.13 Similarly, other stator phase and rotor loop inductances can be obtained. Also $L_{ur} = L_{ru}$ [50].

3.4.2 Mutual Inductances between Stator Winding and Rotor Loops of SM with DC Excitation

In the case of SM with DC excitation, using MWFA, the mutual inductance between stator phase-A and a typical rotor loop has been computed as shown in Figure 3.14.

3.4.3 Mutual Inductances between Stator Winding and Field Windings of SM with DC Excitation

The mutual inductance of the field winding with any stator phase can be computed using MWFA. The mutual inductance of stator phase-A with the standard field winding has been shown in Figure 3.15.

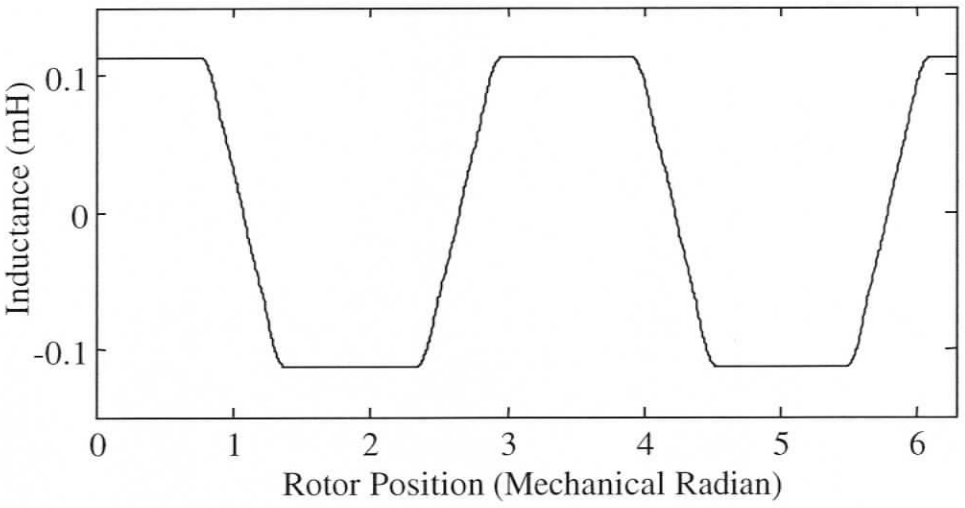

Figure 3.13 Mutual inductance of stator phase-A and a typical rotor loop of RSM

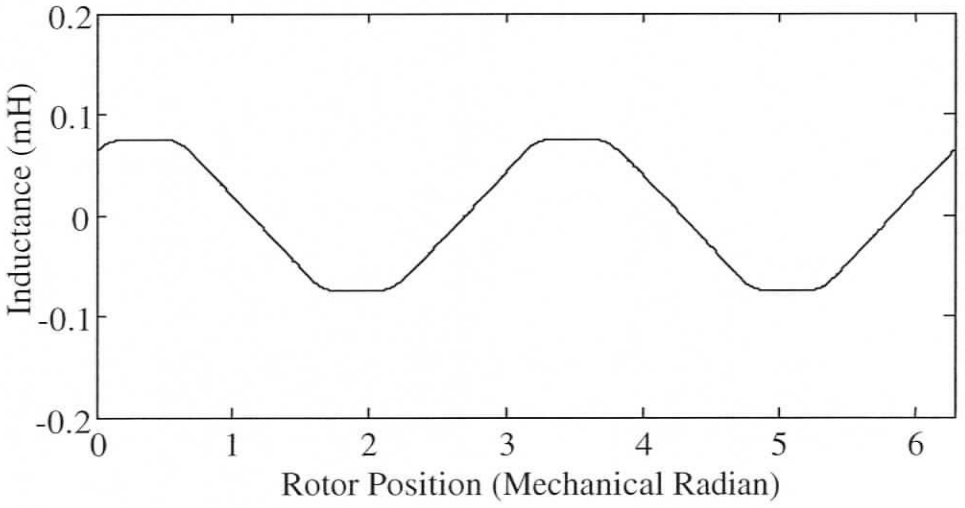

Figure 3.14 Mutual inductance of stator phase-A and a typical rotor loop of SM with DC excitation

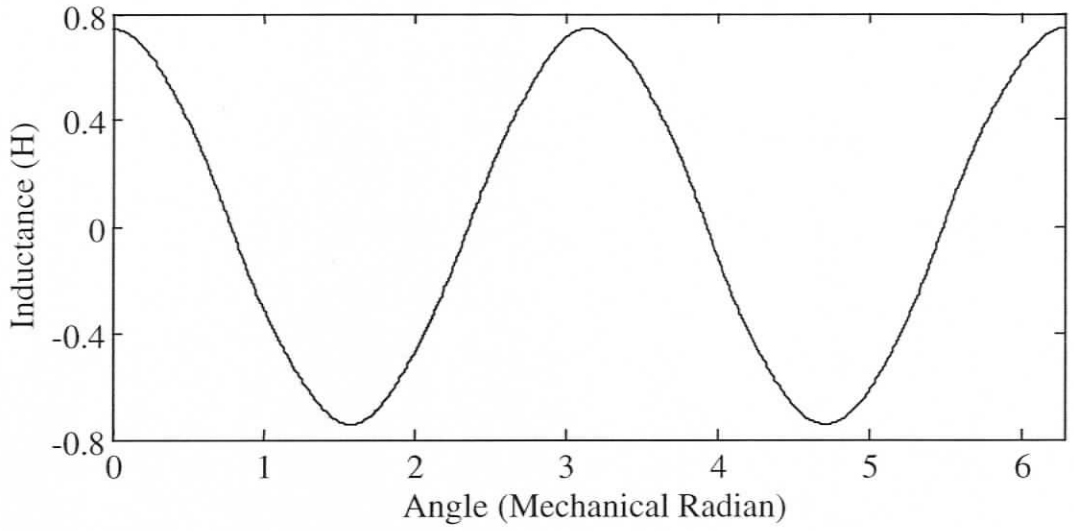

Figure 3.15 Mutual inductance of stator phase-A and standard field winding of SM

3.5 State Space Modeling of Synchronous Machines

3.5.1 Equations for Dynamic Modeling of RSM

The dynamic model of the RSM can be obtained using the coupled circuit approach [48]. The various stator (3-phase) and rotor voltages (*n* loops) of the machine can be expressed as follows:

$$V_s = R_s I_s + L_{ss}\frac{dI_s}{dt} + \omega\frac{dL_{ss}}{d\theta}I_s + L_{sr}\frac{dI_r}{dt} + \omega\frac{dL_{sr}}{d\theta}I_r \tag{3.24}$$

$$\begin{aligned} &V_s = [v_{sA} \quad v_{sB} \quad v_{sC}]^t, I_s = [i_{sA} \quad i_{sB} \quad i_{sC}]^t \\ &and \quad I_r = [i_{r1} \quad i_{r2} \quad \ldots \quad i_{rn} \quad i_e]^t \end{aligned} \tag{3.25}$$

$$R_s = \begin{bmatrix} r_{sA} & 0 & 0 \\ 0 & r_{sB} & 0 \\ 0 & 0 & r_{sC} \end{bmatrix} \tag{3.26}$$

$$L_{ss} = \begin{bmatrix} L_{AA} + L_l & L_{AB} & L_{AC} \\ L_{BA} & L_{BB} + L_l & L_{BC} \\ L_{CA} & L_{CB} & L_{CC} + L_l \end{bmatrix} \tag{3.27}$$

$$L_{sr} = \begin{bmatrix} L_{Ar1} & L_{Ar2} & \cdots & L_{Arn} & L_{Ae} \\ L_{Br1} & L_{Br2} & \cdots & L_{Brn} & L_{Be} \\ L_{Cr1} & L_{Cr2} & \cdots & L_{Crn} & L_{Ce} \end{bmatrix} \tag{3.28}$$

$$V_r = R_r I_r + L_{rs} \frac{dI_s}{dt} + \omega \frac{dL_{rs}}{d\theta} I_s + L_{rr} \frac{dI_r}{dt} \tag{3.29}$$

$$V_r = [v_{r1}\ v_{r2} \ldots\ v_{rn}\ v_e]^t \tag{3.30}$$

$$R_r = \begin{bmatrix} 2(r_b + r_e) & -r_b & 0 & \ldots & 0 & -r_b & -r_e \\ -r_b & 2(r_b + r_e) & -r_b & \ldots & 0 & 0 & -r_e \\ \vdots & \vdots & \vdots & \ldots & \vdots & \vdots & \vdots \\ \vdots & \vdots & \vdots & \ldots & \vdots & \vdots & \vdots \\ 0 & 0 & 0 & \ldots & 2(r_b + r_e) & -r_b & -r_e \\ -r_b & 0 & 0 & \ldots & -r_b & 2(r_b + r_e) & -r_e \\ -r_e & -r_e & -r_e & \ldots & -r_e & -r_e & nr_e \end{bmatrix} \tag{3.31}$$

$L_{rr} =$

$$\begin{bmatrix} L_{r1r1} + 2(L_b + L_e) & L_{r1r2} - L_b & L_{r1r3} & \ldots & L_{r1r(n-1)} & L_{r1rn} - L_b & -L_e \\ L_{r2r1} - L_b & L_{r2r2} + 2(L_b + L_e) & L_{r2r3} - L_b & \ldots & L_{r2r(n-1)} & L_{r2rn} & -L_e \\ \vdots & \vdots & \vdots & \ldots & \vdots & \vdots & \vdots \\ \vdots & \vdots & \vdots & \ldots & \vdots & \vdots & \vdots \\ L_{r(n-1)r1} & L_{r(n-1)r2} & L_{r(n-1)r3} & \ldots & L_{r(n-1)r(n-1)} + 2(L_b + L_e) & L_{r(n-1)rn} - L_b & -L_e \\ L_{rnr1} - L_b & L_{rnr2} & L_{rnr3} & \ldots & L_{rnr(n-1)} - L_b & L_{rnrn} + 2(L_b + L_e) & -L_e \\ -L_e & -L_e & -L_e & \ldots & -L_e & -L_e & nL_e \end{bmatrix}$$

(3.32)

The matrices V_s and I_s are the voltage and current vectors of the stator winding whereas V_r and I_r are the corresponding vectors of rotor circuit. R_s and R_r represent the resistance matrices pertaining to the stator and rotor bars including end rings. L_{ss} and L_{rr} are the matrices consisting of various stator and rotor inductance whereas L_{sr} is the mutual inductance matrix between the stator and rotor circuits. Also, $L_{rs} = L_{sr}^{t}$. θ is the rotor position and ω is the angular speed of the machine. The net electromagnetic torque (T_e) in the machine can be expressed in terms of the magnetic co-energy (W_{co}) as well as the angular acceleration of the rotor as given follows

$$T_e = \frac{\partial W_{co}}{\partial \theta} \tag{3.33}$$

$$T_e = J\frac{d\omega}{dt} + T_l \tag{3.34}$$

$$\omega = \frac{d\theta}{dt} \tag{3.35}$$

$$W_{co} = \frac{1}{2}\left[I_s^{\,t} L_{ss} I_s + I_s^{\,t} L_{sr} I_r + I_r^{\,t} L_{rs} I_s + I_r^{\,t} L_{rr} I_r\right] \tag{3.36}$$

In (3.34), 'T_l' is the load torque. Using (3.24)-(3.32) and (3.35), the machine equations can be rearranged into the standard state-space form and can be solved to obtain stator currents, rotor currents, speed and angular position of the motor [48, 49]. Various inductances of the machine have been computed and the state space equations of the dynamic model have been solved using MATLAB[1].

3.5.2 Equations for Dynamic Modeling of SM with DC Excitation

The dynamic model of SM with DC excitation can also be obtained in a similar manner.

---

[1] MATLAB, The Mathworks Inc., Natic, MA, 2004

$$V_s = R_s I_s + L_{ss}\frac{dI_s}{dt} + \omega\frac{dL_{ss}}{d\theta}I_s + L_{sr}\frac{dI_r}{dt} + \omega\frac{dL_{sr}}{d\theta}I_r + L_{srf}\frac{di_{rf}}{dt} + \omega\frac{dL_{srf}}{d\theta}i_{rf} \tag{3.37}$$

$$L_{srf} = [L_{Arf} \quad L_{Brf} \quad L_{Crf}]^t \tag{3.38}$$

$$V_r = R_r I_r + L_{rs}\frac{dI_s}{dt} + \omega\frac{dL_{rs}}{d\theta}I_s + L_{rr}\frac{dI_r}{dt} + L_{rrf}\frac{di_{rf}}{dt} \tag{3.39}$$

$$L_{rrf} = [L_{r1rf} \quad L_{r2rf} \quad \cdots \quad L_{rnrf} \quad L_{erf}]^t \tag{3.40}$$

$$v_{rf} = r_{rf} i_{rf} + L_{rfrf}\frac{di_{rf}}{dt} + L_{rfs}\frac{dI_s}{dt} + \omega\frac{dL_{rfs}}{d\theta}I_s + L_{rfr}\frac{dI_r}{dt} \tag{3.41}$$

The matrices V_s, I_s, V_r, I_r, R_s and R_r represent the same quantities as in section 3.5.1. v_{rf} and i_{rf} represent the field voltage and field current respectively whereas r_{rf} represents the resistance of the field winding. L_{ss}, L_{rr} and L_{rfrf} are the matrices representing various magnetizing inductances of the stator, rotor and field winding whereas L_{sr}, L_{srf} and L_{rrf} are the mutual inductance matrices between stator-rotor, stator-field and field-rotor circuits respectively. Also, $L_{rs} = L_{sr}^t$, $L_{rfs} = L_{srf}^t$ and $L_{rfr} = L_{rrf}^t$. The net electromagnetic torque in the machine can be expressed in terms of the magnetic co-energy (W_{co}) as well as the angular acceleration of the rotor as given in (3.33)-(3.35). However, in the case of SM with DC excitation, the magnetic co-energy can be given as in (3.42)

$$W_{co} = \frac{1}{2}\begin{bmatrix} I_s{}^t L_{ss} I_s + I_r{}^t L_{rr} I_r + i_{rf} L_{rfrf} i_{rf} + I_s{}^t L_{sr} I_r + I_r{}^t L_{rs} I_s \\ + I_s{}^t L_{srf} i_{rf} + i_{rf} L_{rfs} I_s + I_r{}^t L_{rrf} i_{rf} + i_{rf} L_{rfr} I_r \end{bmatrix} \quad (3.42)$$

Using (3.37)-(3.41) and (3.35), the machine equations can be rearranged into the standard state-space form and can be solved to obtain stator currents, rotor currents, speed and angular position of the motor [48, 49]. Various inductances of the machine have been computed and the state space equations of the dynamic model have been solved using MATLAB[1].

3.6 Validation of Performance of the Machine Models

Now the performance of the simulated models of synchronous machines has been compared with that of the experimental machines.

3.6.1 Performance of Simulated RSM with Full Rotor Pole-arc

First, the performance of simulated RSM without reducing the pole-arc has been studied. Initially, the machine was started under no-load. The transient stator current of the RSM during starting is as shown in Figure 3.16 whereas the corresponding transient speed is as shown in Figure 3.17. Subsequently, at 0.5 seconds, a load torque of 4.5N-m (73% of full-load torque) was applied on the machine. Figure 3.18 shows the transient stator current of the RSM when 4.5N-m load torque is applied. The corresponding transient speed and rotor loop current (a loop next to inter-polar gap) are as shown in Figure 3.19 and Figure 3.20 respectively. The model was stable only up to 73% of full-load. Since the effects of flux barriers, flux crowding at the pole tips due to change in the load angle and saturation were not considered; the model was not stable beyond this operating point.

[1] MATLAB, The Mathworks Inc., Natic, MA, 2004

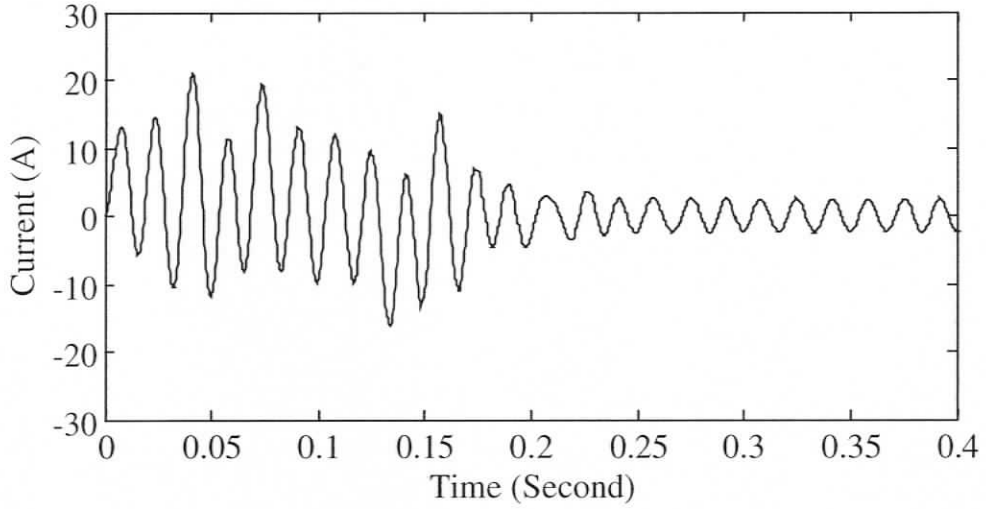

Figure 3.16 Simulated transient stator current of RSM during starting, $J = 0.00651$ Kg-m^2

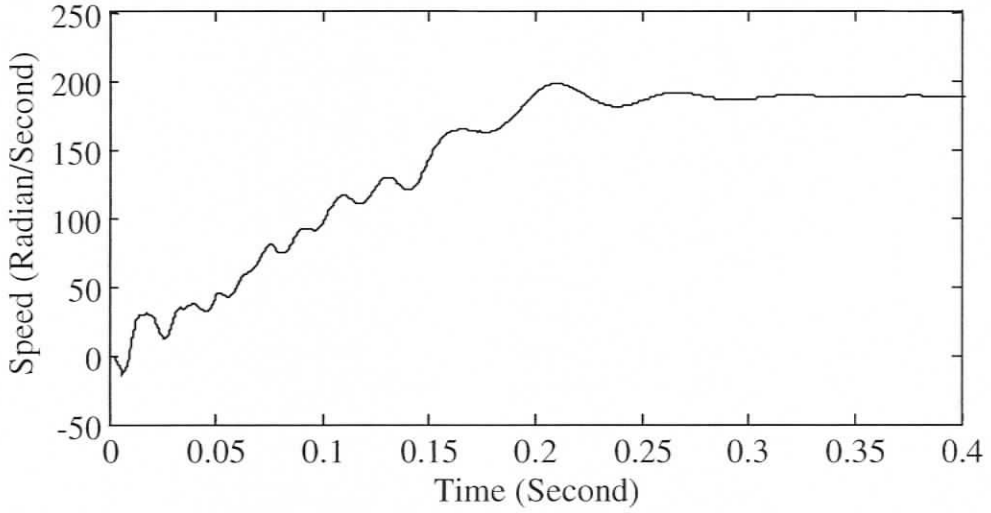

Figure 3.17 Simulated transient speed of RSM during starting, $J = 0.00651$ Kg-m^2

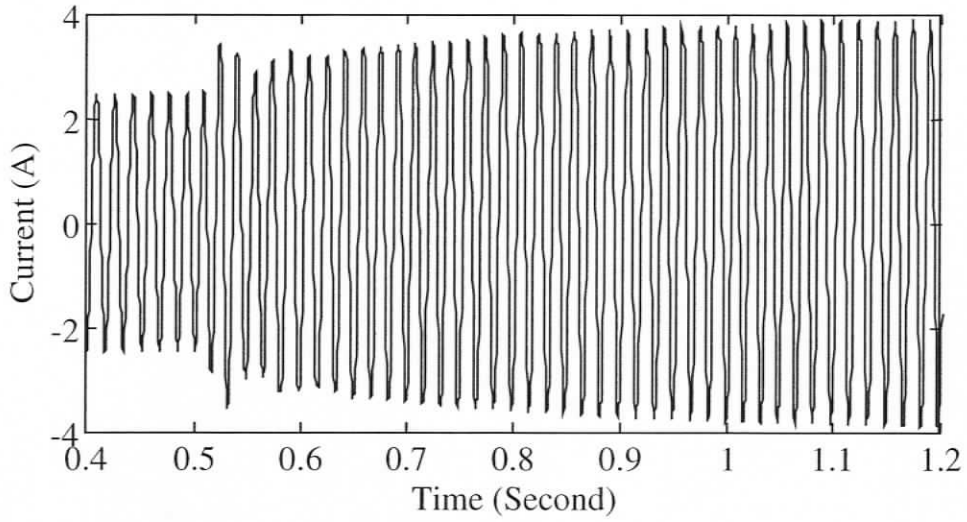

Figure 3.18 Simulated transient stator current of RSM with 73% load, $J = 0.00651$ Kg-m^2

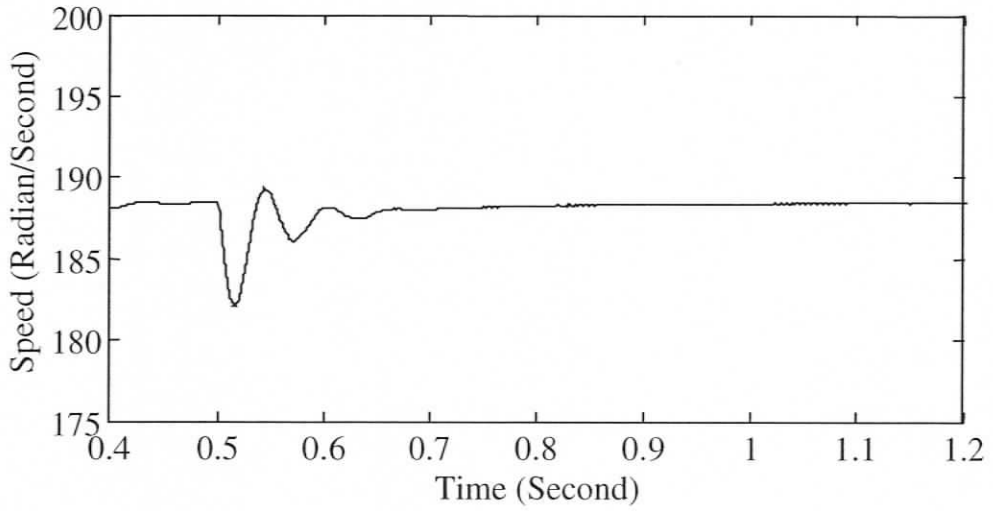

Figure 3.19 Simulated transient speed of RSM with 73% load, $J = 0.00651$ Kg-m^2

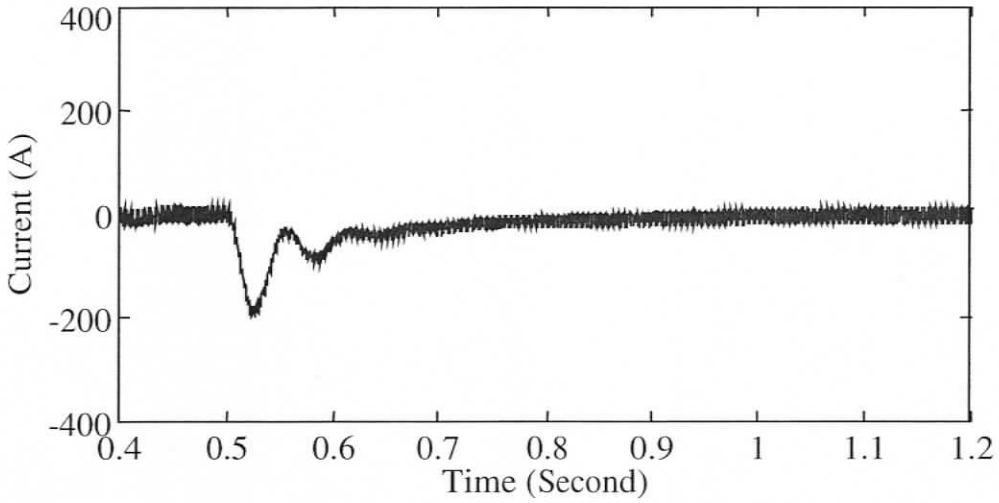

Figure 3.20 Simulated transient rotor loop current of RSM with 73% load, J = 0.00651 Kg-m^2

3.6.2 Verification of Reduction of Effective Rotor Pole-arc using Finite Element Method

Due to the flux barriers, the flux shows a tendency to concentrate at center of the rotor-pole [58]. Also, the flux crowding at the pole tips due to change in the load angle and saturation results in predominant reduction of effective pole-arc. In order to validate this effect, the flux distribution of the RSM has been plotted using the finite element model of the machine with and without flux barriers. This analysis was performed under no-load as well as full-load conditions of the machine. The motor current and rotor position have been set according to the load condition. The effect of the flux barriers was almost negligible under no-load condition. Under this condition, the flux lines were almost symmetrically distributed over the pole-arc of the machine as shown in Figure 3.21 and Figure 3.22. The reduction of the d-pole-arc under loaded condition can be clearly observed in Figure 3.23 and Figure 3.24. The flux lines are even more concentrated near the end of the Y-shaped flux barriers as can be seen in Figure 3.24.

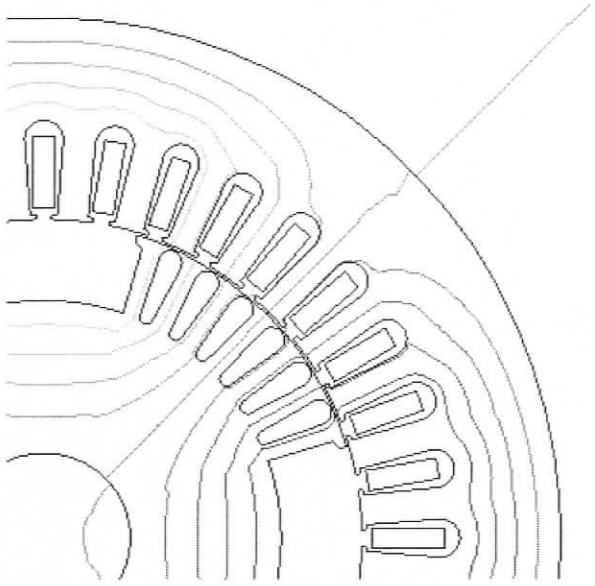

Figure 3.21 Flux distribution of RSM under no-load (without flux barriers)

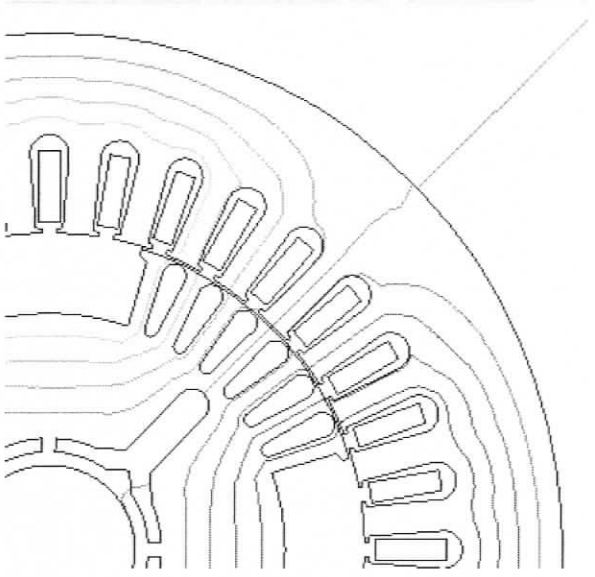

Figure 3.22 Flux distribution of RSM under no-load (with flux barriers)

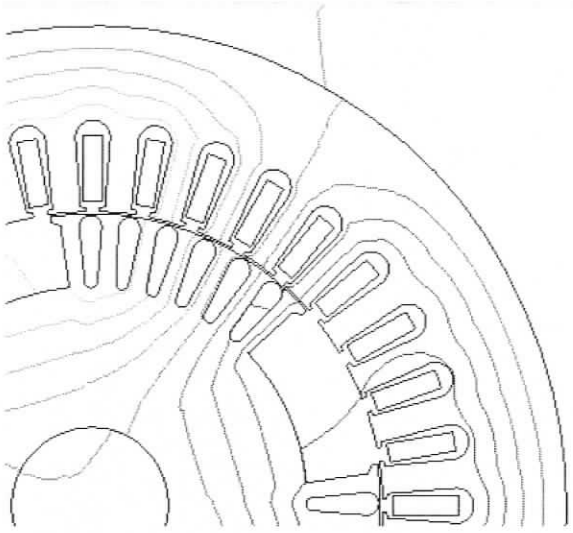

Figure 3.23 Flux distribution of RSM under full-load (without flux barriers).

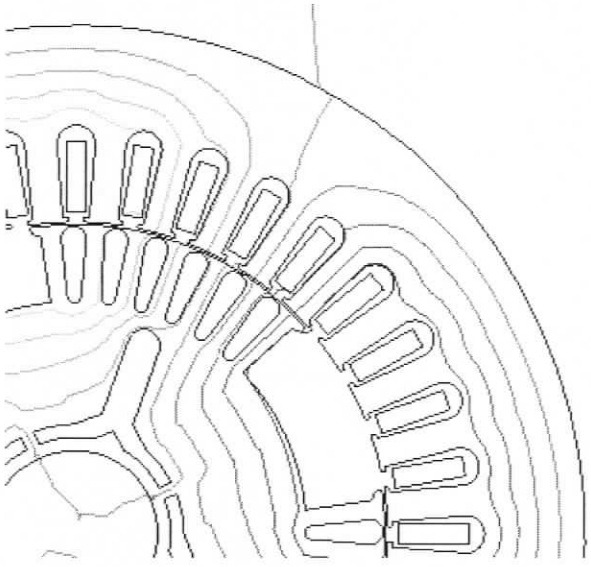

Figure 3.24 Flux distribution of RSM under full-load (with flux barriers)

3.6.3 Experimental Validation of Model of RSM with Reduced Rotor Pole-arc

In order to consider the effective reduction of pole-arc due to the flux barriers and load on the machine, the pole-arc of the simulated machine has been reduced by 6.8 degrees (mechanical) and the inter-polar arc has been increased by the same magnitude. The model was stable at full-load with the changed polar arcs. The value of 6.8 degrees was obtained by trial and error. The transient stator current and speed of the RSM during starting with the changed pole-arc are shown in Figure 3.25 and Figure 3.26 respectively.

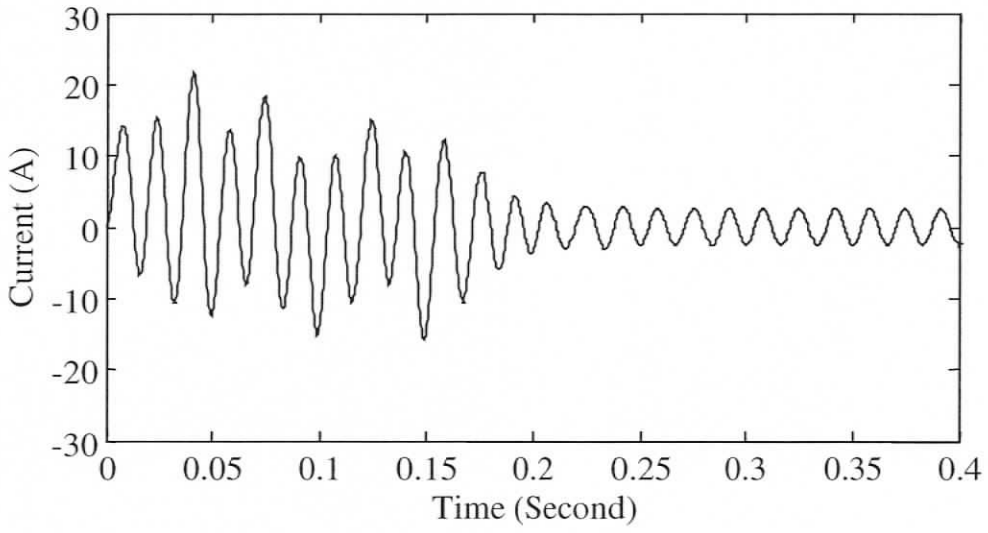

Figure 3.25 Simulated transient stator current of RSM during starting (with changed pole-arc), $J = 0.00651$ Kg-m^2

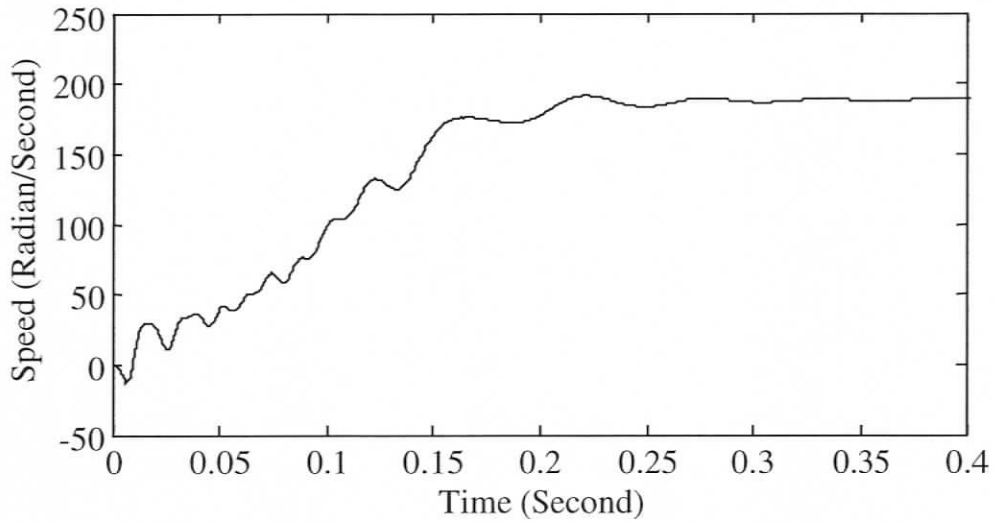

Figure 3.26 Simulated transient speed of RSM during starting (with changed pole-arc), $J = 0.00651$ Kg-m^2

Next, an attempt has been made to validate the simulated model of RSM by comparing its performance with that of the actual motor. The RSM was mounted on the test bed with a DC generator mechanically coupled to it. The DC generator has been used for loading purpose. A small permanent magnet DC machine was also coupled to its shaft to measure the speed transient. First, the moment of inertia (J) of the RSM combined with the other two DC machines was determined from the coasting curve of the machine-set [59]. The value of J was found to be 0.023 Kg-m^2. The simulated model of the RSM was then run with the new value of J. The full-load torque (5.9 N-m) was applied at 0.5 seconds. The transient stator current, speed and rotor loop current (a loop next to inter-polar gap) of the RSM are shown in Figure 3.27, Figure 3.28 and Figure 3.29 respectively.

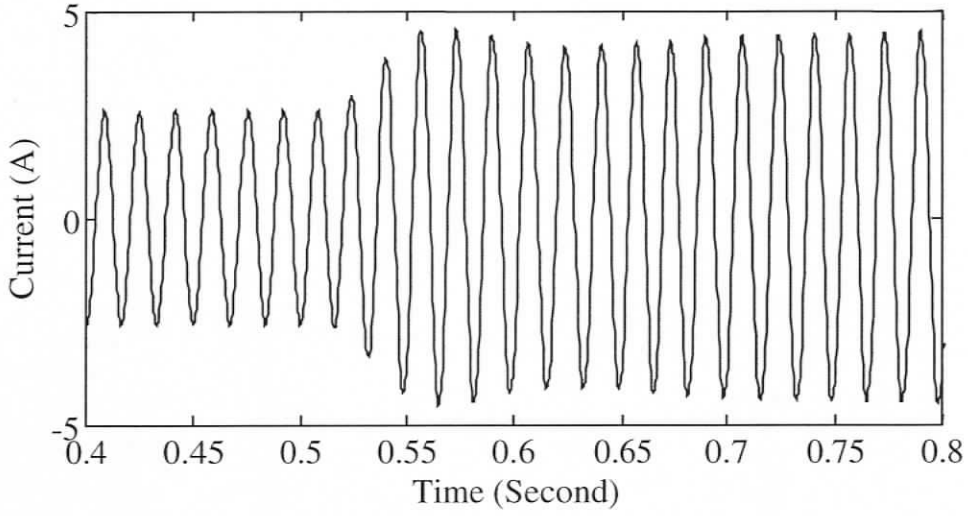

Figure 3.27 Simulated transient stator current of RSM with 100% load (with changed pole-arc), $J = 0.023$ Kg-m^2

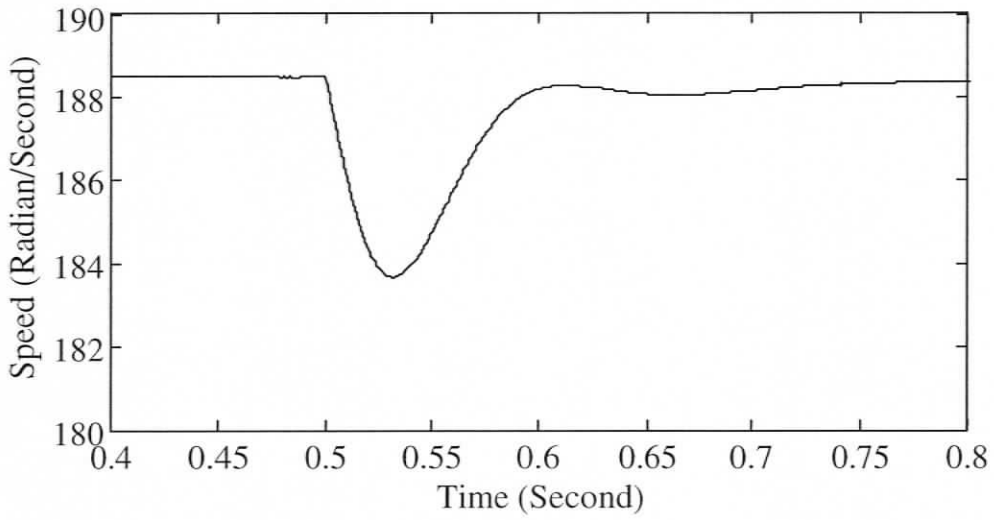

Figure 3.28 Simulated transient speed of RSM with 100% load (with changed pole-arc), $J = 0.023$ Kg-m^2

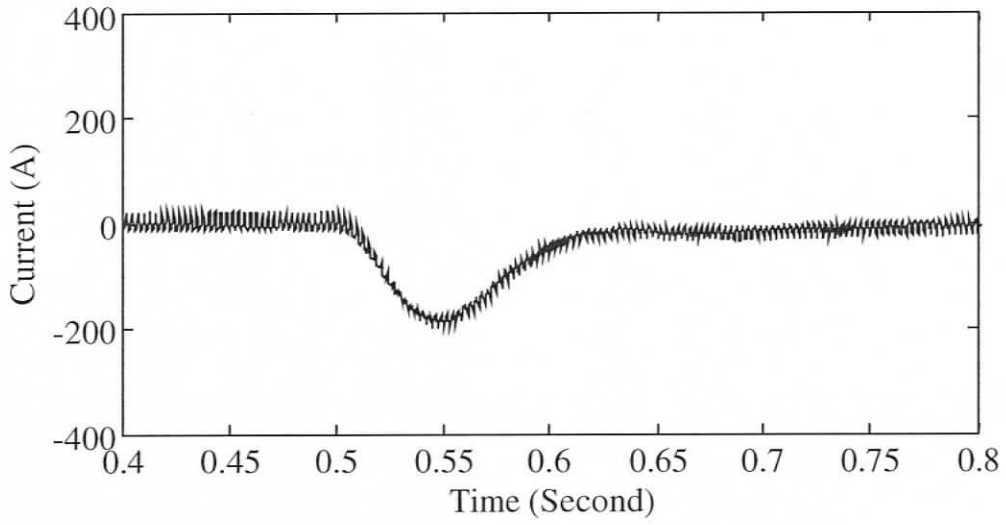

Figure 3.29 Simulated transient rotor loop current of RSM with 100% load (with changed pole-arc), $J = 0.023$ Kg-m^2

The loading transients of the stator current and speed of the actual motor were obtained using a data acquisition system as shown in Figure 3.30 and Figure 3.31 respectively. The terminal voltage of the permanent magnet DC motor has a lot of ripple as shown in Figure 3.31 (top). Hence the acquired data is filtered using a digital finite impulse response (FIR) filter and plotted as shown in Figure 3.31 (bottom). The bandwidth of the filter has been carefully selected so that the filter does not alter the actual response. Though the simulated result of the speed dip upon loading is about one radian/second lower than the experimental one, the settling time for both simulation and the experiment is about 0.1 second. Also the simulated and the experimental transients show similar damping characteristics. Thus it can be said that the loading transients of the simulated model have shown a close match with the corresponding transients obtained from the experiments.

The steady-state performances of the simulated and the actual RSM were also compared. The no-load & full-load simulated current of the RSM is shown in Figure 3.32. The corresponding experimental results are shown in Figure 3.33. A comparison of these figures reveals an excellent average match between the simulation and experimental results. While the RMS values of the line current of the simulated machine under no-load and full-load are 1.82A and 3.32A respectively, the corresponding RMS values of the line current of the actual machine are 1.8A and 3.3A respectively. The experimental setup of the RSM has been shown in Figure 3.34.

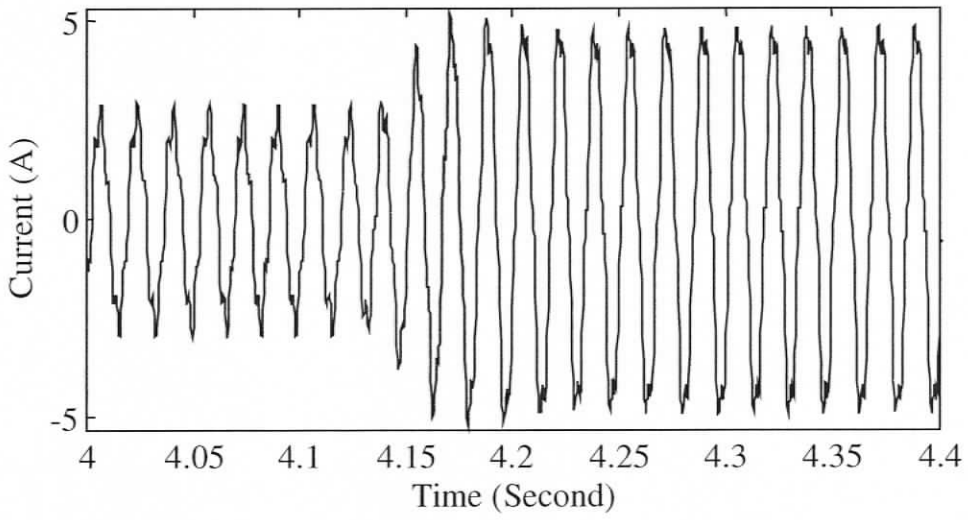

Figure 3.30 Experimental transient stator current of RSM

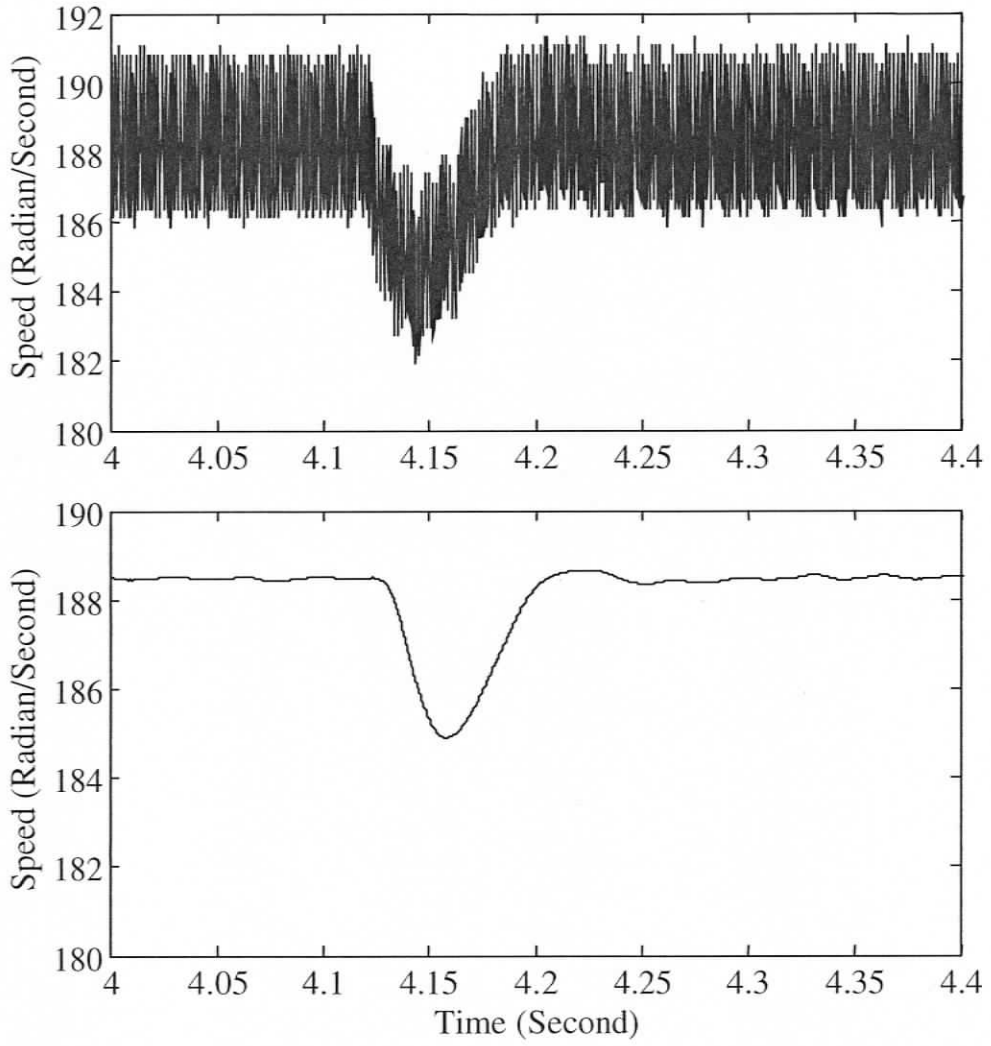

Figure 3.31 Experimental transient speed of RSM, without filtering (top) and with filtering (bottom) (at 100% load)

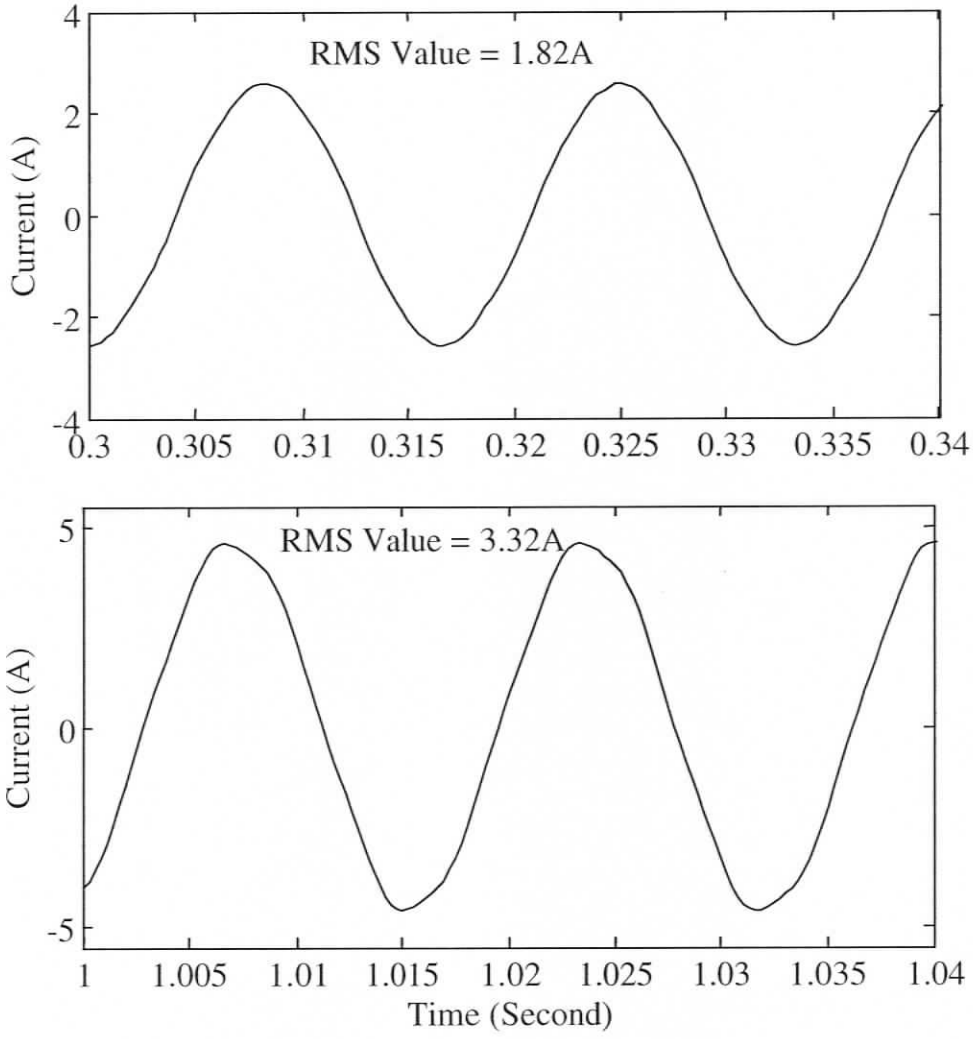

Figure 3.32 Simulated line current of RSM under no-load condition (top) and full-load condition (bottom), $J = 0.023$ Kg-m^2

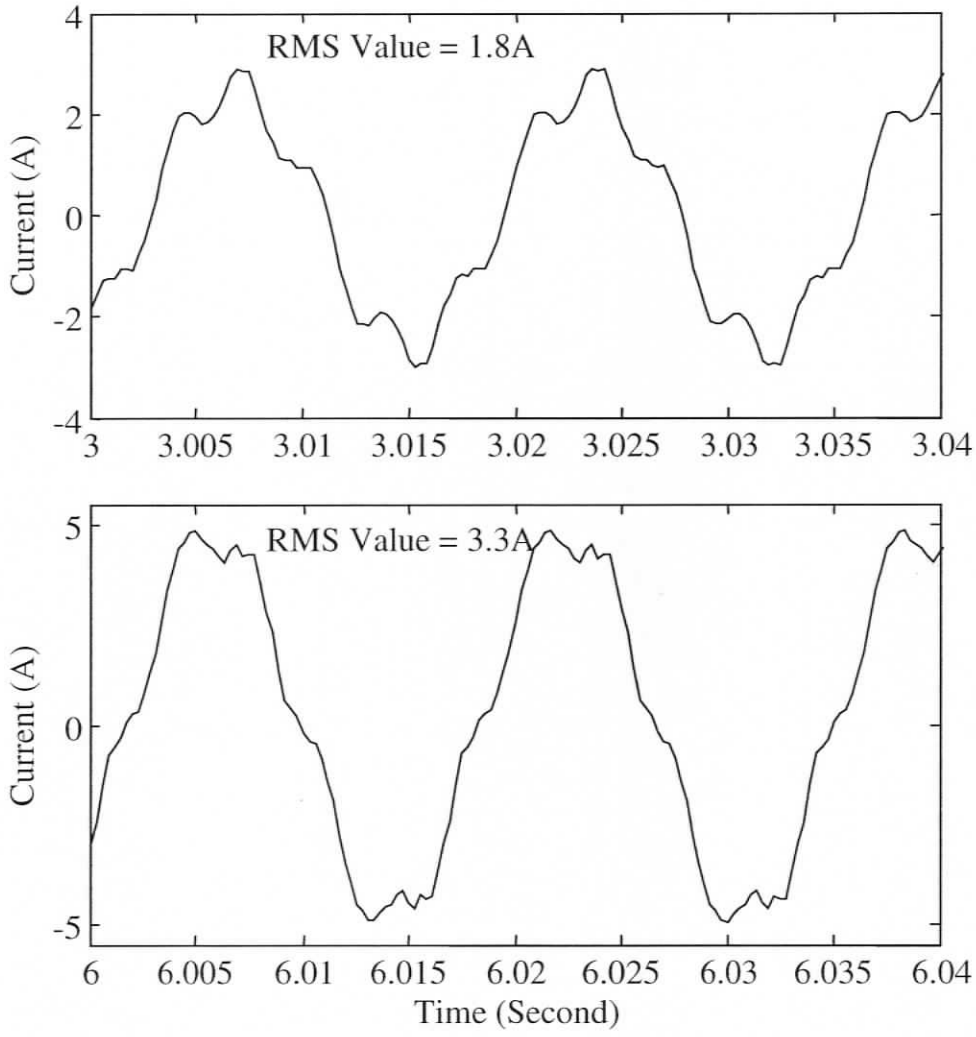

Figure 3.33 Experimental line current of RSM under no-load condition (top) and full-load condition (bottom)

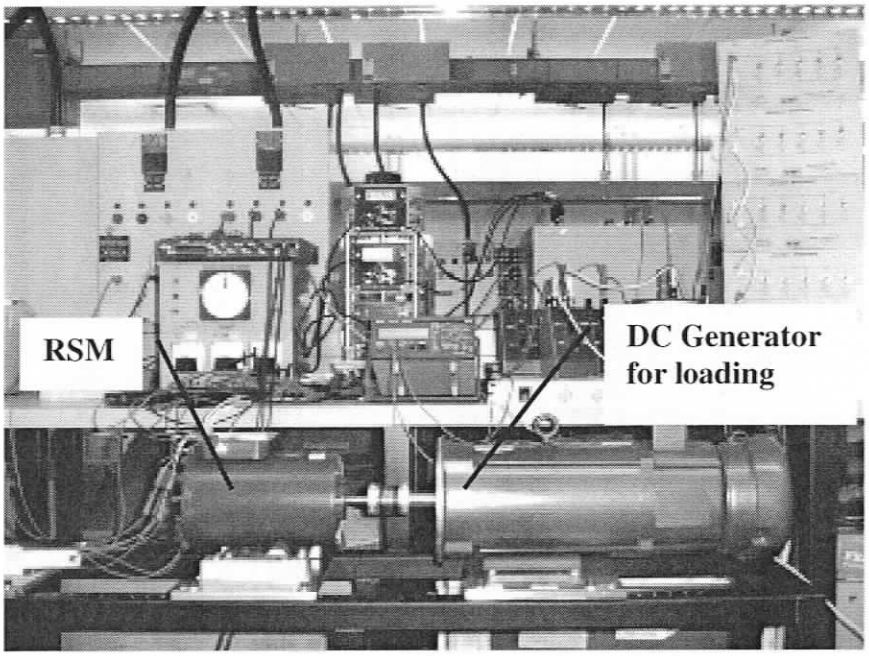

Figure 3.34 Experimental setup of RSM

3.6.4 Experimental Validation of Model of SM with DC Excitation Using Reduced Rotor Pole-arc

The synchronous machine with standard field winding has also been modeled using the coupled circuit approach. Using the above-established facts, the model has been stabilized after reducing the d-pole-arc by 0.5 radians (mechanical). Before starting under no-load condition, the field voltage of the machine model has been set equal to zero. The machine model has been started using the induction torque and speeded up close to the synchronous speed. Then with the help of the reluctance torque the model has been synchronized. The transient stator current and speed under no-load have been shown in Figure 3.35 to Figure 3.36 respectively. After 3.5 seconds, the field voltage has been applied and thereafter the rated load torque has been applied at 4.5 seconds. The transient stator current, speed, rotor loop current and the field current have been shown in Figure 3.37 to Figure 3.40 respectively.

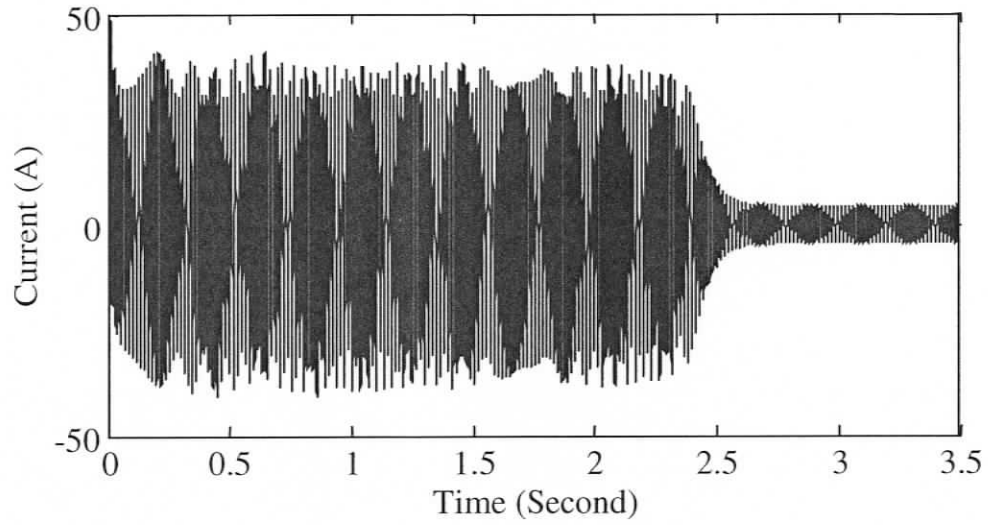

Figure 3.35 Simulated transient stator current of SM with standard field winding during starting

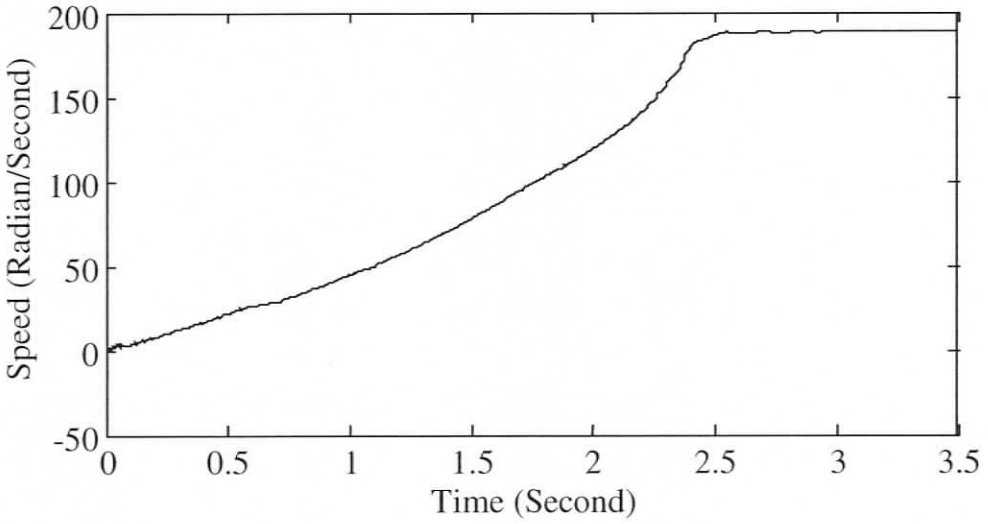

Figure 3.36 Simulated transient speed of SM with standard field winding during starting

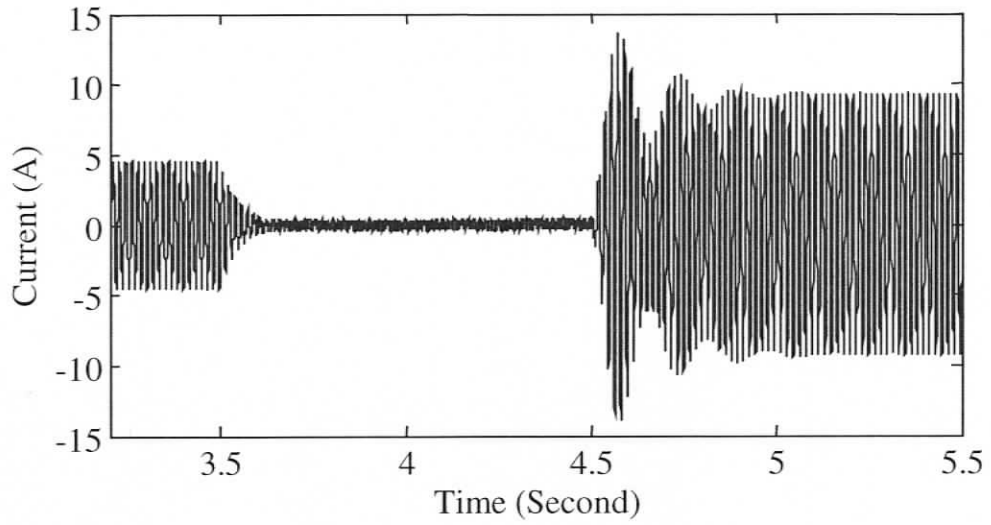

Figure 3.37 Simulated transient stator current of SM with standard field winding at 100% load throw in

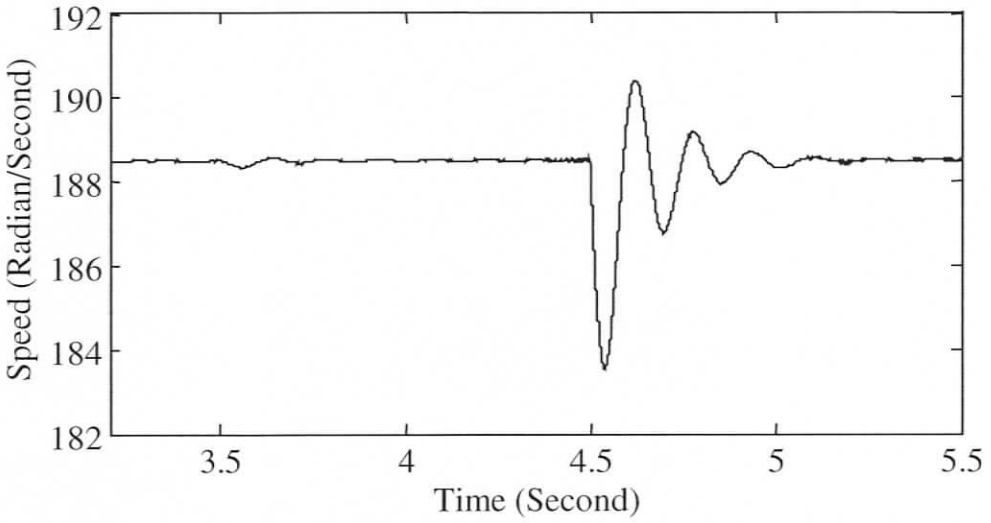

Figure 3.38 Simulated transient speed of SM with standard field winding at 100% load throw in

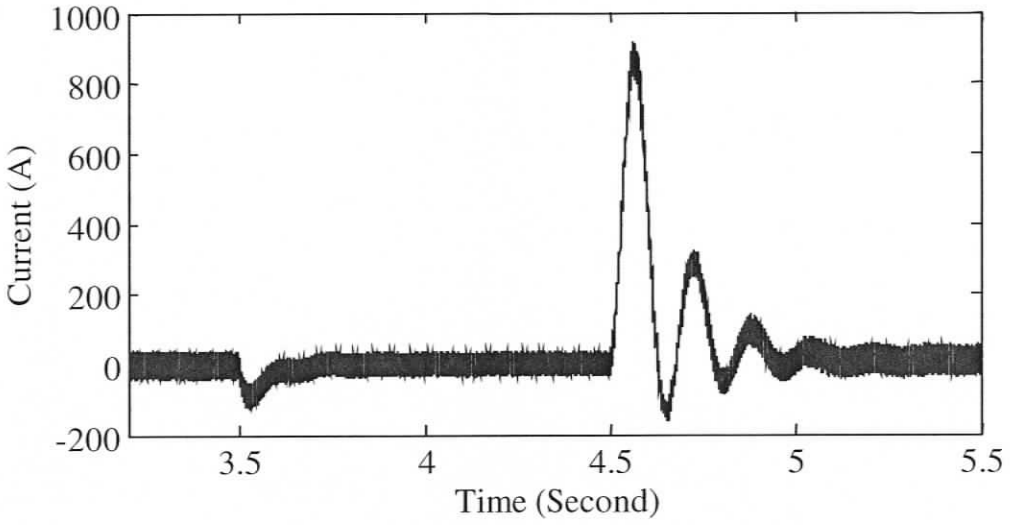

Figure 3.39 Simulated transient rotor loop current of SM with standard field winding at 100% load throw in

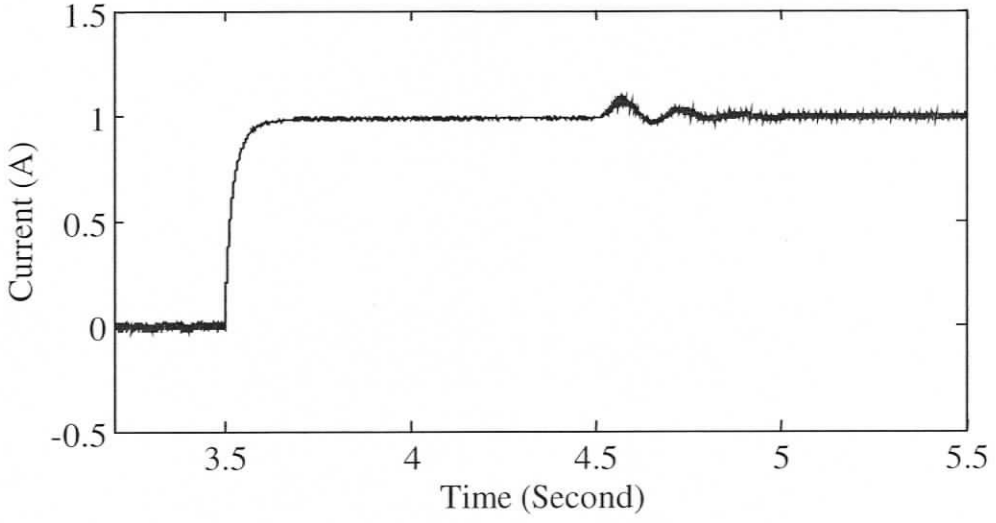

Figure 3.40 Simulated transient field current of SM with standard field winding at 100% load throw in

The experimental transient stator current of SM with DC excitation has been given in Figure 3.41. The corresponding and transient speed has been shown in Figure 3.42. The ripple in the terminal voltage of the tacho generator as seen in Figure 3.42 (top) has been filtered using a digital finite impulse response (FIR) filter and plotted as shown in Figure 3.42 (bottom). Also a comparison of the simulated and experimental stator currents of SM with standard field winding at full-load, 0.88 lagging PF condition has been shown in Figure 3.43. The experimental setup of the SM with DC excitation has been shown in Figure 3.44.

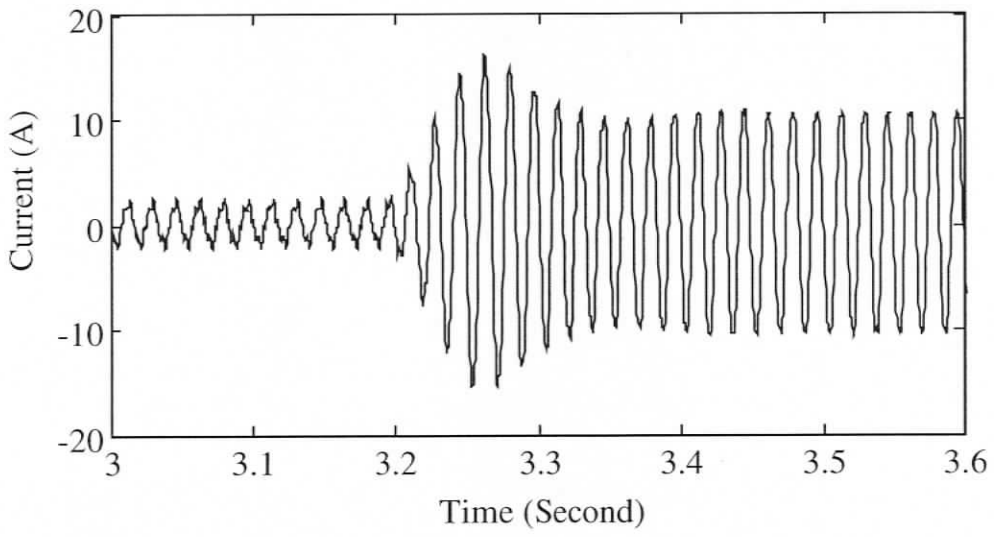

Figure 3.41 Experimental transient stator current of SM with DC excitation

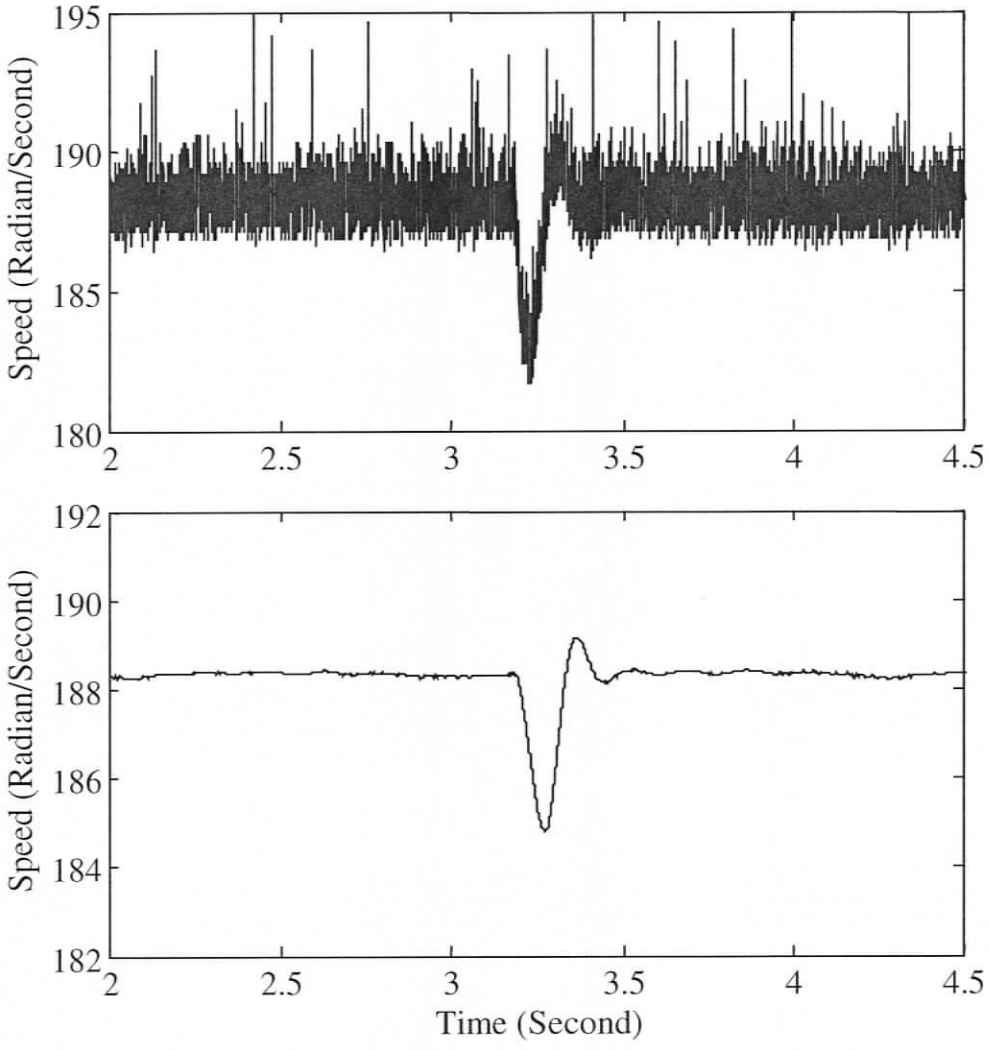

Figure 3.42 Experimental transient speed of SM with DC excitation, without filtering (top) and with filtering (bottom) (at 100% load)

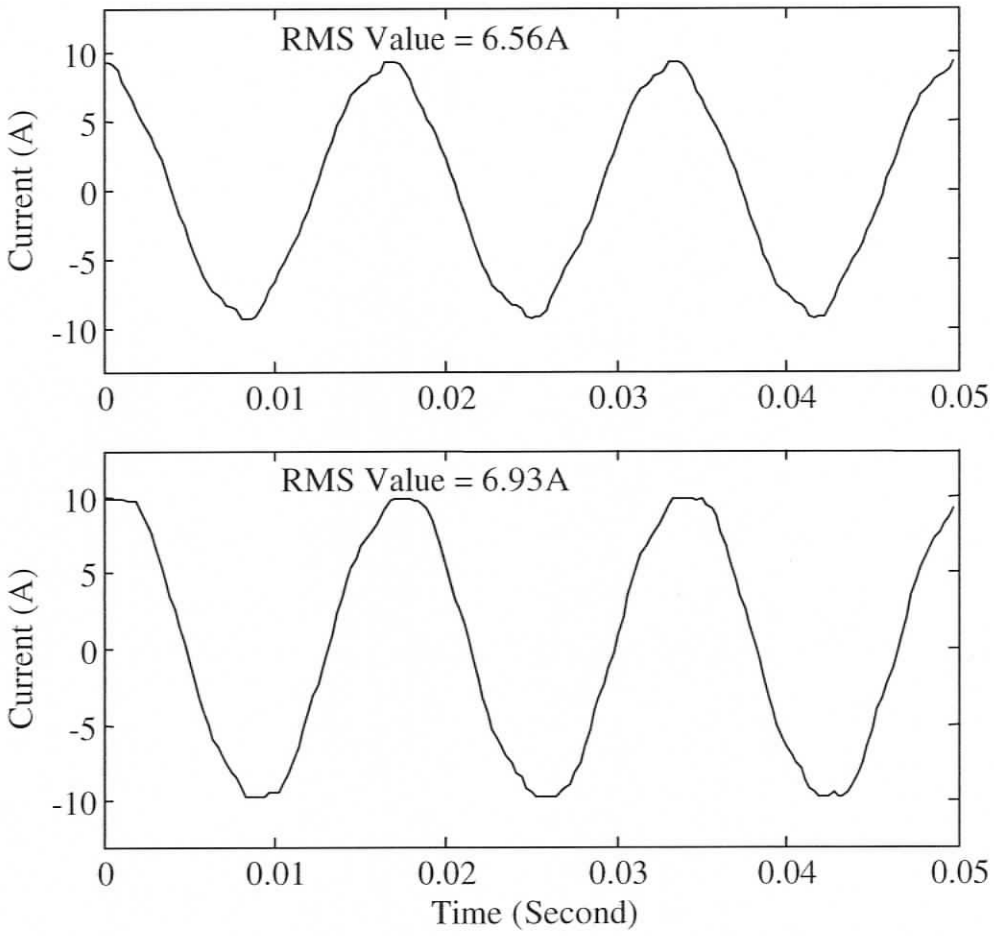

Figure 3.43 Simulated (top) and experimental (bottom) line currents of SM with standard field winding under full-load, 0.88 lagging PF condition

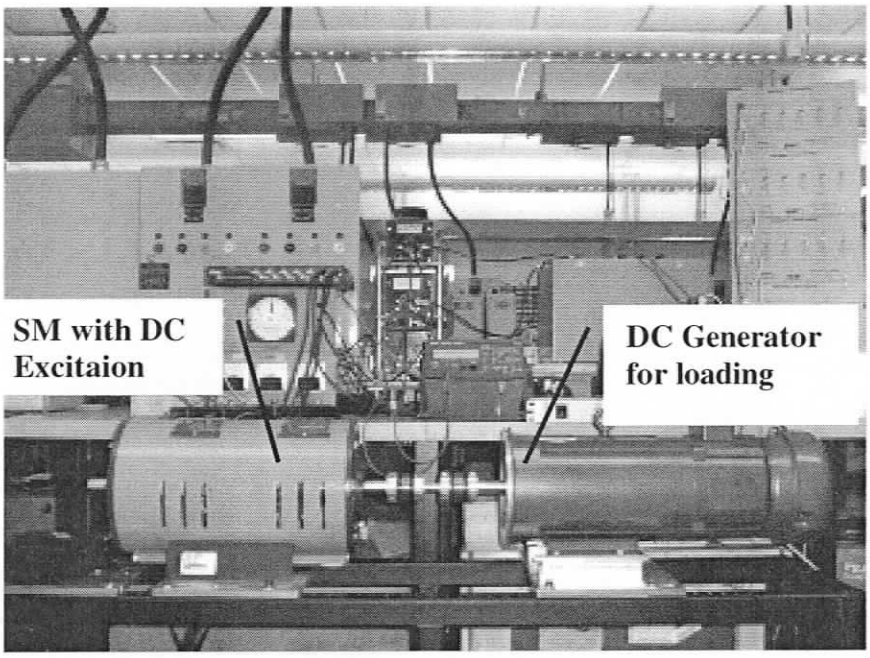

Figure 3.44 Experimental setup of SM with DC excitation

3.7 Discussions on Results and Contributions

In this chapter, several finer aspects of modeling of different synchronous machines have been discussed. A more objective approach to determine the effective air-gap lengths has been introduced using experimentally determined direct and quadrature axes reactances. Generalized expressions for the direct and quadrature axes inductances have been derived that can accommodate any higher winding and permeance related harmonics. WFA and MWFA have been used to model both RSM and SM with DC excitation. Both RSM and SM have been modeled considering the effects of damper bars for the first time. Stabilization of synchronous machine models under full-load condition has been proposed using rotor pole-arc reduction. A detailed verification of performance of these machines has also been put forward using suitable experimental results and a reasonable match has been found. However, the effects of frequency changes on rotor resistance have not been considered. This is

because the frequency and the induced voltage of rotor in a synchronous machine is zero under steady state condition; as it rotates at the same speed as that of the main flux. The higher order induced harmonics are very insignificant.

Chapter 4

Performance Analysis of Synchronous Machines under Healthy, Abnormal Operating Conditions and Stator Inter-turn Faults in Frequency Domain

Following the technique devised in assessing the air-gap lengths effectively and using these values in the healthy machine models it is but natural to compare their performance under healthy condition with those under abnormal operating conditions and stator inter-turn faults. In this study, different abnormal operating conditions such as supply unbalance, time harmonics and internal asymmetry of the machine have been considered. Along with the experimental validation of these results, detailed mathematical proofs have also been provided to explain the presence of various spectral lines in the line current of the machines under different conditions.

4.1 Fault Description

4.1.1 Description of Fault in RSM

The inter-turn faults have been created in the stator winding of synchronous machines. The stator winding of the RSM has 47 conductors per slot per phase with 282 turns in each phase. The phase-A has two coils in series with the first coil having coil-pitch 1-12, 2-11 and 3-10. Results have been obtained with 1 to 4 consecutive shorted turns in the outermost layer (1-12) of phase-A as shown in Figure 4.1.

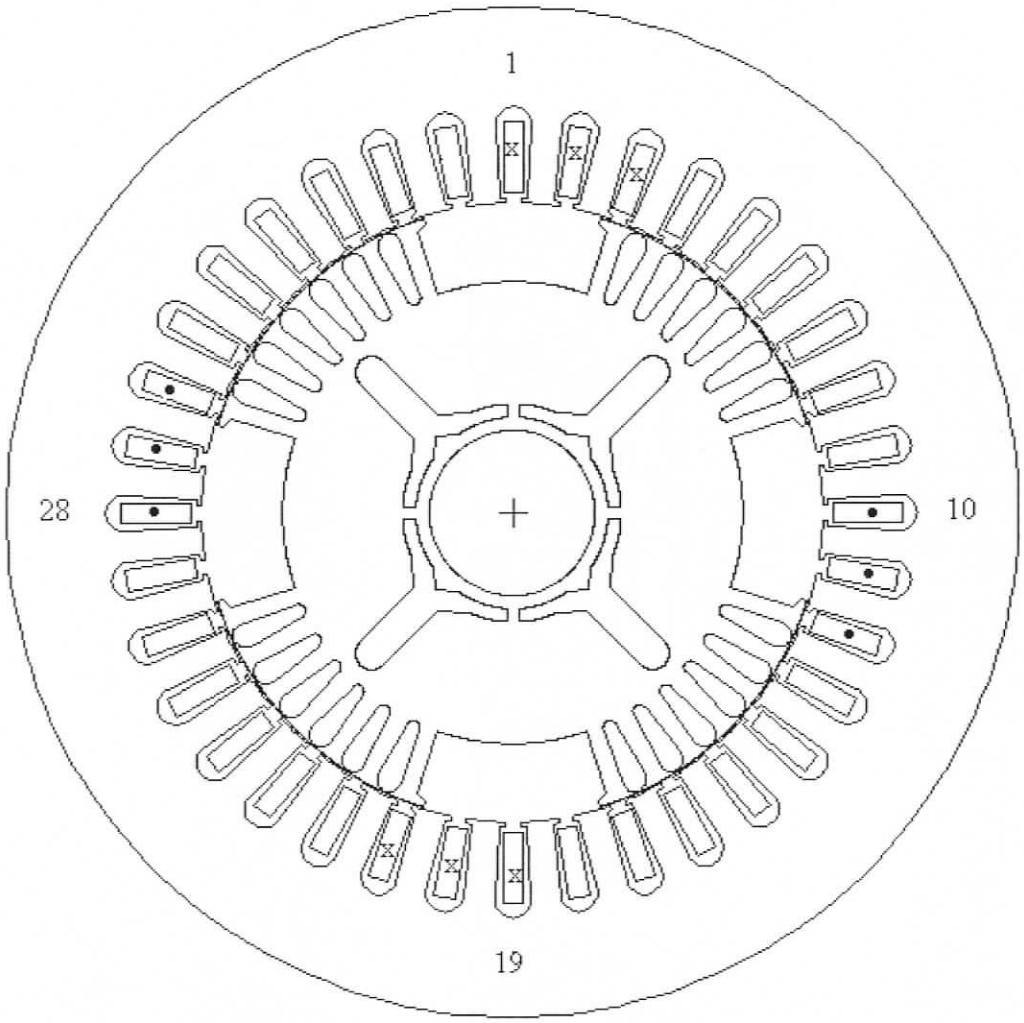

Figure 4.1 Stator phase-A winding of RSM

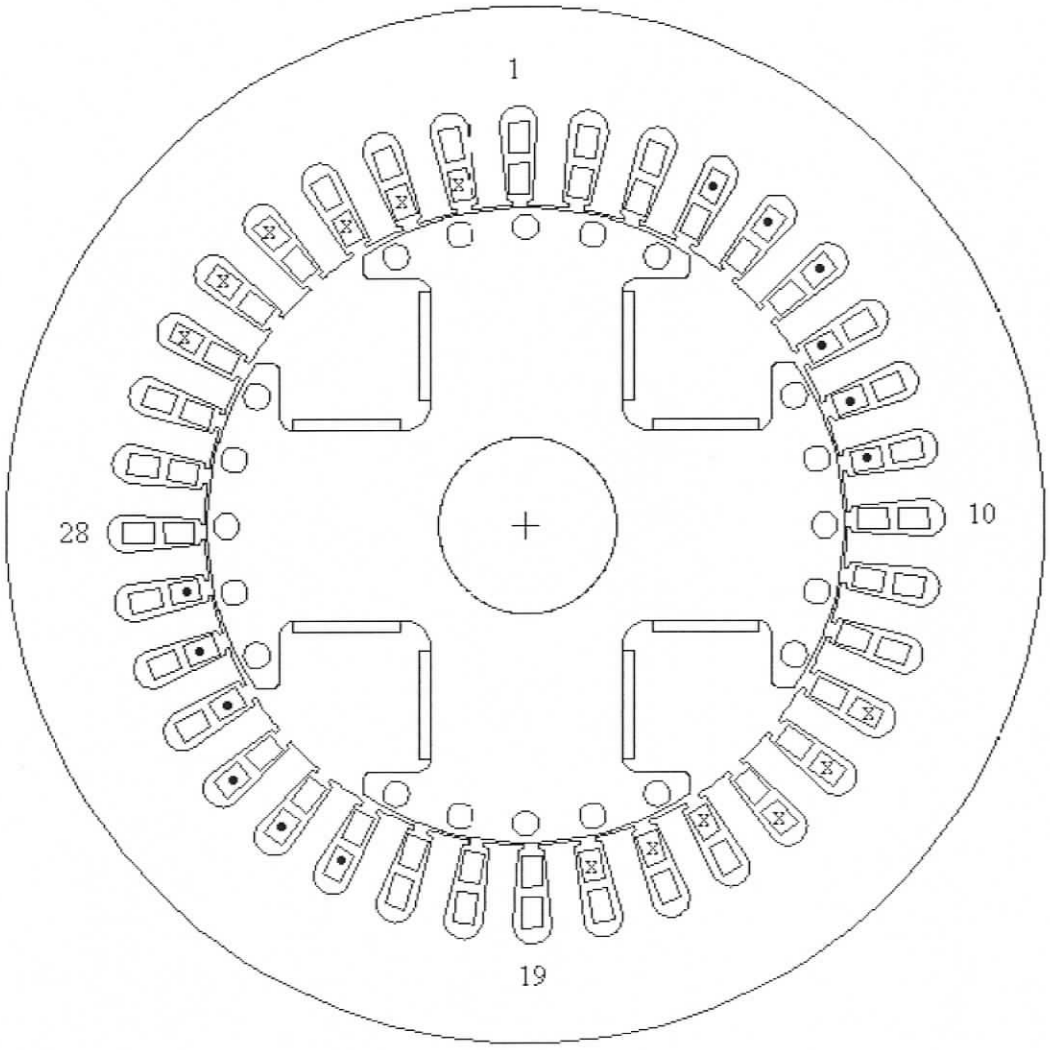

Figure 4.2 Stator phase-A winding of SM with DC excitation

4.1.2 Description of Fault in SM with DC Excitation

The stator of SM with DC excitation has a double layer lap winding with 26 conductors per slot per phase (312 turns/phase). Results have been obtained with 1 to 4 consecutive shorted turns in stator slots 27-33 of phase-A as shown in Figure 4.2.

4.2 Computation of Machine Inductances with Stator Inter-Turn Faults

In order to model both RSM and the SM with DC excitation having inter-turn faults, various inductances have been computed using WFA and MWFA. All the inductances of the faulty machine remain the same as that of the healthy machine except for those pertaining to the faulty phase of the stator winding. The faulty phase can be viewed as a combination of a healthy part and a faulty part.

4.2.1 Computation of Inductances of RSM

The turns functions of healthy, faulty (with 4 shorted turns) and healthy part of stator phase-A of RSM have been shown in Figure 4.3 to Figure 4.5 respectively. The Fourier expansion of the faulty part of phase-A (in Figure 4.4) can be as given in (4.1)

$$\begin{aligned} n_{Af}(\phi) &= a_{osf} + \sum_{c=1,2,3,\ldots}^{\infty} a_{csf} \cos(c\phi) \\ a_{osf} &= \frac{11 N_s}{36}, a_{csf} = \frac{2 N_s}{\pi c}\left\{\sin\left(\frac{11\pi c}{36}\right)\right\}, c = 1,2,3,\ldots \end{aligned} \tag{4.1}$$

The turns function of healthy part of phase-A can be given as

$$n_{Ah}(\phi) = n_A(\phi) - n_{Af}(\phi) \tag{4.2}$$

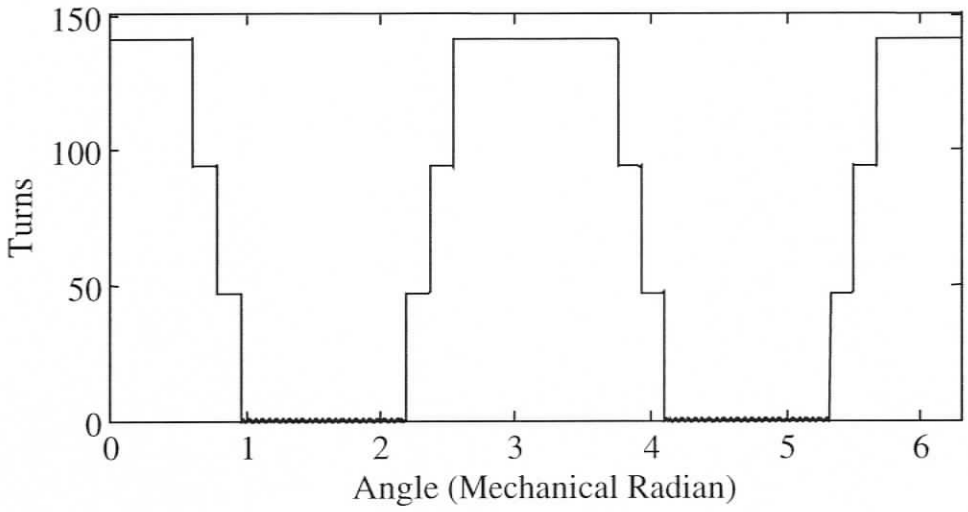

Figure 4.3 Turns function of stator phase-A of healthy RSM

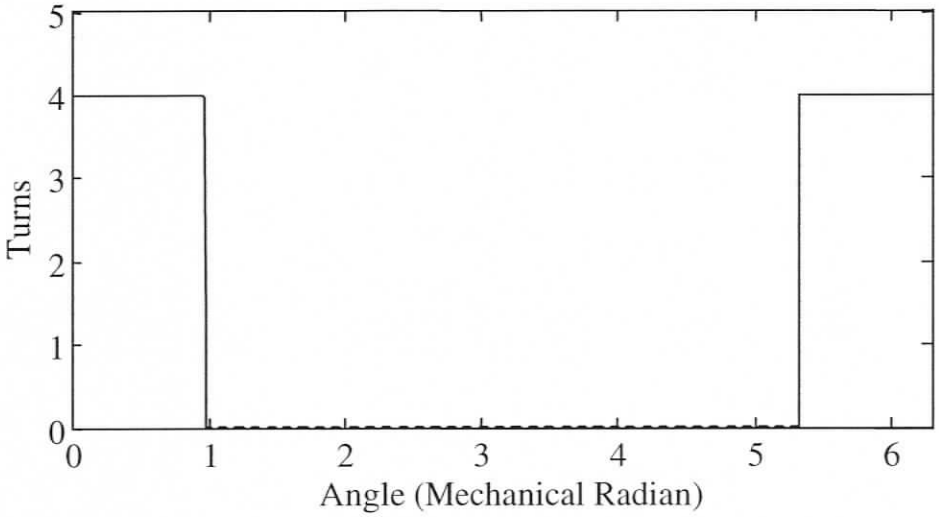

Figure 4.4 Turns function of faulty part of stator phase-A (with 4 shorted turns) of RSM

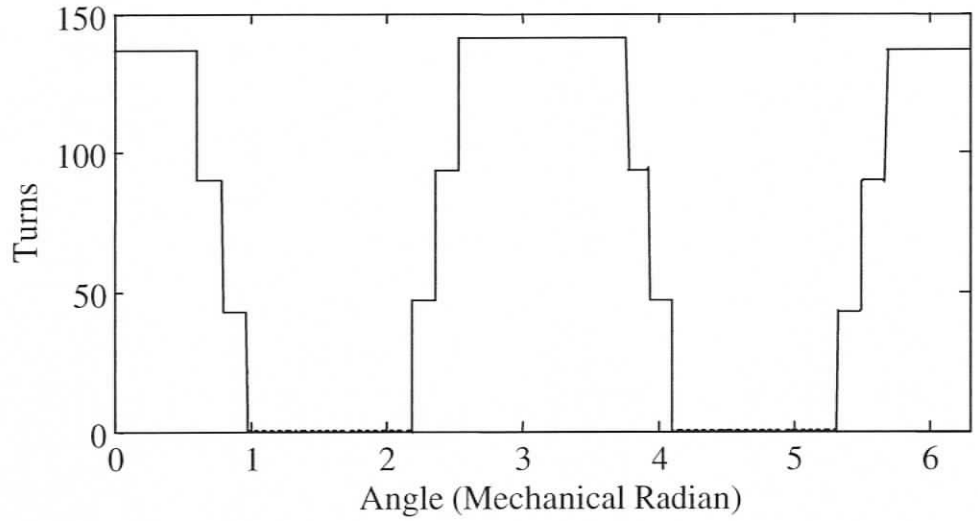

Figure 4.5 Turns function of healthy part of stator phase-A of RSM

Using (3.10) and choosing suitable turns functions of the winding, various inductances of the faulty phase of the RSM have been computed. The magnetizing inductance of faulty part of stator phase-A has been shown in Figure 4.6. The mutual inductance between healthy and faulty parts of phase-A of the RSM has been shown in Figure 4.7. The mutual inductances of healthy and faulty parts of stator phase-A with a typical rotor loop of RSM have been shown in Figure 4.8 and Figure 4.9 respectively.

4.2.2 Computation of Inductances in SM with DC Excitation

The turns functions of healthy, faulty (with 4 shorted turns) and healthy part of stator phase-A of SM with DC excitation have been shown in Figure 4.10 to Figure 4.12 respectively. The Fourier expansion of the faulty part of phase-A can be as given in (4.3)

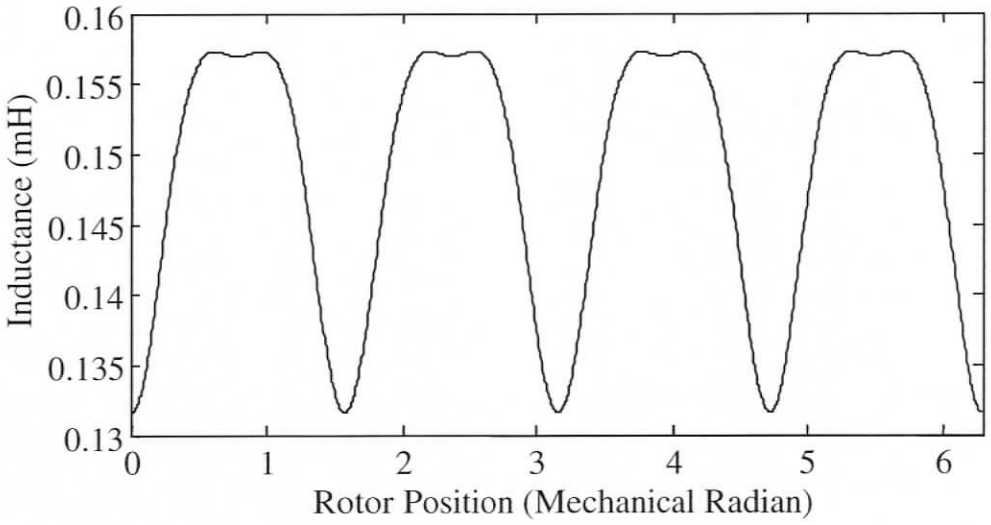

Figure 4.6 Magnetizing inductance of faulty part of stator phase-A (with 4 shorted turns) of RSM

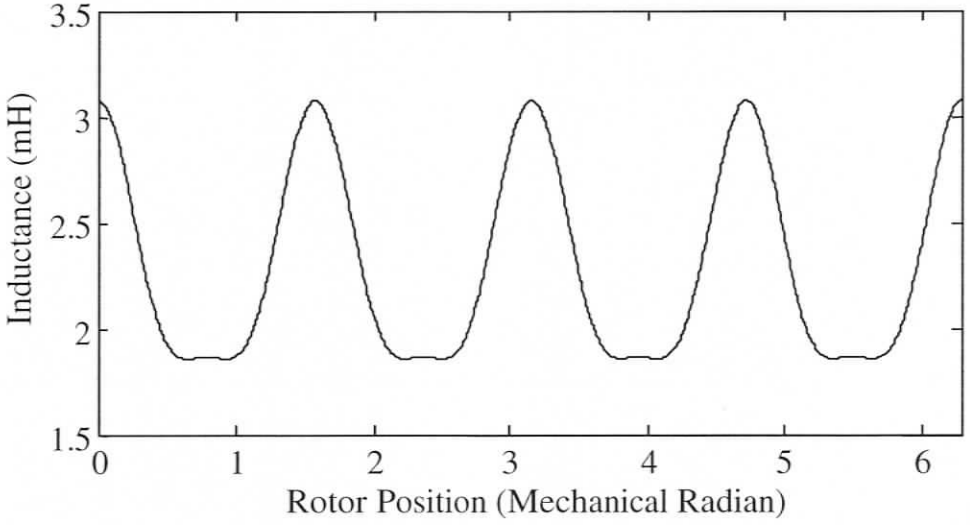

Figure 4.7 Mutual inductance between healthy and faulty parts (with 4 shorted turns) of phase-A of RSM

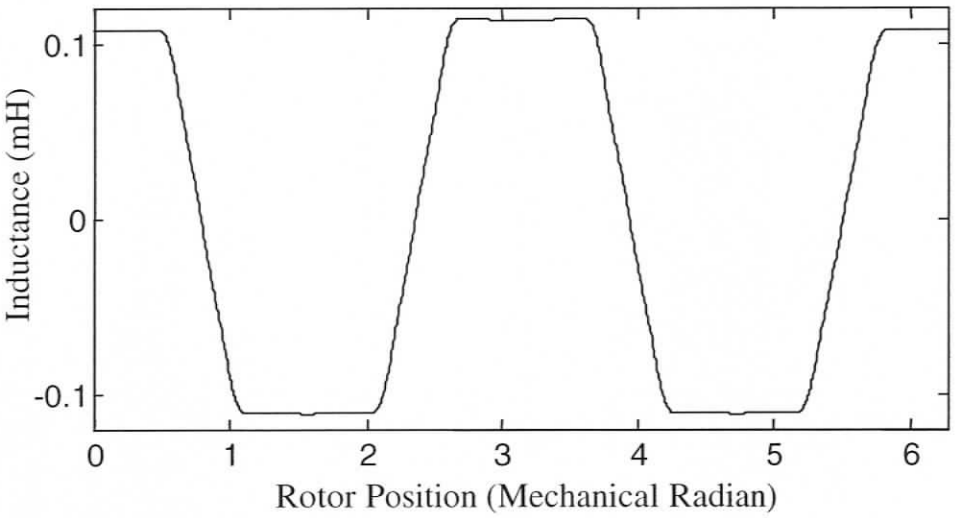

Figure 4.8 Mutual inductance between healthy part of stator phase-A and a typical rotor loop of RSM

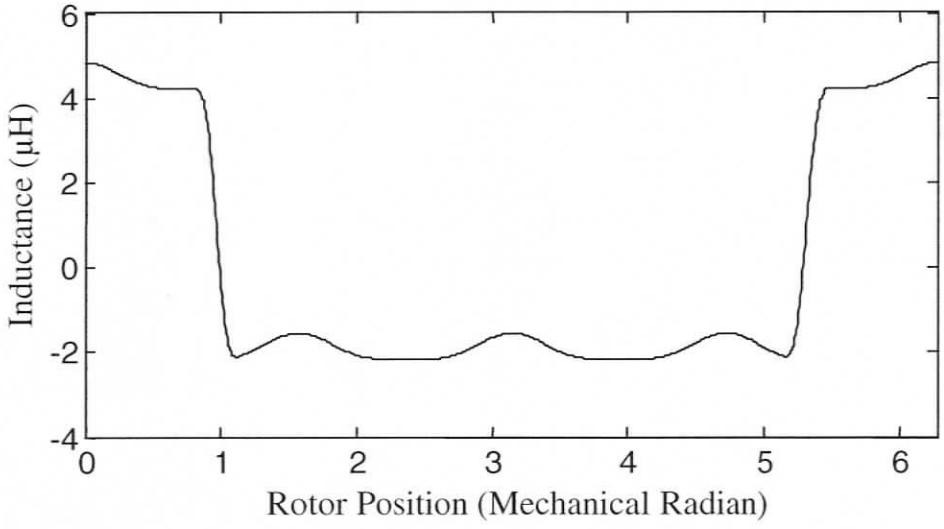

Figure 4.9 Mutual inductance between faulty part of stator phase-A and a typical rotor loop of RSM

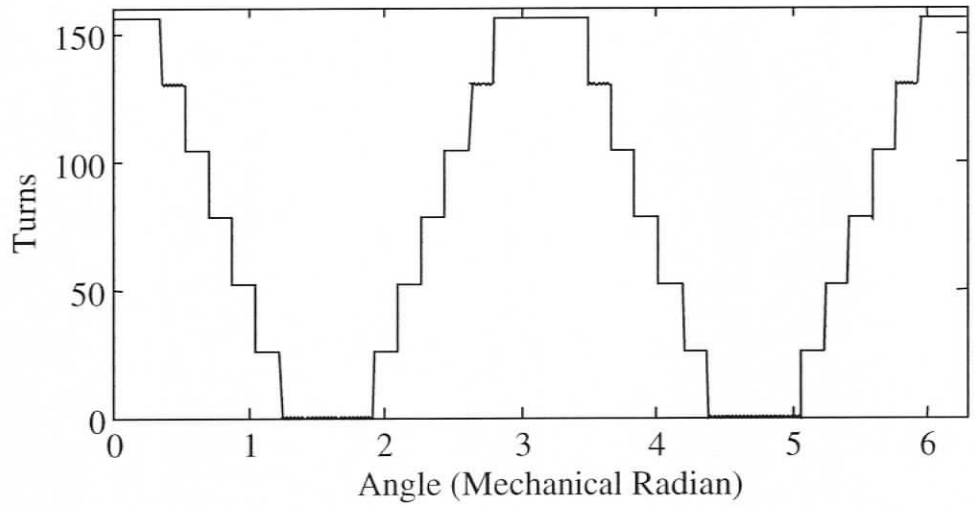

Figure 4.10 Turns function of healthy stator phase-A of SM with DC excitation

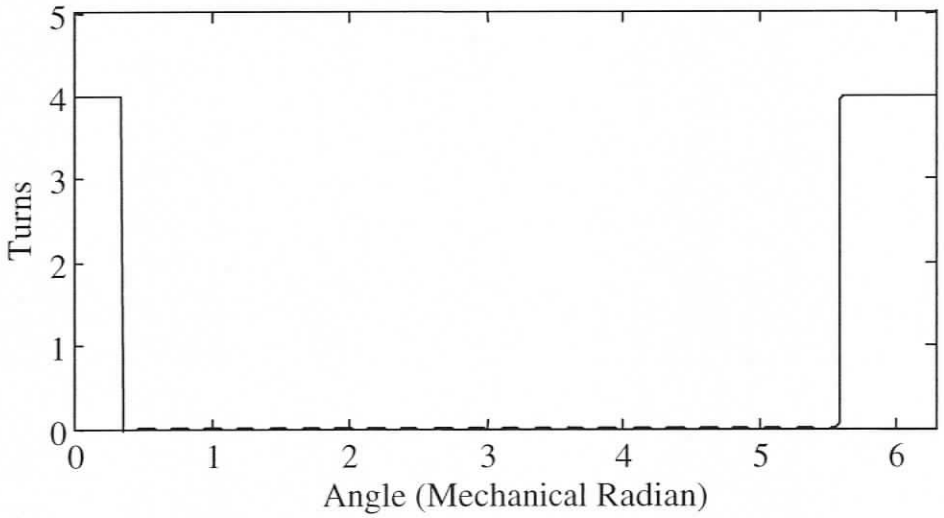

Figure 4.11 Turns function of faulty part of stator phase-A (with 4 shorted turns) of SM with DC excitation

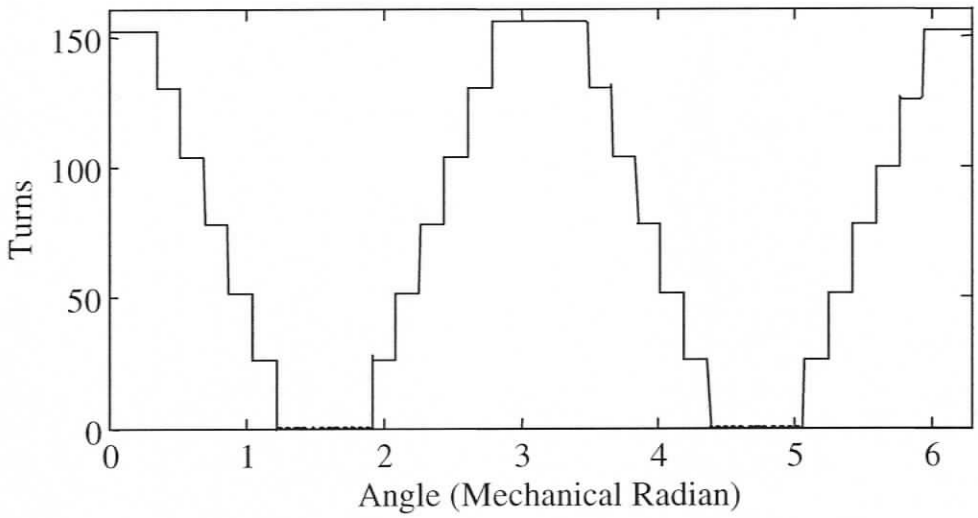

Figure 4.12 Turns function of healthy part of stator phase-A of SM with DC excitation

$$n_{Af}(\phi) = a_{osf} + \sum_{c=1,2,3,\ldots}^{\infty} a_{csf} \cos\left\{c\left(\phi + \frac{\pi}{18}\right)\right\}$$
$$a_{osf} = \frac{N_s}{6},\ a_{csf} = \frac{2N_s}{\pi c}\left\{\sin\left(\frac{\pi c}{6}\right)\right\} \tag{4.3}$$

Using (3.10) and choosing suitable turns functions of the winding, various inductances of the faulty phase of the SM with DC excitation have been computed. The magnetizing inductance of faulty part of stator phase-A has been shown in Figure 4.13 and the mutual inductance between healthy and faulty parts of phase-A of the SM with DC excitation has been shown in Figure 4.14. The mutual inductance of healthy and faulty parts of stator phase-A and a typical rotor loop of SM with DC excitation has been shown in Figure 4.15 and Figure 4.16 respectively. The mutual inductance of healthy and faulty parts of stator phase-A with standard field winding of SM has been shown in Figure 4.17 and Figure 4.18 respectively.

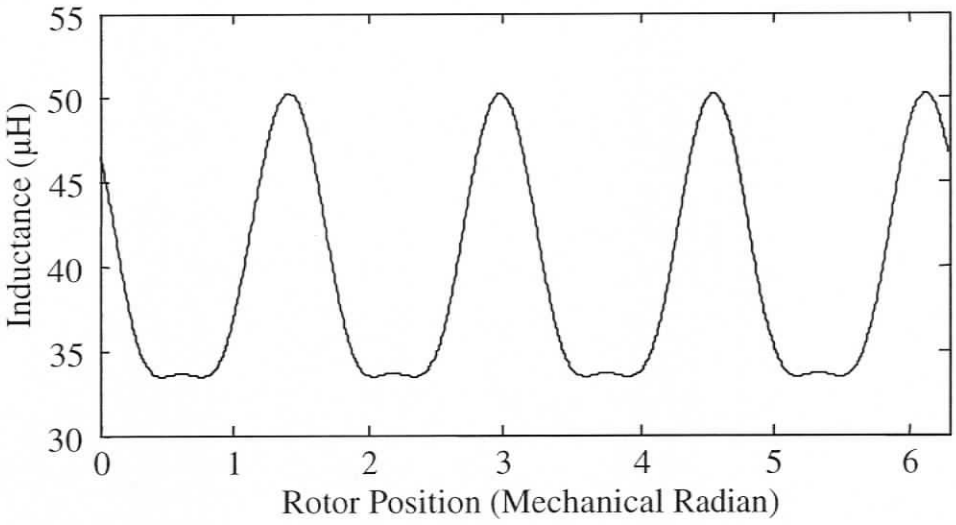

Figure 4.13 Magnetizing inductance of faulty part of stator phase-A (with 4 shorted turns) of SM with DC excitation

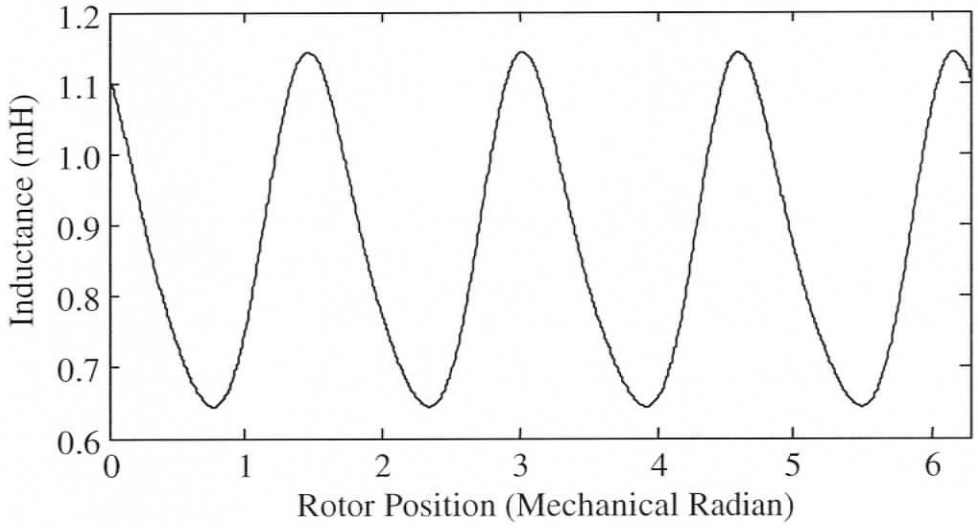

Figure 4.14 Mutual inductance between healthy and faulty parts (with 4 shorted turns) of phase-A of SM with DC excitation

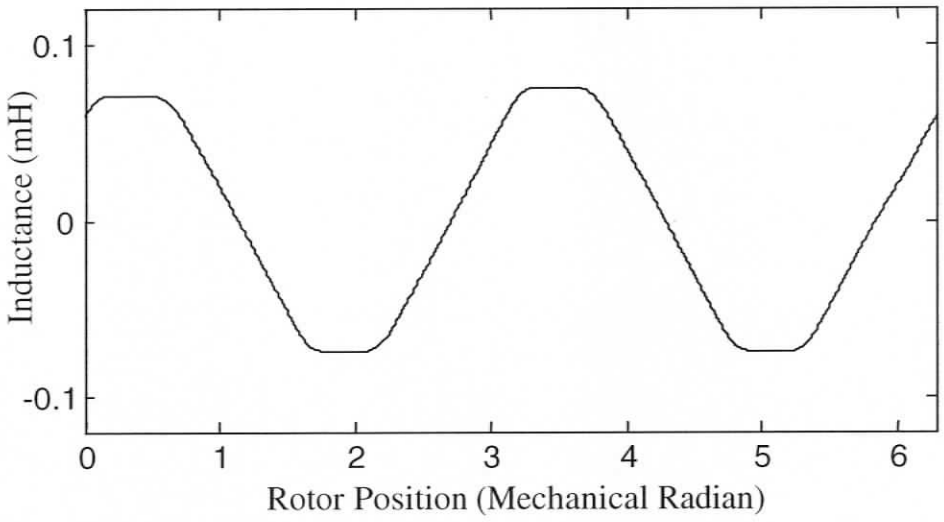

Figure 4.15 Mutual inductance between healthy part of stator phase-A and a typical rotor loop of SM with DC excitation

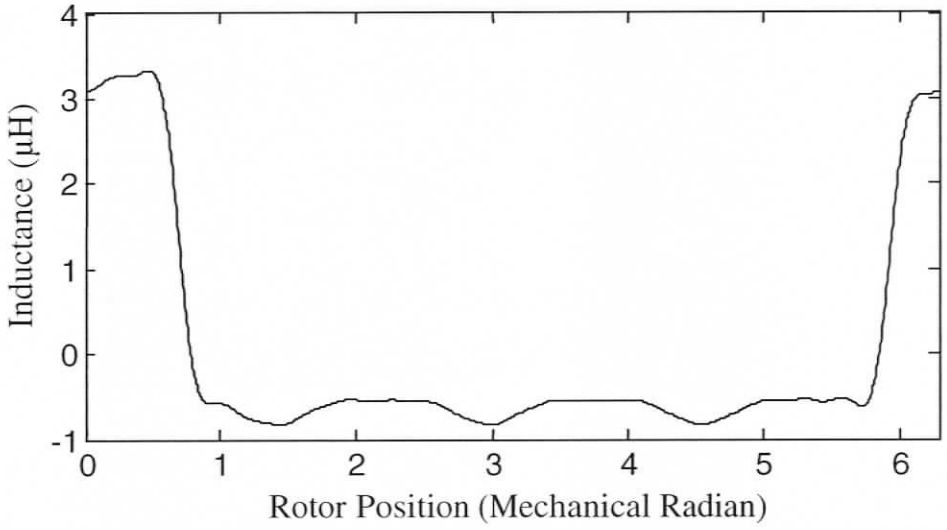

Figure 4.16 Mutual inductance between faulty part of stator phase-A and a typical rotor loop of SM with DC excitation

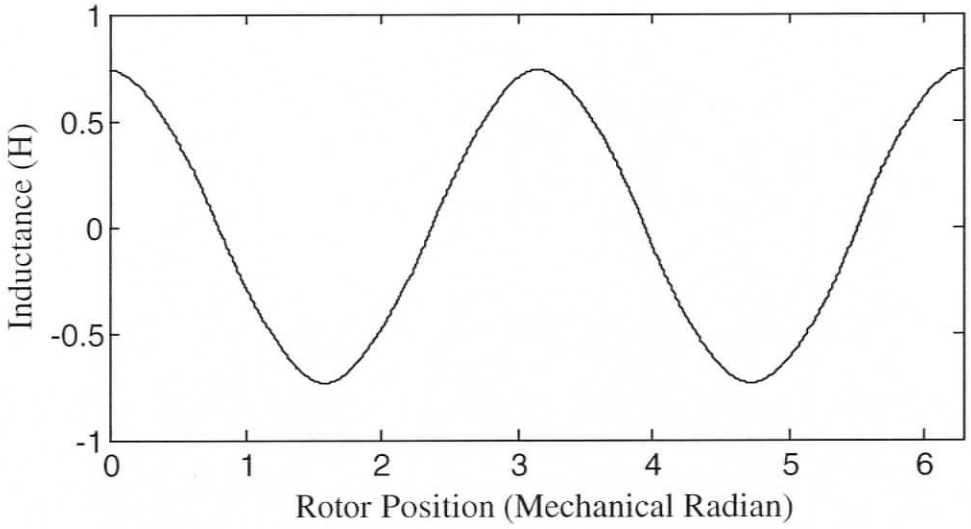

Figure 4.17 Mutual inductance between healthy part of stator phase-A and standard field winding of SM

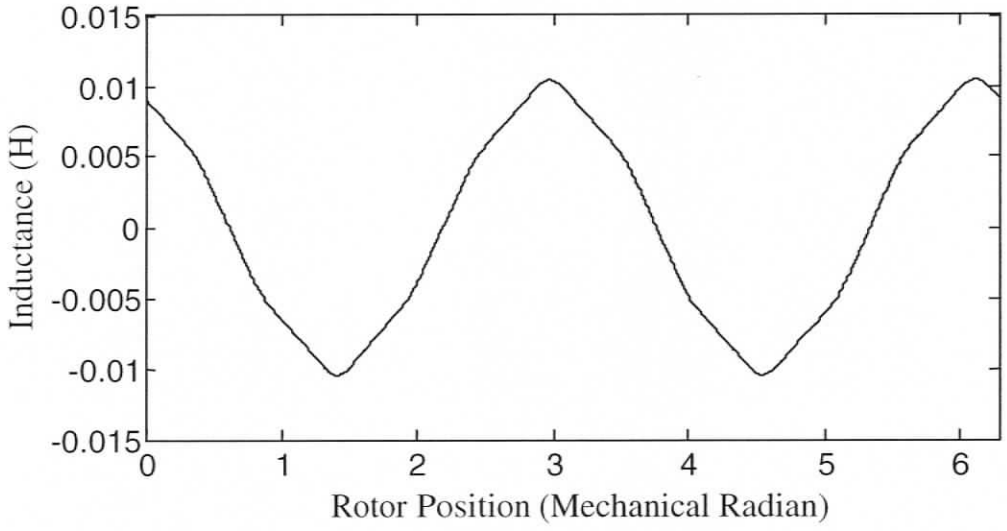

Figure 4.18 Mutual inductance between faulty part of stator phase-A and standard field winding of SM

4.3 State Space Modeling of Synchronous Machines with Stator Inter-Turn Faults

4.3.1 Equations for Dynamic Modeling of RSM

The following equations describe RSM with stator inter-turn fault:

$$V_{sh} = R_{sh} I_{sh} + \frac{d\Lambda_{sh}}{dt} + V_g \tag{4.4}$$

$$\begin{aligned} V_{sh} &= [v_{sAh} \quad v_{sB} \quad v_{sC}]^t, \; I_{sh} = [i_{sAh} \quad i_{sB} \quad i_{sC}]^t, \\ \Lambda_{sh} &= [\lambda_{sAh} \quad \lambda_{sB} \quad \lambda_{sC}]^t \quad and \quad V_g = v_g [1 \quad 1 \quad 1]^t \end{aligned} \tag{4.5}$$

$$R_{sh} = \begin{bmatrix} r_{sAh} & 0 & 0 \\ 0 & r_{sB} & 0 \\ 0 & 0 & r_{sC} \end{bmatrix} \tag{4.6}$$

$$0 = r_{sAf} i_{sAf} + \frac{d\lambda_{sAf}}{dt} \tag{4.7}$$

$$V_r = R_r I_r + \frac{d\Lambda_{sr}}{dt} \tag{4.8}$$

v_{sAh}, v_{sB} & v_{sC} are the stator voltages, i_{sAh}, i_{sB} & i_{sC} are the stator currents whereas r_{sAh} is the resistance of healthy part of stator phase-A and r_{sB} & r_{sC} are the resistances of phase-B and Phase-C respectively. v_g is the neutral voltage, V_r is the vector consisting of rotor voltages and I_r is the vector consisting of rotor currents whereas R_r is the rotor resistance matrix. i_{sAf} and r_{sAf} are the current and the resistance of the shorted turns. Various flux linkages can be expressed as follows:

$$\lambda_{sAh} = L_{sAhAh} i_{sAh} + L_{sAhB} i_{sB} + L_{sAhC} i_{sC} + L_{sAhAf} i_{sAf} + L_{sAhr} I_r \tag{4.9}$$

$$\lambda_{sB} = L_{sBAh}\, i_{sAh} + L_{sBB}\, i_{sB} + L_{sBC}\, i_{sC} + L_{sBAf}\, i_{sAf} + L_{sBr}\, I_r \quad (4.10)$$

$$\lambda_{sC} = L_{sCAh}\, i_{sAh} + L_{sCB}\, i_{sB} + L_{sCC}\, i_{sC} + L_{sAfC}\, i_{sAf} + L_{sCr}\, I_r \quad (4.11)$$

$$\lambda_{sAf} = L_{sAfAh}\, i_{sAh} + L_{sAfB}\, i_{sB} + L_{sAfC}\, i_{sC} + L_{sAfAf}\, i_{sAf} + L_{sAfr}\, I_r \quad (4.12)$$

$$\Lambda_{sr} = L'_{sAhr}\, i_{sAh} + L'_{sBr}\, i_{sB} + L'_{sCr}\, i_{sC} + L'_{sAfr}\, i_{sAf} + L_{rr} I_r \quad (4.13)$$

$$L_{sXr} = [L_{sXr\,1}, L_{sXr\,2}, \ldots\ldots, L_{sXrn}, L_{sXre}]$$
$$L_{XY} = L_{YX}{}^{t}$$
with $X = Y = Ah, B, C, or\ sAf$; *re refers to the end ring whereas* $1,2,\ldots.. n$ *to the rotor loops .The letter* $'h'$ *in the suffixes represents the healthy part of Phase* $- A$. (4.14)

The electromagnetic torque, T_e, has to be dynamically computed from the magnetic co-energy (Wco) as follows:

$$Wco = \frac{1}{2}\begin{bmatrix} I_{sh}{}^{t} L_{ssh} I_{sh} + I_{sh}{}^{t} L_{shr} I_r + I_r{}^{t} L_{rsh} I_{sh} + I_r{}^{t} L_{rr} I_r + i_{sAf} L_{sAfAf} i_{sAf} \\ + I_{sh}{}^{t} L_{shsAf} i_{sAf} + i_{sAf} L_{sAfsh} I_{sh} + I_r{}^{t} L_{rsAf} i_{sAf} + i_{sAf} L_{sAfr} I_r \end{bmatrix} \quad (4.15)$$

Here, L_{ssh} consists of the self and mutual inductances of the healthy part of stator phase-A, phase-B and phase-C. L_{shr} represents the mutual inductances between the healthy part of stator phase-A, phase-B and phase-C with the rotor loops and end ring. L_{shsAf} represents the mutual inductances between the healthy part of stator phase-A, phase-B and phase-C with the faulty part of phase-A whereas L_{rsAf} represents the mutual inductances between the rotor loops and end ring with the faulty part of phase-A. Further, L_{sAfAf} represents the self-inductance of the faulty part of phase-A. Also, $L_{rsh} = L_{rsh}{}^{t}$, $L_{sAshf} = L_{shsAf}{}^{t}$ and $L_{sAfr} = L_{rsAf}{}^{t}$. Various inductances pertaining to the faulty phase of stator winding can be expressed as follows:

$$L_{sAhAf} = L_{sAAf} - L_{sAfAf} \tag{4.16}$$

$$L_{sAhAh} = L_{sAA} - 2L_{sAAf} + L_{sAfAf} \tag{4.17}$$

$$L_{sAhB} = L_{sAB} - L_{sAfB} \tag{4.18}$$

$$L_{sAhC} = L_{sAC} - L_{sAfC} \tag{4.19}$$

$$L_{sAhr1} = L_{sAr1} - L_{sAfr1} \tag{4.20}$$

4.3.2 Equations for Dynamic Modeling of SM with DC Excitation

In the case of SM with DC excitation, (4.4)-(4.8) hold good with various flux linkages suitably substituted. In addition, the field circuit can be described as

$$v_{rf} = r_{rf} i_{rf} + \frac{d\lambda_{rf}}{dt} \tag{4.21}$$

The various flux linkages can be expressed as follows:

$$\begin{aligned}\lambda_{sAh} = {} & L_{sAhAh} i_{sAh} + L_{sAhB} i_{sB} + L_{sAhC} i_{sC} + L_{sAhAf} i_{sAf} + L_{sAhr} I_r \\ & + L_{sAhrf} i_{rf}\end{aligned} \tag{4.22}$$

$$\lambda_{sB} = L_{sBAh} i_{sAh} + L_{sBB} i_{sB} + L_{sBC} i_{sC} + L_{sBAf} i_{sAf} + L_{sBr} I_r + L_{sBrf} i_{rf} \tag{4.23}$$

$$\lambda_{sC} = L_{sCAh} i_{sAh} + L_{sCB} i_{sB} + L_{sCC} i_{sC} + L_{sCAf} i_{sAf} + L_{sCr} I_r + L_{sCrf} i_{rf} \tag{4.24}$$

$$\lambda_{sAf} = L_{sAfAh} i_{sAh} + L_{sAfB} i_{sB} + L_{sAfC} i_{sC} + L_{sAfAf} i_{sAf} + L_{sAfr} I_r + L_{sAfrf} i_{rf} \tag{4.25}$$

$$\Lambda_{sr} = L_{sAhr} i_{sAh} + L_{sBr} i_{sB} + L_{sCr} i_{sC} + L_{sAfr} i_{sAf} + L_{rr} I_r + L'_{rfr} i_{rf} \tag{4.26}$$

$$\lambda_{rf} = L_{rfsAh} i_{sAh} + L_{rfsB} i_{sB} + L_{rfsC} i_{sC} + L_{rfsAf} i_{sAf} + L_{rfr} I_r + L_{rfrf} i_{rf} \tag{4.27}$$

$$L_{sXr} = [L_{sXr1}, L_{sXr2}, ..., L_{sXrn}, L_{sXre}]$$
$$L_{XY} = L_{YX}^{\ t}$$
with $X = Y = Ah, B, C, sAf$ *or* rf; *re refers to the end ring whereas* $1,2,.....n$ *to the rotor loops .* (4.28)

The electromagnetic torque, T_e, has to be dynamically computed from the magnetic co-energy (Wco) as follows:

$$Wco = \frac{1}{2}\begin{bmatrix} I_{sh}^{\ t} L_{ssh} I_{sh} + I_{sh}^{\ t} L_{shr} I_r + I_r^{\ t} L_{rsh} I_{sh} + I_r^{\ t} L_{rr} I_r \\ + i_{sAf} L_{sAfAf} i_{sAf} + I_{sh}^{\ t} L_{shsAf} i_{sAf} + i_{sAf} L_{sAfsh} I_{sh} + I_r^{\ t} L_{rsAf} i_{sAf} \\ + i_{sAf} L_{sAfr} I_r + i_{rf} L_{rfrf} i_{rf} + I_{sh}^{\ t} L_{shrf} i_{rf} + i_{rf} L_{rfsh} I_{sh} \\ + I_r^{\ t} L_{rrf} i_{rf} + i_{rf} L_{rfr} I_r + i_{sAf} L_{sAfrf} i_{rf} + i_{rf} L_{rfsAf} i_{sAf} \end{bmatrix} \tag{4.29}$$

Here, L_{rfrf} represents the self-inductance of the field winding. L_{shrf} represents the mutual inductances between the healthy part of stator phase-A, phase-B and phase-C with the field winding whereas L_{sAfrf} represents the mutual inductances between the faulty part of phase-A with the field winding Also, $L_{rfsh} = L_{shrf}^{\ t}$ and $L_{rfsAf} = L_{sAfrf}^{\ t}$. Various inductances pertaining to the faulty phase of stator winding can be expressed using (4.16)-(4.20) in addition to the following:

$$L_{sAhrf} = L_{sArf} - L_{sAfrf} \tag{4.30}$$

4.4 Mathematical Proofs for Various Harmonic Components

The following are the detailed mathematical proofs for the existence of various harmonic components in the synchronous machines under healthy, faulty and abnormal operating conditions.

4.4.1 Harmonic Components in the Synchronous Machines under Healthy Condition

The existence of odd harmonics in the line current of synchronous machines under steady-state (healthy) condition can be explained as follows. The magneto motive force (MMF) produced by a balanced three-phase winding excited by a three-phase supply can be given as

$$F_1 = M_1 \cos\left[np\,\phi \pm \omega t\right] \tag{4.31}$$

ϕ = Angular position with respect to the stator, p = number of pole pairs, $n = (6h\pm1)$ other than fundamental, h = any positive integer and ω = angular frequency. This MMF, interacting with the average specific permeance (P_0), can produce a flux density with respect to stator, given as

$$B_{s1} = P_0 M_1 \cos\left[np\,\phi \pm \omega t\right] \tag{4.32}$$

With respect to rotor, this flux density can be given as

$$B_{r1} = P_0 M_1 \cos\left[np\,\phi' + (n \pm 1)\omega t + \varphi_1\right] \tag{4.33}$$

Here $\phi' = \phi - \omega_r t$, is the angular position with respect to rotor and $\omega_r = \omega / p$. For example, with $n = 5$, the flux is reverse rotating. Hence,

$$\begin{aligned} B_{r1} &= P_0 M_1 \cos\left[5p\phi' + (5+1)\omega t + \varphi_1\right] \\ &= P_0 M_1 \cos\left[5p\phi' + 6\omega t + \varphi_1\right] \end{aligned} \tag{4.34}$$

For $n = 7$, the flux is forward rotating. Hence,

$$\begin{aligned} B_{r1} &= P_0 M_1 \cos\left[7p\phi' + (7-1)\omega t + \varphi_1\right] \\ &= P_0 M_1 \cos\left[7p\phi' + 6\omega t + \varphi_1\right] \end{aligned} \tag{4.35}$$

This induces a current pulsating at $6f$ frequency in the rotor bars. Where, f is the supply frequency. By considering higher values of 'n', the existence of other $6hf$ frequencies in the damper bars can be proved.

The rotors of synchronous machines have discontinuous bars. The adjacent bars to the discontinuity form a loop. This loop, carrying $6hf$ frequency currents, can produce two oppositely revolving fields based on double revolving field theory [60, 61]. The MMF produced by this loop, can be given as

$$F_2 = M_2 \cos\left(w\phi' \pm 6h\omega t\right) \tag{4.36}$$

Here 'w' is any positive integer. Interacting with P_0, this MMF produces a flux density, with respect to rotor, that can be given as

$$B_{r2} = M_2 P_0 \cos\left(w\phi' \pm 6h\omega t\right) \tag{4.37}$$

This flux density, with respect to stator, can be given as

$$B_{s2} = M_2 P_0 \cos\left\{w\phi - \left(\frac{w}{p} \pm 6h\right)\omega t + \varphi_2\right\} \tag{4.38}$$

With $w = 2$, $h = 1$, 5^{th} and 7^{th} harmonics can be induced in the stator. Existence of other odd harmonics can be shown with higher values of $w = np$, i.e., when the pole-pair of a particular frequency component in the flux matches with one of the pole-pairs produced by the winding itself [63].

4.4.2 Harmonic Components in the Synchronous Machines under Abnormal Operating Conditions and Stator Inter-turn Fault

Under abnormal operating conditions, the existence of odd triplen harmonics in the line current of synchronous machines can be explained as follows. The supply unbalance, internal asymmetry or a turn fault in synchronous machine produces a reverse rotating field, which can induce currents in the rotor bars pulsating at $2f$, $4f$, $8f$, $10f$ etc. This can be explained using (4.33) with proper sign before 'ω'. As an example, the reverse rotating field, with $n = 1$, can produce the following flux density component with a '+' sign before ω:

$$\begin{aligned} B_{r3} &= P_0 M_1 \cos\left[p\phi' + (1+1)\omega t + \varphi_1\right] \\ &= P_0 M_1 \cos\left[p\phi' + 2\omega t + \varphi_1\right] \end{aligned} \tag{4.39}$$

Thus the $2f$ frequency component can be induced in the damper bars. Here, the additional harmonic components $2f$, $4f$ (caused by $n = 5$ and '-'sign before 'ω'), $8f$ (caused by $n = 7$ and '+'sign before 'ω'), $10f$ (caused by $n = 11$ and '-'sign before 'ω') etc. can be observed along with the $6hf$ components.

The $2f$ frequency component produces a third harmonic flux density, with respect to stator, that can be given as

$$\begin{aligned} B_{s3} &= P_0 M_3 \cos\left[p(\phi + \omega_r t) + 2\omega t + \varphi_3\right] \\ &= P_0 M_3 \cos\left[p\phi + (2\omega + p\omega_r)t + \varphi_3\right] \\ &= P_0 M_3 \cos\left[p\phi + 3\omega t + \varphi_3\right] \end{aligned} \tag{4.40}$$

Similar to (4.38), we can have

$$B_{s3} = P_0 M_3 \cos\left\{ w\phi - \left(\frac{w}{p} \pm 2 \right) \omega t + \varphi_3 \right\} \tag{4.41}$$

With w = 2, 3rd harmonic can be induced in the stator. Other odd triplen harmonics in the stator current can be shown to exist with higher values of $w = np$.

4.5 Performance Analysis of RSM under Abnormal Operating Conditions and Stator Inter-turn Fault

Initially, the performance analysis of RSM model has been presented under healthy, stator inter-turn fault and abnormal operating conditions such as supply unbalance, time harmonics and internal asymmetry. The corresponding experimental results have also been furnished to validate the claims.

4.5.1 Simulation Results of RSM

The model of RSM has been run under different operating conditions and both rotor and stator currents have been analyzed. The PSD of the rotor loop current of RSM under balanced supply condition has been shown in Figure 4.19 that shows all the $6hf$ frequency components in it. The PSD of the rotor loop current of RSM under unbalanced supply condition has been shown in Figure 4.20 that shows $2f$, $4f$, $8f$ and $10f$ etc. components along with the $6hf$ components

The model of RSM has been run under steady-state full-load condition with balanced supply. The PSD of its line current has been shown in Figure 4.21 where all the odd harmonics other than triplens can be observed. Next this model has been run with 2.5% of supply unbalance. The triplen harmonics appeared in the line current as shown in Figure 4.22.

Now, a 4-turn short fault has been created in the stator phase-A of the machine model. The line current showed an increase in the triplen harmonics as shown in Figure 4.23.

Detailed mathematical proofs for the existence of various harmonics components have been given in the previous sections of this chapter.

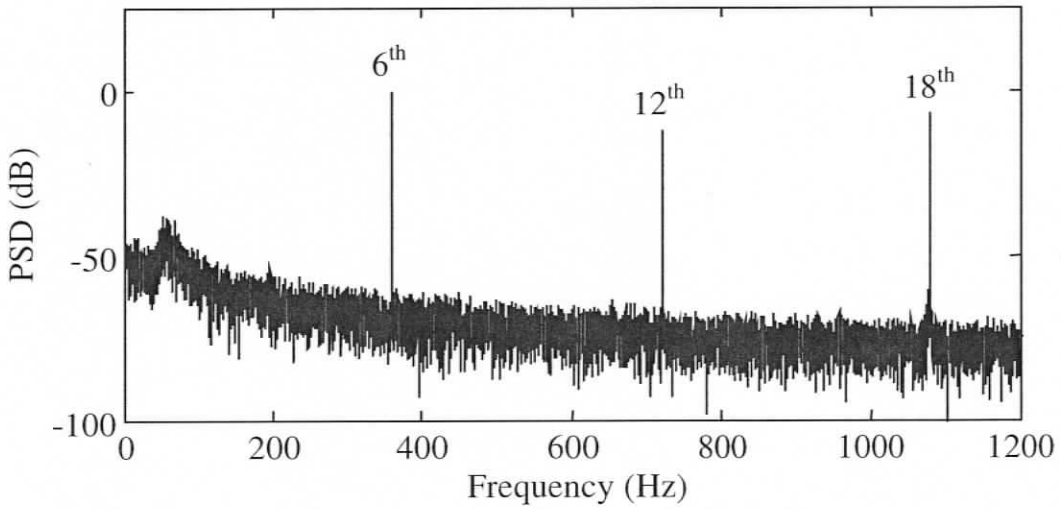

Figure 4.19 Simulated PSD of rotor loop current of RSM under balanced supply condition

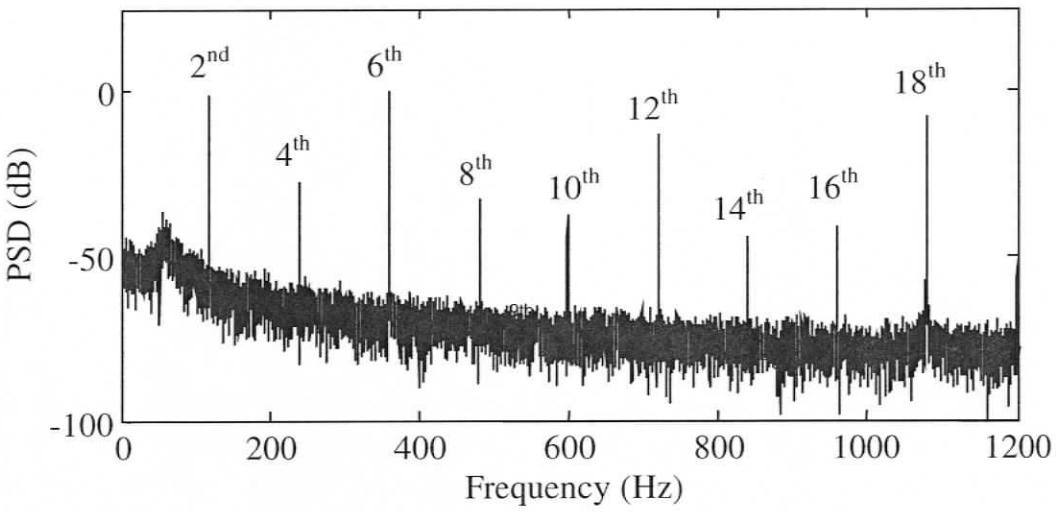

Figure 4.20 Simulated PSD of rotor loop current of RSM under unbalanced supply condition

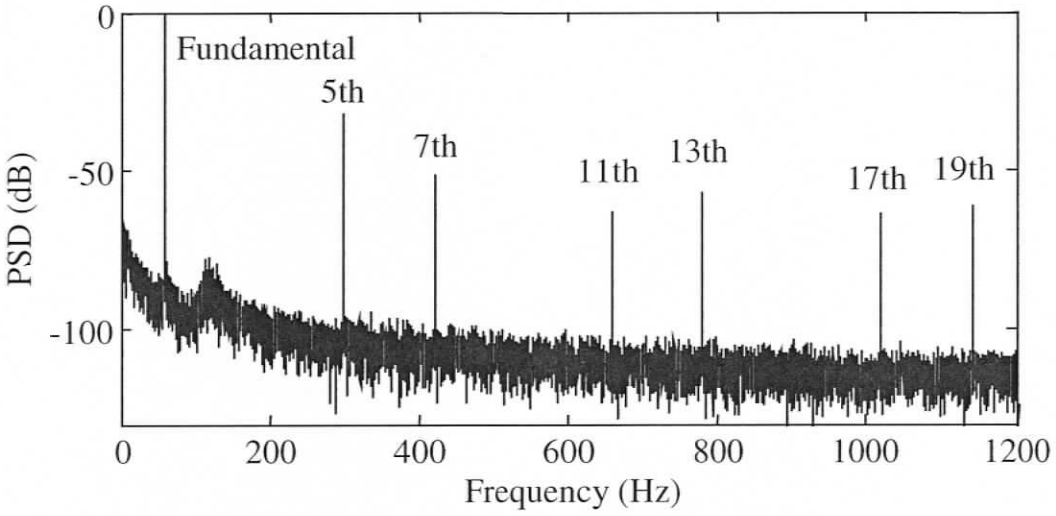

Figure 4.21 Simulated PSD of stator current of RSM run by balanced supply at full-load condition

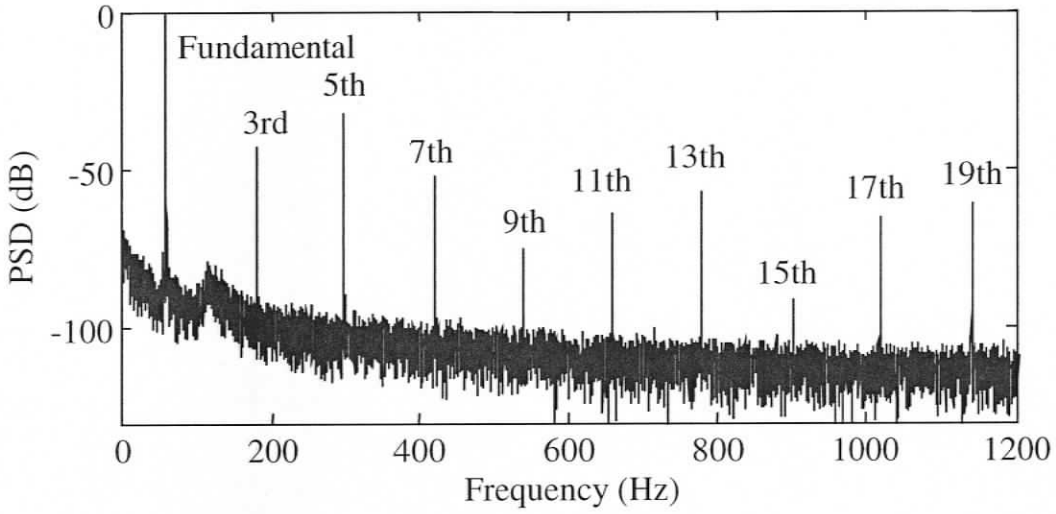

Figure 4.22 Simulated PSD of stator current of RSM run by unbalanced supply at full-load condition

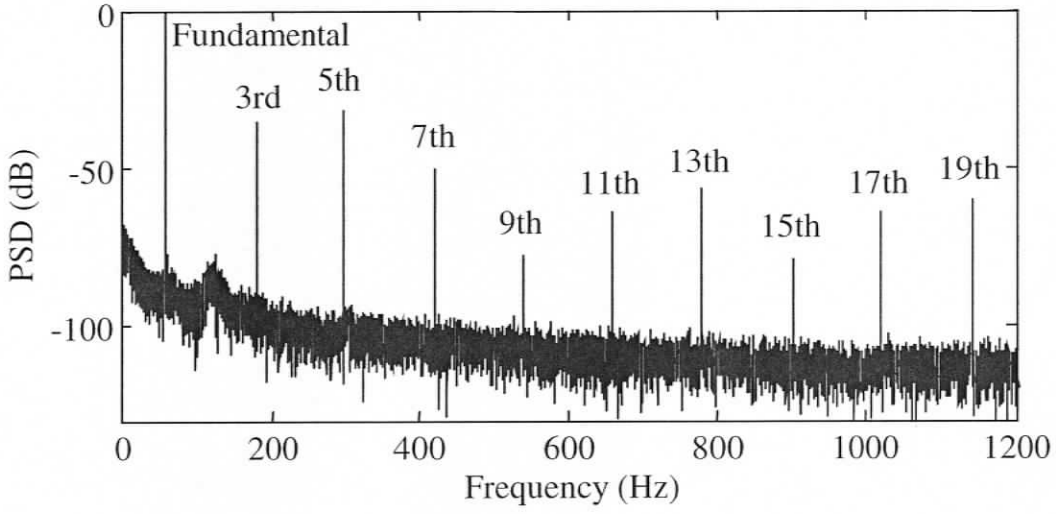

Figure 4.23 Simulated PSD of stator current of RSM with 4-turn short in the stator phase-A at full-load condition

4.5.2 Experimental Results of RSM

In order to validate the simulation results, suitable experimental results have also been presented. The PSD of line current of the experimental motor under balanced and unbalanced (2.5% unbalance) supply have been shown in Figure 4.24 and Figure 4.25 respectively. The triplen harmonics in the line current showed an increase under unbalanced supply condition. However, the triplen harmonics appeared in the line current of RSM under balanced supply condition itself. This can be due to supply time harmonics and internal asymmetry of the machine.

The voltage has all the time harmonics as shown in Figure 4.26. In order to study the influence of time harmonics, the simulated model has been run by the voltage data collected from the utility supply. The triplen harmonics appeared in the line current as shown in Figure 4.27.

In order to consider the influence of internal asymmetry, a separate model of RSM has been obtained that has some internal asymmetry. By removing two turns from the phase-A of the model, internal asymmetry has been created. The asymmetric model has been now fed by the voltage data collected from the utility supply. A large increase in the triplen harmonics has been observed as shown in Figure 4.28. A better match between the simulated and experimental results has also been observed.

The experimental plot of the machine with a 4-turn fault has been as shown in Figure 4.29. Increase in the magnitudes of the triplen harmonics under both abnormal and faulty operating conditions clearly indicated ambiguity. A detailed comparison of magnitudes of triplen harmonics in the line current of the experimental machine under healthy, abnormal operating conditions and stator inter-turn fault (with different faulty turns) has been given in Table 4.1. Here, HB represents a healthy machine fed by a balanced supply; HU represents a healthy machine fed by unbalanced supply whereas T1 to T4 represents 1 to 4-turn short in the stator phase-A

at full-load condition of the machine. It can be observed that the supply unbalance could bring larger increase in the 3rd and 15th harmonics than the inter-turn faults in the machine. Also, the supply unbalance could cause larger increase in the 9th harmonic than a 1-turn fault in the machine. From 3-turn fault onwards, the 9th harmonics showed a very large increase. However, keeping in view the fact that the triplen harmonics can be sensitive to the supply unbalance, internal asymmetry of the machine and time harmonics, it may not be recommended to use these harmonics to detect stator inter-turn faults in RSM.

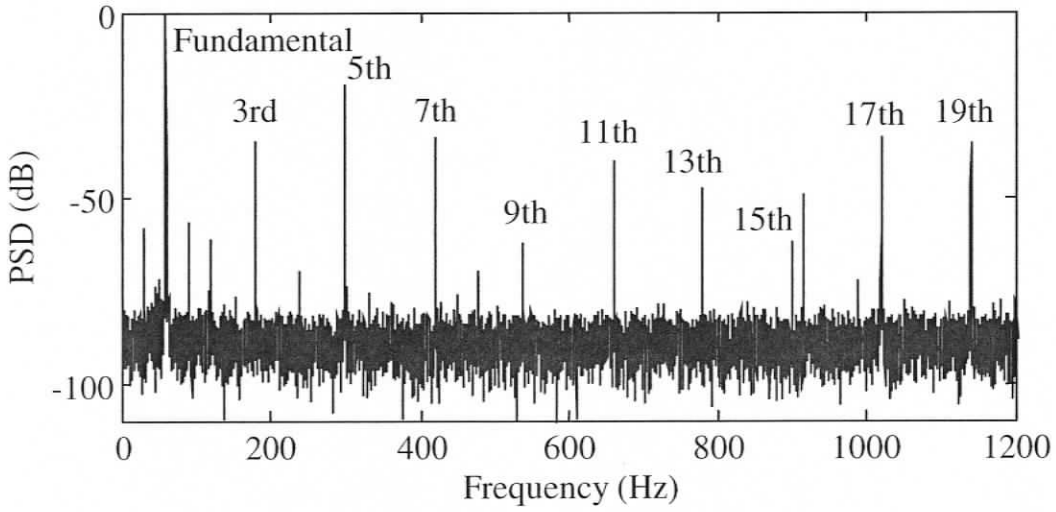

Figure 4.24 Experimental PSD of stator current of RSM run by balanced supply at full-load condition

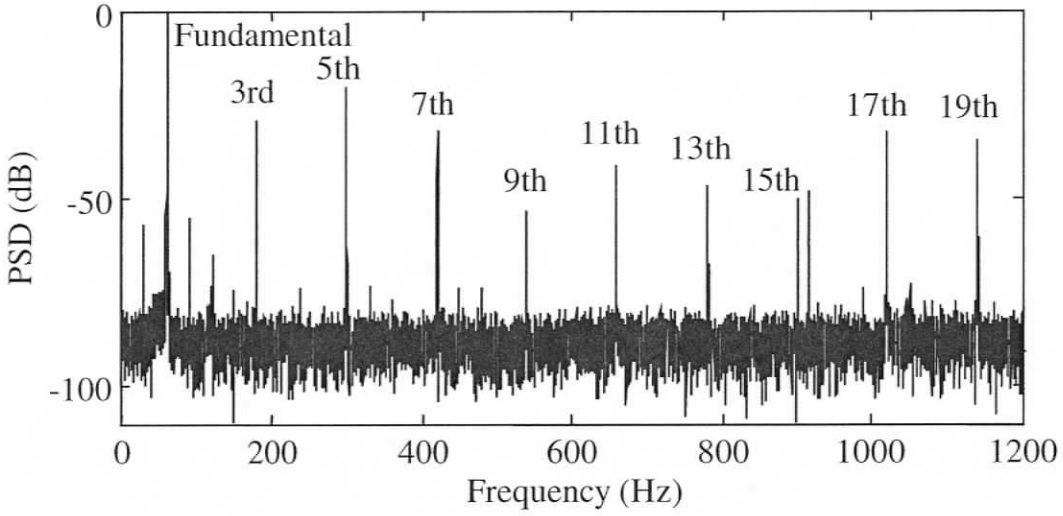

Figure 4.25 Experimental PSD of stator current of RSM run by unbalanced supply at full-load condition

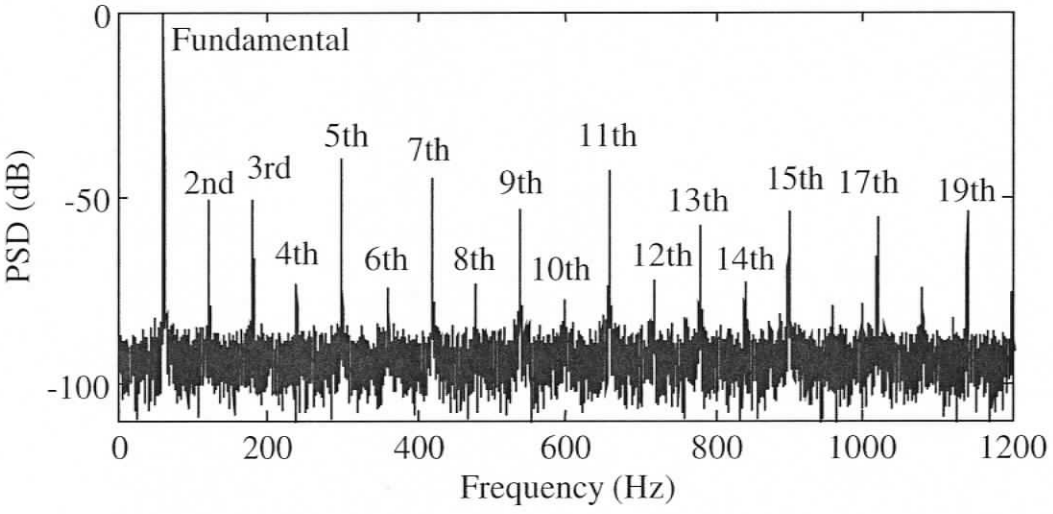

Figure 4.26 Experimental PSD of line voltage of RSM

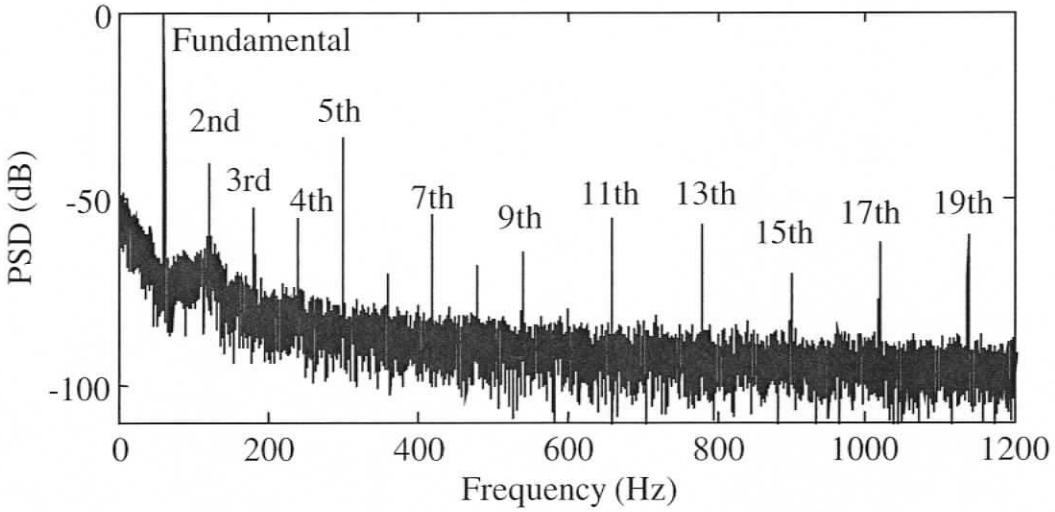

Figure 4.27 Simulated PSD of stator current of symmetric RSM run by experimental balanced supply data at full-load condition

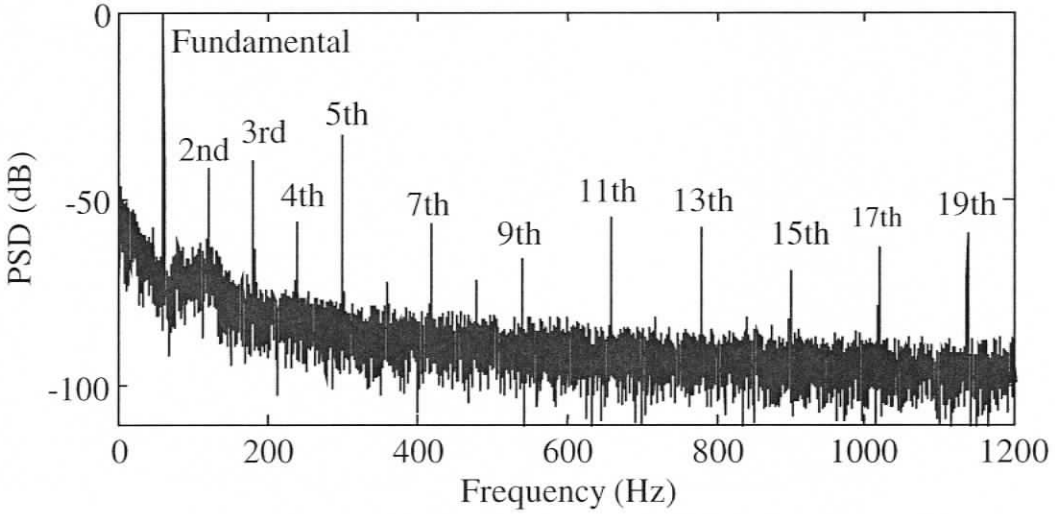

Figure 4.28 Simulated PSD of stator current of asymmetric RSM run by experimental balanced supply data at full-load condition

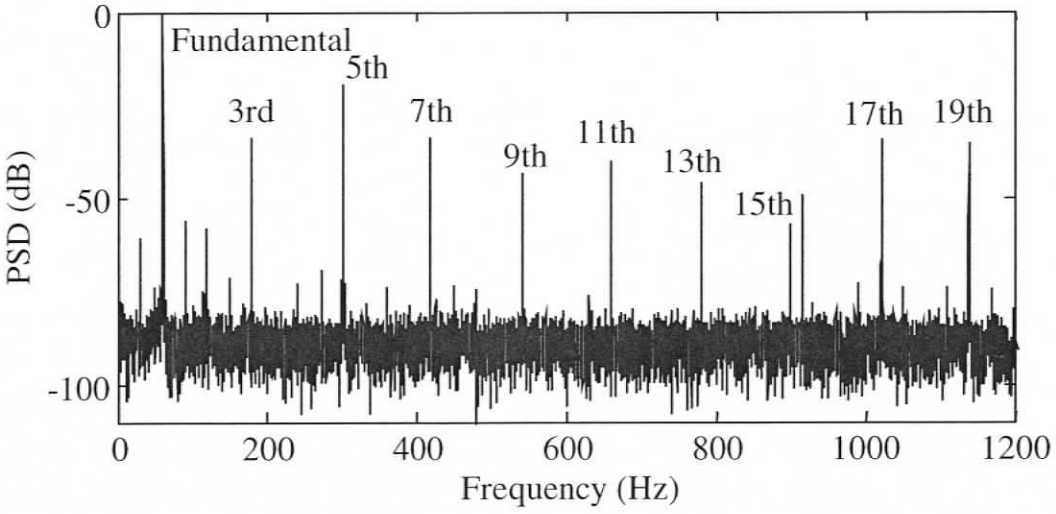

Figure 4.29 Experimental PSD of stator current of RSM with 4-turn short in the stator phase-A at full-load condition

Table 4.1 Triplen harmonics in RSM at full-load condition (Experimental)

Condition of motor	3^{rd} harmonic (dB)	9^{the} harmonic (dB)	15^{th} harmonic (dB)
HB	-34.63	-60.78	-62.19
HU	-29.0	-53.83	-49.46
T1	-35.32	-64.86	-61.36
T2	-34.27	-52.44	-59.06
T3	-34.95	-46.52	-59.73
T4	-33.83	-42.88	-56.84

4.6 Performance Analysis of SM with DC Excitation under Abnormal Operating Conditions and Stator Inter-turn Fault

Next, the performance analysis of the simulated model of SM with standard field winding has been presented under healthy, faulty and abnormal operating conditions such as supply unbalance, time harmonics and internal asymmetry. The corresponding experimental results have also been furnished to validate the claims.

4.6.1 Simulation Results of SM with Standard Field Winding

The model of the SM with standard field winding has been run under steady state, full-load condition with balanced supply. The PSD of its line current has been shown in Figure 4.30 where all the odd harmonics other than triplens can be observed. Now this model has been run with 2.5% of supply unbalance. The triplen harmonics appeared in the line current as shown in Figure 4.31.

Also, a 4-turn short fault has been created in the stator phase-A of the machine model. The line current showed an increase in the triplen harmonics as shown in Figure 4.32.

4.6.2 Experimental Results of SM with Standard Field Winding

In order to validate the simulation results, suitable experimental results have also been presented. The PSD of line current of the experimental motor under balanced and unbalanced (2.5% unbalance) supply, and with 4-turn fault have been shown in Figure 4.33, Figure 4.34 and Figure 4.35 respectively. An increase in the triplen harmonics under both abnormal and faulty operations clearly indicated ambiguity.

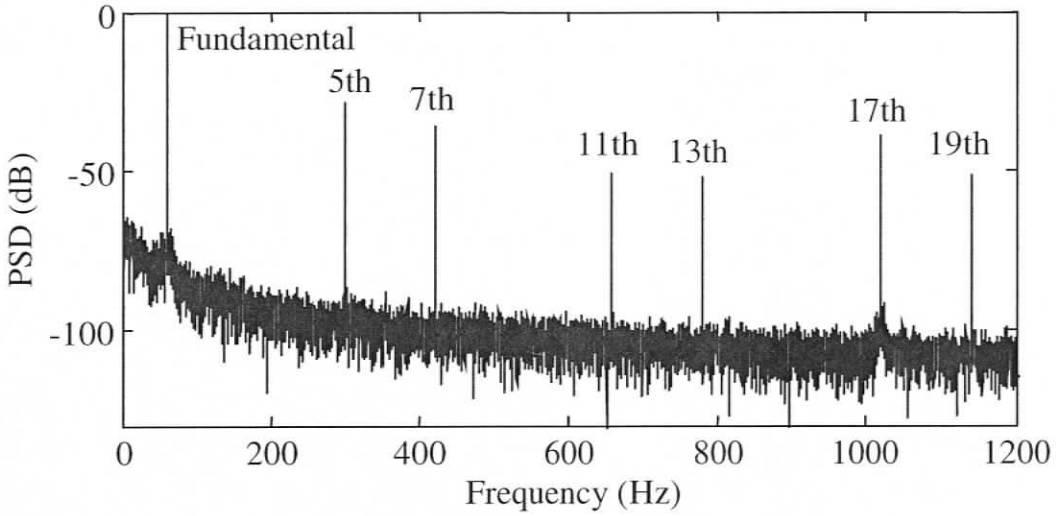

Figure 4.30 Simulated PSD of stator current of SM with standard field winding run by balanced supply at full-load, 0.88 lagging PF condition

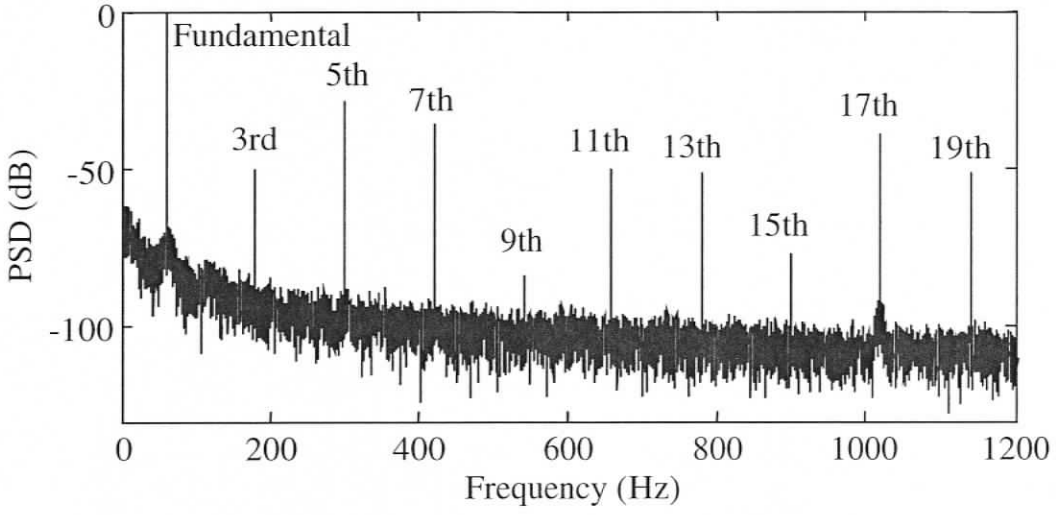

Figure 4.31 Simulated PSD of stator current of SM with standard field winding run by unbalanced supply at full-load, 0.88 lagging PF condition

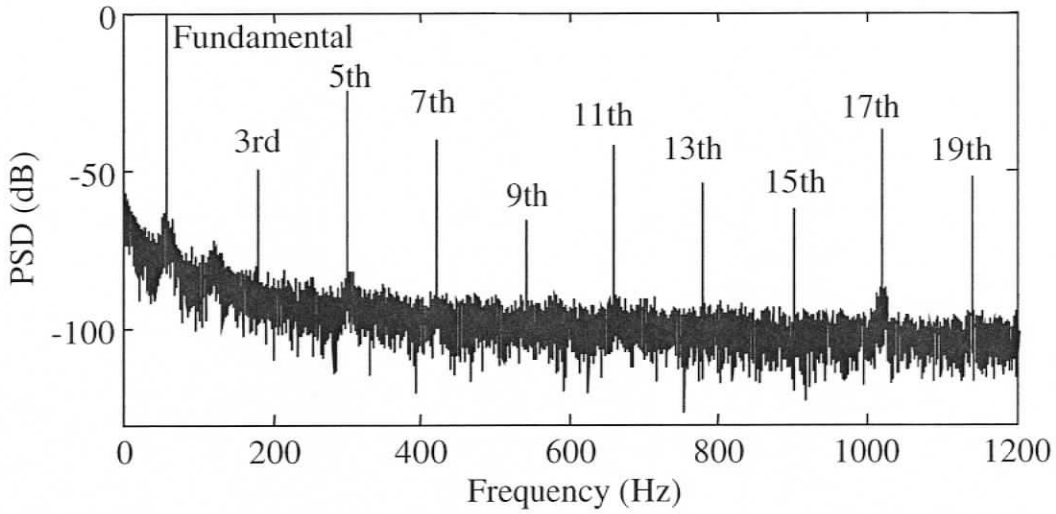

Figure 4.32 Simulated PSD of stator current of SM with standard field winding having 4-turn short in the stator phase-A at full-load, 0.88 lagging PF condition

A comparison of magnitudes of triplen harmonics in the line current of the experimental machines under healthy, faulty (with different faulty turns) and abnormal operating conditions, at full-load, 0.8 lagging PF condition, has been given in Table 4.2. It can be observed that the 3^{rd}, 9^{th} and 15^{th} harmonics did not show significant changes under turn-fault condition. Also their variation under supply unbalance showed ambiguity. Hence, keeping in view the sensitivity of triplen harmonics to the supply unbalance, internal asymmetry of the machine and time harmonics, it has been confirmed that these harmonics cannot be good indicators of stator inter-turn faults in SM with DC excitation.

Detailed mathematical proofs for the existence of various harmonics components have been given in the previous sections of this chapter.

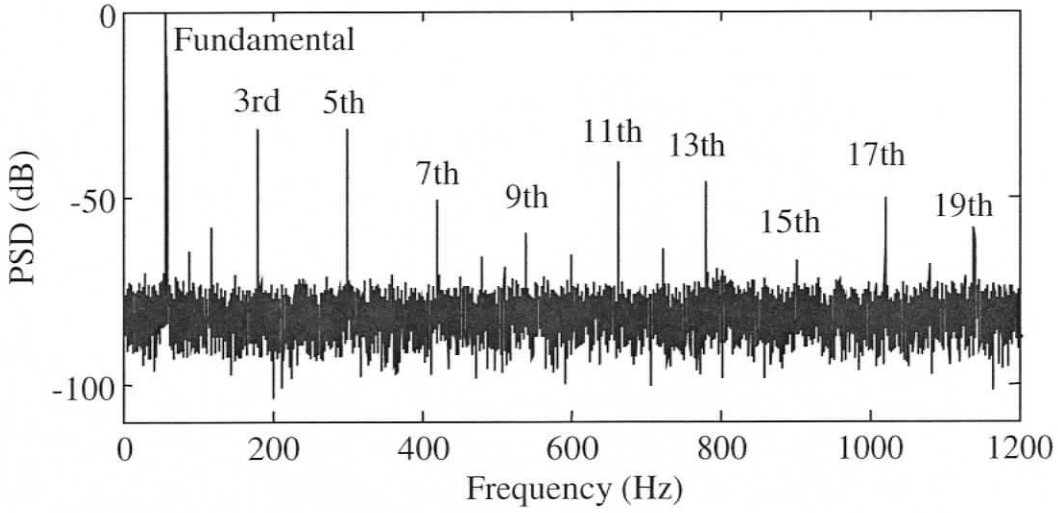

Figure 4.33 Experimental PSD of stator current of SM with standard field winding run by balanced supply at full-load, 0.8 lagging PF condition

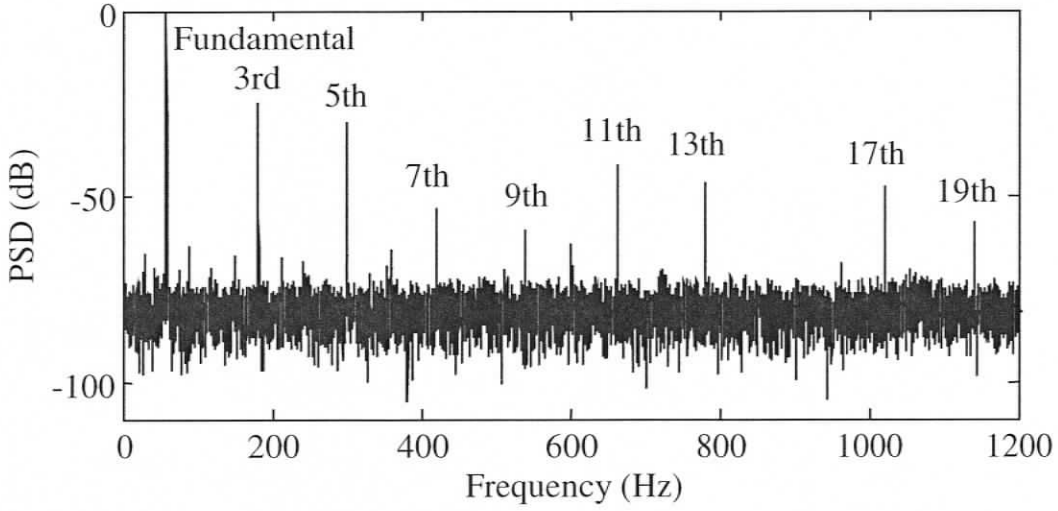

Figure 4.34 Experimental PSD of stator current SM with standard field winding run by unbalanced supply at full-load, 0.8 lagging PF condition

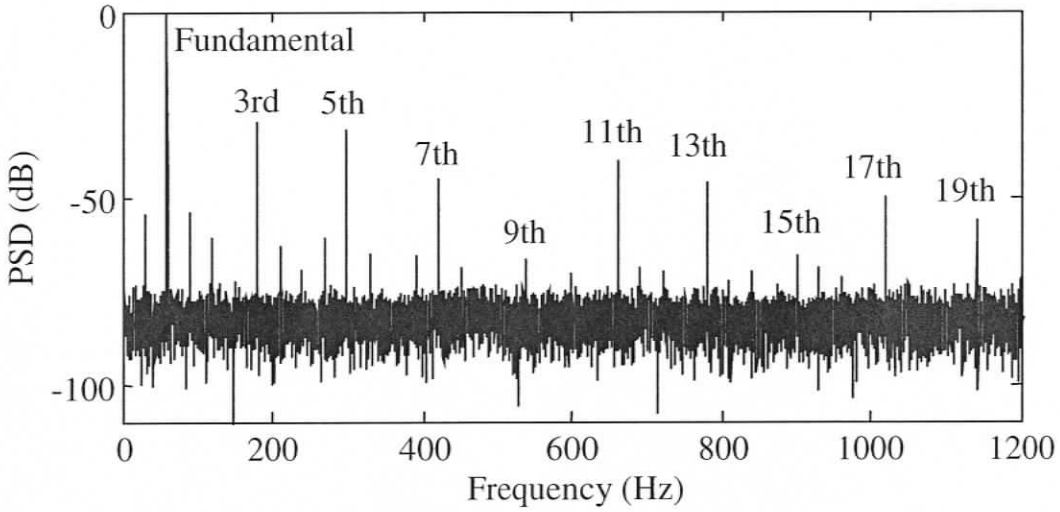

Figure 4.35 Experimental PSD of stator current of synchronous motor with standard field winding having 4-turn short in the stator phase-A at full-load, 0.8 lagging PF condition

Table 4.2 Triplen harmonics in SM with standard field winding at full-load, 0.8 lagging PF condition (Experimental)

Condition of motor	3^{rd} harmonic (dB)	9^{the} harmonic (dB)	15^{th} harmonic (dB)
HB	-31.49	-59.72	-66.76
HU	-24.69	-59.17	-72.07
T1	-31.21	-65.96	-70.34
T2	-30.36	-66.38	-68.09
T3	-29.91	-70.72	-70.28
T4	-29.41	-66.45	-65.55

4.7 Discussions on Results and Contributions

In this chapter, a detailed performance analysis of the synchronous machines has been conducted under healthy, faulty and abnormal operating conditions. In this study, different abnormal operating conditions such as supply unbalance; time harmonics and internal asymmetry of the machines have been included. Also, faults involving different number of shorted turns have been considered.

Further, it has been established that the triplen harmonics in the line currents of these machines cannot be good indicators of stator inter-turn faults. However, the other harmonic components did not show significant changes. Results have been validated using necessary theoretical proofs, simulation studies and suitable experiments.

Chapter 5

Detection of Stator Inter-turn Faults in Reluctance Synchronous Machine using Stored Magnetic Energy after Supply Disconnection

In the previous chapter, it has been demonstrated that triplen harmonics in the stator current of RSM can be very strongly influenced by the supply unbalance, time harmonics and internal asymmetry of the machine. Hence, in order to obtain better diagnostic results against stator inter-turn fault in RSM, a different method has been considered that involves analysis of the stator terminal voltages after supply disconnection. This method utilizes the stored magnetic energy in the machine which gets transferred to the rotor cage after supply disconnection [25] & [62]. Such a method has been used to detect stator inter-turn faults in induction motors [25]. Since the motor has been tested after disconnecting it from the supply bus, the influence of supply unbalance and time harmonics can be totally eliminated. As a first step, a transient model of RSM has been obtained to study its performance after its supply disconnection. Next, the simulation results have been validated using suitable experiments and necessary theory.

5.1 Stator Voltages after Supply Disconnection

Soon after the supply disconnection, the stored energy in the machine gets transferred to the rotor circuit. Hence, the rotor bars will carry current even after the supply disconnection. These currents will die out after a finite period of time due to iron

losses & resistive losses in the rotor cage. Meanwhile, these transient currents produce a flux that can induce voltages across the stator terminals. The voltages thus induced can be used for fault analysis.

5.2 State Space Modeling of RSM after Supply Disconnection [25]

In order to implement this scheme, first, the RSM has been modeled to run in the transient state after the supply disconnection. For steady-state operation, the dynamic model of RSM with stator inter-turn fault can be obtained using (4.4)-(4.15). Using constant flux linkage theorem, the flux linkages of the shorted part of the stator winding and rotor circuit of the machine at the instant of supply disconnection can be obtained as

$$\Lambda_{sfo} = L_{sfs} I_{sfso} + L_{sAfr} I_{ro} \tag{5.1}$$

$$\Lambda_{ro} = L_{rsfs} I_{sfso} + L_{rr} I_{ro} \tag{5.2}$$

Here, $L_{sfs} = [L_{sAfAf} \quad L_{sAfAh} \quad L_{sAfB} \quad L_{sAfC}]$ and $L_{rsfs} = [L'_{sAfr} \quad L'_{sAhr} \quad L'_{sBr} \quad L'_{sCr}]$. I_{sfso} and I_{ro} are the currents in the stator (including shorted part) and the rotor loops at the time of supply disconnection. The initial currents in the rotor and the shorted part of the machine after the supply disconnection can be obtained as

$$\begin{bmatrix} i_{sAfi} \\ I_{ri} \end{bmatrix} = L_1^{-1} L_2 \begin{bmatrix} I_{sfso} \\ I_{ro} \end{bmatrix} \tag{5.3}$$

$$L_1 = \begin{bmatrix} L_{sAfAf} & L_{sAfr} \\ L'_{sAfr} & L_{rr} \end{bmatrix} and \; L_2 = \begin{bmatrix} L_{sfs} & L_{sAfr} \\ L_{rsfs} & L_{rr} \end{bmatrix} \tag{5.4}$$

After the supply disconnection, with stator currents equal to zero, various voltages of the machine can be expressed as

$$V_{sh} = \frac{d\Lambda_{sh}}{dt} + V_g \tag{5.5}$$

$$V_{sh} = [v_{sAh} \quad v_{sB} \quad v_{sC}]^t, \ \Lambda_{sh} = [\lambda_{sAh} \quad \lambda_{sB} \quad \lambda_{sC}]^t$$
$$and \quad V_g = v_g[1 \quad 1 \quad 1]^t \tag{5.6}$$

$$R_{sh} = \begin{bmatrix} r_{sAh} & 0 & 0 \\ 0 & r_{sB} & 0 \\ 0 & 0 & r_{sC} \end{bmatrix} \tag{5.7}$$

$$V_r = R_r I_r + \frac{d\Lambda_r}{dt} \tag{5.8}$$

$$0 = r_{sAf} i_{sAf} + \frac{d\lambda_{sAf}}{dt} \tag{5.9}$$

After the supply disconnection, the various flux linkages can be expressed as

$$\lambda_{sAh} = L_{sAhr} I_r + L_{sAhAf} i_{sAf} \tag{5.10}$$

$$\lambda_{sB} = L_{sBr} I_r + L_{sBAf} i_{sAf} \tag{5.11}$$

$$\lambda_{sC} = L_{sCr} I_r + L_{sCAf} i_{sAf} \tag{5.12}$$

$$\Lambda_r = L_{rr} I_r + L'_{rsAf} i_{sAf} \tag{5.13}$$

$$\lambda_{sAf} = L_{sAfr} I_r + L_{sAfAf} i_{sAf} \tag{5.14}$$

From (5.8), (5.9), (5.13) and (5.14) we have,

$$\begin{bmatrix} \frac{di_{sAf}}{dt} \\ \frac{dI_r}{dt} \end{bmatrix} = -L_1^{-1} M_1 \begin{bmatrix} i_{sAf} \\ I_r \end{bmatrix} \tag{5.15}$$

$$M_1 = \begin{bmatrix} R_{sAf} & \omega \frac{dL_{sAfr}}{d\theta} \\ \omega \frac{dL'_{sAfr}}{d\theta} & R_r \end{bmatrix} \tag{5.16}$$

Substituting (5.10)-(5.12) in (5.5)-(5.7) after solving (5.15) we have

$$v_{sA} = \omega \frac{dL_{sAr}}{d\theta} I_r - L_4 L_1^{-1} M_1 \begin{bmatrix} I_r \\ i_{sAf} \end{bmatrix} + v_g \tag{5.17}$$

$$v_{sB} = \omega \frac{dL_{sBr}}{d\theta} I_r - L_5 L_1^{-1} M_1 \begin{bmatrix} I_r \\ i_{sAf} \end{bmatrix} + v_g \tag{5.18}$$

$$v_{sC} = \omega \frac{dL_{sCr}}{d\theta} I_r - L_6 L_1^{-1} M_1 \begin{bmatrix} I_r \\ i_{sAf} \end{bmatrix} + v_g \tag{5.19}$$

$$\begin{aligned} &L_4 = [L'_{sAfAh} \quad L_{sAhr}],\ L_5 = [L'_{sAfB} \quad L_{sBr}] \\ &and\ L_6 = [L'_{sfC} \quad L_{sCr}] \end{aligned} \tag{5.20}$$

The terminal voltages after supply disconnection can be expressed as

$$v_{AB} = \omega \frac{d(L_{sAhr} - L_{sBr})}{d\theta} I_r - (L_4 - L_5) L_1^{-1} M_1 \begin{bmatrix} i_{sAf} \\ I_r \end{bmatrix} \tag{5.21}$$

$$v_{BC} = \omega \frac{d(L_{sBr} - L_{sCr})}{d\theta} I_r - (L_5 - L_6) L_1^{-1} M_1 \begin{bmatrix} i_{sAf} \\ I_r \end{bmatrix} \tag{5.22}$$

$$v_{CA} = \omega \frac{d(L_{sCr} - L_{sAhr})}{d\theta} I_r - (L_6 - L_4) L_1^{-1} M_1 \begin{bmatrix} i_{sAf} \\ I_r \end{bmatrix} \tag{5.23}$$

5.3 Mathematical Proofs for Various Harmonic Components

The following are detailed mathematical proofs for the existence of various harmonic components in the terminal voltages of RSM after supply disconnection under healthy, unbalanced and faulty operating conditions.

5.3.1 Harmonics in the Terminal Voltage of Healthy Machine after Supply Disconnection

In the case of healthy RSM with balanced or unbalanced supply, odd harmonics other than triplens exist in the terminal voltages after supply disconnection. After supply disconnection, the rotor loops carry non-pulsating currents that decay exponentially depending on rotor loop time constant. The rotors of synchronous machines have discontinuous bars. The adjacent bars to the discontinuity form a loop. Hence, the flux density produced by this loop, carrying non-pulsating current, with respect to rotor can be given as

$$B_{r4} = M_4 P_0 \cos\ (w\phi') \tag{5.24}$$

'w' is any positive integer. With respect to stator, this flux density can be given as

$$B_{s4} = M_4 P_0 \cos\left(w\phi - \frac{w}{p}\omega t + \varphi_4 \right) \tag{5.25}$$

by substituting $\phi' = \phi - (\omega / p)t$. This flux can produce infinite series of time harmonics. Those harmonics, whose pole pairs match with that of the balanced stator winding, will be induced in the terminal voltage [63]. A balanced three-phase winding produces $p(6h\pm1)$ pole-pairs, other than the fundamental pole-pair, $p = 2$. Hence 5^{th}, 7^{th}, 11^{th}, 13^{th}, etc. harmonics can be induced in the terminal voltage after switch-off.

5.3.2 Harmonics in the Terminal Voltage of Faulty Machine after Supply Disconnection

In case of RSM with stator inter-turn fault, the existence of odd triplen harmonics in the terminal voltages of the machine, after supply disconnection, can be proved as follows.

a) The shorted turns in the stator also carry current after supply disconnection and induce these components following the mechanism described while deriving (4.41).

b) The shorted turns of stator winding can act as a search coil picking them up from components described by (5.25) and inducing these harmonics.

As an example, with $w = 6$ in (5.25), 3^{rd} harmonic can be induced in the shorted turn. The MMF produced by the third harmonic current flowing in the shorted loop can be given as

$$F_{sf3} = A_{f3} \cos\left[c\phi \pm 3\omega t \right] \tag{5.26}$$

Here, 'c' is any positive integer. Interacting with P_0, this MMF produces a flux density, with respect to stator, that can be given as

$$B_{sf3} = P_0 A_{f3} \cos\left[c\phi \pm 3\omega t\right] \tag{5.27}$$

With c = 2, the third harmonic can be induced in the healthy part of the stator winding. Similarly, with w = 18 in (5.25), 9th harmonic can be induced in the shorted turn. Following a mechanism similar to the one described in (5.26) and (5.27), 9th harmonic can be induced in the healthy part of the stator winding.

5.4 Performance Analysis of RSM under Healthy, Supply Unbalance and Faulty Conditions after Supply Disconnection

Both simulation and experimental results have been presented to validate the scheme to detect the stator inter-turn faults in RSM.

5.4.1 Simulation Results after Supply Disconnection

The model of RSM has been run under transient-state immediately after disconnecting the supply. Before disconnection, the simulated model was run under no-load condition. After supply disconnection, the short-time FFT of all the three terminal voltages have been analyzed under healthy, faulty and unbalanced supply conditions. The short-time FFT of the line voltage V_{AB} of the healthy RSM after disconnecting a balanced supply has been shown in Figure 5.1. In this case, all the odd harmonics other than triplens can be observed. Then results have been obtained for the healthy model of RSM after disconnecting an unbalanced voltage (with 2.5% unbalance). The short time FFT of its line voltage V_{AB} has been shown in Figure 5.2. The spectrum has only odd harmonics other than triplens even after disconnecting the unbalanced supply. Now an inter-turn fault (5-turn short) in the stator phase-A has been introduced in the machine model and the spectra of terminal voltages have been obtained after supply disconnection. The triplen harmonics appeared in the line

voltage V_{AB} as shown in Figure 5.3. The corresponding spectra of other two terminal voltages, V_{CA} and V_{BC}, under faulty condition have been shown in Figure 5.4 and Figure 5.5 respectively. These plots clearly revealed the fact that a minimum increase of triplen harmonics occurred in the line voltage (V_{BC}) that did not include the faulty phase. Thus, this method can also be used for identifying the faulty phase of the machine as well.

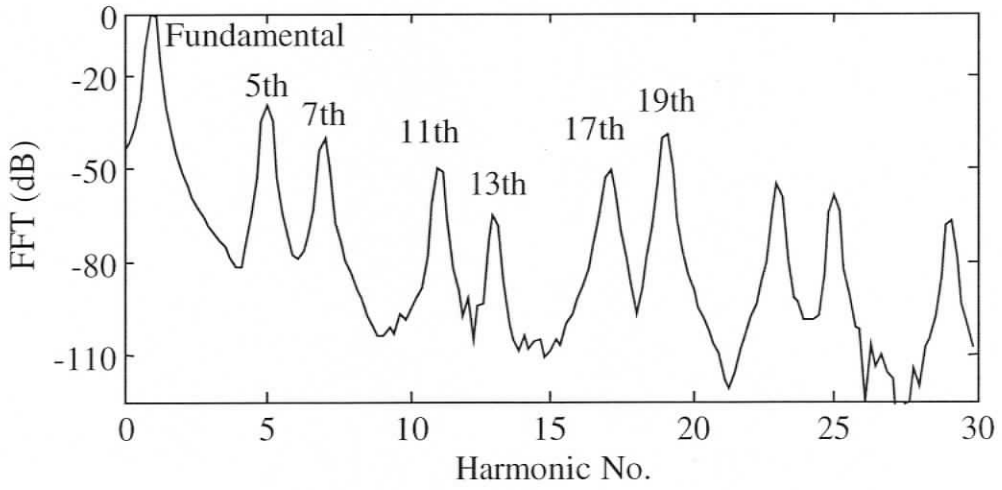

Figure 5.1 Simulated normalized short time FFT of V_{AB} of healthy RSM after disconnecting balanced supply

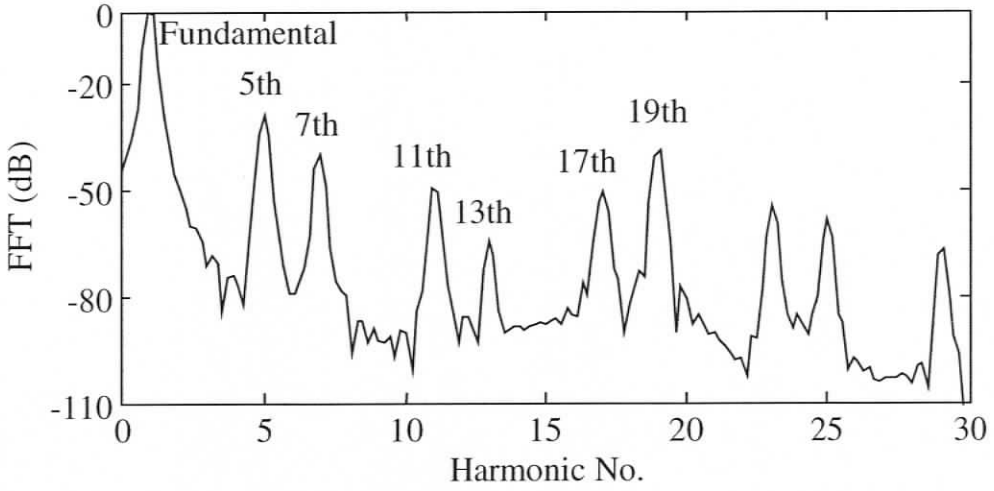

Figure 5.2 Simulated normalized short time FFT of V_{AB} of healthy RSM after disconnecting unbalanced supply

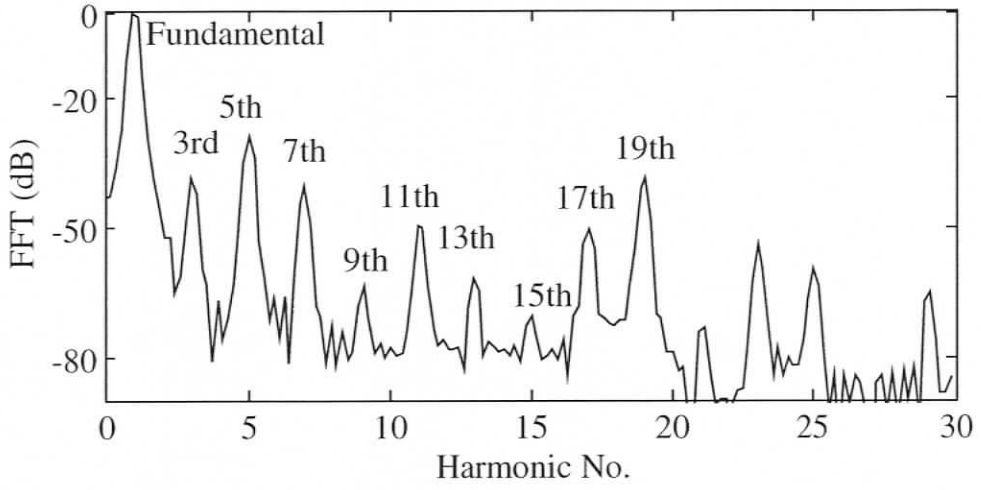

Figure 5.3 Simulated normalized short time FFT of V_{AB} of RSM with 5-turn fault in phase-A after supply disconnection

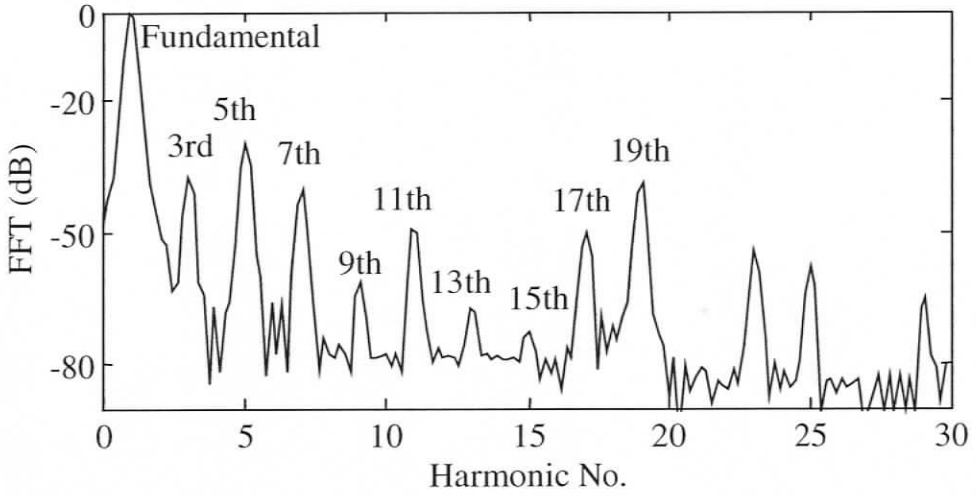

Figure 5.4 Simulated normalized short time FFT of V_{CA} of RSM with 5-turn fault in phase-A after supply disconnection

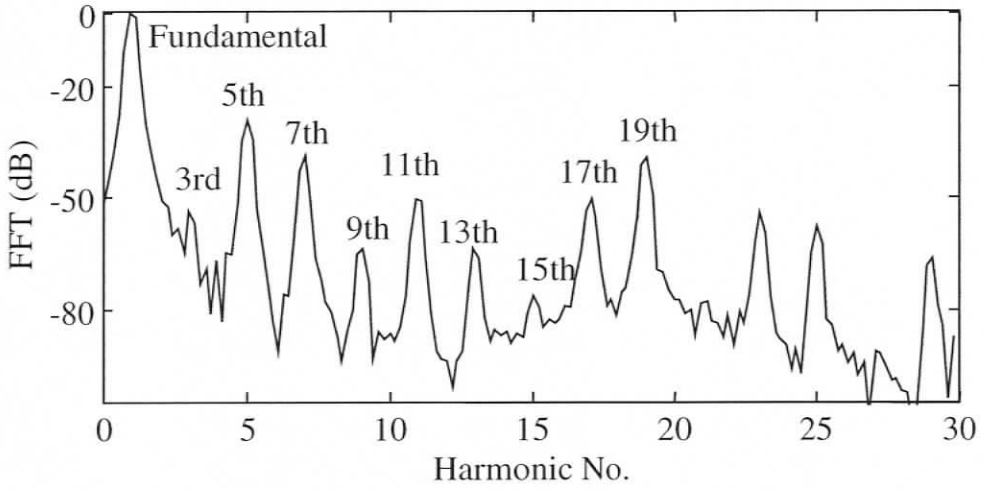

Figure 5.5 Simulated normalized short time FFT of V_{BC} of RSM with 5-turn fault in phase-A after supply disconnection

5.4.2 Experimental Results after Supply Disconnection

The experimental RSM has been run under transient-state immediately after disconnecting the supply. Before disconnection, the machine was first run under no-load condition. After supply disconnection, the short time FFT of all the three terminal voltages have been analyzed under healthy, faulty and unbalanced supply conditions. The short time FFT of its line voltage V_{AB} after disconnecting a balanced supply from the healthy RSM has been shown in Figure 5.6. All the odd harmonics other than triplens can be observed. Then results have been obtained for a healthy machine after disconnecting an unbalanced voltage (with 2.5% unbalance). The FFT of its line voltage V_{AB} has been shown in Figure 5.7. Even in this case, the spectrum has only odd harmonics other than triplens. Now an inter-turn fault (5-turn short) in the stator phase-A has been introduced in the machine and the spectra of terminal voltages have been obtained after supply disconnection. The triplen harmonics appeared in the line voltage V_{AB} as shown in Figure 5.8. The spectra of other two terminal voltages, V_{CA} and V_{BC}, under faulty condition have been shown in Figure 5.9 and Figure 5.10 respectively. These plots clearly revealed the fact that a minimum increase of triplen harmonics occurred in the line voltage (V_{BC}) that did not include the faulty phase. Thus, this method can also be used for identifying the faulty phase of the machine as well. The experimental results clearly supported the simulation results.

The RSM has been thoroughly tested under healthy, abnormal and faulty (with different fault levels) conditions. In order to ensure the dependability of these harmonic components, five samples of data have been collected for each test point. The average and the sample standard deviation have been computed for the harmonics at each test point. A detailed comparison of various triplen harmonics in all the three line voltages under different conditions of RSM after disconnecting supply at no-load has been given in Table 5.1. The sample standard deviation has

been shown in brackets below each of the average value. The corresponding results of the machine under full-load condition have also been obtained as shown in Table 5.2. Here, HB, HU and T1 to T5 represent different conditions of RSM as mentioned before (section 4.5.2, page number 112). *Under both no-load and full-load conditions, the triplen harmonics in the terminal voltages after supply disconnection could detect even one-turn fault very clearly.*

In a recent work [64], fault analysis of induction motor has been presented using residual saturation harmonics. Particularly the third harmonic has been projected to be sensitive to the stator inter-turn faults in induction motors, which arises out of saturation in the machine and a stator inter-turn fault. The results are much more reliable and encouraging in the case of RSM since saliency, which is absent in case of an induction motor, enhances the effect of residual saturation. Hence, results are helpful in detecting even a 1-turn fault.

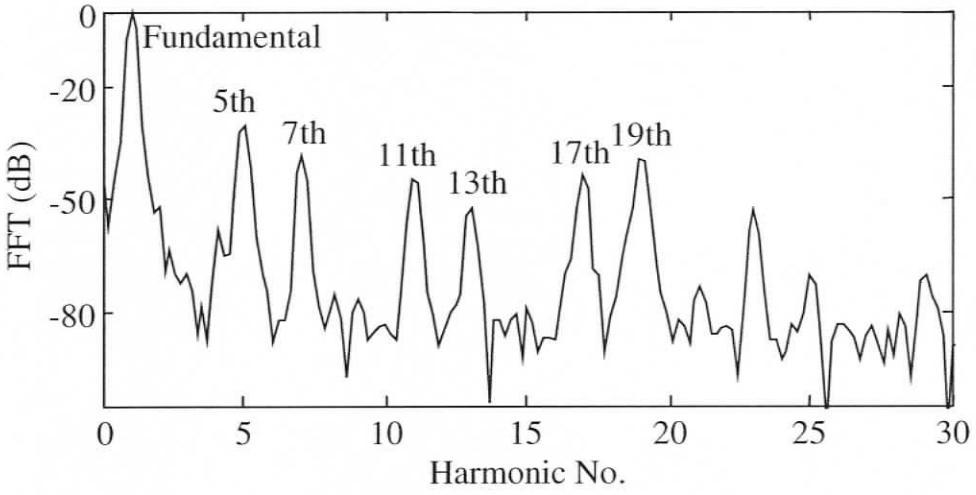

Figure 5.6 Experimental normalized short time FFT of V_{AB} of healthy RSM after disconnecting balanced supply

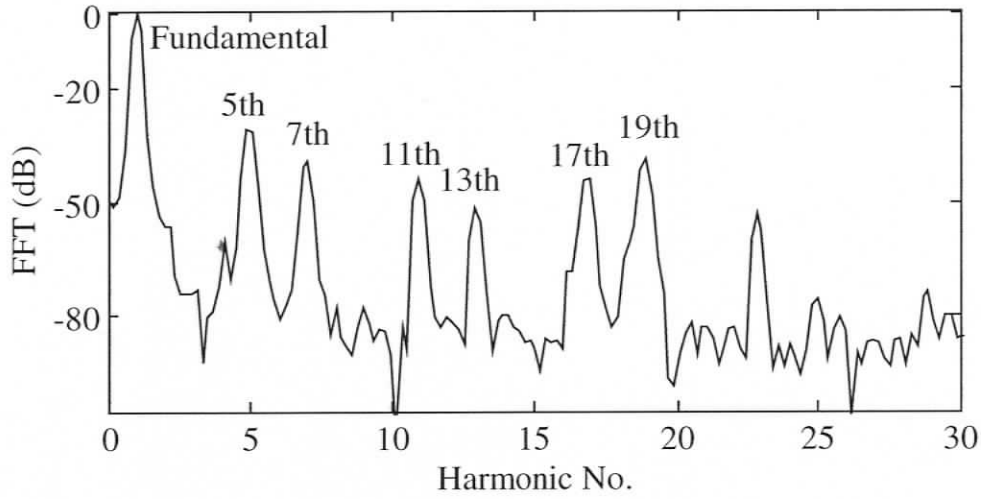

Figure 5.7 Experimental normalized short time FFT of V_{AB} of healthy RSM after disconnecting unbalanced supply

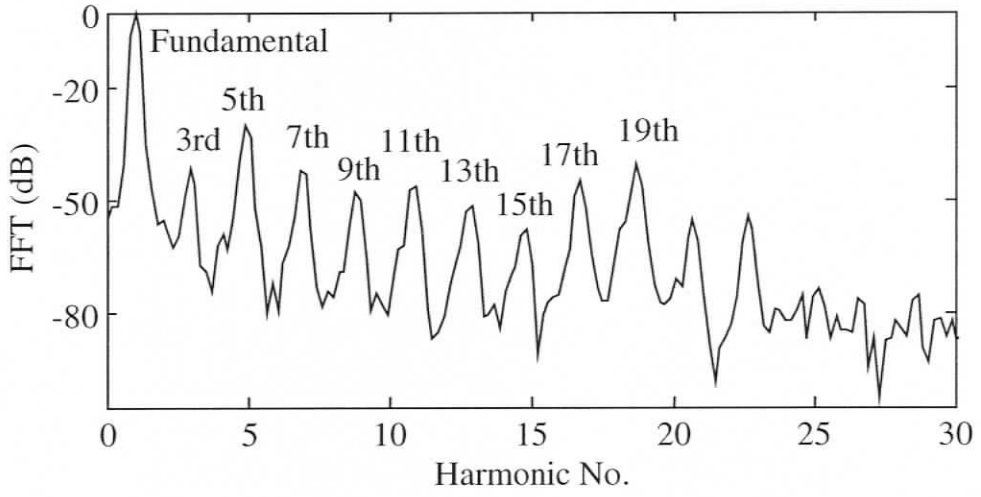

Figure 5.8 Experimental normalized short time FFT of V_{AB} of RSM with 5-turn fault in phase-A after supply disconnection

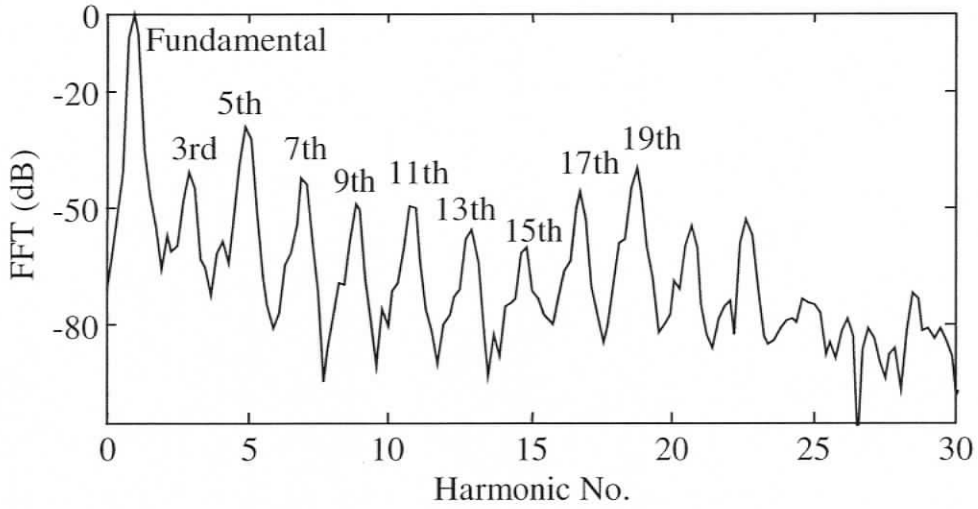

Figure 5.9 Experimental normalized short time FFT of V_{CA} of RSM with 5-turn fault in phase-A after supply disconnection

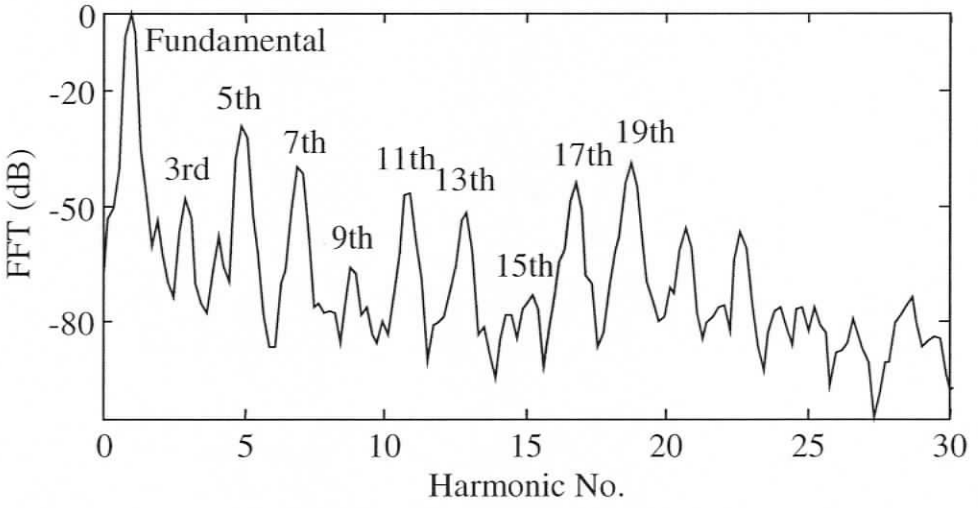

Figure 5.10 Experimental normalized short time FFT of V_{BC} of RSM with 5-turn fault in phase-A after supply disconnection

Table 5.1 Triplen harmonics in the terminal voltages of the experimental RSM after supply disconnection at no-load

	Harmonics in V_{AB}			Harmonics in V_{BC}			Harmonics in V_{CA}		
	3^{rd} (dB)	9^{th} (dB)	15^{th} (dB)	3^{rd} (dB)	9^{th} (dB)	15^{th} (dB)	3^{rd} (dB)	9^{th} (dB)	15^{th} (dB)
HB	-70.21 (1.11)	-77.53 (4.24)	-82.89 (3.22)	-64.40 (0.79)	-68.26 (1.11)	-77.50 (1.67)	-63.44 (0.74)	-66.83 (0.56)	-85.06 (1.77)
HU	-70.53 (0.92)	-75.92 (2.59)	-84.41 (3.93)	-63.98 (0.41)	-67.74 (0.51)	-78.98 (3.04)	-63.70 (0.76)	-66.63 (0.34)	-82.53 (1.48)
T1	-60.10 (0.67)	-71.74 (0.65)	-73.50 (1.80)	-60.67 (1.11)	-70.45 (0.94)	-79.89 (3.40)	-58.58 (0.88)	-64.10 (0.42)	-73.61 (2.06)
T2	-50.43 (0.39)	-62.20 (0.25)	-66.24 (0.81)	-55.90 (0.30)	-74.69 (0.74)	-76.52 (2.31)	-49.73 (0.31)	-59.93 (0.31)	-66.43 (1.06)
T3	-45.71 (0.10)	-55.64 (0.23)	-65.79 (0.84)	-52.53 (0.29)	-74.27 (1.67)	-73.06 (1.19)	-44.85 (0.19)	-55.91 (0.17)	-68.45 (0.92)
T4	-43.51 (0.47)	-51.12 (0.31)	-61.02 (0.15)	-50.65 (0.50)	-68.12 (1.33)	-71.21 (1.92)	-42.60 (0.44)	-51.56 (0.15)	-63.83 (0.72)
T5	-41.95 (0.54)	-48.47 (0.47)	-58.51 (0.35)	-48.88 (0.74)	-65.65 (0.32)	-74.33 (1.38)	-40.96 (0.55)	-49.25 (0.54)	-59.97 (0.43)

Table 5.2 Triplen harmonics in the terminal voltages of the experimental RSM after supply disconnection at full-load

	Harmonics in V_{AB}			Harmonics in V_{BC}			Harmonics in V_{CA}		
	3^{rd} (dB)	9^{th} (dB)	15^{th} (dB)	3^{rd} (dB)	9^{th} (dB)	15^{th} (dB)	3^{rd} (dB)	9^{th} (dB)	15^{th} (dB)
HB	-60.63 (1.34)	-75.53 (3.35)	-75.47 (1.75)	-55.82 (1.85)	-65.10 (0.86)	-72.63 (2.20)	-58.18 (0.63)	-64.78 (0.51)	-77.90 (4.09)
HU	-59.15 (2.90)	-76.10 (3.83)	-75.74 (2.99)	-58.26 (3.03)	-65.11 (1.71)	-71.84 (2.87)	-57.38 (1.60)	-64.40 (1.21)	-74.22 (1.59)
T1	-54.64 (1.85)	-70.99 (1.66)	-74.51 (2.42)	-57.22 (1.08)	-66.63 (1.16)	-71.24 (2.81)	-55.11 (2.00)	-68.25 (2.00)	-73.33 (1.75)
T2	-51.16 (0.66)	-59.77 (0.40)	-70.14 (1.58)	-54.08 (1.49)	-65.02 (0.59)	-73.58 (3.04)	-50.10 (0.78)	-66.27 (0.93)	-69.04 (2.58)
T3	-46.70 (0.86)	-56.39 (2.61)	-66.86 (4.00)	-53.06 (1.14)	-63.10 (2.64)	-69.86 (7.59)	-45.57 (0.34)	-61.12 (3.70)	-65.47 (3.45)
T4	-45.15 (0.30)	-51.63 (0.33)	-68.60 (2.09)	-52.08 (1.03)	-59.75 (0.69)	-72.20 (2.64)	-44.37 (0.18)	-54.94 (0.64)	-65.57 (1.63)
T5	-43.23 (0.95)	-50.15 (0.24)	-70.87 (2.12)	-49.97 (1.21)	-59.15 (0.78)	-74.50 (2.71)	-42.63 (0.74)	-53.44 (0.33)	-65.75 (1.47)

5.5 Discussions on Results and Contributions

In this chapter, an offline diagnostic scheme, based on the stored magnetic energy after supply disconnection, has been implemented on RSM to detect stator inter-turn faults. In an earlier study, this scheme has been implemented for detecting stator inter-turn faults in induction motors [25]. Now the same principle is applied to the RSM since it has damper bars. Simulation results have been validated using suitable experiments and necessary theoretical proofs. This method has been capable of unambiguously detecting the faults involving even one turn. However, this method can only be useful for detecting faults in the machines that are employed in specific applications where supply to the machine is frequently disconnected. Further, as stated in chapter-2, the modified online fault detection scheme based on negative

sequence quantities cannot unambiguously detect faults involving very few shorted turns in RSM and can result in a false positive under unbalanced supply conditions, particularly in case of faults involving very few shorted turns. Hence it is essential to reassess the condition of the RSM after supply disconnection. Thus the fault detection scheme, using stored magnetic energy after switch-off, can be very useful to validate the on-line schemes used for monitoring of the continuous duty motors.

Chapter 6

Feasibility Analysis on Harmonic Components Suitable for Detecting Faults in Synchronous Machines with DC Excitation

For online detection of faults in electric machines, it has been quite a bit of challenge to identify a signal that can show clear variations under incipient stage of a fault but show minimal changes under abnormal operating conditions. This fact can be clearly understood from the earlier studies as mentioned in Chapter 1 and from the results presented in Chapter 4. Presently, in an attempt to develop online fault diagnostic schemes to detect the stator inter-turn faults in SM with DC excitation, initially a feasibility analysis has been conducted. This analysis has been primarily intended to find out the frequency components that are minimally influenced by the abnormal operating conditions of the machine.

It is well known that a fault detection scheme for the synchronous machines based on field current monitoring can bring several advantages since only one signal has to be measured and processed. In general, the field current of a synchronous machine consists of several frequency components. In a 4-pole, 60 Hz machine, they can be categorized as follows. One set of harmonic components are present at 360, 720, 1080 Hz etc., which can arise as a result of the non-sinusoidal space distribution of the stator windings. Another set of harmonic components are present at 120, 240, 480 Hz etc., which can arise as a result of supply unbalance, internal asymmetry or any other abnormal operating condition. Apart from these frequency components in

the field current, some more components are present at 30, 60, 150, 210, 270 Hz etc., which have not been used for fault diagnosis in any of the earlier attempts. So far, the source of these harmonics is also not clearly known in a presumably healthy machine. Hence, in this study, an in-depth investigation has been conducted to determine the origin of these frequency components in the field current of synchronous machines. In addition, a feasibility analysis has been carried out to explore the capability of these frequency components to unambiguously detect the faults. For this purpose, a detailed analysis has also been put forward by considering the influence of supply unbalance and time harmonics on these frequency components. As a first step, a theoretical analysis has been presented by considering the constructional asymmetries in the stator as well as field windings. Next, these theoretical results have been verified by using different simulated models of the machines. Subsequently, to validate both theory and simulations, experimental results have also been presented by analyzing the field current and the voltage induced in a rotor-mounted search-coil of the synchronous machines.

In an attempt to comprehensively establish the proposed theory, synchronous machines with two different types of field windings have been analysed and the results have been presented case by case. The findings of such a study will be very useful in developing unambiguous fault diagnostic tools in general.

6.1 Existence of Various Harmonic Components in the Field Current of Symmetric Synchronous Machines

Presence of various frequency components in the field circuit of a symmetric synchronous machine can be explained as follows. The flux density, with respect to the rotor, produced by a symmetric 3-phase stator when excited by a 3-phase supply has been given in (4.33). A mechanism, similar to the one that produces $6hf$ frequencies in the damper bars, can also produce these frequencies in the symmetric

field windings of both structures. In (4.33), the pole-pair numbers associated with $6f$ frequency are 10 & 14. Since these pole-pairs can be produced by the symmetric field windings of both structures, as given in (3.5) and (3.6), the $6f$ frequency components can be induced in these windings. Similarly the existence of other $6hf$ frequencies (360, 720, 1080Hz etc.) can be explained.

In the case of supply unbalance, a reverse rotating field exists in the machine. A mechanism similar to the one that produces the $2f$, $4f$, $8f$, $10f$ etc. frequencies in the damper bars can also produce these frequencies in the symmetric field windings of both structures. In (4.39), the pole-pair number associated with $2f$ frequency is 2. Since this pole-pair can be produced by the symmetric field windings of both structures, the $2f$ frequency components can be induced in these windings. The existence of the $4f$, $8f$ and $10f$ etc. frequencies can be explained in a similar manner.

6.2 Existence of Various Harmonic Components in the Field Current of Synchronous Machines with Structural Asymmetries

Due to manufacturing imperfections and non-homogeneity of iron, it is certain that every electric machine will possess asymmetries to certain extent. The asymmetries can be in the magnetic path, stator winding, air-gap and/or rotor cage/winding. Presence of various frequency components in the field circuit of an asymmetric synchronous machine can be proved as follows. The MMF produced by an asymmetric stator when excited by a balanced 3-phase supply can be given as

$$F_{sa} = A_{sa} \cos \left[h\phi \pm \omega t\right] \tag{6.1}$$

Where, h = 1, 2, 3 ... etc. This has been obtained by using the turns function of the asymmetric stator winding as given in (6.5). Considering the DC part of the specific

permeance function (P_0), the flux density produced by this MMF, with respect to stator, can be given as

$$B_{sa} = A_{sa} P_0 \cos\left(h\phi \pm \omega t\right) \tag{6.2}$$

With respect to rotor, this flux density can be given as

$$B_{ra} = A_{sa} P_0 \cos\left[h\phi' + \{(h/p) \pm 1\}\omega t + \varphi_5\right] \tag{6.3}$$

by substituting $\phi = \phi' + (\omega / p)t$. B_{ra} can induce a particular frequency component in a winding if and only if the pole-pair of B_{ra} corresponding to that frequency matches with one of the pole-pairs of the winding [63]. With h = 10 or 14, (6.3) can induce 360Hz component in the symmetric as well as asymmetric field windings of both structures since the pole-pairs associated with this frequency match with the pole-pairs of all these field windings which can be observed in (3.5), (3.6) and (6.6). It can be inferred that with h = 1, the flux density given in (6.3) can produce 30Hz and 90Hz components. Similarly, with h = 3, 30Hz and 150Hz components can be produced. All these component can be induced only in the asymmetric field winding, since the asymmetric winding can produce all h = 1, 2, 3... pole-pairs, as given in (6.6). Table 6.1 shows, for different values of h and p = 2, various harmonics that can be theoretically induced in the asymmetric field winding of both structures for 60Hz supply frequency.

Table 6.1 Harmonic components in field current

h	1	2	3	4	5	6	7	8	9	10
Freq. (Hz)	30	0	30	60	90	120	150	180	210	240
	90	120	150	180	210	240	270	300	330	360

6.3 Modeling of Synchronous Machine with Asymmetries in the Stator and the Field Windings

In order to validate the theory developed in the earlier section, the synchronous machines have been simulated using structural asymmetries in the stator as well as in the field windings. This study has been carried out on synchronous machines with standard and two-coil field windings. The following machine models have been developed using coupled circuit approach:

a) Symmetric machine with standard field winding
b) Asymmetric machine with standard field winding
c) Symmetric machine with two-coil field winding
d) Asymmetric machine with two-coil field winding

Modeling of case a) has been presented in Chapter 3. The case c) can be modeled on the similar line with suitably choosing the turns function of two-coil field winding as given in (3.6). For case b) and case d), modeling of these machines with structural asymmetries can be achieved as follows. Both stator and the field windings consist of different coils. An asymmetric winding can be modeled by choosing different number of turns in one of the coils of the winding. In order to introduce asymmetry, few turns from the stator winding (15 turns in phase-A, 5 turns in phase-B and 10 turns in phase-C, out of 312 turns / phase) have been removed. Similarly, asymmetry in the field winding has been introduced by removing 50 turns from one of its coils out of 1260 turns. The effects of damper bars have also been considered in the present modeling.

The turns function of a symmetric stator winding of phase-A can be given as in (3.1). The turns function of the part of phase-A which has been removed to introduce asymmetry, can be given as in (6.4). Hence the turns function of the asymmetric

stator winding (phase-A) can be given as in (6.5). Asymmetry in phase-B and phase-C has been introduced in a similar manner.

$$n_a(\phi) = a_{oa} + \sum_{h=1,2,3...}^{\infty} a_{ha} \cos(h\phi)$$
$$a_{oa} = \frac{N_a}{6},\ N_a = 15,\ a_{ha} = \frac{2N_a}{\pi h} \sin\left(\frac{\pi h}{6}\right) \tag{6.4}$$

$$n_{Aa}(\phi) = n_A(\phi) - n_a(\phi) \tag{6.5}$$

The Fourier series expansions of the turns functions of the symmetric standard and two-coil field windings are expressed in (3.5) and (3.6) respectively. Fourier series expansion given in (6.6) represents the general form of asymmetric field winding. This has been obtained in a similar manner as that of asymmetric stator phase-A. The coefficients will be different for the standard and two-coil structures. The turns functions of asymmetric field windings of both standard and two-coil structures are shown in Figure 6.1 and Figure 6.2 respectively.

$$n_{rfa}(\phi,\theta) = a_{orfa} + \sum_{w=1,2,3,...}^{\infty} a_{wrfa} \cos\left[w(\phi - \theta)\right] \tag{6.6}$$

After computing various magnetizing and mutual inductances of the machine using modified winding function approach (MWFA) [49, 50], the dynamic models of the synchronous machines have been obtained using the coupled circuit approach [48, 49].

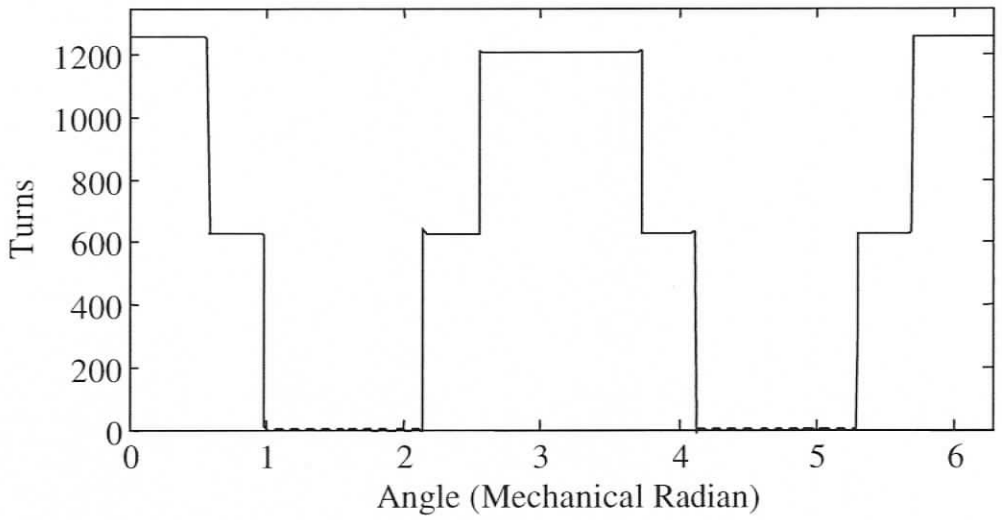

Figure 6.1 Turns functions of the asymmetric standard field winding

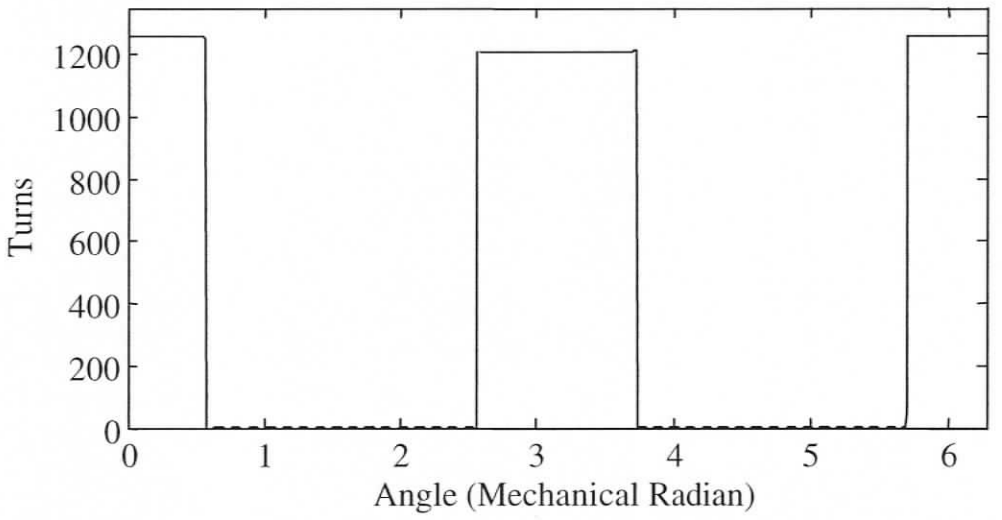

Figure 6.2 Turns functions of the asymmetric two-coil field winding

6.4 Simulations and Experimental Results under Healthy and Abnormal Operating Conditions

The simulated models of the SM with DC excitation are analyzed next under healthy and abnormal operating conditions. Four different models of the machine, as mentioned in the earlier section, have been used for this purpose. Subsequently, experimental results have been obtained for synchronous machines with standard and two-coil field windings. The voltage induced in a rotor-mounted search-coil has also been examined to validate the claims.

6.4.1 Simulation Study to Show the Origin of Various Frequency Components in the Field Current

The field current signatures of the symmetric synchronous machine models with standard and two-coil field structures, when fed by a balanced supply, have been shown in Figure 6.3 and Figure 6.4 respectively. Only the 360Hz component (normalized to DC component which is at 0 dB) has been identified as predicted. This component appears in the field current as a result of the non-sinusoidal distribution of stator windings as predicted in the earlier sections. The similar plots with unbalanced supply have been shown in Figure 6.5 and Figure 6.6 respectively. The 240, 480, 600Hz, etc., components also have been identified as a result of supply unbalance as predicted.

The field current signatures of asymmetric models of the synchronous machines with standard and two-coil field structures, when fed by a balanced supply, have been shown in Figure 6.7 and Figure 6.8 respectively. The different frequency components at the 30, 60, 90Hz... have been identified as predicted. These components appear in the field current as a result of the internal asymmetries of the windings. The 60Hz component has been observed to be much larger in the case of two-coil field winding

as opposed to the standard field winding. This can be because of the fact that the two-coil winding can produce the pole-pairs pertaining to the 60Hz component under symmetric condition itself.

6.4.2 Simulation Study to Show the Influence of Supply Unbalance on the Field Current Signature

An unbalanced supply causes a reverse rotating field in the machine that induce the harmonic components at 120, 240 Hz etc. The asymmetric models have been subjected to an unbalanced voltage (with 2.7% unbalance). The influence of supply unbalance has been found to be minimal on the 90 and 150Hz components. Thus they can be much superior indicators of faults in the machine as opposed to the even harmonics such as the 120Hz. The variation of the 90, 120 and 150Hz frequency components is shown for standard and two-coil field windings in Table 6.2 and Table 6.3 respectively.

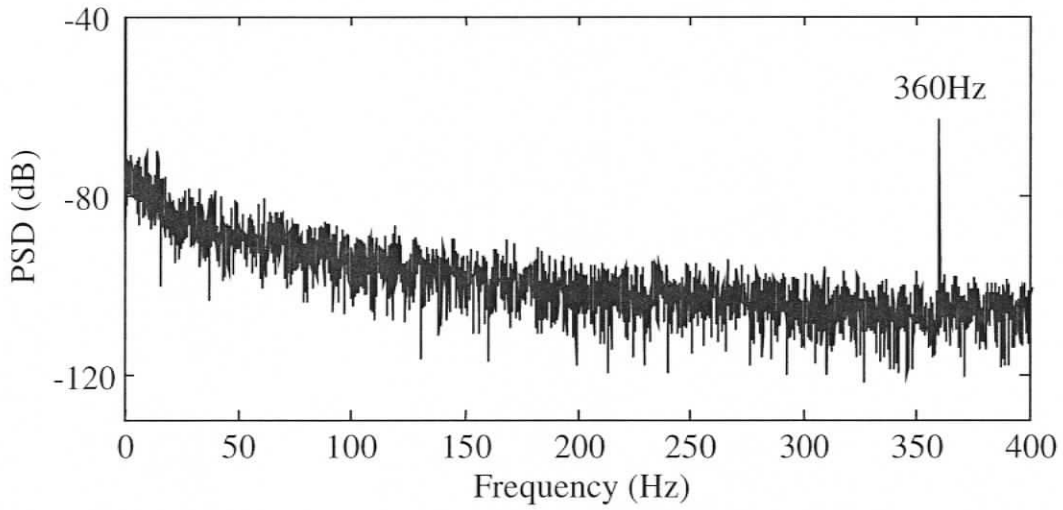

Figure 6.3 Simulated PSD of field current of the symmetric machine with standard field winding fed by balanced supply

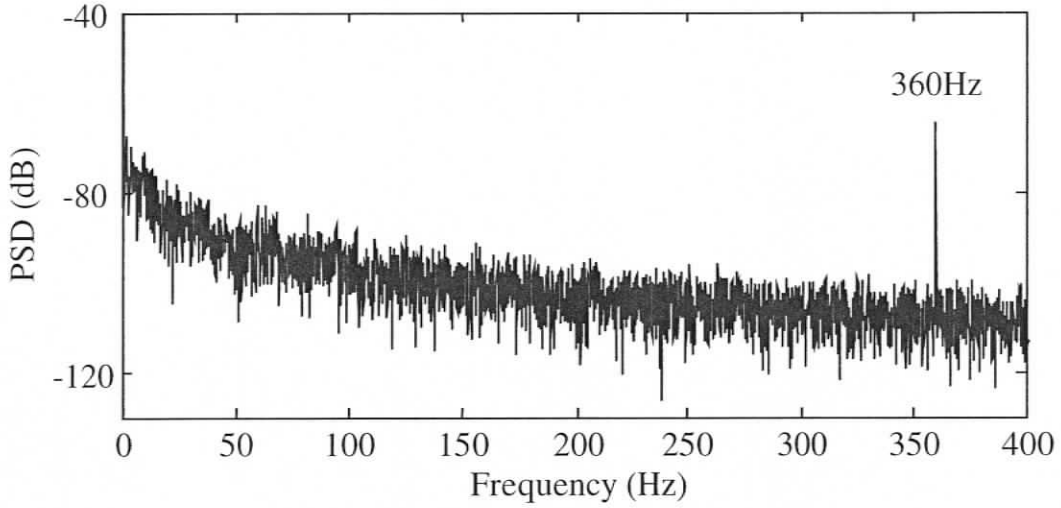

Figure 6.4 Simulated PSD of field current of the symmetric machine with two-coil field winding fed by balanced supply

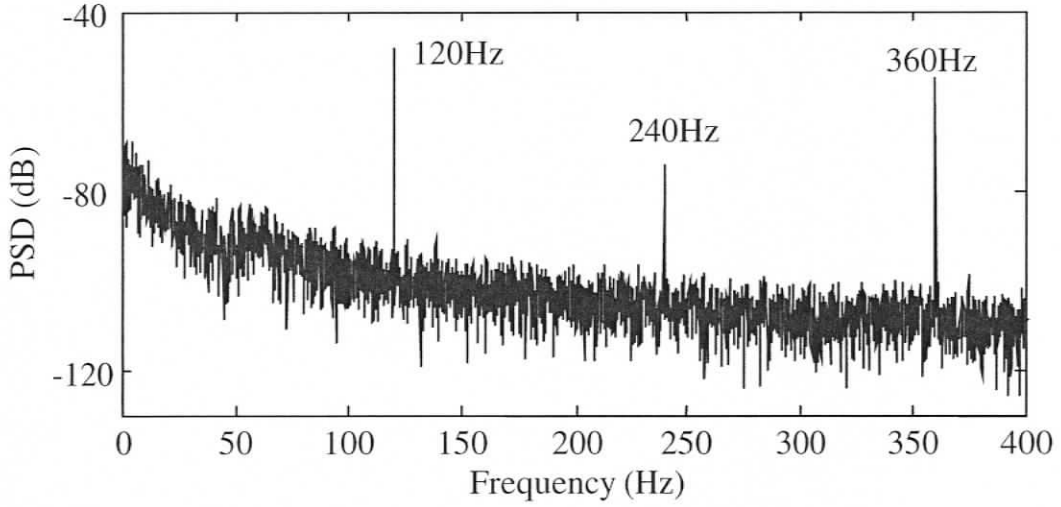

Figure 6.5 Simulated PSD of field current of the symmetric machine with standard field winding fed by unbalanced supply

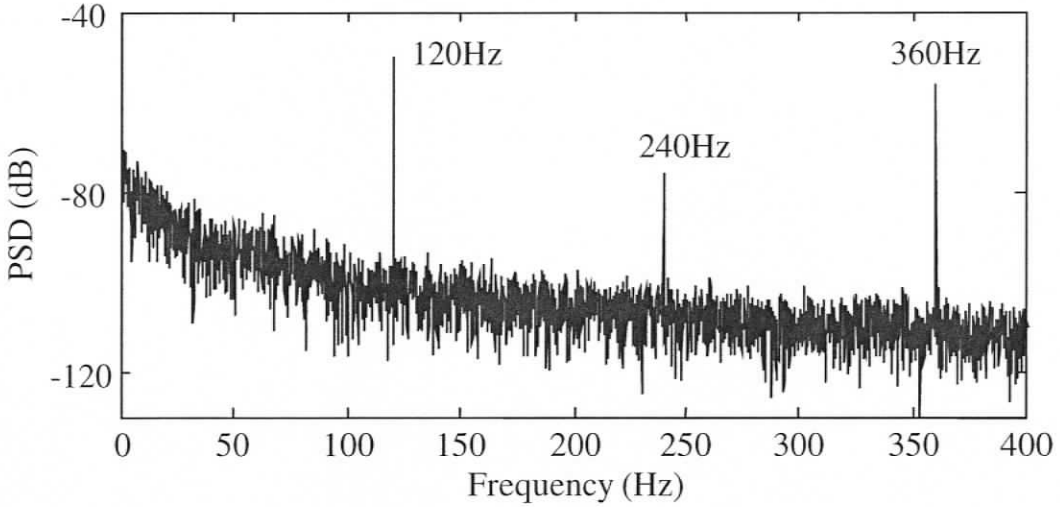

Figure 6.6 Simulated PSD of field current of the symmetric machine with two-coil field winding fed by unbalanced supply

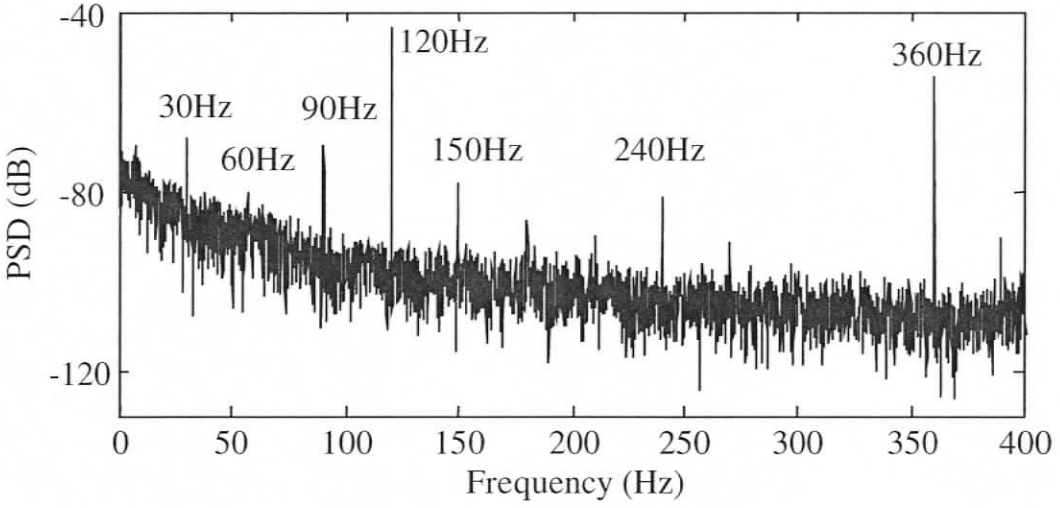

Figure 6.7 Simulated PSD of field current of the asymmetric machine with standard field winding fed by balanced supply

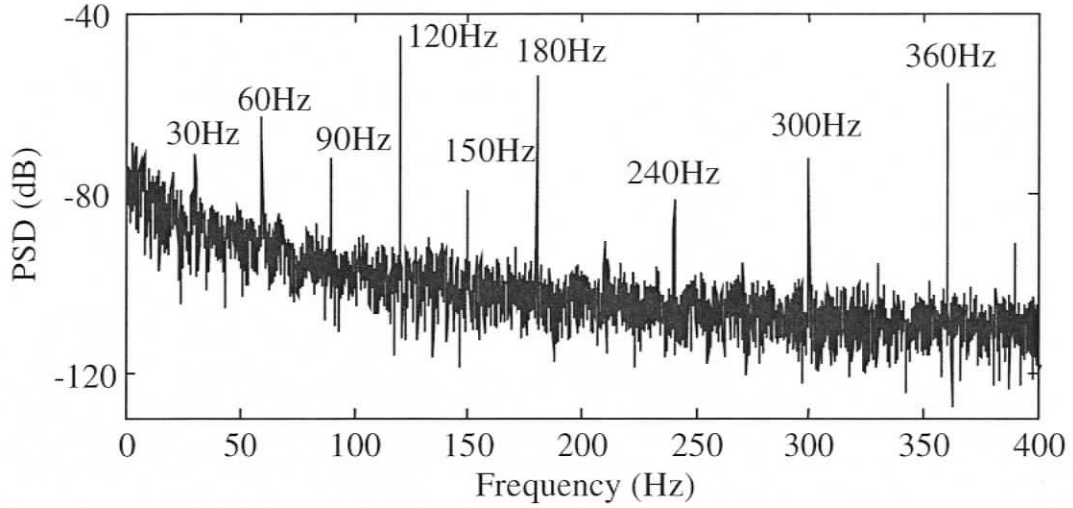

Figure 6.8 Simulated PSD of field current of the asymmetric machine with two-coil field winding fed by balanced supply

Table 6.2 Harmonics in field current of an asymmetric machine model (with standard field winding) (Simulated)

Supply Condition	90 Hz (dB)	120 Hz (dB)	150 Hz (dB)
Balanced Supply	-69.64	-43.36	-78.08
Unbalanced Supply	-70.78	-37.70	-78.40

Table 6.3 Harmonics in field current of an asymmetric machine model (with two-coil field winding) (Simulated)

Supply Condition	90 Hz (dB)	120 Hz (dB)	150 Hz (dB)
Balanced Supply	-72.35	-44.84	-79.50
Unbalanced Supply	-71.50	-39.16	-79.99

6.4.3 Simulation Study to Show the Influence of Time Harmonics on the Field Current Signature

The utility supply has many time harmonics, which can also induce some frequency components in the field current. In order to investigate the influence of these time harmonics on the proposed fault detector components, first the spectra of the line voltage and the line current of the experimental motor (with two-coil structure) have been obtained as shown in Figure 6.9 and Figure 6.10 respectively. It is interesting to note that the line current has more harmonics than the line voltage, such as 30, 90,150 Hz. etc. It is therefore very clear that these additional harmonics are due to causes internal to the machine. Now, to study the influence of time harmonics on the signature of field current, the simulated asymmetric models have been run using the voltage data collected from the utility supply. With the kind of asymmetry considered for simulation, only supply voltage harmonics have been reflected back in the field current as shown in Figure 6.11 and Figure 6.12 but not the 90 and 150 Hz components. Tables similar to Table 6.1 can evaluate the influence of other time harmonics. Table 6.4 and Table 6.5 show the influence of the 120 and 180 Hz time harmonics, the predominant ones in the supply voltage and the line current, as seen in Figure 6.9 and Figure 6.10 respectively, on the field harmonics. However, with the kind of asymmetry considered for simulation, the supply voltage harmonics did not

produce the 30, 90 and 150 Hz etc. components in the field current as shown in Figure 6.11 and Figure 6.12. Hence, it can be concluded that time harmonics have minimal influence on the 30, 90 and 150 Hz etc. components in the field current.

Table 6.4 Harmonics components in field current due to 120 Hz time harmonic in stator voltage and current

w	1	2	3	4	5	6	7	8	9	10
Freq. (Hz)	90	60	30	0	30	60	90	120	150	180
	150	180	210	240	270	300	330	360	390	420

Table 6.5 Harmonics components in field current due to 180 Hz time harmonic in stator voltage and current

w	1	2	3	4	5	6	7	8	9	10
Freq. (Hz)	150	120	90	60	30	0	30	60	90	120
	210	240	270	300	330	360	390	420	450	480

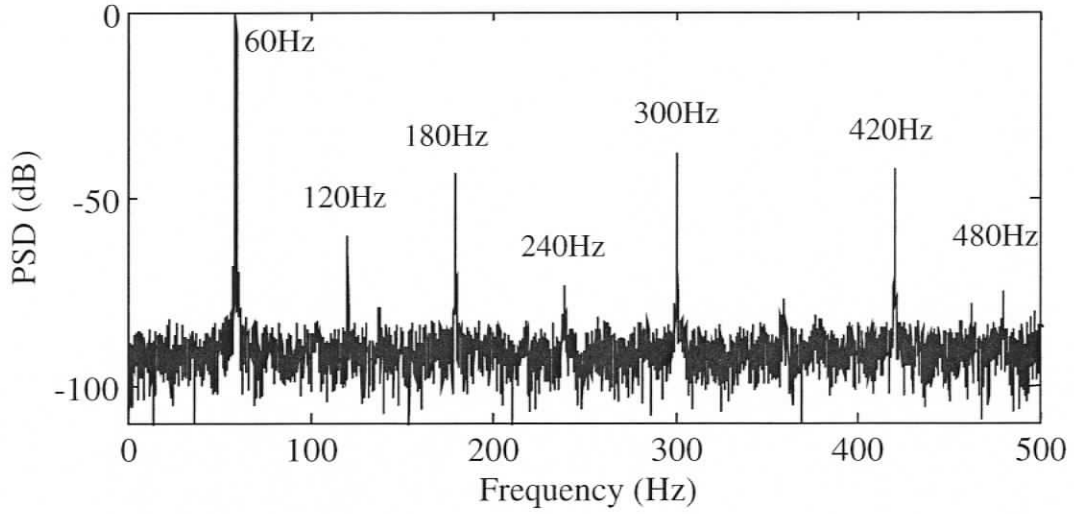

Figure 6.9 PSD of line voltage of experimental machine with two-coil field winding

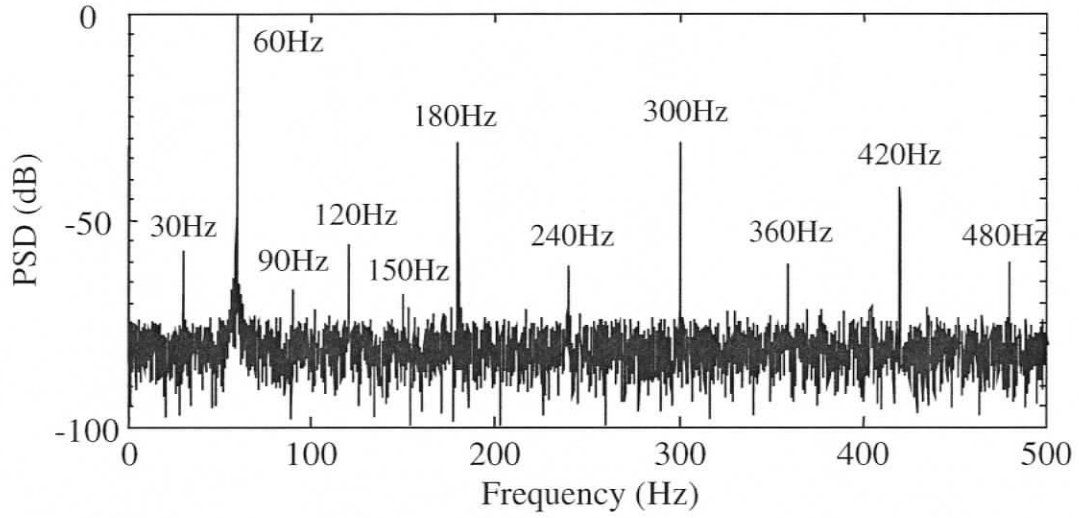

Figure 6.10 PSD of line current of experimental machine with two-coil field winding

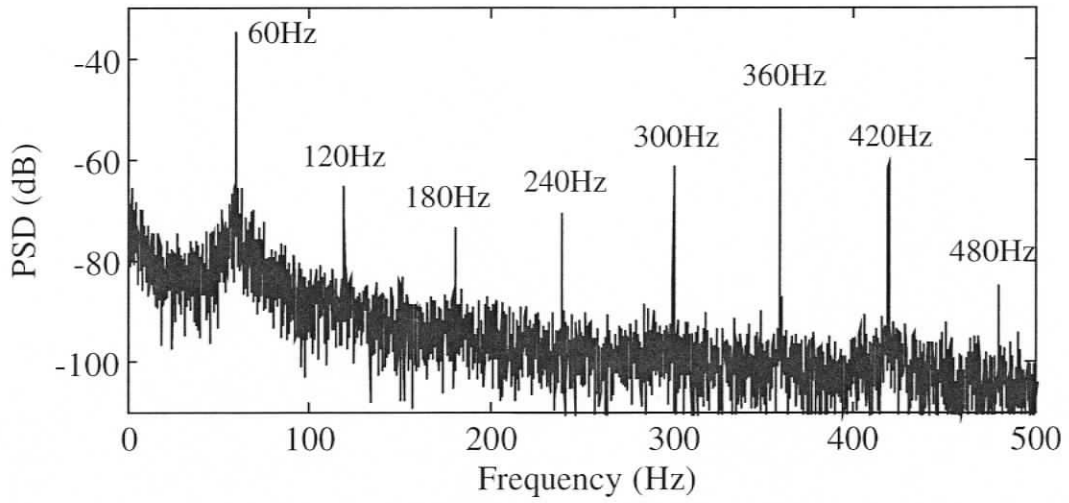

Figure 6.11 PSD of field current of the simulated machine with asymmetric standard field winding with utility voltage data

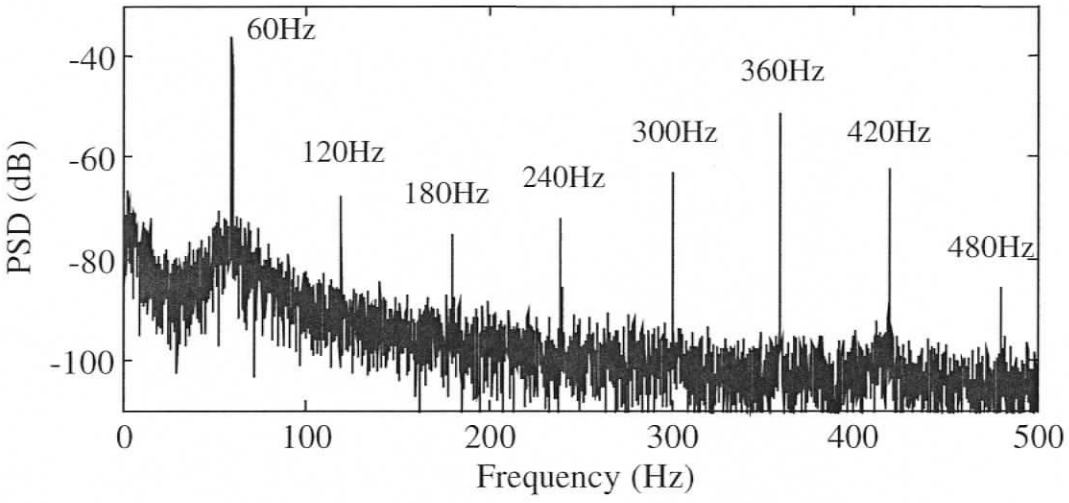

Figure 6.12 PSD of field current of the simulated machine with asymmetric two-coil field winding with utility voltage data

6.4.4 Experimental Analysis of Field Current and Search-coil Voltage of SM with Standard and Two-coil Field Windings

In order to validate the simulation results, the synchronous machines with both standard and two-coil field structures have been tested in the lab under balanced and unbalanced supply (about 2.5% unbalance) conditions. The field current of the motor has been analyzed under full-load, 0.8 PF lagging condition. The voltage induced in a rotor-mounted search-coil also validated these results. The spectra of the field current have been normalized to DC component whereas the spectra of the voltage induced in the rotor search-coil have been normalized to 30Hz component. At full-load, 0.8 lagging PF, the field current spectra under balanced and unbalanced supply conditions of the SM with standard field winding have been shown in Figure 6.13. A relative comparison of the magnitudes of these components has been shown in Table 6.6. The corresponding results of SM with two-coil field winding have been shown in Figure 6.14 and Table 6.7. In both field structures, the even harmonic components such as 120 Hz showed a very clear increase under supply unbalance. However, the 30, 90, 150 Hz did not show any significant increase under supply unbalance; corroborating the simulation results.

These results have also been validated using the voltage induced in the rotor-mounted search-coil. The experimental spectra of the voltage induced in the rotor-mounted search-coil under balanced and unbalanced conditions have been shown in Figure 6.15. A relative comparison of the magnitudes of various frequency components has been given in Table 6.8. These results also confirmed that the 30, 90, 150 Hz can be minimally influenced by supply unbalance whereas as 120Hz showed a very clear increase. Since the supply unbalance and time harmonics showed a minimal influence on the 90 and 150Hz components, such components in the field current and voltage induced in the rotor-mounted search-coil can be used for detecting faults unambiguously.

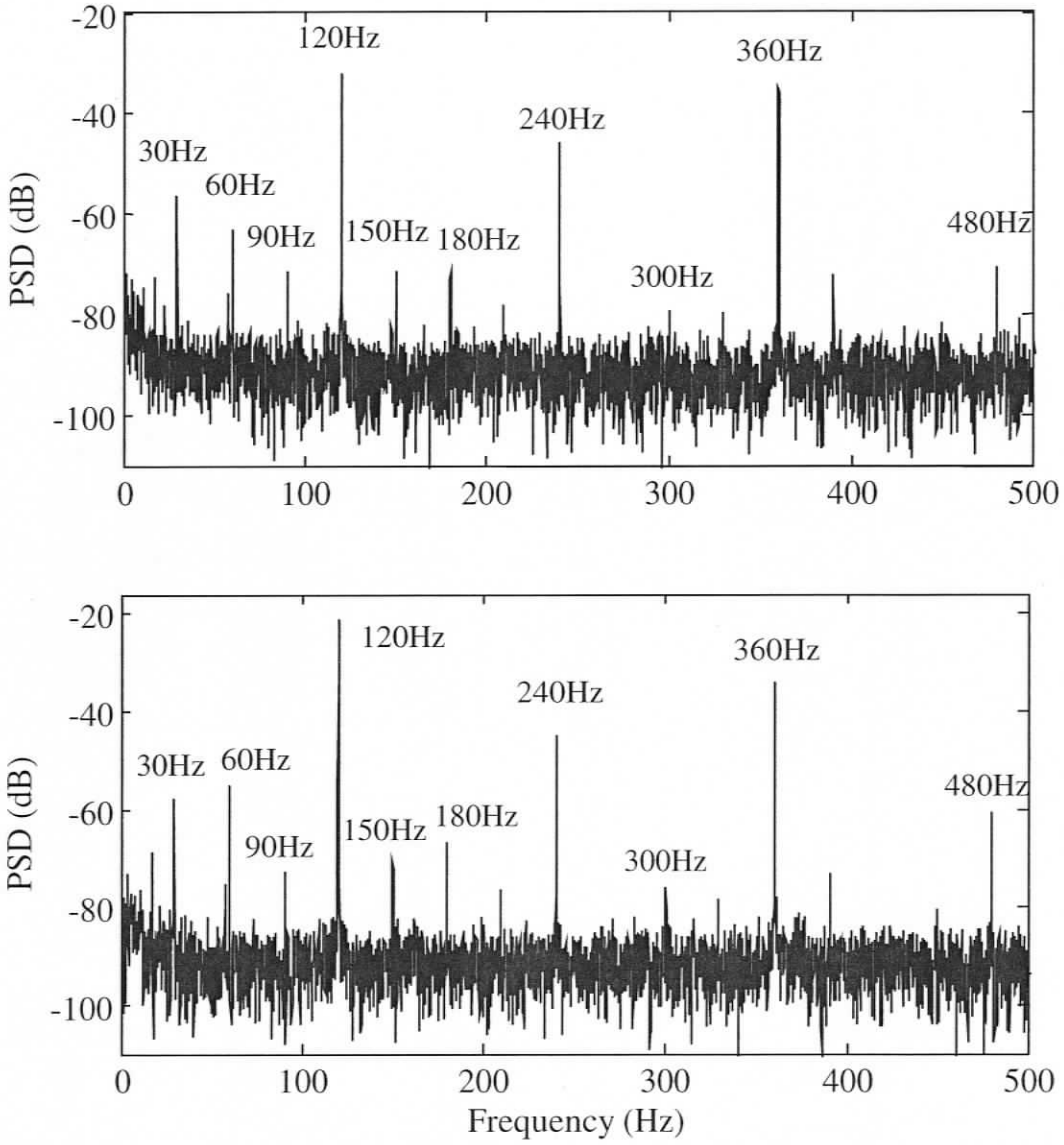

Figure 6.13 Experimental PSD of field current under full-load, 0.8 lagging PF condition with balanced supply (top) and with unbalanced supply (bottom) for a standard field winding

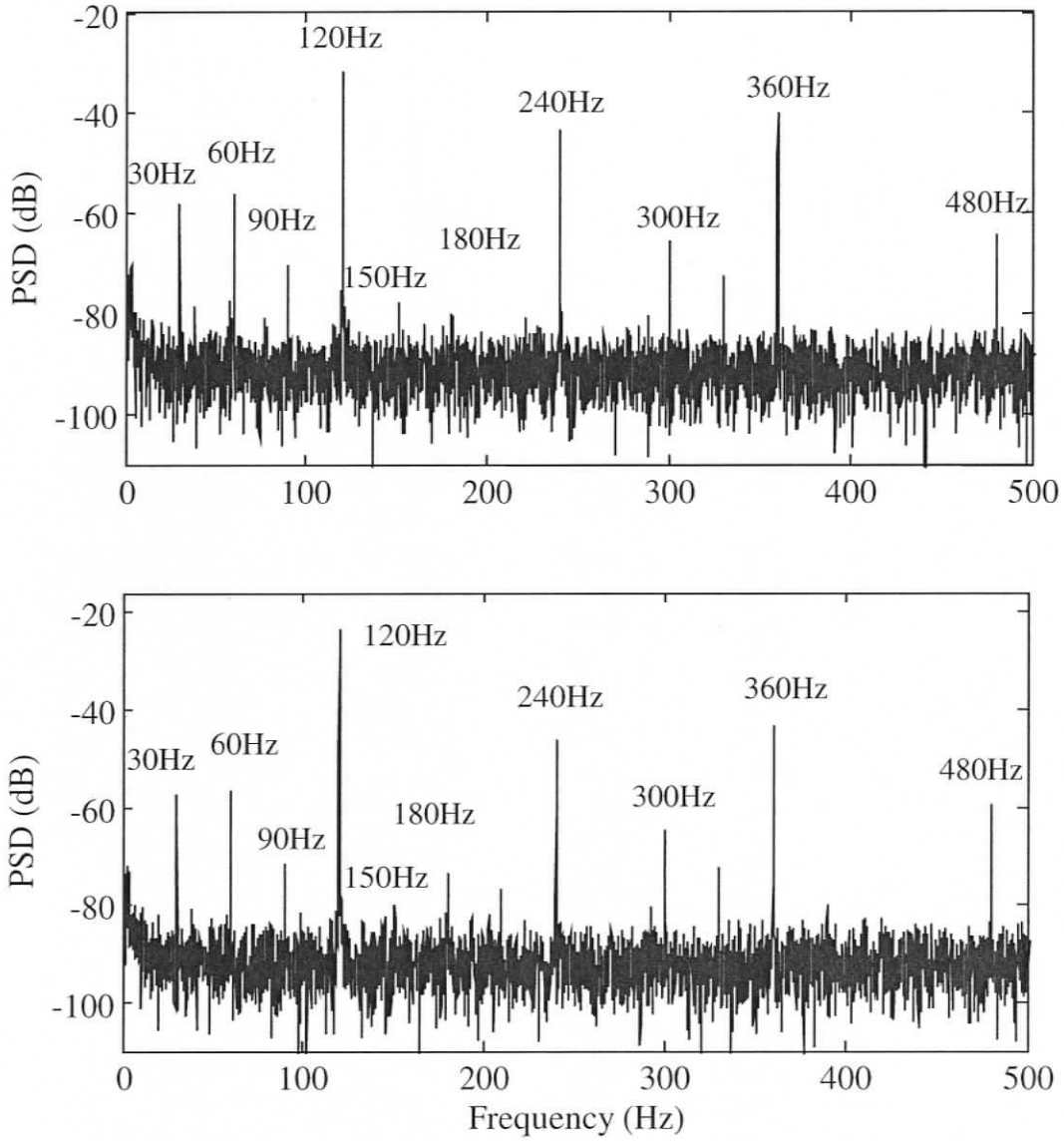

Figure 6.14 Experimental PSD of field current under full-load, 0.8 lagging PF condition with balanced supply (top) and with unbalanced supply (bottom) for two-coil field winding

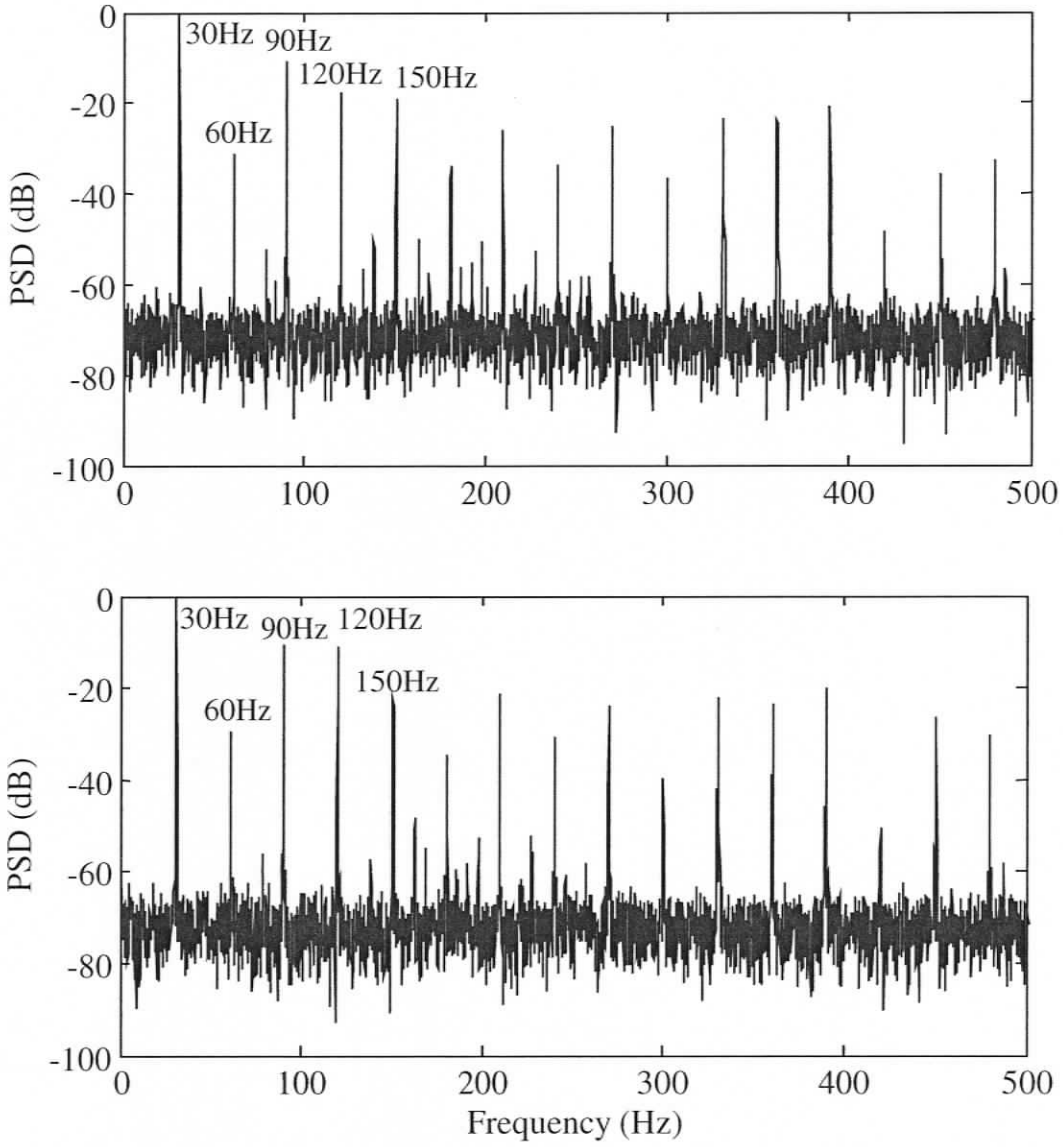

Figure 6.15 Experimental PSD of the voltage in rotor-mounted search-coil under full-load, 0.8 lagging PF condition with balanced supply (top) and with unbalanced supply (bottom) for the SM with standard field winding

Table 6.6 Harmonics in the field current of SM at full-load, 0.8 PF lagging (with standard field winding) (Experimental)

Supply Condition	90 Hz (dB)	120 Hz (dB)	150 Hz (dB)
Balanced Supply	-71.39	-31.98	-71.31
Unbalanced Supply	-72.52	-21.03	-70.50

Table 6.7 Harmonics in the field current of SM at full-load, 0.8 PF lagging (with two-coil field winding) (Experimental)

Supply Condition	90 Hz (dB)	120 Hz (dB)	150 Hz (dB)
Balanced Supply	-70.24	-31.47	-77.57
Unbalanced Supply	-71.53	-23.41	-79.88

Table 6.8 Harmonics in the voltage of rotor-mounted search-coil of SM at full-load, 0.8 PF lagging (with standard field winding) (Experimental)

Supply Condition	90 Hz (dB)	120 Hz (dB)	150 Hz (dB)
Balanced Supply	-10.51	-17.79	-19.18
Unbalanced Supply	-10.67	-11.05	-22.39

6.5 Discussions on Results and Contributions

In this chapter, an investigation has been conducted to find out the origin of various frequency components in the field current of the synchronous machines. Also a feasibility analysis has been put forward to use these components for unambiguous detection of faults in the synchronous machines. The constructional asymmetries in the stator and the field windings have been included in the machine model for this purpose. The theory and simulations have been verified by analyzing the field current and the voltage induced in a rotor-mounted search-coil of the experimental machines. The simulation results are used only to locate the harmonic components but not for comparison with the magnitudes of the experimentally obtained harmonic components. In order to comprehensively establish the proposed theory, results have been obtained for both standard and two-coil field windings of the machine. The supply unbalance and time harmonics seems to have minimal influence on the 90 and 150Hz etc. frequency components. Thus, the pursuit of such frequency components for the purpose of fault analysis in synchronous machines holds distinct promise.

In order to increase the detectability of diagnostic schemes, that could not be achieved under steady state conditions, the sensitivity of certain harmonic components in the field current and air-gap flux to the stator inter-turn faults has been analyzed next in chapter 7. Also the experimental machines have been rigorously tested under different operating conditions to demonstrate the usefulness of the technique.

Chapter 7

Detection of Stator Inter-turn Faults in Synchronous Machines Using Field current and Rotor Search-coil Signature Analysis

As proposed in chapter 6, in this chapter the stator inter-turn faults in the synchronous machines have been detected online, under steady state condition, using the 90, 150, 210 and 270 Hz etc. frequency components in the rotor field current and rotor-mounted search-coil. Owing to the structural asymmetries of the field winding, it has been found that the stator inter-turn faults could clearly increase these frequency components in the field current. These findings have been supported using necessary mathematical proofs, simulations and experiments. Faults involving few turns can be detected using these harmonics in the field current even under supply unbalance and time harmonics. The diagnosis results have also been verified using a rotor-mounted search-coil, which itself can be used to detect even a 1-turn stator fault unambiguously under all load conditions.

7.1 Theory of Detecting Stator Inter-turn Faults Using Asymmetry in Field Winding

It is well known that due to manufacturing imperfections and non-homogeneity of iron, every electric machine will possess asymmetries to certain extent. The induction of various frequency components in the field winding of a synchronous motor with stator inter-turn fault can be proved using the asymmetries in the field winding in the following way.

A shorted loop in the stator winding carrying current at supply frequency can generate two counter-rotating MMF waves [60, 61], given as

$$F_{sf} = A_f \cos\left[c\phi \pm \omega t\right] \tag{7.1}$$

Here, c = 1, 2, 3 ... etc. Considering the DC part of the specific permeance function (P_0), the flux density produced by this MMF, with respect to stator, can be given as

$$B_{sf} = A_f P_0 \cos\left(c\phi \pm \omega t\right) \tag{7.2}$$

With respect to rotor, this flux density can be given as

$$B_{rf} = A_f P_0 \cos\left[c\phi' + \{(c/p) \pm 1\}\omega t + \varphi_5\right] \tag{7.3}$$

by substituting $\phi = \phi' + (\omega / p)t$. B_{rf} can produce an infinite series of frequency components. The components that showed promise in the experiments are 60, 90, 150, 210 and 270 Hz. With p = 2 and c = 4, from (7.3), the 60 Hz component can be produced. Since the associated pole-pair with this frequency is c = 4, the 60Hz component can be induced in the symmetric winding with two-coil structure. The 60 Hz component can also be induced in the asymmetric windings with both structures since these winding can produce all c = 1, 2, 3...pole-pairs, as given in (6.6). However its magnitude is expected to be much higher for the two-coil structure since the pole pair number 4 arises out of the symmetric structure itself, as given in (3.6). Similarly, with c = 1, 3, 5, 7 and 9, the 90, 150, 210 and 270Hz components can be induced in the asymmetric field winding. These components cannot be induced in the ideal standard and two-coil field windings, since these windings produce pole pair numbers 2, 6, 10...etc. (3.5) and 2, 4, 6...etc. (3.6) respectively. Using a similar argument, it can be shown that all other even harmonics (120, 240, 360, 480 Hz, ... etc.) can also be induced in the ideal two-coil, four-coil as well as asymmetric field winding due to an inter-turn fault in the stator winding. Table 7.1 shows, for different values of 'c'

and $p = 2$, the various frequency components that a stator inter-turn fault can be induced in the asymmetric field winding with 60 Hz utility supply.

Table 7.1 Harmonic components in field current

c	1	2	3	4	5	6	7	8	9	10
Freq. (Hz)	30	0	30	60	90	120	150	180	210	240
	90	120	150	180	210	240	270	300	330	360

7.2 Modeling of Stator Inter-turn Faults in Synchronous Machine with Asymmetric Field Windings

In order to carry out a detailed simulation study, different models of the salient-pole synchronous machine have been considered with different field windings. Following are the four different cases considered for this study:

a) Healthy synchronous machine with symmetric field winding
b) Faulty synchronous machine with symmetric field winding
c) Healthy synchronous machine with asymmetric field winding
d) Faulty synchronous machine with asymmetric field winding

These four cases have been separately studied for both standard and two-coil field windings. Thus, totally eight different models have been developed. The detailed modeling aspects of cases (a) and (b) have been discussed in Chapter-3 and Chapter-4 respectively. Modeling of the synchronous machines with asymmetries in the stator and field windings, under healthy condition, has been discussed in Chapter-6. Case (c) can be modeled in a similar way by considering asymmetry only in the field

winding. The modeling of case (d) can be obtained by suitably combining case (b) and case (c). The models of faulty machine can accommodate different number of shorted turns in the stator winding. The effects of damper bars have also been considered in the present modeling. The asymmetric field winding has been modeled by choosing 100 less turns in one coil (out of 1260 total number of turns) in the field winding.

A comparison of the mutual inductance of the stator phase-A winding with symmetric and asymmetric two-coil field winding has been shown in Figure 7.1 where a similar comparison in the case of standard field winding has been shown in Figure 7.2.

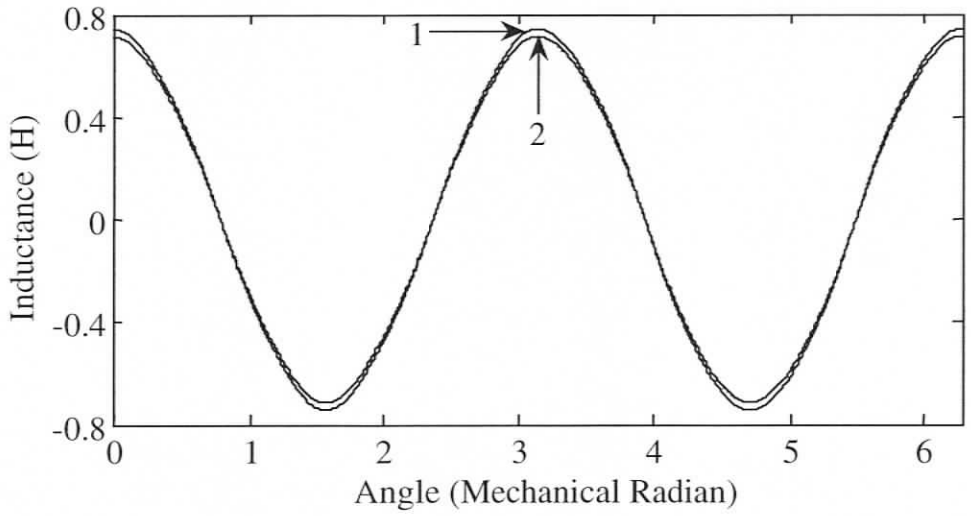

Figure 7.1 Mutual inductance between the stator phase-A and the two-coil field winding, symmetric (1) and asymmetric (2)

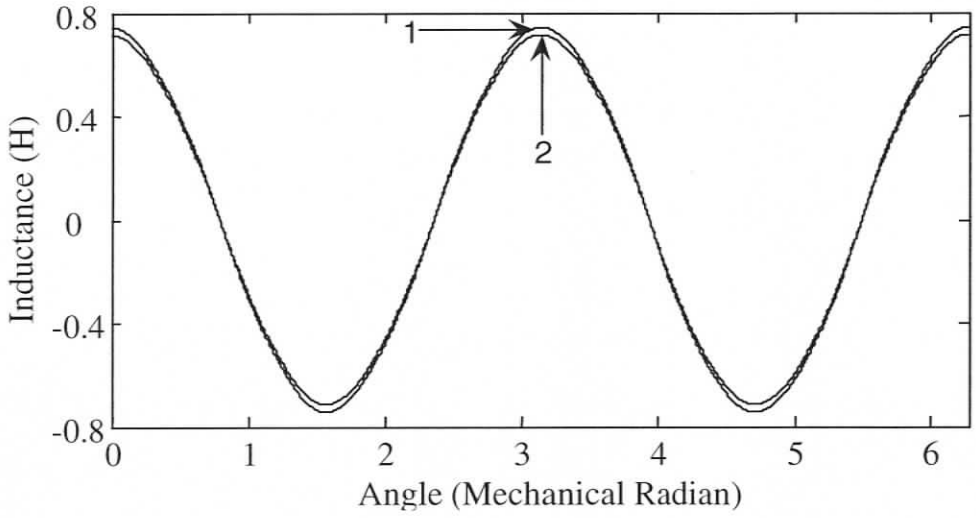

Figure 7.2 Mutual inductance between the stator phase-A and the standard field winding, symmetric (1) and asymmetric (2)

7.3 Simulation Results under Healthy, Faulty and supply Unbalance Conditions

A thorough simulation study was carried out using the eight different models of the machine as mentioned in the earlier section. The results of simulations are then analyzed to validate the theory for detecting stator inter-turn faults in synchronous machines using structural asymmetries of the field winding.

The simulation results have been obtained at full-load, 0.88 lagging power factor and rated field current of the machine. The field current spectra of the motor models with asymmetric two-coil and standard field windings, fed by unbalanced supply, have been shown in Figure 7.3 and Figure 7.4 respectively. Only the 120, 240, 360 Hz etc. harmonics appeared. Also, the field current spectra of the faulty motor models (having 4-turn fault in stator phase-A) with asymmetric two-coil and standard field

windings have been shown in Figure 7.5 and Figure 7.6 respectively. With stator inter-turn fault, the 30, 60, 90 Hz etc. components also appeared in the field current. Since the coefficients of the cosine functions in (6.6) are different for the two structures, the frequency components in these two windings have dissimilar magnitudes. However no components other than those predicted by Table 7.1 showed up, proving the theory presented in section 7.1 conclusively. A detailed comparative study of the various frequency components in the field current of all the eight different models has also been presented as shown in Figure 7.7 to Figure 7.10, under different conditions of the machine. The condition of the machine has been shown on x-axis of the plots. HB and HU denote the healthy machine fed by balanced and unbalanced supplies respectively whereas T1 to T4 represent 1 to 4 turn short in the stator winding. The plots have been normalized with respect to the DC component of the field current. As predicted earlier, the 120 and 480 Hz components showed up with supply unbalance as well as with turn faults. This was observed in the case of symmetric as well as asymmetric field windings of both structures. Hence the changes in the even harmonics may not clearly distinguish the faulty and unbalanced supply conditions.

In the case of both symmetric and asymmetric two-coil structures of field winding, the 60 Hz components were sensitive to the inter-turn faults as predicted. However, this component did not show any increase in the symmetric standard field winding as predicted and did not increase significantly even in the case of asymmetric winding for the chosen amount of asymmetry.

Most importantly, in the case of asymmetric windings of both structures, the 90 and the 150Hz components showed a clear increase only with stator faults as predicted. Also, in the case of healthy machine with both symmetric and asymmetric field windings, these components were absent with supply unbalance as shown in Figure 7.7 to Figure 7.10.

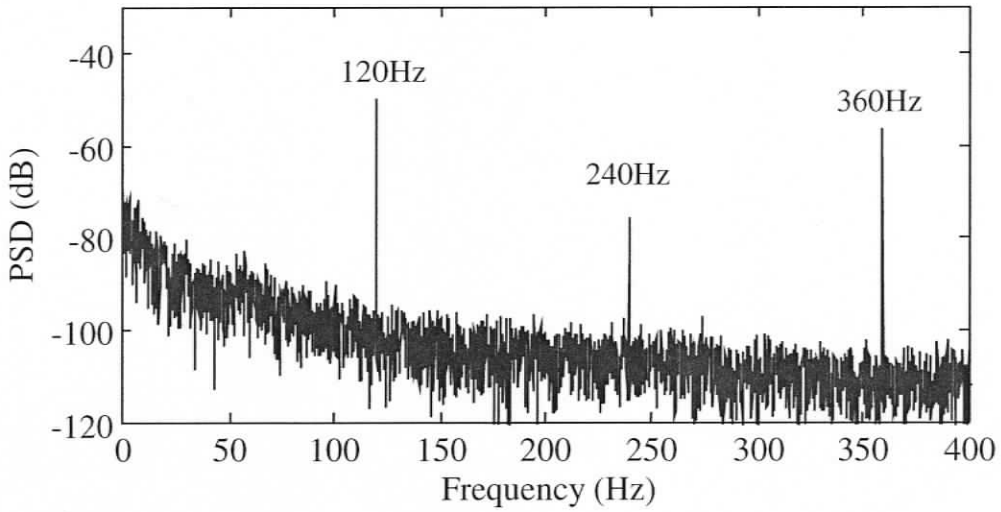

Figure 7.3 Simulated PSD of field current of the synchronous machine with asymmetric two-coil field winding fed by unbalanced supply

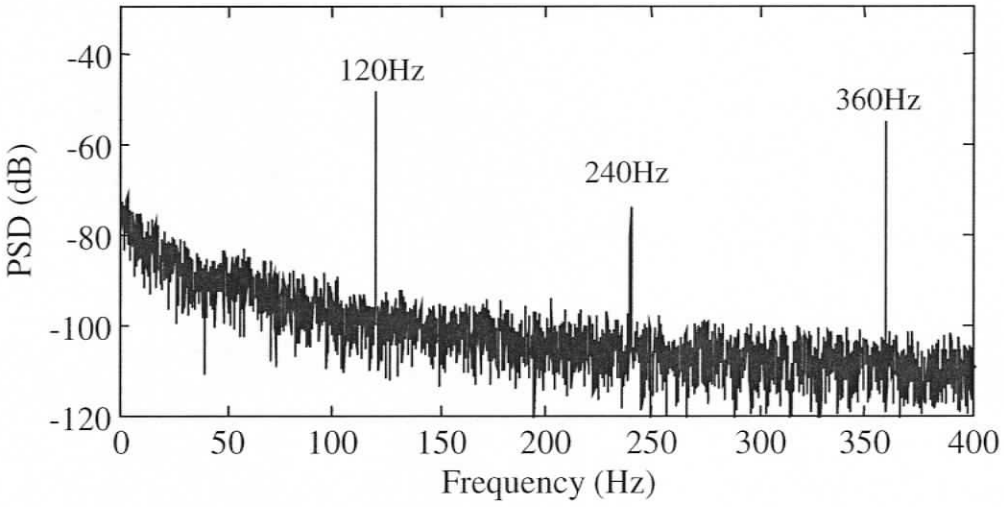

Figure 7.4 Simulated PSD of field current of the synchronous machine with asymmetric standard field winding fed by unbalanced supply

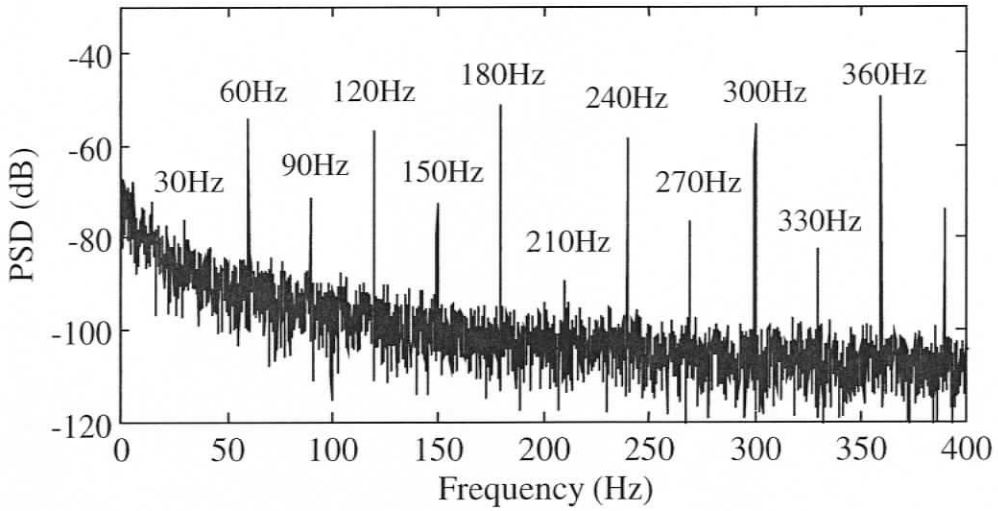

Figure 7.5 Simulated PSD of field current of the synchronous machine with asymmetric two-coil field winding and having 4-turn fault

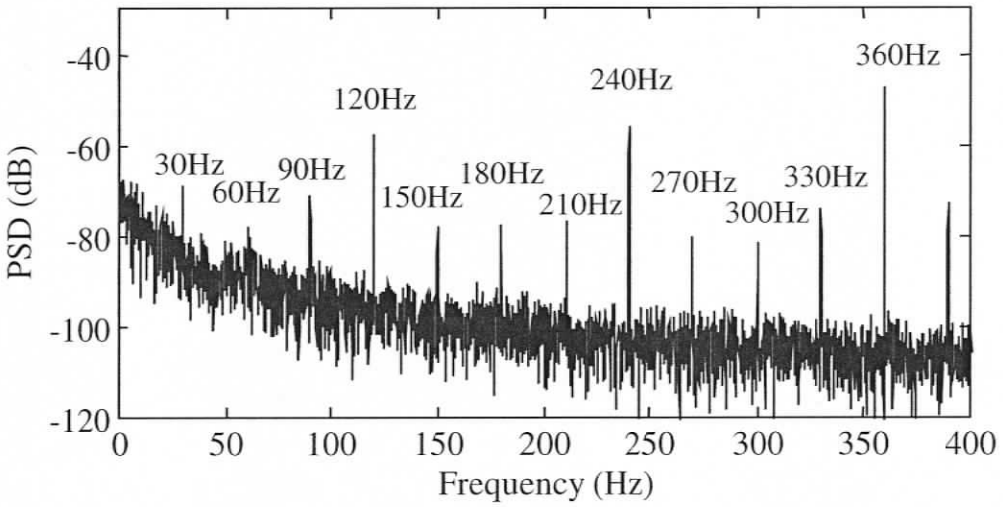

Figure 7.6 Simulated PSD of field current of the synchronous machine with asymmetric standard field winding and having 4-turn fault

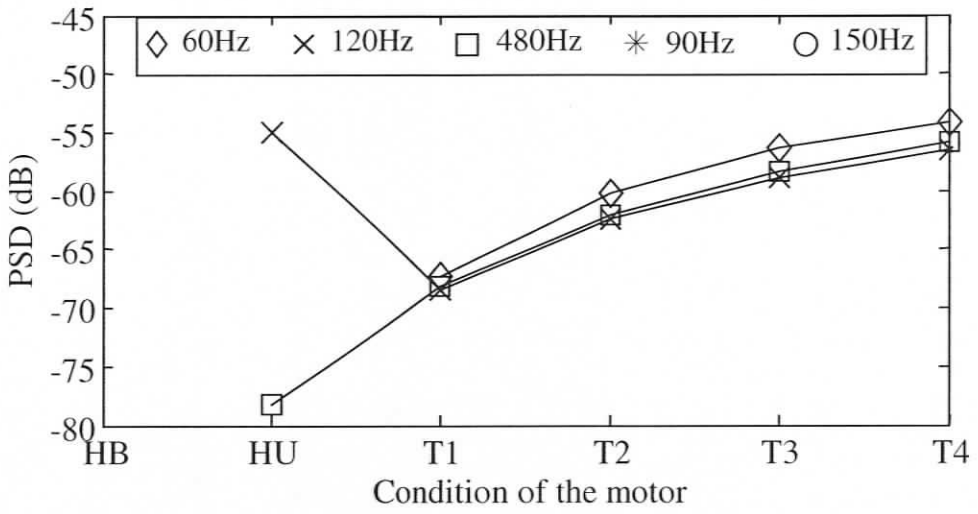

Figure 7.7 The frequency components in the field current of the simulated synchronous machine with symmetric two-coil field winding under different conditions of the machine

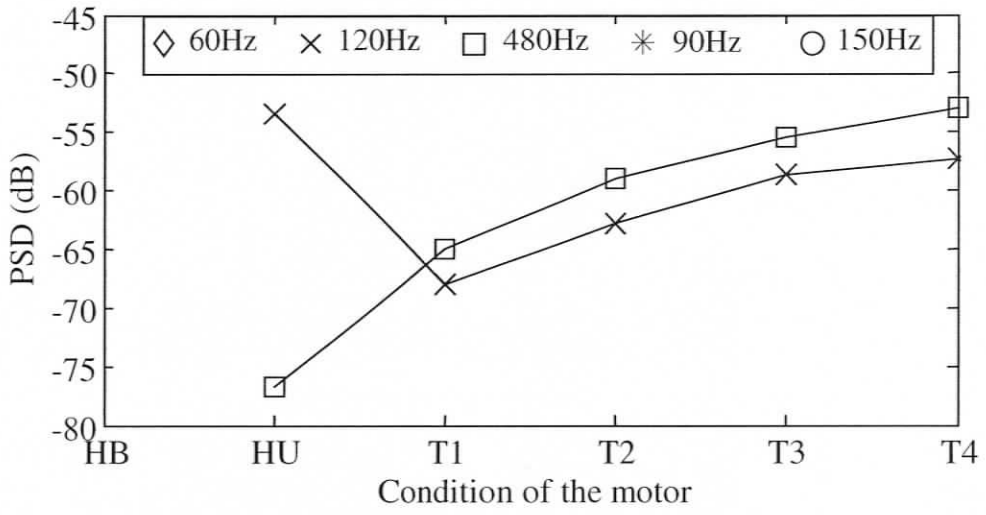

Figure 7.8 The frequency components in the field current of the simulated synchronous machine with symmetric standard field winding under different conditions of the machine

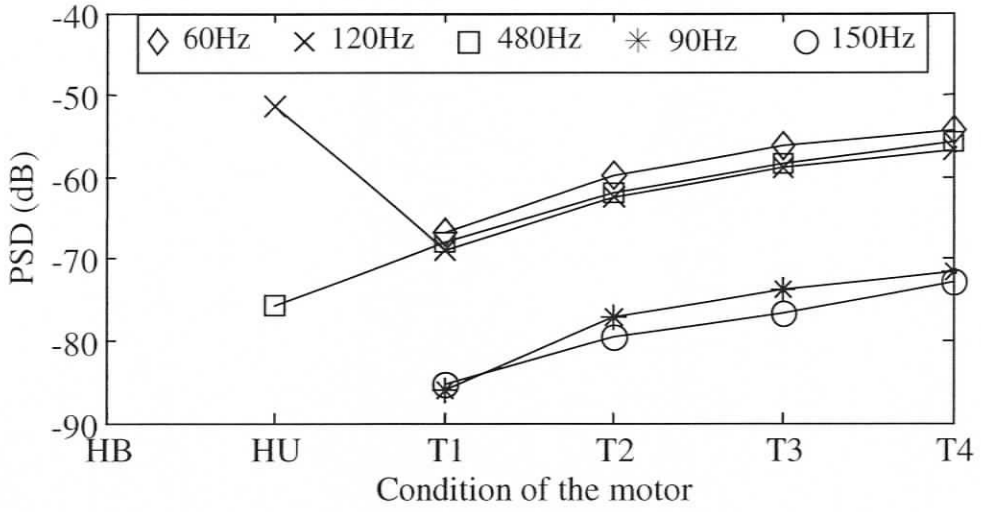

Figure 7.9 The frequency components in the field current of the simulated synchronous machine with asymmetric two-coil field winding under different conditions of the machine

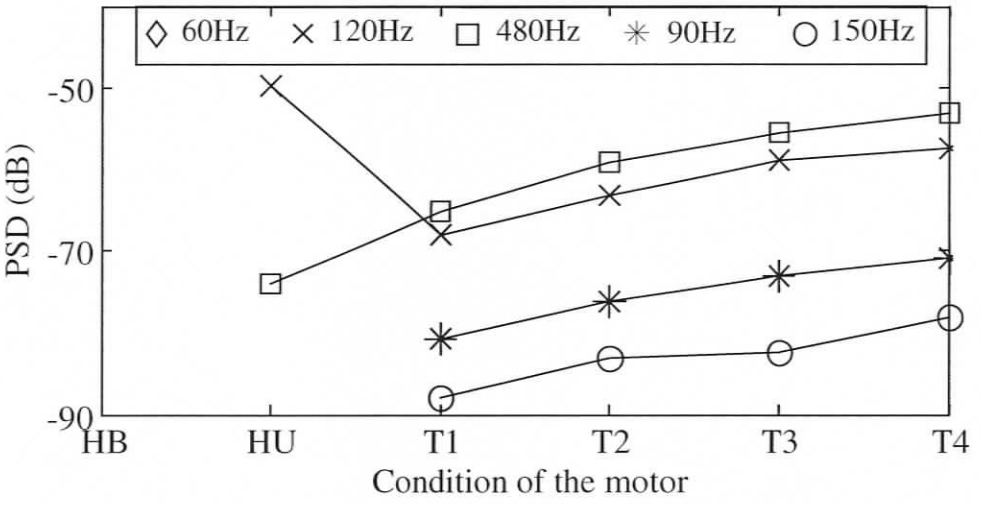

Figure 7.10 The frequency components in the field current of the simulated synchronous machine with asymmetric standard field winding under different conditions of the machine

7.4 Experimental Results under Healthy, Faulty and Supply Unbalance Conditions

7.4.1 Experimental Results with Two-coil Field Winding

Initially, by varying the fault severity, a motor that has a two-coil field winding has been rigorously tested. In order to ensure unambiguous detection of the faulty state of the machine, the influence of supply unbalance on the test results was carefully observed. It was also noticed that the sensitivity of the current sensor is vitally important in detecting the harmonics. Otherwise they may get lost in the noise floor.

A significant increase in the 120 and 480 Hz was observed in the field current signature of the machine with unbalanced supply (V_{ab}=199.9V, V_{bc}=208.1V and V_{ca}=206.9V). An increase of these components under a 4-turn fault has also been observed as shown in Figure 7.11. Also, a comparison of the 120 and 480 Hz under supply unbalance and different fault severity of the motor at full-load (0.8 lag) is shown in Figure 7.12. An even larger increase of these harmonics under supply unbalance as compared to the faulty conditions clearly indicates the ambiguity.

The 150 Hz components in the excitation current showed the most prominent increase with the faults involving few turns. This was observed for all the three power factors at no-load, half-load and full-load conditions as shown in Figure7.13. The supply unbalance seems to have minimal influence on this harmonic.

Further, the frequency spectra of the voltage induced in the rotor-mounted search-coil under healthy, supply unbalance and a 4-turn fault have been shown in Figure 7.14. The harmonic analysis of voltage induced in the rotor-mounted search-coil showed a predominant increase of these frequency components with the stator inter-turn faults. The rotor search-coil can accept a frequency of any pole-pair number independent of the asymmetry in the machine. The 90 Hz in the rotor search-coil

voltage was found to be a very promising indicator of even one-turn fault at all operating conditions. Further, this component was least affected by supply unbalance as shown in Figure 7.15. The magnitudes of different harmonics have been normalized with respect to the DC and the 30 Hz components of the field current and the rotor search-coil voltage respectively.

In order to test the dependability of these harmonics, five sets of data have been collected under different conditions of the motor; healthy motor with balanced supply (HB), healthy motor with unbalanced supply (HU) and with 1 to 4 turn shorts (T1 to T4). This was repeated under no-load, half-load and full-load conditions at three power factors (0.8 lag, 0.8 lead and UPF). The average values of the 90, 150 and 210 Hz components in the field current as well as in the rotor search-coil voltage are shown in Table 7.2 to Table 7.10. The corresponding sample standard deviation has been shown in brackets below each of the average value. Low values of the standard deviation imply less fluctuation of these harmonics under the given conditions of the motor. Most importantly, the 150 Hz components in the field current and the 90 Hz components in the rotor search-coil stood out prominently.

It was observed that the magnitudes of these harmonics seem to be dependent on the operating point of the machine. A probable reason may be explained by looking closely at Table 7.1. For example, the 90Hz component can be caused by both $c = 1$ and 5. Similarly, the 150Hz component can be caused by both $c = 3$ and 7. Due to the variations in the load and power factor, the space distribution of these components may change resulting in the variation of detection. Other factors such as, change in the saturation, other time harmonics, eccentricity related low frequency components might also cause minor changes in them. A possible way to circumvent this problem is to have a look-up table describing the best harmonic to be selected in the field current or the rotor search coil voltage under a given operating condition.

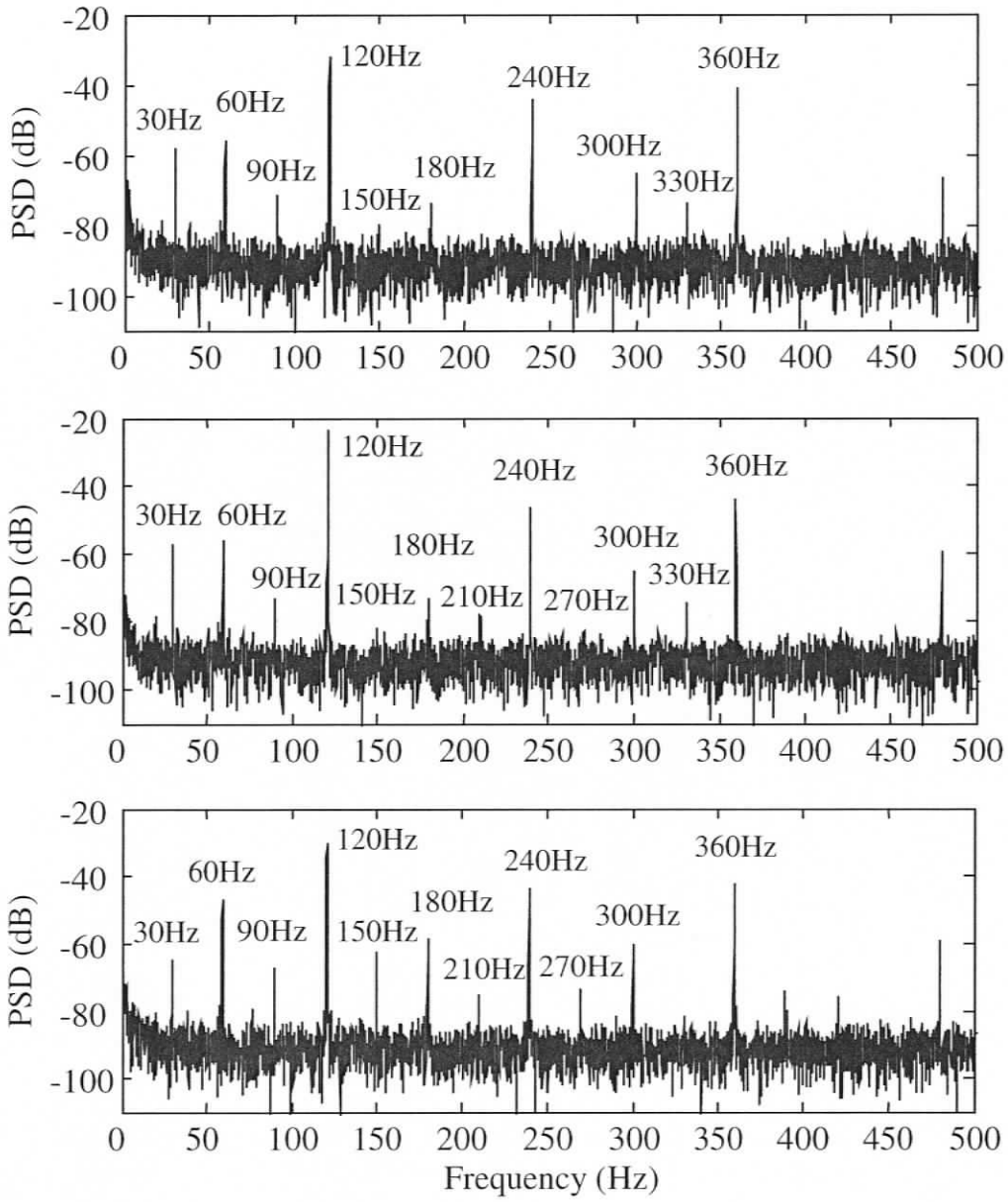

Figure 7.11 Experimental PSD of field current under full-load, 0.8 lagging PF condition with balanced supply (top), with unbalanced supply (middle) and with 4-turn fault (bottom) for two-coil field winding

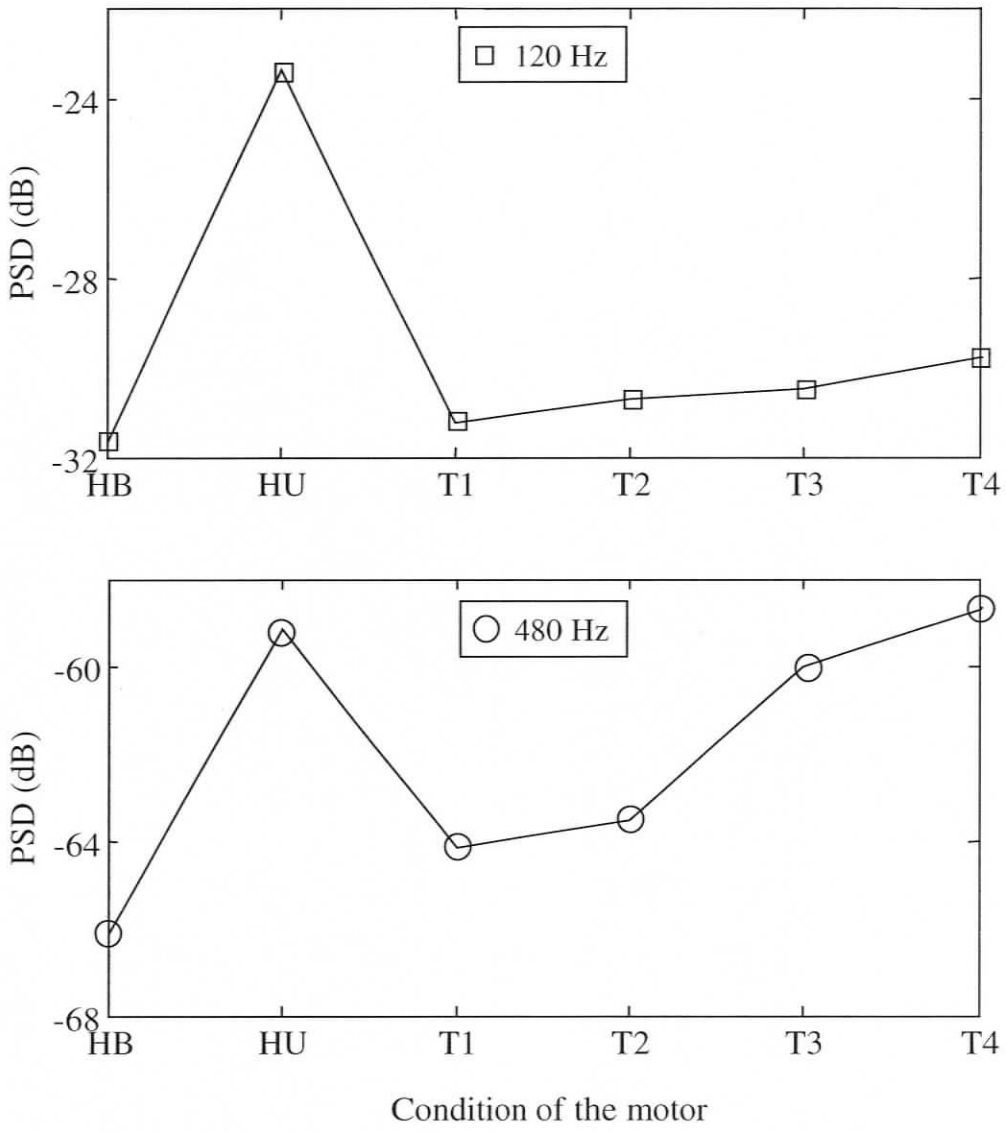

Figure 7.12 The 120Hz (top) and the 480Hz (bottom) components in the field current of two-coil winding under full-load, 0.8 lagging PF condition (Experimental)

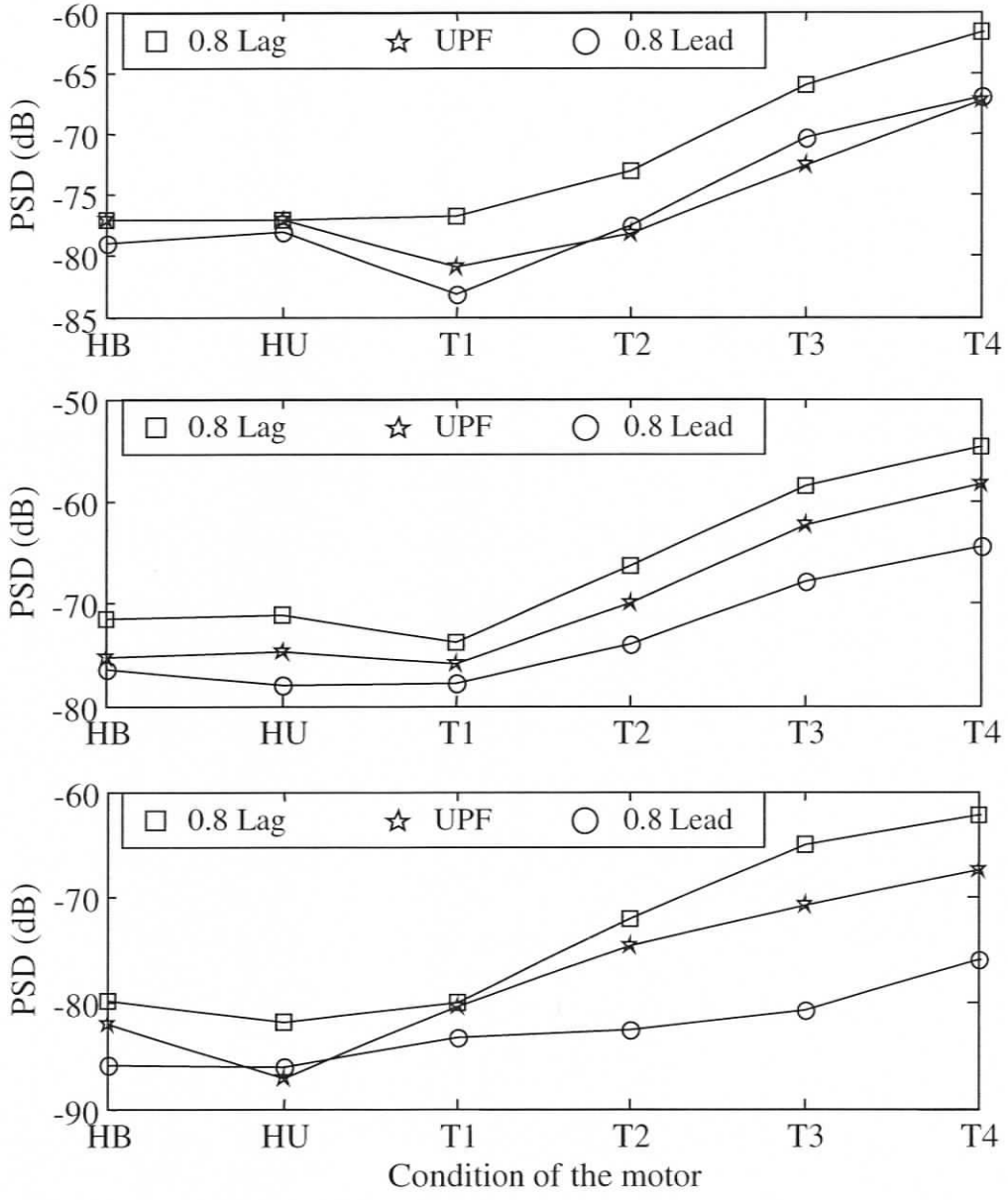

Figure 7.13 The 150Hz component in the field current of two-coil winding under no-load (top), half-load (middle) and full-load (bottom), (Experimental)

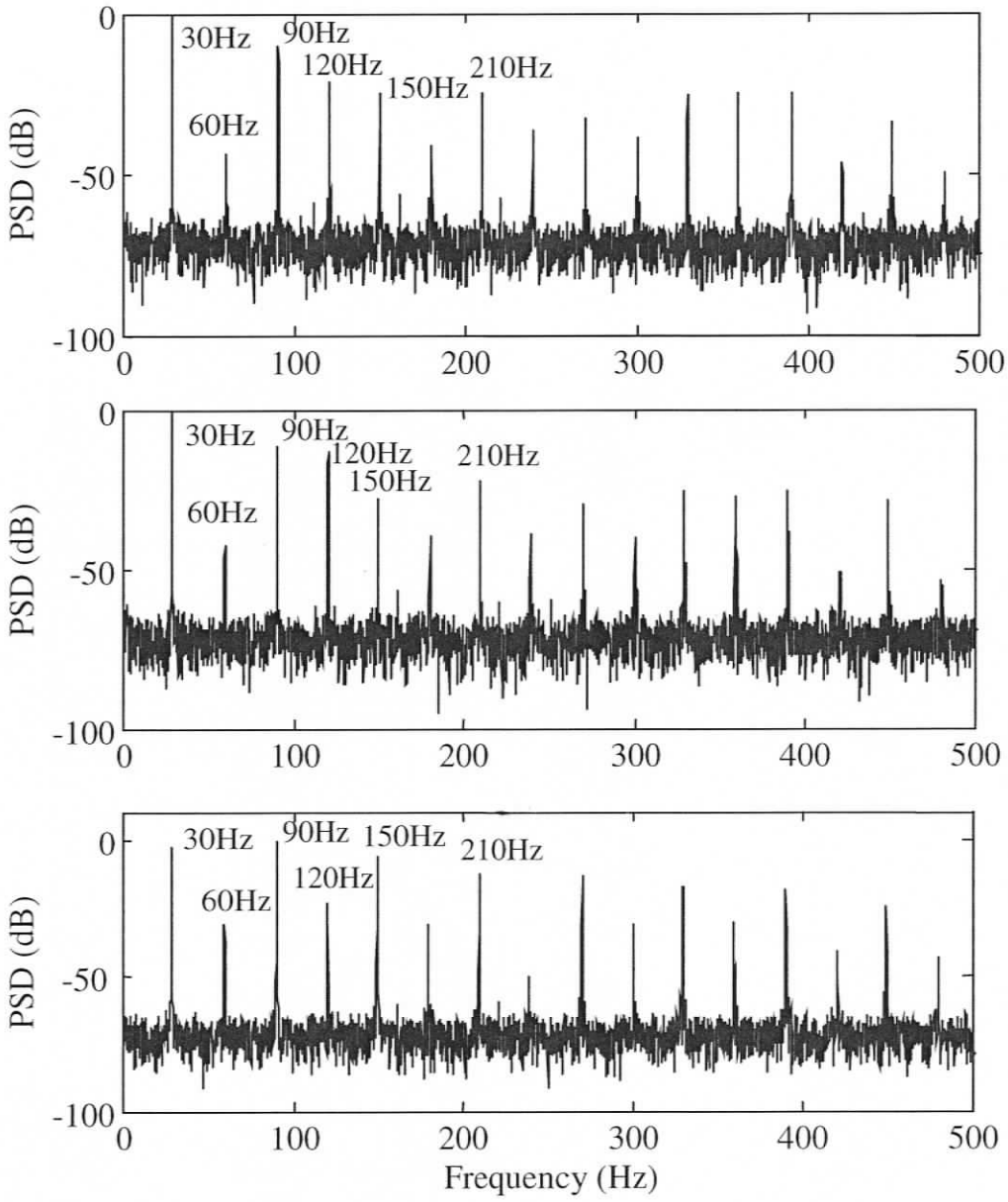

Figure 7.14 Experimental PSD of the voltage induced in the rotor search-coil under full-load, 0.8 lagging PF condition with balanced supply (top), with unbalanced supply (middle) and with 4-turn fault (bottom) for two-coil field winding

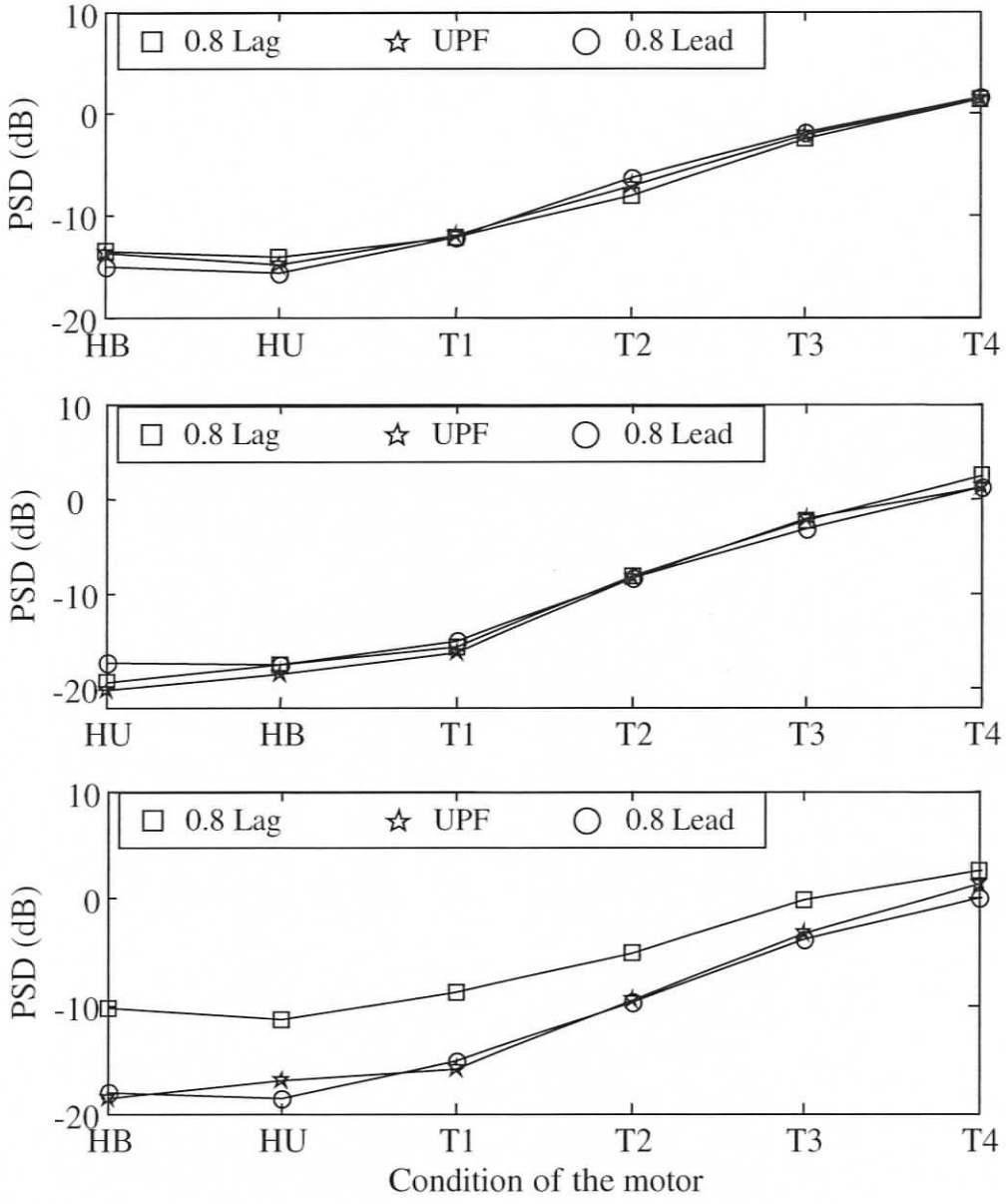

Figure 7.15 The 90Hz component in the rotor search-coil of the SM with two-coil field winding under no-load (top), half-load (middle) and full-load (bottom), (Experimental)

Table 7.2 Harmonics at no-load (0.8 lagging PF) condition (for two-coil structure)

	HB	HU	T1	T2	T3	T4
	Field Current					
90 Hz	-68.26 (0.76)	-68.78 (0.81)	-68.7 (0.22)	-68.71 (0.49)	-67.89 (0.44)	-68.31 (0.51)
150 Hz	-76.55 (0.49)	-76.78 (1.45)	-76.12 (0.94)	-72.17 (1.36)	-65.59 (0.56)	-61.72 (0.28)
210 Hz	-85.18 (1.46)	-82.6 (1.29)	-84.53 (0.83)	-78.96 (2.89)	-72.18 (0.29)	-68.47 (0.46)
	Rotor Search-coil					
90 Hz	-13.5 (0.09)	-13.72 (0.2)	-11.99 (0.16)	-7.46 (0.89)	-2.3 (0.49)	1.46 (0.25)
150 Hz	-23.48 (0.35)	-22.86 (0.54)	-24.74 (0.11)	-15.49 (2.09)	-5.33 (0.8)	0.55 (0.35)
210 Hz	-26.94 (0.52)	-21.42 (0.31)	-26.92 (0.18)	-21.5 (1.3)	-13.75 (0.58)	-8.78 (0.35)

Table 7.3 Harmonics at no-load (0.8 leading PF) condition (for two-coil structure)

	HB	HU	T1	T2	T3	T4
	Field Current					
90 Hz	-69.21 (0.86)	-69.98 (0.74)	-68.66 (0.07)	-69.31 (0.36)	-69.09 (0.28)	-70.11 (0.29)
150 Hz	-79.07 (0.88)	-77.17 (0.71)	-82.26 (2.26)	-77.4 (0.64)	-70.31 (0.42)	-66.93 (0.28)
210 Hz	-86.14 (2.37)	-87.25 (2.27)	-86.22 (2.65)	-81.35 (0.86)	-76.16 (0.98)	-73.37 (0.59)
	Rotor Search-coil					
90 Hz	-15.06 (0.05)	-15.58 (0.06)	-12.17 (0.15)	-6.36 (0.14)	-1.72 (0.06)	1.5 (0.01)
150 Hz	-19.43 (0.2)	-21 (0.23)	-22.06 (0.33)	-13.03 (0.4)	-4.47 (0.1)	0.62 (0.02)
210 Hz	-26.77 (0.37)	-18.96 (0.24)	-26.11 (0.5)	-19.74 (0.42)	-13.19 (0.11)	-8.99 (0.08)

Table 7.4 Harmonics at no-load (UPF) condition (for two-coil structure)

	HB	HU	T1	T2	T3	T4
	Field Current					
90 Hz	-67.86 (0.49)	-68.7 (0.33)	-67.95 (0.29)	-68.45 (0.18)	-68.91 (0.39)	-70.14 (0.36)
150 Hz	-79.45 (1.73)	-75.68 (0.79)	-79.44 (1.26)	-77.38 (0.86)	-71.31 (0.81)	-67.17 (0.54)
210 Hz	-86.53 (1.96)	-85.34 (2.1)	-86.07 (1.96)	-81.64 (1.55)	-76.59 (1.58)	-73.65 (1.46)
	Rotor Search-coil					
90 Hz	-13.67 (0.05)	-14.96 (0.07)	-11.81 (0.08)	-6.9 (0.49)	-2.15 (0.31)	1.47 (0.15)
150 Hz	-21.16 (0.17)	-21.83 (0.23)	-22.28 (0.19)	-15.1 (1.15)	-5.64 (0.56)	0.21 (0.31)
210 Hz	-26.18 (0.22)	-20.02 (0.41)	-25.89 (0.17)	-20.98 (0.45)	-14.23 (0.49)	-9.24 (0.47)

Table 7.5 Harmonics at half-load (0.8 lagging PF) condition (for two-coil structure)

	HB	HU	T1	T2	T3	T4
	Field Current					
90 Hz	-80.28 (2.20)	-78.75 (1.31)	-77.35 (1.90)	-69.52 (0.80)	-63.53 (0.22)	-59.65 (0.28)
150 Hz	-72.46 (1.24)	-72.03 (0.91)	-75.15 (1.07)	-66.05 (0.64)	-58.25 (0.39)	-54.55 (0.28)
210 Hz	-81.45 (0.83)	-77.62 (1.66)	-79.26 (2.29)	-73.86 (1.94)	-67.14 (0.57)	-63.06 (0.29)
	Rotor Search-coil					
90 Hz	-19.45 (0.22)	-17.58 (0.03)	-15.58 (0.14)	-8.29 (0.51)	-2.46 (0.17)	2.44 (0.14)
150 Hz	-23.96 (0.28)	-24.20 (0.10)	-32.04 (0.25)	-13.88 (0.63)	-4.21 (0.19)	1.05 (0.16)
210 Hz	-35.66 (0.55)	-22.93 (0.08)	-28.33 (0.71)	-19.76 (0.31)	-12.01 (0.21)	-6.60 (0.10)

Table 7.6 Harmonics at half-load (0.8 leading PF) condition (for two-coil structure)

	HB	HU	T1	T2	T3	T4
	Field Current					
90 Hz	-74.30 (0.28)	-75.26 (1.01)	-74.28 (0.81)	-71.35 (0.21)	-68.79 (0.54)	-66.00 (0.10)
150 Hz	-76.71 (0.61)	-77.09 (1.04)	-78.38 (1.03)	-74.34 (0.64)	-68.28 (0.36)	-63.99 (0.38)
210 Hz	-90.53 (1.79)	-82.51 (1.86)	-87.53 (1.08)	-82.15 (1.91)	-76.80 (0.27)	-72.89 (0.41)
	Rotor Search-coil					
90 Hz	-17.39 (0.01)	-17.54 (0.04)	-15.01 (0.19)	-8.71 (0.16)	-3.42 (0.39)	1.21 (0.10)
150 Hz	-25.97 (0.05)	-42.29 (0.59)	-26.32 (0.26)	-14.81 (0.40)	-6.59 (0.44)	-0.69 (0.25)
210 Hz	-26.54 (0.04)	-21.15 (0.18)	-24.72 (0.54)	-19.59 (0.45)	-13.55 (0.42)	-9.00 (0.35)

Table 7.7 Harmonics at half -load (UPF) condition (for two-coil structure)

	HB	HU	T1	T2	T3	T4
	Field Current					
90 Hz	-75.68 (0.81)	-76.34 (0.88)	-74.98 (0.24)	-70.28 (0.52)	-65.09 (0.15)	-62.51 (0.71)
150 Hz	-74.94 (0.61)	-75.54 (0.89)	-76.41 (0.71)	-70.11 (0.25)	-62.53 (0.21)	-58.60 (0.56)
210 Hz	-85.88 (0.97)	-81.64 (1.25)	-81.69 (2.14)	-78.31 (1.44)	-71.22 (0.51)	-67.06 (0.21)
	Rotor Search-coil					
90 Hz	-20.10 (0.11)	-18.57 (0.09)	-16.03 (0.46)	-8.42 (0.08)	-2.21 (0.10)	1.85 (0.46)
150 Hz	-25.85 (0.29)	-28.87 (0.33)	-28.91 (0.30)	-13.93 (0.15)	-4.77 (0.21)	0.44 (0.55)
210 Hz	-30.90 (0.44)	-23.04 (0.21)	-25.40 (0.16)	-18.63 (0.13)	-12.13 (0.36)	-7.22 (0.21)

Table 7.8 Harmonics at full-load (0.8 lagging PF) condition (for two-coil structure)

	HB	HU	T1	T2	T3	T4
	Field Current					
90 Hz	-70.6 (0.53)	-71.48 (0.79)	-71.26 (0.43)	-73.83 (0.57)	71.18 (0.58)	-67.11 (0.62)
150 Hz	-79.67 (2.28)	-81.68 (1.65)	-77.19 (1.97)	-71.18 (1.14)	65.66 (0.40)	-62.63 (0.42)
210 Hz	-81.28 (2.12)	-77.43 (1.13)	-78.51 (0.75)	-77.32 (1.41)	75.78 (0.61)	-75.08 (0.69)
	Rotor Search-coil					
90 Hz	-10.29 (0.12)	-11.22 (0.07)	-8.69 (0.05)	-5.01 (0.03)	-0.21 (0.08)	2.66 (0.04)
150 Hz	-24.45 (0.12)	-27.52 (0.21)	-36.2 (0.32)	-17.56 (0.15)	-7.69 (0.2)	-3.23 (0.11)
210 Hz	-24.95 (0.3)	-21.58 (0.47)	-21.51 (0.15)	-16.12 (0.1)	-1.67 (0.42)	-9.39 (0.23)

Table 7.9 Harmonics at full-load (0.8 leading PF) condition (for two-coil structure)

	HB	HU	T1	T2	T3	T4
	Field Current					
90 Hz	-81.05 (1.7)	-82.8 (1.21)	-78.55 (0.59)	-78.19 (0.75)	-75.87 (0.19)	-73.88 (0.34)
150 Hz	-85.27 (1.51)	-83.98 (1.56)	-84.45 (1.31)	-83.38 (0.94)	-80.06 (1.01)	-76.24 (0.66)
210 Hz	-89.32 (1.25)	-84.47 (1.44)	-89.37 (0.93)	-86.58 (0.76)	-85.88 (1.03)	-83.84 (1.13)
	Rotor Search-coil					
90 Hz	-18.1 (0.05)	-18.63 (0.05)	-15.15 (0.05)	-9.58 (0.11)	-3.72 (0.12)	0.37 (0.23)
150 Hz	-26.16 (0.27)	-28.7 (0.51)	-24.35 (0.22)	-17.45 (0.11)	-9.68 (0.16)	-4.55 (0.59)
210 Hz	-25.66 (0.18)	-20.68 (0.19)	-23.41 (0.18)	-19.25 (0.07)	-14.34 (0.24)	-10.67 (0.37)

Table 7.10 Harmonics at full-load (UPF) condition (for two-coil structure)

	HB	HU	T1	T2	T3	T4
	Field Current					
90 Hz	-85.16 (2.19)	-89.15 (0.46)	-84.72 (2.35)	-85.84 (1.04)	-74.83 (0.58)	-69.66 (0.45)
150 Hz	-80.7 (1.01)	-84.82 (1.37)	-80.01 (1.28)	-75.67 (0.9)	-70.66 (0.47)	-66.86 (0.48)
210 Hz	-85.7 (2.6)	-83.34 (1.86)	-84.31 (1.86)	-81.6 (0.81)	-78.56 (1.31)	-75.26 (0.59)
	Rotor Search-coil					
90 Hz	-18.63 (0.03)	-16.98 (0.25)	-15.7 (0.16)	-9.54 (0.16)	-2.99 (0.25)	1.45 (0.12)
150 Hz	-28.75 (0.04)	-34.98 (0.67)	-31.6 (0.29)	-17.83 (0.26)	-8.13 (0.36)	-2.44 (0.25)
210 Hz	-27.18 (0.16)	-22.39 (0.41)	-24.72 (0.42)	-18.83 (0.46)	-12.87 (0.48)	-8.73 (0.34)

7.4.2 Experimental Results with Standard Field Winding

Now, in order to further validate the proposed scheme, a machine that has a standard field winding has also been rigorously tested in the laboratory with different fault levels at various loads and power factors. Once again a significant increase in the 120 and 480 Hz was observed in the field current signature under unbalanced supply (V_{ab}=201.1V, V_{bc}=208.1V and V_{ca}=207.4V) as well as a 4-turn fault condition as shown in Figure 7.16. The comparison of the 120 and 480 Hz under supply unbalance and different fault severity of the motor at full-load (0.8 lag) is shown in Figure 7.17. A larger increase of the 120 and 248Hz components under supply unbalance compared to faulty conditions caused serious ambiguity.

The 150 Hz components in the excitation current has been found to be the sensitive to the faults involving few turns under half-load and full-load conditions at all the three power factors as shown. The 270 Hz component also showed a marked

increase under no-load condition at all the three power factors as shown in Figure 7.18. Most importantly, the supply unbalance could cause minimal variations in these harmonic components.

Also, these frequency components showed a very large increase in the voltage induced in the rotor-mounted search-coil only in the event of stator inter-turn fault. The 90 Hz in the rotor search-coil voltage was found to be a very promising indicator of even a one-turn fault at all operating loads and was least affected by supply unbalance as shown in Figure 7.19. The magnitudes of different harmonics have been normalized with respect to the DC and the 30 Hz components of the field current and the rotor search-coil voltage respectively. Also, the PSD plots of voltage induced in the rotor search-coil under HB, HU and T4 at full-load, 0.8 PF lagging have been shown in Figure 7.20.

In order to examine the dependability of these harmonics, five sets of data have been collected under all conditions of the motor; HB, HU and T1 to T4 under various loads and power factors. The average values of the 90, 150 and 270 Hz components in the field current as well as in the rotor search-coil voltage are shown in Table 7.11 to Table 7.19. The corresponding sample standard deviation has been shown in brackets below each of the average value. Low values of the standard deviations indicate less variation of these harmonics under a given conditions of the motor. In this case, the 150 and the 270 Hz components in the field current, and the 90 Hz components in the rotor search-coil were found to be very good indicators of stator inter-turn faults.

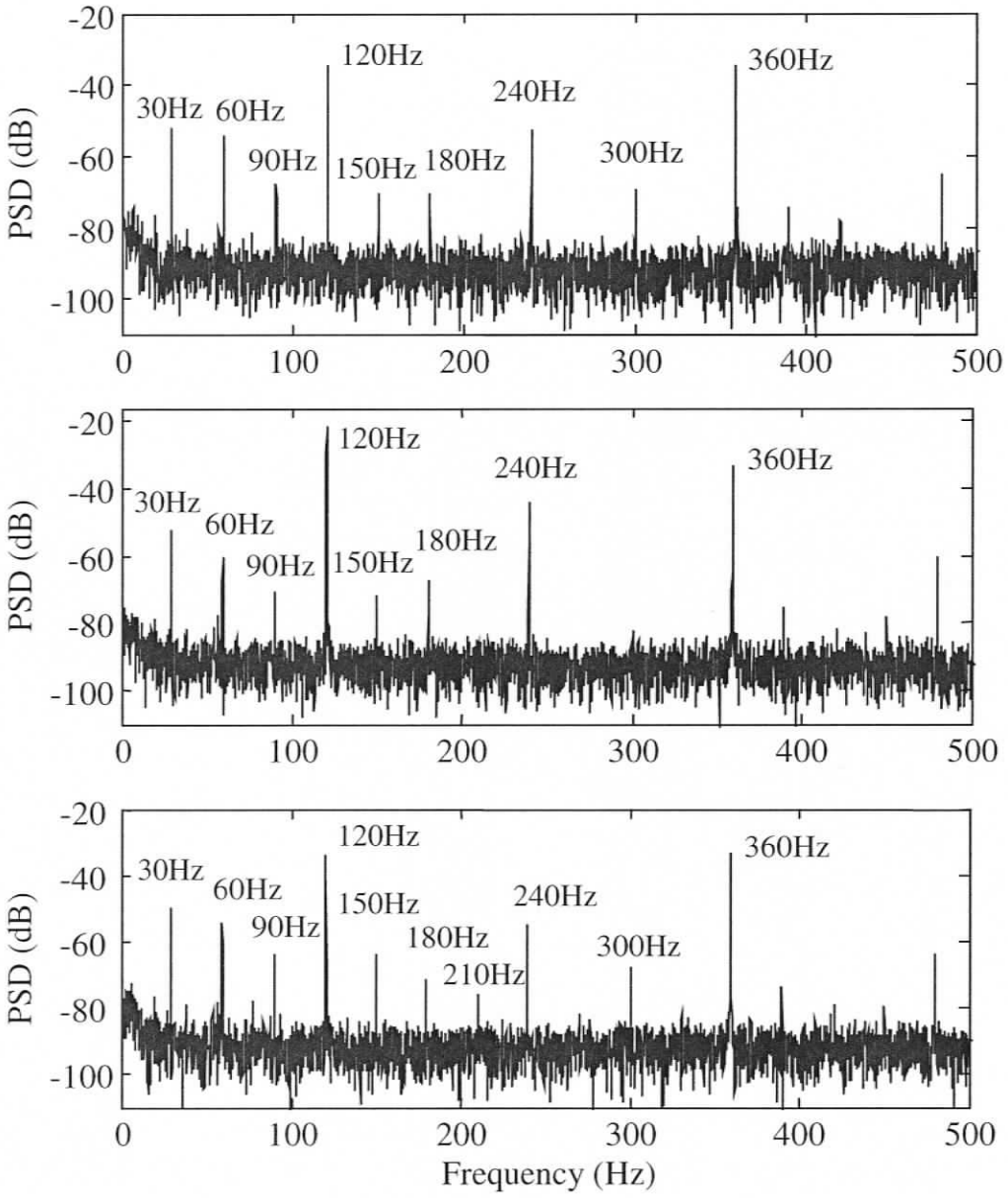

Figure 7.16 Experimental PSD of field current under full-load, 0.8 lagging PF condition with balanced supply (top), with unbalanced supply (middle) and with 4-turn fault (bottom) for standard field winding

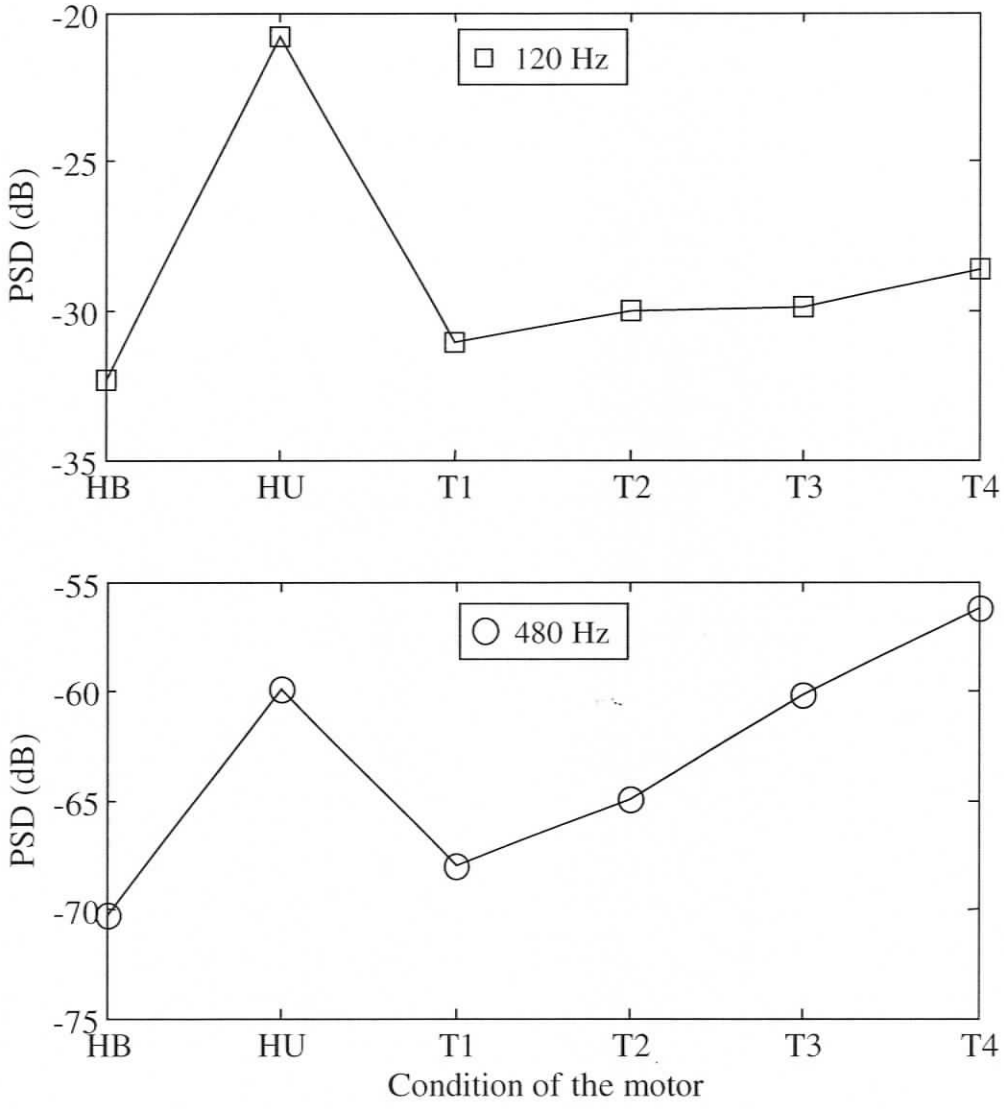

Figure 7.17 The 120Hz (top) and the 480Hz (bottom) components in the field current of standard winding under full-load, 0.8 lagging PF condition (Experimental)

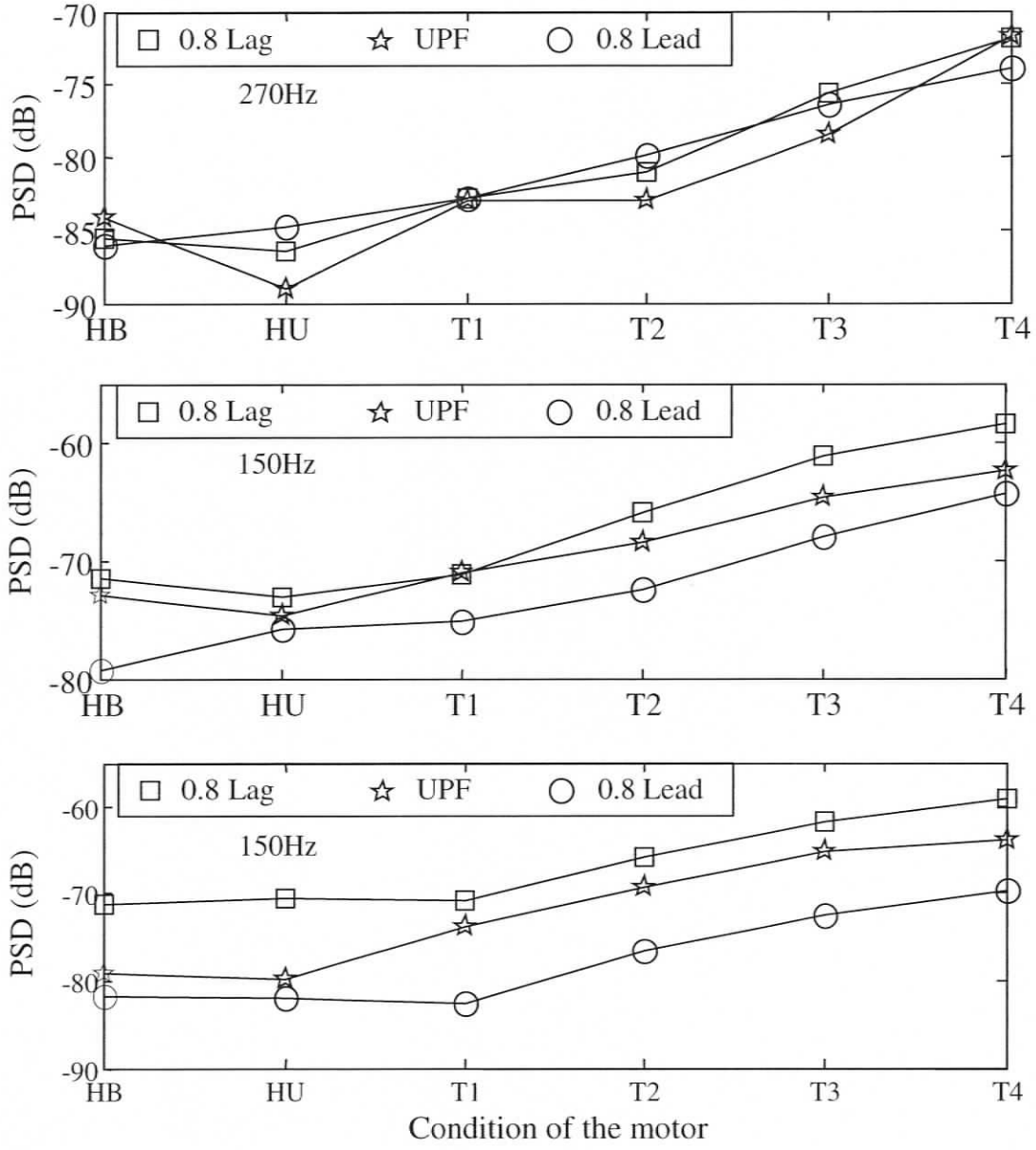

Figure 7.18 The 270Hz component under no-load (top) and the 150Hz component under half-load (middle) and full-load (bottom) in the field current of standard winding (Experimental)

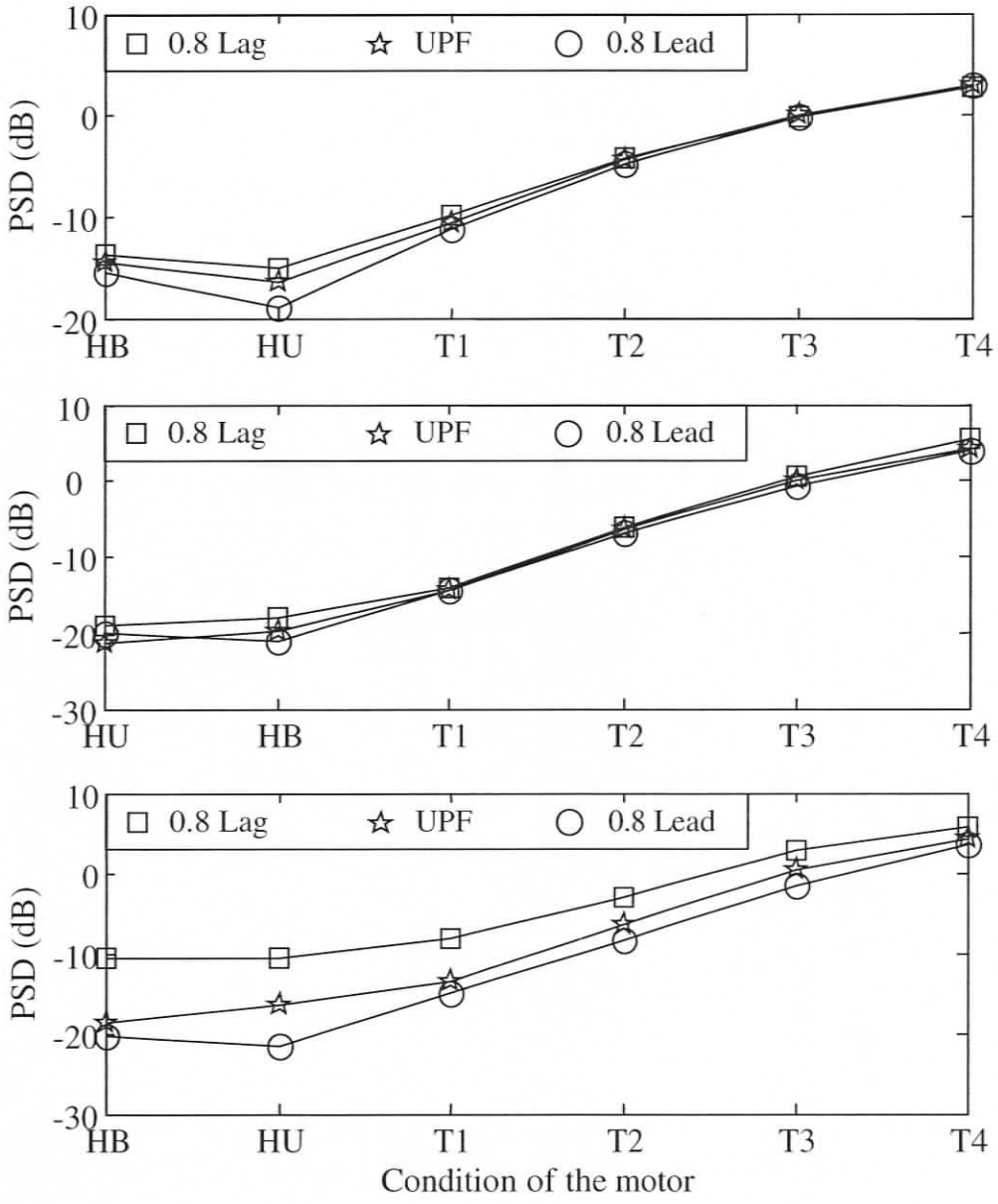

Figure 7.19 The 90Hz component in the rotor search-coil of the SM with standard field winding under no-load (top), half-load (middle) and full-load (bottom) (Experimental)

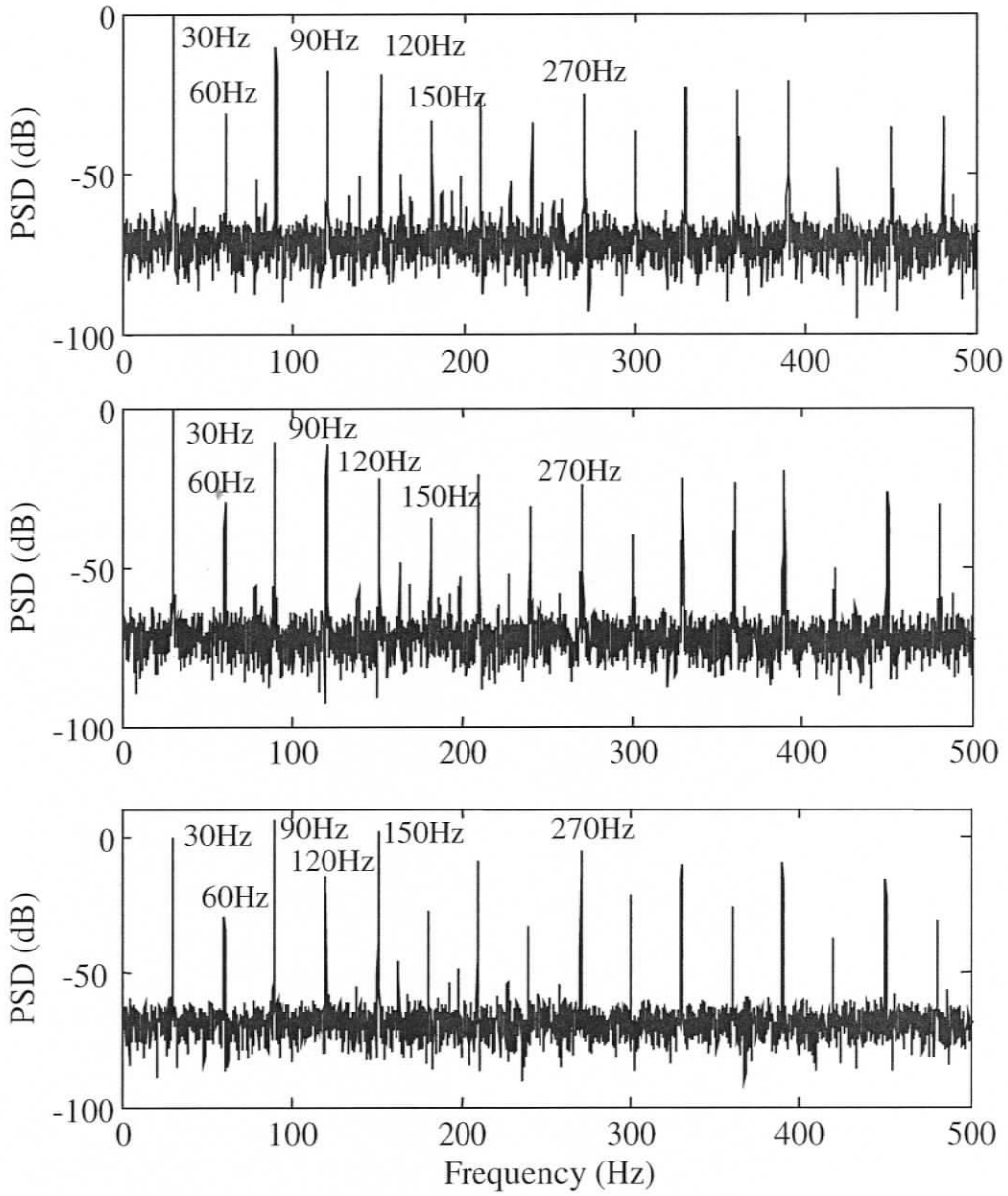

Figure 7.20 Experimental PSD of voltage induced in the rotor-mounted search-coil under full-load, 0.8 lagging PF condition with balanced supply (top), with unbalanced supply (middle) and 4-turn fault (bottom) for the SM with standard field winding

Table 7.11 Harmonics at no-load (0.8 lagging PF) condition (for standard structure)

	HB	HU	T1	T2	T3	T4
	Field Current					
90 Hz	-65.64 (0.68)	-69.38 (0.28)	-64.92 (0.24)	-64.79 (0.16)	-64.09 (0.46)	-64.41 (0.47)
150 Hz	-71.97 (0.83)	-70.69 (0.46)	-74.64 (0.71)	-77.22 (1.14)	-79.03 (1.50)	-76.24 (0.88)
270 Hz	-84.51 (1.19)	-84.36 (2.65)	-85.89 (2.18)	-80.96 (0.72)	-75.85 (0.46)	-72.11 (0.52)
	Rotor Search-coil					
90 Hz	-13.67 (0.06)	-15.30 (0.26)	-9.90 (0.09)	-4.24 (0.05)	0.17 (0.17)	2.79 (0.20)
150 Hz	-15.36 (0.19)	-18.19 (0.29)	-18.79 (0.16)	-8.22 (0.15)	-0.95 (0.49)	2.89 (0.53)
270 Hz	-39.13 (0.69)	-32.06 (0.47)	-32.46 (0.46)	-24.74 (0.47)	-20.88 (0.32)	-17.97 (0.47)

Table 7.12 Harmonics at no-load (0.8 leading PF) condition (for standard structure)

	HB	HU	T1	T2	T3	T4
	Field Current					
90 Hz	-66.28 (0.27)	-71.09 (0.45)	-65.79 (0.25)	-65.57 (0.25)	-64.65 (0.20)	-64.40 (0.24)
150 Hz	-74.33 (0.38)	-73.82 (0.48)	-74.16 (0.41)	-75.77 (1.14)	-79.07 (1.61)	-73.53 (1.12)
270 Hz	-87.85 (2.14)	-85.15 (2.34)	-85.25 (2.72)	-81.22 (1.59)	-77.91 (1.01)	-73.72 (0.63)
	Rotor Search-coil					
90 Hz	-15.36 (0.07)	-18.76 (0.11)	-11.14 (0.08)	-4.85 (0.06)	-0.09 (0.06)	2.84 (0.07)
150 Hz	-14.18 (0.23)	-16.25 (0.31)	-18.20 (0.22)	-8.97 (0.15)	-1.11 (0.18)	3.12 (0.16)
270 Hz	-34.73 (0.25)	-29.91 (0.40)	-29.80 (0.42)	-23.02 (0.43)	-19.36 (0.58)	-16.73 (0.55)

Table 7.13 Harmonics at no-load (UPF) condition (for standard structure)

	HB	HU	T1	T2	T3	T4
	Field Current					
90 Hz	-65.66 (0.17)	-69.65 (0.35)	-65.99 (0.46)	-65.10 (0.45)	-64.37 (0.23)	-64.23 (0.18)
150 Hz	-71.59 (0.66)	-72.31 (0.23)	-73.81 (0.80)	-75.75 (0.61)	-79.22 (0.89)	-75.52 (0.61)
270 Hz	-84.79 (1.55)	-84.29 (3.00)	-84.72 (1.54)	-83.33 (2.24)	-76.82 (1.52)	-72.42 (0.86)
	Rotor Search-coil					
90 Hz	-14.46 (0.02)	-16.59 (0.15)	-10.45 (0.13)	-4.57 (0.07)	0.03 (0.05)	2.87 (0.01)
150 Hz	-14.33 (0.09)	-17.47 (0.43)	-18.57 (0.27)	-8.63 (0.19)	-1.02 (0.13)	3.21 (0.03)
270 Hz	-36.86 (0.36)	-30.05 (0.33)	-31.36 (0.57)	-24.41 (0.57)	-20.20 (0.51)	-17.21 (0.09)

Table 7.14 Harmonics at half-load (0.8 lagging PF) condition (for standard structure)

	HB	HU	T1	T2	T3	T4
	Field Current					
90 Hz	-65.98 (0.49)	-67.20 (0.40)	-63.99 (0.22)	-61.01 (0.18)	-58.40 (0.18)	-56.92 (0.16)
150 Hz	-71.84 (0.95)	-71.86 (1.21)	-70.91 (0.53)	-65.51 (0.39)	-61.57 (0.41)	-58.30 0.34)
270 Hz	-81.03 (1.91)	-82.96 (1.65)	-81.35 (2.16)	-83.71 (1.02)	-75.84 (2.03)	-70.51 (0.72)
	Rotor Search-coil					
90 Hz	-18.86 (0.15)	-18.02 (0.08)	-13.95 (0.05)	-6.01 (0.07)	0.42 (0.13)	5.43 (0.06)
150 Hz	-19.23 (0.35)	-22.63 (0.17)	-24.65 (0.08)	-9.64 (0.16)	-1.11 (0.37)	5.10 (0.26)
270 Hz	-39.80 (0.49)	-33.11 (0.30)	-30.61 (0.50)	-21.48 (0.46)	-15.73 (0.45)	-11.72 (0.49)

Table 7.15 Harmonics at half-load (0.8 leading PF) condition (for standard structure)

	HB	HU	T1	T2	T3	T4
	Field Current					
90 Hz	-73.39 (0.80)	-73.80 (0.50)	-70.06 (0.44)	-67.74 (0.36)	-66.68 (0.27)	-64.25 (0.26)
150 Hz	-79.40 (1.62)	-75.18 (0.56)	-75.62 (0.90)	-72.28 (0.53)	-68.25 (0.44)	-64.44 (0.20)
270 Hz	-88.40 (2.02)	-88.81 (1.92)	-88.68 (0.71)	-90.97 (1.01)	-84.75 (3.26)	-78.83 (0.90)
	Rotor Search-coil					
90 Hz	-20.07 (0.05	-21.00 (0.05)	-14.35 (0.06)	-6.71 (0.05)	-0.69 (0.05)	3.87 (0.06)
150 Hz	-19.70 (0.24)	-24.87 (0.16)	-21.51 (0.15)	-10.50 (0.09)	-2.42 (0.14)	3.36 (0.08)
270 Hz	-32.43 (0.41)	-28.25 (0.19)	-29.04 (0.34)	-20.81 (0.16)	-14.92 (0.39)	-11.14 (0.12)

Table 7.16 Harmonics at half-load (UPF) condition (for standard structure)

	HB	HU	T1	T2	T3	T4
	Field Current					
90 Hz	-69.60 (0.48)	-69.77 (0.42)	-67.59 (0.25)	-65.37 (0.30)	-63.16 (0.19)	-61.78 (0.16)
150 Hz	-72.68 (0.93)	-74.18 (0.75)	-71.32 (0.18)	-68.29 (0.57)	-64.69 (0.23)	-61.94 (0.53)
270 Hz	-84.54 (2.53)	-85.42 (0.38)	-84.31 (1.84)	-87.53 (1.62)	-81.83 (2.03)	-75.59 (0.99)
	Rotor Search-coil					
90 Hz	-21.39 (0.07)	-19.85 (0.11)	-14.44 (0.05)	-6.42 (0.03)	0.01 (0.03)	4.48 (0.17)
150 Hz	-19.35 (0.13)	-23.63 (0.09)	-23.31 (0.10)	-10.11 (0.05)	-1.29 (0.06)	3.68 (0.45)
270 Hz	-35.52 (0.40)	-31.28 (0.11)	-28.69 (0.19)	-20.96 (0.24)	-15.82 (0.29)	-12.13 (0.26)

Table 7.17 Harmonics at full-load (0.8 lagging PF) condition (for standard structure)

	HB	HU	T1	T2	T3	T4
	Field Current					
90 Hz	-71.64 (0.24)	-72.41 (0.42)	-70.58 (0.89)	-69.62 (0.67	-64.40 (0.25)	-61.89 (0.52)
150 Hz	-72.07 (0.70)	-71.52 (1.11)	-71.62 (1.22)	-66.28 (0.44)	-62.30 (0.41)	-58.81 (0.26)
270 Hz	-83.53 (0.59)	-83.65 (1.44)	-84.26 (1.05)	-84.82 (2.67)	-81.02 (2.82)	-79.69 (1.46)
	Rotor Search-coil					
90 Hz	-10.33 (0.15)	-10.76 (0.15	-8.39 (0.20)	-2.93 (0.09	2.58 (0.11)	5.80 (0.05)
150 Hz	-19.28 (0.40)	-22.65 (0.32)	-26.80 (0.48)	-12.28 (0.10)	-2.96 (0.34)	1.81 (0.10)
270 Hz	-24.76 (0.44)	-23.96 (0.60)	-22.87 (0.36)	-14.87 (0.17)	-9.35 (0.57)	-5.69 (0.19)

Table 7.18 Harmonics at full-load (0.8 leading PF) condition (for standard structure)

	HB	HU	T1	T2	T3	T4
	Field Current					
90 Hz	-77.13 (1.03)	-77.40 (1.28)	-73.40 (0.61)	-71.99 (1.03)	-70.14 (0.45)	-68.18 (0.35)
150 Hz	-81.59 (1.25)	-82.11 (2.12)	-82.45 (1.14)	-77.26 (0.92)	-72.27 (0.67)	-70.03 (0.30)
270 Hz	-92.99 (1.57)	-93.79 (1.11)	-92.00 (1.39)	-86.16 (1.51)	-81.67 (0.63)	-79.45 (0.62)
	Rotor Search-coil					
90 Hz	-20.15 (0.20)	-21.33 (0.18)	-14.96 (0.10)	-8.04 (0.32)	-1.47 (0.12)	3.27 (0.14)
150 Hz	-22.57 (0.35)	-29.61 (0.51)	-22.95 (0.23)	-14.53 (0.41)	-6.11 (0.31)	0.11 (0.40)
270 Hz	-27.28 (0.45)	-25.78 (0.46)	-27.29 (0.42)	-24.11 (0.36)	-18.20 (0.58)	-13.65 (0.43)

Table 7.19 Harmonics at full-load (UPF) condition (for standard structure)

	HB	HU	T1	T2	T3	T4
	Field Current					
90 Hz	-72.69 (0.87)	-74.77 (0.81)	-70.09 (0.68)	-67.54 (0.25)	-64.96 (0.30)	-64.43 (0.43)
150 Hz	-78.27 (0.82)	-78.75 (0.85)	-73.56 (0.50)	-69.18 (0.27)	-65.19 (0.15)	-63.74 (0.71)
270 Hz	-89.06 (2.63)	-89.22 (1.49)	-88.61 (2.21)	-87.93 (2.00)	-81.90 (1.10)	-76.88 (1.16)
	Rotor Search-coil					
90 Hz	-18.80 (0.11)	-16.55 (0.07)	-13.59 (0.05)	-6.21 (0.10)	0.27 (0.08)	4.58 (0.30)
150 Hz	-22.21 (0.08)	-28.33 (0.33)	-24.42 (0.10)	-12.52 (0.14)	-3.58 (0.15)	1.52 (0.62)
270 Hz	-30.52 (0.36)	-26.10 (0.57)	-26.97 (0.20)	-20.36 (0.19)	-14.53 (0.46)	-10.20 (0.23)

7.5 Discussions on Results and Contributions

In this chapter, a novel scheme for detecting the stator inter-turn faults in SM with DC excitation has been proposed. Theory has been validated using necessary mathematical proofs, simulations and experiments. This scheme has been successfully implemented on the synchronous machines with both two-coil and standard field windings. From the results, it can be inferred that in both structures of the field windings the detectability of stator inter-turn faults is almost the same. The internal asymmetry of the machine that has adversely affected the earlier fault diagnosis results has now been used to an advantage for the first time. The results have also been validated using the voltage induced in the rotor-mounted search-coil. Using the rotor-mounted search-coil, even one-turn faults can be effectively detected. The supply unbalance and time harmonics seems to have minimal influence on the test results. Thus, monitoring of such frequency components in the rotor circuit of any

salient-pole synchronous machine with DC excitation can thoroughly detect the stator inter-turn faults in these machines. However, for synchronous motors without a rotor search-coil, other techniques have to be used.

Chapter 8

DSP-Based Fault Detection of Line and Inverter-fed SM with DC Excitation

The rapid advancement of semiconductor technology and availability of digital signal processors (DSP) has opened a new horizon in the area of electric drives. The recent trend has been to add fault diagnostic capability to these drives. Some researchers have attempted to use the computational capabilities of this processor to implement the fault diagnosis of the machines as mentioned in Chapter 1 of this thesis. In this chapter, using a DSP, a scheme has been proposed to detect stator inter-turn faults in the utility or inverter driven SM. An algorithm has been written that can perform Discrete Fourier Transform (DFT) using a DSP to monitor a particular harmonic component in the rotor search-coil voltage while the supply frequency changes in the variable speed drive. Also all the necessary hardware has been built to generate a trip signal and disconnect the machine in the event of a fault. Such a fault detector can play a very vital role in preventing fire hazards, explosion, potential loss of property and human life rather than saving the machine itself.

The following are the challenges in implementing DSP based fault diagnosis of the electric machine used in an inverter-fed variable speed drive:

- Limited memory space
- Time shared operation of DSP
- Relatively larger number of computations to implement DFT
- Changing supply frequency and
- Extremely noisy environment.

In order to overcome the above challenges, a scheme has been proposed to implement DFT using a DSP and to detect stator inter-turn faults in the machines.

8.1 Scheme for DSP-based Fault Detection of Line and Inverter-fed SM with DC excitation

A very innovative technique has been evolved in order to avoid the long computation time involved with DFT. This method has been found to be very useful since the DSP has a limited memory and the processor operates in a time-shared mode. A schematic block-diagram of the fault detection scheme has been given in Figure 8.1. The following is a detailed description of the functionalities of the scheme.

8.1.1. Signals for Detecting Stator Inter-turn Faults

The rotor search-coil voltage has been analyzed to detect stator inter-turn faults in the machine. The line current has been used to track the changing supply frequency. The rotor search-coil voltage to obtain the fault signature and the line current signal to obtain frequency information are suitably translated using simple electronics interface and are supplied to the DSP.

8.1.2. Implementing DFT on Rotor Search-coil Voltage

The DSP receives the signals from the electronic interface and does the necessary DFT computations for detecting the stator faults.

8.1.3. Generating a Trip Signal

Once the predicted harmonic level exceeds a certain preset limit, the DSP generates a trip signal to activate the relay that opens a contactor to disconnect the machine from the service.

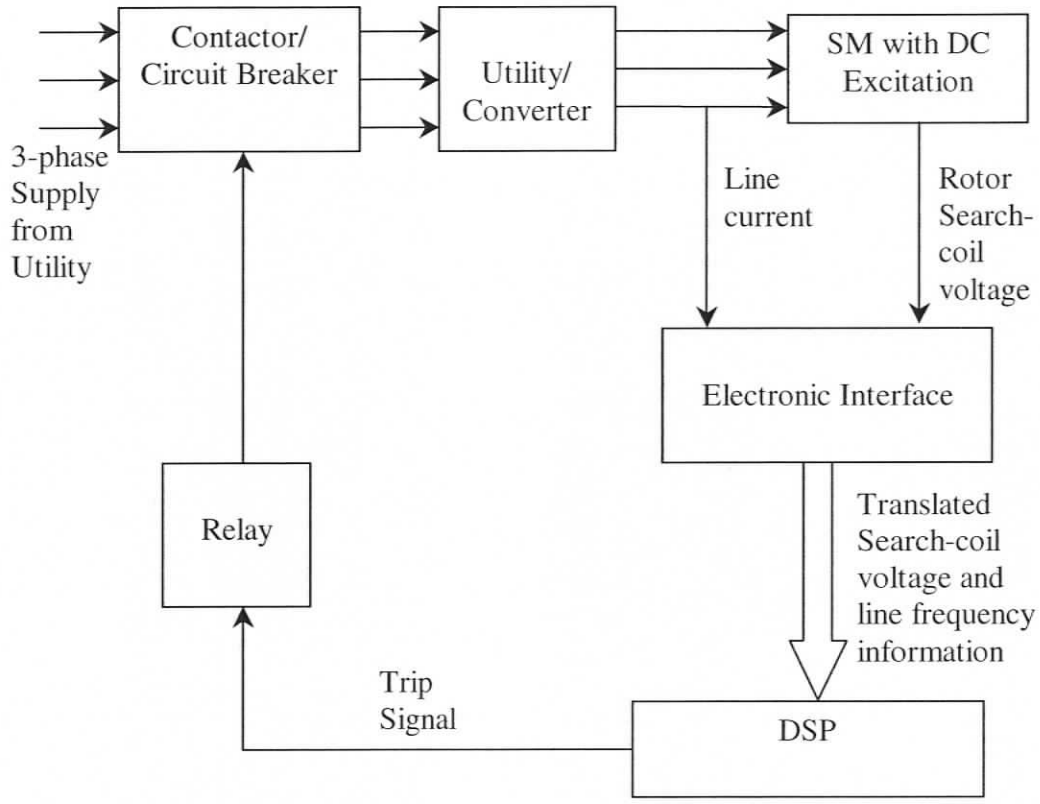

Figure 8.1 Block-diagram of the DSP-based fault detection scheme for the variable speed drive with SM with DC excitation

8.2 Performance of the DSP-based Fault Detection Scheme

The performance of the fault detection scheme has been tested in the case of an inverter-fed SM supplied at 60Hz. The DSP-based fault detection scheme could detect the stator inter-turn faults very quickly and disconnect the machine from the service. The typical time of operation of the DSP-based fault detection scheme under different number of shorted turns (T1-T5) has been shown in Figure 8.2. The

variation in fault clearance time is due to the detection algorithm that takes a decision depending upon the average of several readings. This is to avoid false tripping. The maximum time taken to generate a trip signal under any severity of fault is 2.15 seconds. This is deemed sufficient to prevent any fire hazard and explosion that can typically follow a stator fault. The trip signal has been monitored without contactor operation as shown in Figure 8.3. In order to thoroughly validate the scheme, tests have been conducted at different supply conditions of SM. Various signals (line voltage, line current, field current, trip signal and the voltage across the shorted turns) in each case of line-fed, inverter-fed (60Hz operation) and inverter-fed (30Hz operation) have been shown in Figure 8.4 to Figure 8.6 respectively for a 1-turn fault. The voltage across the shorted turn is reduced to zero at the instant of initiation of the fault. After detecting the fault, the trip signal is made and held low by the DSP that opens the contactor and disconnects the machine from the supply shown in Figure 8.4 to Figure 8.6. Further, diagnostic tool has been repeatedly tested under no-load 0.8 power factor (lead) at 60Hz operation. The diagnostic tool could successfully trip the machine for ten out of ten times in the event of 1-turn fault. The plots from Figure 8.3 to Figure 8.6 have been obtained using a data acquisition system.

8.3 Discussions on Results and Contributions

A very fast and effective instrument has been designed and built to detect stator inter-turn faults in the SM with DC excitation. Predicted harmonic components in the rotor search-coil voltage have been shown to work very well for detecting these faults using a DSP. With this instrument the harmonic components can be tracked even under changing supply frequency in the case of variable speed drives. More details on the device cannot be reported at this time due to the potential conflict with patent disclosure issues.

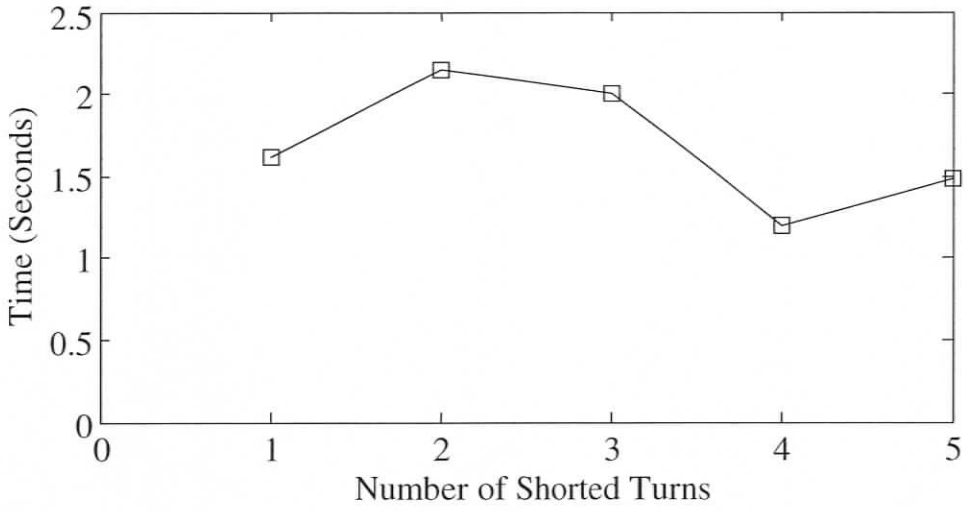

Figure 8.2 Typical time of operation of the DSP-based fault detection scheme for the inverter-fed SM

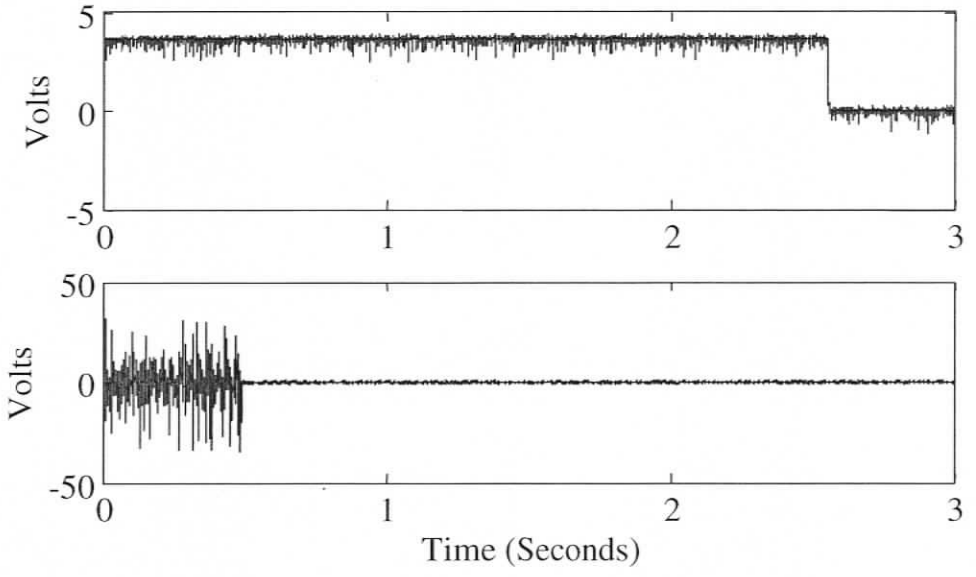

Figure 8.3 Initiation of trip signal after a fault (without contactor operation)

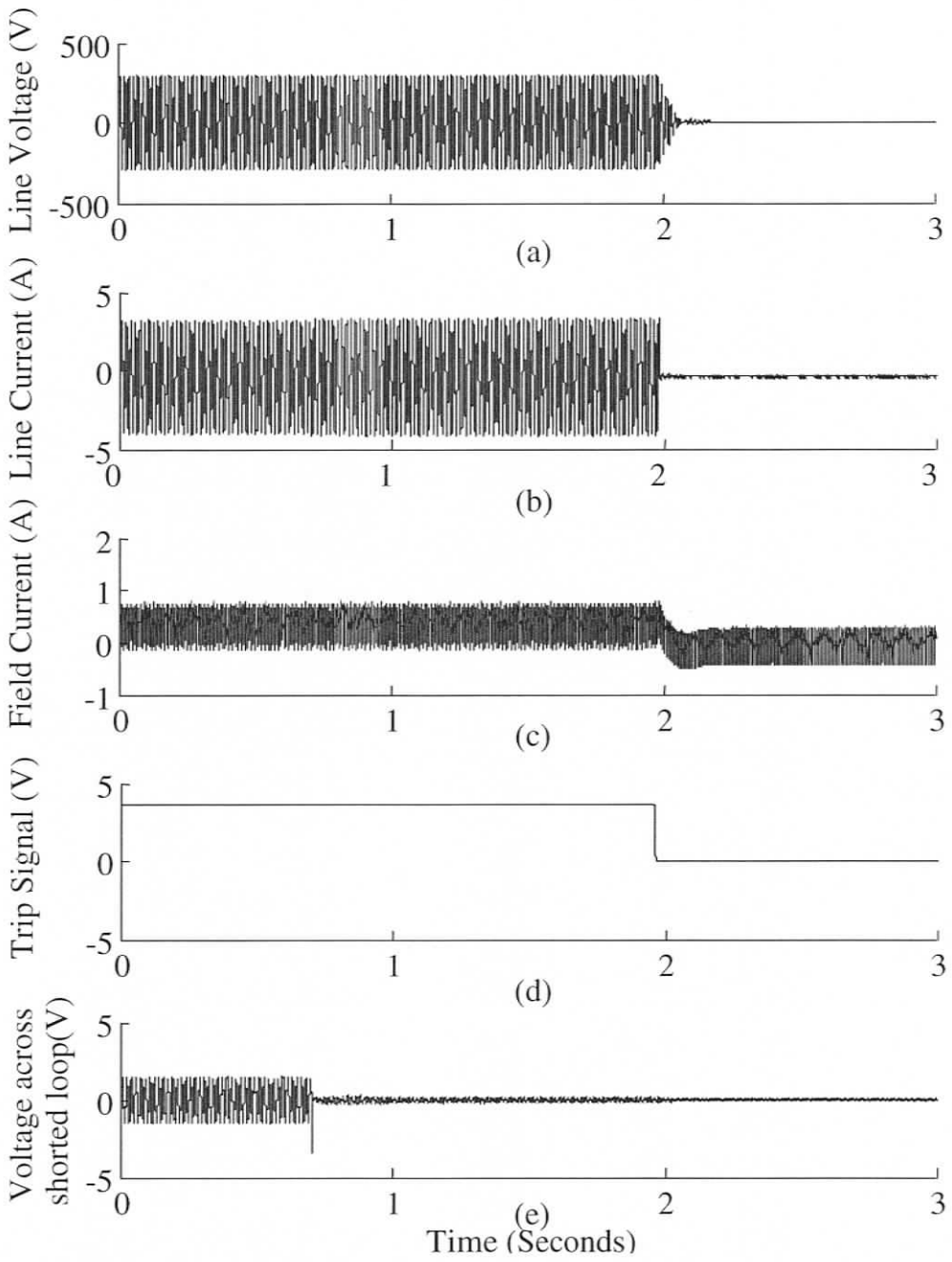

Figure 8.4 Various signals of the fault detection scheme for the line-fed SM for a single turn fault, a) line voltage, b) line current, c) field current, d) trip signal and e) voltage across the shorted turn

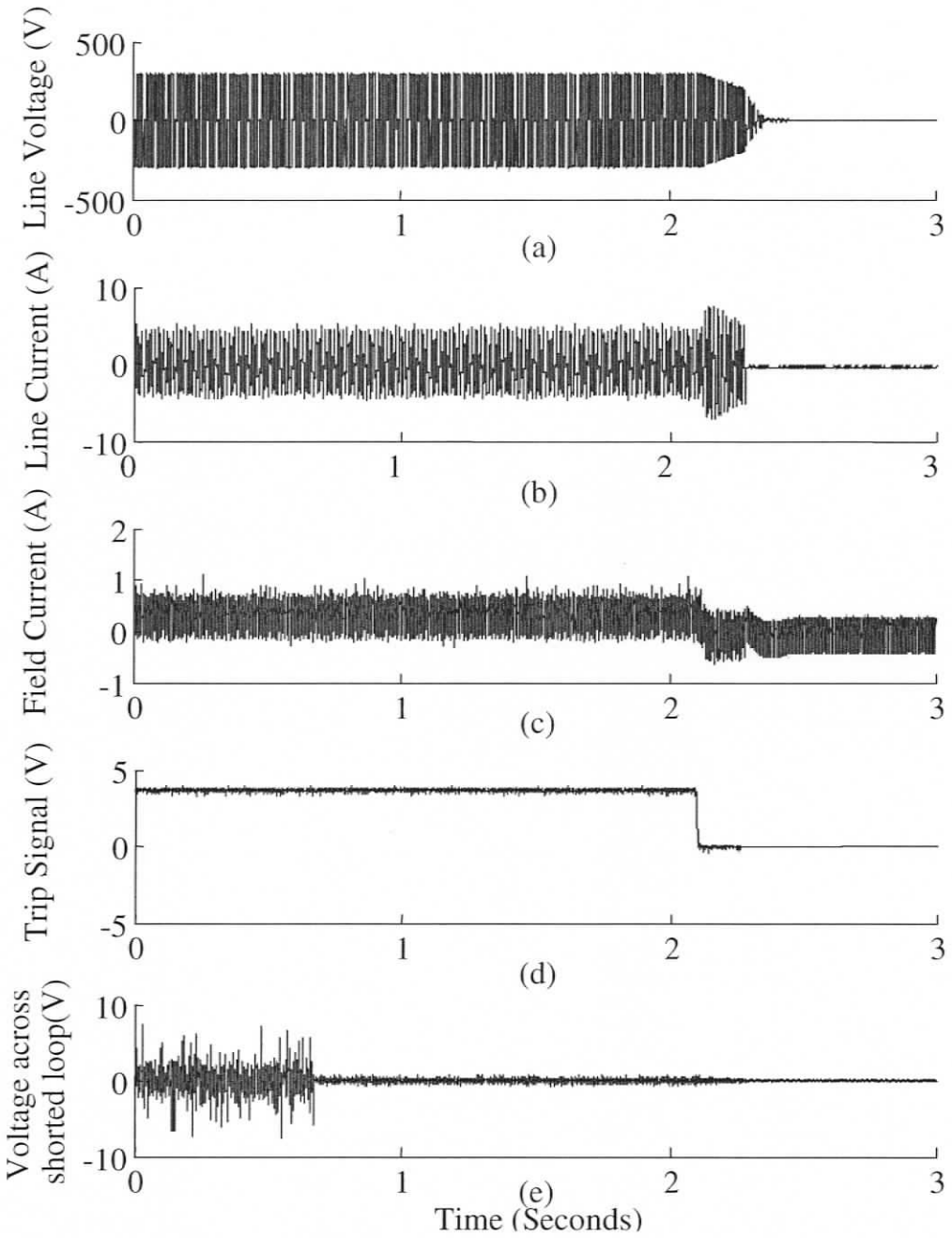

Figure 8.5 Various signals of the fault detection scheme for the inverter-fed SM (operated at 60Hz) for a single turn fault, a) line voltage, b) line current, c) field current, d) trip signal and e) voltage across the shorted turn

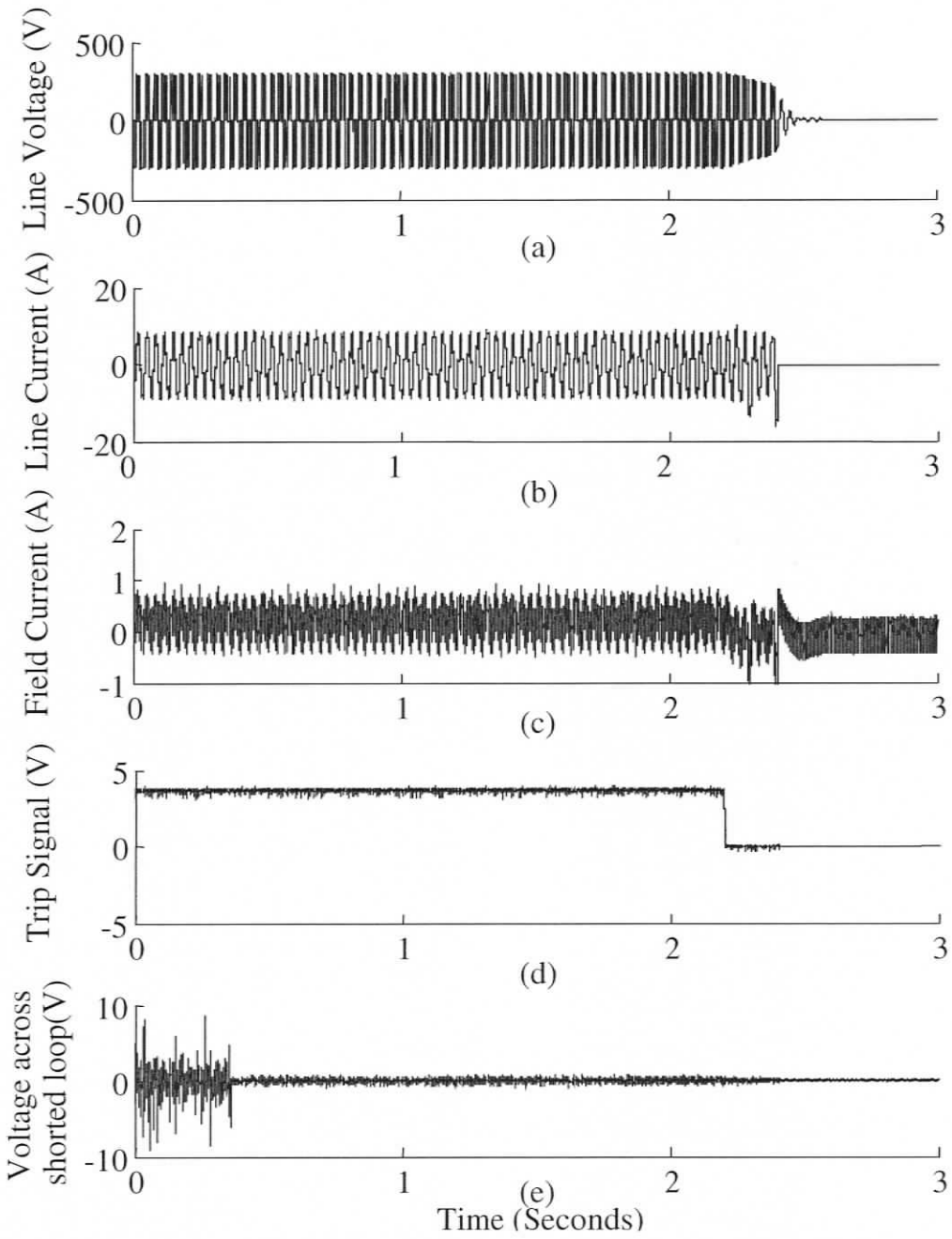

Figure 8.6 Various signals of the fault detection scheme for the inverter-fed SM (operated at 30Hz) for a single turn fault, a) line voltage, b) line current, c) field current, d) trip signal and e) voltage across the shorted turn

Chapter 9

Conclusions and Future Scope

9.1 Conclusions

In this work, the condition monitoring of synchronous machines has been addressed against stator inter-turn faults. Different diagnostic schemes have been proposed and analyzed to detect these faults involving few turns, in both reluctance synchronous machines and synchronous machines with DC excitation. Detailed analysis of each scheme has been put forward including the influence of supply unbalance, time harmonics and internal asymmetry of the machines on the diagnosis results.

For each diagnostic scheme, necessary theory has been developed such as explanation of the origin of various spectral components in the voltage and/or current signals that can be used for detecting faults.

Coupled circuit approach has been adopted for the modeling of synchronous machines under healthy, asymmetric and stator inter-turn fault conditions. Various inductances of the machines have been computed using WFA and MWFA. Further, most of these inductances have been verified using the finite element analysis.

Rigorous experimental study has been carried out which involves testing the machines under healthy, stator inter-turn fault and abnormal operating conditions. In order to carry out experimental study under faulty condition, specially rewound synchronous machines have been used to create inter-turn faults. For RSM, a comparison of the merits and demerits of various diagnostic schemes has been summarized in Table 9.1. A similar comparison in the case of SM with DC excitation has been put forward in Table 9.2.

Table 9.1 Comparison of various diagnostic schemes for RSM

	Triplen harmonics in the terminal voltage after switch-off	Negative sequence current (Using K_1 and K_2)	
		At no-load condition	At full-load condition
Sensitivity	1-Turn fault	3-Turn fault	2-Turn fault
Effect of supply unbalance	Nil	Minimal	Minimal
Effect of time harmonics	Minimal	Minimal	Minimal
Effect of internal asymmetry	Minimal	Minimal	Minimal
No. of sensors	3	6	6
Applications	RSM used in elevators, hoists etc., validation of other online schemes	Any	Any

Table 9.2 Comparison of various diagnostic schemes for SM with DC excitation

	Harmonics in field current	Harmonics in rotor search-coil voltage	Negative sequence current (Using K_0, K_1 and K_2)	
			At no-load condition	Other than no-load condition
Sensitivity	3-Turn fault	1-Turn fault	4-Turn fault	2-Turn fault
Effect of supply unbalance	Minimal	Minimal	Minimal	Minimal
Effect of time harmonics	Minimal	Minimal	Minimal	Minimal
Effect of internal asymmetry	Minimal	Minimal	Minimal	Minimal
No. of sensors	1	1	6	6
Applications	Any	Any	Any	Any

Also, an instrument has been built that uses the computational capabilities of the DSP board to generate a trip signal in the event of a stator inter-turn fault. Necessary software as well as hardware have been developed and tested. The fault detector has very high sensitivity and speed to detect the faults involving even one shorted turn within 2 seconds. This instrument can tack the harmonic components even in the case of variable speed drives by sensing the changing frequency. Hence this scheme can facilitate incorporation of in-built fault diagnostic feature in the DSP based synchronous drives.

However, the fault detectability of these diagnostic schemes has not been tested by changing the location of the fault inside the machine.

9.2 Contributions

As a first step towards the goals of this thesis, it has been shown that the effective negative sequence impedance of the synchronous machines is sensitive to the changing supply unbalance that can lead to a serious ambiguity in the fault detection. Further, critical modifications have been suggested for the improved detection of stator inter-turn faults using negative sequence current, particularly under changing supply unbalance. However, the modified method failed to detect the faults involving few turns. Hence, there was a need to investigate the other techniques based on frequency domain analysis.

In this work, in order to perform fault analysis in the frequency domain, detailed models of RSM and SM with DC excitation have been obtained under symmetric, asymmetric and stator inter-turn fault conditions. The effects of the damper bars have also been included in these models. A new method has been proposed for the determination of the effective air-gap lengths of the synchronous machines along their direct and quadrature axes. Also, generalized expressions have been derived to theoretically compute the direct and the quadrature axes inductances of the machines

for any higher space and permeance related harmonics. It has also been proposed to stabilize the models of the synchronous machines under full-load condition by reducing the rotor pole-arc.

Theoretical proofs have been provided to explain the presence of different spectral lines in various currents and voltages of synchronous machines under healthy, asymmetric, stator inter-turn fault and various other abnormal operating conditions.

It has been established that triplen harmonics in the line currents of synchronous machines cannot be good indicators of stator inter-turn faults.

A scheme, based on the stored magnetic energy of the machine after switch-off, has been implemented to detect stator inter-turn faults in RSM. This is shown to be sensitive enough to detect even a 1-turn fault. Thus an improved scheme has been proposed to detect these faults in RSM that uses the stored magnetic energy after switch-off to validate the trip signal generated by the modified scheme based on negative sequence quantities. In this case the machine can be put back into service without losing much time and manpower in the event of a false positive.

A feasibility analysis on various frequency components in the field current has been conducted to detect faults in SM with DC excitation. A new scheme, based on field current analysis, has been proposed to detect stator inter-turn faults in the synchronous machines with DC excitation that uses the structural asymmetries of the field winding. Another scheme, based on the analysis of rotor search-coil voltage, has also been proposed to detect stator inter-turn faults in the synchronous machines with DC excitation. Even a single turn fault can be detected using rotor search-coil voltage.

An instrument has been built to detect the stator inter-turn faults with high sensitivity and speed that uses the computational capabilities of DSP. Necessary software and hardware have been developed and tested. The instrument has the capability to track the predicted harmonic component even under changing supply

frequency in the case of variable speed drives. This scheme can be easily implemented in the existing DSP-based synchronous machine drives.

9.3 Future scope

Based on the results furnished in this thesis, it can be inferred that further improvement of fault diagnostic schemes is required for the online detection of one-turn faults in the RSM under steady-state condition. The diagnostic schemes similar to the ones based on the field current analysis and rotor search-coil voltage analysis can be implemented for slip-ring induction machines since their rotor circuit can be accessed. The improvements suggested for the negative sequence current detectors could be implemented on other AC machines such as squirrel cage and slip-ring induction machines. Also a prototype can be devised to incorporate the inherent fault diagnosis capability in other types of DSP based electric drives.

Bibliography

[1] G. B. Kliman, W. J. Premerlani, R. A. Koegl, and D. Hoeweler, "A new approach to on-line turn fault detection in AC motors," *IEEE Industry Applications Society Annual Meeting Conference*, vol. 1, pp. 687-693, Oct. 1996.

[2] M. Hajiaghajani, H. A. Toliyat and I. M. S. Panahi, "Advanced fault diagnosis of a DC motor," *IEEE Transactions on Energy Conversion*, vol. 19, no. 1, pp. 60-65, Mar. 2004.

[3] M. Hajiaghajani, Lei Hao, S. M. Madani and H. A. Toliyat, "A method for detection of eccentricity in permanent magnet machines," *IEEE Industry Applications Society Annual Meeting Conference*, vol. 3, pp. 1833-1838, Oct. 2003.

[4] S. Nandi, H. A. Toliyat and X. Li, "Condition monitoring and fault diagnosis of electrical motors - a review," *IEEE Transactions on Energy Conversion*, vol. 20, no. 4, pp. 719-729, Dec. 2005.

[5] R. M. Tallam, S. B. Lee, G. Stone, G. B. Kliman, J. Yoo, T. G. Habetler and R. G. Harley, "A survey of methods for detection of stator related faults in induction machines," *4th IEEE International Symposium on Diagnostics for Electric Machines, Power Electronics and Drives*, pp. 35 – 46, Aug. 2003.

[6] M. E. H. Benbouzid, "A review of induction motors signature analysis as a medium for faults detection," *IEEE Transactions on Industrial Electronics*, vol. 47, no. 5, pp. 984-993, Oct. 2000.

[7] P. J. Tavner and J. Penman, *Condition Monitoring of Electrical Machines*, Letchworth, U.K.: Res. Studies Press, 1987.

[8] A. H. Bonnett, "Available insulation systems for PWM inverter-fed motors", *IEEE Industry Applications Magazine*, vol. 4, no. 1, pp.14-26, Jan./Feb. 1998.

[9] IEEE Standard 522-2004, "IEEE guide for testing turn insulation of form-wound stator coils of alternating-current electric machines," 2004.

[10] G. Stone and J. Kapler, "Stator winding monitoring," *IEEE Industry Applications Magazine*, vol. 4, no. 5, pp. 15-20, Sep./Oct. 1998.

[11] J. L. Kohler, J. Sottile and F. C. Trutt, "Alternatives for assessing the electrical integrity of induction motors", *IEEE Transactions on Industry Applications*, vol. 28, no. 5, pp.1109-1117, Sept./Oct. 1992.

[12] J. L. Kohler, J. Sottile and F. C. Trutt, "Condition monitoring of stator windings in induction motors. I. Experimental investigation of the effective negative-sequence impedance detector," *IEEE Transactions on Industry Applications*, vol. 38, no. 5, pp. 1447-1453, Sept./Oct. 2002.

[13] J. Sottile, F. C. Trutt and J. L. Kohler, "Condition monitoring of stator windings in induction motors. II. Experimental investigation of voltage mismatch detectors," *IEEE Transactions on Industry Applications*, vol. 38, no. 5, pp. 1454-1459, Sept./Oct. 2002.

[14] R. M. Tallam, T. G. Habetler and R. G. Harley, "Transient model for induction machines with stator winding turn faults," *IEEE Transactions on Industry Applications*, vol. 38, no.3, pp. 632-637, May/June 2002.

[15] M. Arkan, D. K. Perovic, and P. Unsworth, "Online stator fault diagnosis in induction motors," *IEE Proceedings on Electric Power Applications*, vol. 148, no. 6, pp. 537-547, Nov. 2001.

[16] Sang Bin Lee, R. M. Tallam and T. G. Habetler, "A robust, on-line turn-fault detection technique for induction machines based on monitoring the sequence component impedance matrix," *IEEE Transactions on Industry Applications*, vol. 18, no.3, pp. 865-872, May 2003.

[17] G. M. Joksimovic, and J. Penman, "The detection of inter-turn short circuits in the stator windings of operating motors," *IEEE Transactions on Industrial Electronics*, vol. 47, no.5, pp. 1078-1084, Oct. 2000.

[18] M. E. H. Benbouzid, M. Vieira, and C. Theys, "Induction motors' faults detection and localization using stator current advanced signal processing techniques," *IEEE Transactions on Power Electronics*, vol. 14, no. 1, pp.14-22, Jan. 1999.

[19] S. M. A. Cruz and A. J. M. Cardoso, "Stator winding fault diagnosis in three-phase synchronous and asynchronous motors, by the extended Park's vector approach," *IEEE Transactions on Industry Applications*, vol. 37, no.5, pp. 1227-1233, Sept./Oct. 2001.

[20] R. M. Tallam, T. G. Habetler, R. G. Harley, D. J. Gritter and B. H. Burton, "Neural network based on-line stator winding turn fault detection for induction

motors," *IEEE Industry Applications Society Annual Meeting Conference*, vol. 1, pp. 375-380, Oct. 2000.

[21] T. Liu and J. Huang, "A Novel Method for Induction Motors Stator Interturn Short Circuit Fault Diagnosis by Wavelet Packet Analysis," *Proceedings of 8th International Conference on Electrical Machines and Systems*, vol. 3, pp. 2254-2258, Sept. 2005.

[22] J. Penman, H. G. Sedding, B. A. Lloyd, and W. T. Fink, "Detection and location of interturn short circuits in the stator windings of operating motors," *IEEE Transactions on Energy Conversion*, vol. 9, no. 4, pp. 652-658, Dec. 1994.

[23] H. Henao, C. Demian, and G. A. Capolino, "A frequency-domain detection of stator winding faults in induction machines using an external flux sensor," *IEEE Transactions on Industry Applications*, vol. 39, no. 5, pp. 1272-1279, Sep./Oct. 2003.

[24] M. A. Cash, T. G. Habetler and G. B.Kliman, "Insulation failure prediction in AC machines using line-neutral voltages," *IEEE Transactions on Industry Applications*, vol. 34, no.6, pp. 1234-1239, Nov./Dec. 1998.

[25] S. Nandi and H. A. Toliyat, "Novel frequency-domain-based technique to detect stator interturn faults in induction machines using stator-induced voltages after switch-off," *IEEE Transactions on Industry Applications*, vol. 38, no.1, pp. 101-109, Jan./Feb. 2002.

[26] J. S. Hsu (Htsui) and J. Stein, "Shaft signals of salient-pole synchronous machines for eccentricity and shorted-field-coil detections," *IEEE Transactions on Energy Conversion*, vol. 9, no. 3, pp. 572-578, Sept. 1994.

[27] D. W. Auckland, I. E. D. Pickup, R. Shuttleworth, Y. T. Wu and C. Zhou, "Novel approach to alternator field winding interturn fault detection," *IEE Proceedings on Generation, Transmission and Distribution*, Volume 142, Issue 2, pp. 97 – 102, March 1995.

[28] R. J. Streifel, R. J. Marks II, M.A. El-Sharkawi, and I. Kerszenbaum, "Detection of shorted-turns in the field winding of turbine-generator rotors using novelty detectors - development and field test," *IEEE Transactions on Energy Conversion*, vol. 11, no. 2, pp. 312-317, June 1996.

[29] S. Wan, H. Li, Y. Li and Y. Wang, "The diagnosis method of generator rotor winding inter-turn short circuit fault based on excitation current harmonics,"

IEEE International Conference on Power Electronics and Drive Systems, vol. 2, pp. 1669-1673, Nov. 2003.

[30] X. H. Wang, Y.G. Sun, B. Ouyang, W. J. Wang, Z.Q. Zhu and D. Howe, "Transient behavior of salient-pole synchronous machines with internal stator winding faults," *IEE Proceedings on Electric Power Applications*, vol. 149, no.2, pp. 143-151, Mar. 2002.

[31] J. Sottile, F. C. Trutt and A.W. Leedy, "Condition monitoring of brushless three-phase synchronous generators with stator winding or rotor circuit deterioration," *IEEE Industry Applications Society Annual Meeting Conference*, vol. 3, pp. 1587-1594, Sept./Oct. 2001.

[32] J. Penman and H. Jiang, "The detection of stator and rotor winding short circuits in synchronous generators by analysing excitation current harmonics," *International Conference on Opportunities and Advances in International Electric Power Generation*, Conf. Publ. no. 419, pp.137-142, March 1996.

[33] F. C. Trutt, J. Sottile and J. L. Kohler,, "Detection of AC machine winding deterioration using electrically excited vibrations", *IEEE Transactions on Industry Applications*, vol. 37, no. 1, pp.10-14, Jan./Feb. 2001.

[34] F. Briz, M. W. Degner, A. Zamarron, and J. M. Guerrero, "Online stator winding fault diagnosis in inverter-fed AC machines using high-frequency signal injection," *IEEE Transactions on Industry Applications*, vol. 39, no. 4, pp. 1109-1117, Jul./Aug. 2003.

[35] Y. Lee and T.G. Habetler, "A Phase Variable Simulation Model for Interior PM Synchronous Motor Drives with Stator Turn Faults," *12th IEEE International Power Electronics and Motion Control Conference*, pp.1074 – 1079, Aug. 2006.

[36] S. M. A. Cruz and A. J. M. Cardoso, "Diagnosis of stator inter-turn short circuits in DTC induction motor drives," *IEEE Transactions on Industry Applications*, vol. 40, no. 5, pp. 1349-1360, Sep./Oct. 2004.

[37] S. M. A. Cruz, H. A. Toliyat and A. J. M. Cardoso, "DSP implementation of the multiple reference frames theory for the diagnosis of stator faults in a DTC induction motor drive," *IEEE Transactions on Energy Conversion*, vol. 20, no. 2, pp. 329-335, June 2005.

[38] Y. Lee and T.G. Habetler, "A Stator Turn Fault Tolerant Strategy for Induction Motor Drives in Safety Critical Applications," *37th IEEE Power Electronics Specialists Conference,* pp.1 – 7, June 2006.

[39] A. Vagati, "The synchronous reluctance solution: a new alternative in ac drives," *Industrial Electronics, Control and Instrumentation, IECON*, vol. 1, pp. 1-13, Sept. 1994.

[40] W. D. Stevenson, Jr., "*Elements of Power System Analysis*", McGraw-Hill, New York, 1955.

[41] O. I. Elgerd, "*Electric Energy Systems Theory: An Introduction*", McGraw-Hill, New York, 1971.

[42] J. Faiz, H. Ebrahimpour, and P. Pillay, "Influence of unbalanced voltage on the steady-state performance of a three-phase squirrel-cage induction motor," *IEEE Transactions on Energy Conversion*, vol. 19, no. 4, pp. 657–662, Dec. 2004.

[43] A. F. Puchstein and T. C. Lloyd, *Alternating-current machines*, John Wiley: New York, 1936.

[44] P. L. Alger, *The nature of induction machines*, Gordon and Breach: New York, 1965.

[45] A. S. Langsdorf, *Theory of alternating current machines*, 2nd edition, Mc Graw Hill-Kogakusha: Tokyo, 1955.

[46] X. Luo, Y. Liao, H. A. Toliyat, A. El-Antably and T. A. Lipo, "Multiple coupled circuit modeling of induction machines," *IEEE Transactions on Industry Applications*, vol. 31, no.2, pp. 311-318, Mar./Apr. 1995.

[47] H. A. Toliyat and T. A. Lipo, "Transient analysis of cage induction machines under stator, rotor bar and end ring faults," *IEEE Transactions on Energy Conversion*, vol. 10, no.2, pp. 241-247, Jun. 1995.

[48] H. A. Toliyat, M. S. Arefeen and A. G. Parlos, "A method for dynamic simulation of air-gap eccentricity in induction machines," *IEEE Transactions on Industry Applications*, vol. 32, no.4, pp. 910-918, Jul./Aug. 1996.

[49] N. A. Al-Nuaim and H. A. Toliyat, "A novel method for modeling dynamic air-gap eccentricity in synchronous machines based on modified winding function theory," *IEEE Transactions on Energy Conversion*, vol. 13, no.2, pp. 156-162, Jun. 1998.

[50] S. Nandi, R. M. Bharadwaj and H. A. Toliyat, "Mixed eccentricity in three phase induction machines: analysis, simulation and experiments," *Proceeding of IEEE Industry Applications Society Annual Meeting Conference*, vol. 3, pp. 1525-1532, Oct. 2002.

[51] D. A. Staton, W. L. Soong and T. J. E. Miller, "Unified theory of torque production in switched reluctance and synchronous reluctance motors," *IEEE Transactions on Industry Applications*, vol. 31, no.2, pp. 329-337, March/April 1995.

[52] T. J. E. Miller, A. Hutton, C. Cossar and D. A. Staton, "Design of synchronous reluctance motor drive," *IEEE Transactions on Industry Applications*, vol. 27, no.4, pp. 741-749, Jul./Aug. 1991.

[53] A. A. Fock and P. M. Hart, "New methods for measuring xd and xq based on p-q diagram of the lossy salient-pole machine," *IEE proceedings*, vol. 131, pp. 259-262, Nov. 1984.

[54] P. Y. P. Wung and H. B. Puttgen, "Synchronous reluctance motor operating point dependent parameter determination," *IEEE Transactions on Industry Applications*, vol. 28, no.2, pp. 358-363, Mar./Apr. 1992.

[55] A.Chiba, F. Nakamura, T. Fukao and M. A. Rahman, "Inductances of cageless reluctance- synchronous machines having nonsinusoidal space distributions," *IEEE Transactions on Industry Applications*, vol. 27, no.1, pp. 44-51, Jan./Feb. 1991.

[56] A. E. Fitzgerald, C. Kingsley, Jr. and S. D. Umans, *Electric machinery*, McGraw hill: New York, 1990.

[57] M.G. Say, *Alternating current machines*, Pitman: London, 1983.

[58] D. A. Staton, T. J. E. Miller and S. E. Wood, "Maximising the saliency ratio of the synchronous reluctance motor," *IEE Proceedings on Electric Power Applications*, vol. 140, no.4, pp. 249-259, July 1993.

[59] W. Leonhard, *Control of electrical drives*, Springer-Verlag: Berlin, 2001.

[60] P. C. Sen, *Principles of electric machines and power electronics*. John wiley & sons, 2nd ed., New York, 1997.

[61] G. B. Kliman, R. A. Koegl, J. Stein, R. D. Endicott and M. W. Madden, "Noninvasive detection of broken rotor bars in operating induction motors," *IEEE Transactions on Energy Conversion*, vol. 3, no.4, pp. 873-879, Dec. 1988.

[62] J. Milimonfared, H. M. Kelk, S. Nandi, A. D. Minassians and H. A. Toliyat, "A novel approach for broken-rotor-bar detection in cage induction motors," *IEEE*

Transactions on Industry Applications, vol. 35, no.5, pp. 1000-1006, Sept./Oct. 1999.

[63] G. Kron, *Equivalent circuits of electric machinery*, Wiley New York, 1951.

[64] S. Nandi, "Detection of stator faults in induction machines using residual saturation harmonics," *IEEE Transactions on Industry Applications*, vol. 42, no.5, pp. 1201-1208, Sept./Oct. 2006.

Appendix A

Details of RSM

The details of the RSM under consideration are as follows:

End-ring leakage inductance = 2.69E-08 H

End-ring resistance = 5.35E-06 Ohm

Frequency = 60Hz

Moment of inertia of the rotor = 0.00651 kg-m^2

Number of phases = 3

Number of poles = 4

Number of rotor bars = 24 (6 bars per pole)

Number of stator slots = 36

Rated power = 1.5 hp

Rotor bar leakage inductance = 0.168E-06 H

Rotor bar resistance = 100E-06 Ohm

Rotor outer diameter = 92.716 mm

Speed = 1800 rpm

Stack length = 114.055 mm

Stator inner diameter = 93.50 mm

Number of shorted turns per phase = 1 to 10

Number of turns per phase = 282

Stator leakage inductance = 0.0472 H/phase

Stator resistance = 3.4 Ohm/phase

Stator voltage = 460V

Type of stator winding = Single layer, concentric

θ_d = 0.9833 Radian (before reduction of pole arc)

θ_q = 0.5875 Radian (before reduction of pole arc)

θ_d = 0.8653 Radian (after reduction of pole arc)

θ_q = 0.7055 Radian (after reduction of pole arc)

Details of Synchronous Machine with DC excitation

The details of the synchronous motor under consideration are as follows:

End-ring leakage inductance = 0.175e-07 H

End-ring resistance = 4.531e-07 Ohm

Field winding resistance = 81 Ohm

Field winding inductance = 6 H

Frequency = 60Hz

Moment of inertia of the rotor = 0.05 kg-m^2

Number of phases = 3

Number of poles = 4

Number of rotor bars = 20 (5 bars per pole)

Number of stator slots = 36

Rated power = 2 kW

Rotor bar leakage inductance = 0.34e-07 H

Rotor bar resistance = 58.27e-07 Ohm

Rotor outer diameter = 146.8 mm

Speed = 1800 rpm

Stack length = 76 mm

Stator inner diameter = 148 mm

Number of shorted turns per phase = 1 to 10

Number of turns per phase = 312

Stator leakage inductance = 0.0079 H/phase

Stator resistance = 0.6 Ohm/phase

Stator voltage = 208V

Type of stator winding = Double layer, lap

θ_d = 1.1652 Radian (before reduction of pole arc)

θ_q = 0.4056 Radian (before reduction of pole arc)

θ_d = 0.6652 Radian (after reduction of pole arc)

θ_q = 0.9056 Radian (after reduction of pole arc)

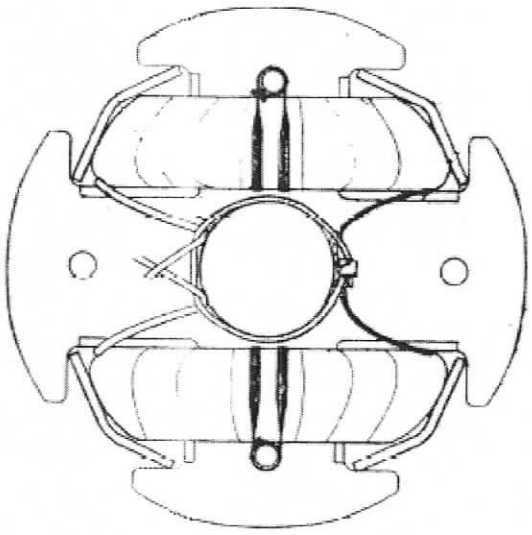

Figure A.1 Cross-section of the rotor of SM with two-coil field winding

Appendix B

Sample Calculation of $\tilde{K}_1$ and $\tilde{K}_2$

Let

$$\alpha = \cos\left[\frac{2\pi}{3}\right] + j\sin\left[\frac{2\pi}{3}\right] = -0.5000 + j0.8660$$

$$\alpha^2 = \cos\left[-\frac{2\pi}{3}\right] + j\sin\left[-\frac{2\pi}{3}\right] = -0.5000 - j0.8660$$

$$\alpha_{+30} = \cos\left[\frac{\pi}{6}\right] + j\sin\left[\frac{\pi}{6}\right] = 0.8660 + j0.5000$$

$$\alpha_{-30} = \cos\left[-\frac{\pi}{6}\right] + j\sin\left[-\frac{\pi}{6}\right] = 0.8660 - j0.5000$$

$$T = \begin{bmatrix} 1 & 1 & 1 \\ 1 & \alpha & \alpha^2 \\ 1 & \alpha^2 & \alpha \end{bmatrix}$$

From the terminal measurement of the machine, we can read the magnitudes of the three line voltages as given below:

$$\left|\tilde{V}_{AB}\right| = 208.0929\text{V},\ \left|\tilde{V}_{BC}\right| = 211.2273\text{V},\ \left|\tilde{V}_{CA}\right| = 209.5628\text{V}$$

The phase angles of the line voltages can be obtained as [40]

$$\phi_{Av} = \cos^{-1}\left[\frac{\left|\tilde{V}_{BC}\right|^2 - \left|\tilde{V}_{AB}\right|^2 - \left|\tilde{V}_{CA}\right|^2}{-2\left|\tilde{V}_{AB}\right|\left|\tilde{V}_{CA}\right|}\right] = 1.0605\,\text{rad}$$

$$\phi_{Bv} = \cos^{-1}\left[\frac{\left|\tilde{V}_{AB}\right|^2 - \left|\tilde{V}_{BC}\right|^2 - \left|\tilde{V}_{CA}\right|^2}{-2\left|\tilde{V}_{BC}\right|\left|\tilde{V}_{CA}\right|}\right] = -1.0346\,\text{rad}$$

$$\phi_{Cv} = \pi\,\text{rad}$$

The three line voltages vectors can be computed as

$$\tilde{V}_{ABCLine} = \begin{bmatrix} |\tilde{V}_{AB}|\{\cos(\phi_{Av}) + j\sin(\phi_{Av})\} \\ |\tilde{V}_{BC}|\{\cos(\phi_{Bv}) + j\sin(\phi_{Bv})\} \\ |\tilde{V}_{CA}|\{\cos(\phi_{Cv}) + j\sin(\phi_{Cv})\} \end{bmatrix} = 100 \begin{bmatrix} 1.0165 + j1.8158 \\ 1.0792 - j1.8158 \\ -2.0956 + j0.0000 \end{bmatrix}$$

The sequence components of the line voltages can be computed as

$$[\tilde{V}_{012Line}] = \frac{1}{3}[T][\tilde{V}_{ABCLine}] = 100 \begin{bmatrix} 0.0000 + j\,0.0000 \\ 1.0324 + j\ 1.8244 \\ -0.0159 - j\,0.0086 \end{bmatrix}$$

The sequence components per phase can be computed as [40]

$$[\tilde{V}_{012}] = \frac{1}{\sqrt{3}} \begin{bmatrix} \tilde{V}_{012Line}(1,1) \\ \tilde{V}_{012Line}(2,1)\alpha_{-30} \\ \tilde{V}_{012Line}(3,1)\alpha_{+30} \end{bmatrix} = 100 \begin{bmatrix} 0.0000 - j0.0000 \\ 1.0429 + j\,0.6142 \\ -0.0055 - j0.0089 \end{bmatrix}$$

From the terminal measurement of the machine, we can read the magnitudes of the three line currents as given below:

$$|\tilde{I}_A| = 8.9385\text{A}, \quad |\tilde{I}_B| = 8.4524\text{A}, \quad |\tilde{I}_C| = 8.9406\text{A}$$

The phase angles (not in reference to the line voltages) of the line currents can be obtained as

$$\phi_{Ai} = \cos^{-1}\left[\frac{|\tilde{I}_B|^2 - |\tilde{I}_A|^2 - |\tilde{I}_C|^2}{-2|\tilde{I}_A||\tilde{I}_C|}\right] = 0.9848\,\text{rad}$$

$$\phi_{Bi} = \cos^{-1}\left[\frac{|\tilde{I}_A|^2 - |\tilde{I}_B|^2 - |\tilde{I}_C|^2}{-2|\tilde{I}_B||\tilde{I}_C|}\right] = -1.0782\,\text{rad}$$

$$\phi_{Ci} = \pi\,\text{rad}$$

Considering the power factor = 0.707, power factor angle = 45 degrees = 0.7854 radian, the $\tilde{I}_C$ lags $\tilde{V}_{CA}$ by (30+45) = 75 degrees = 1.3090 radian.

Hence,

$$\phi_{Ci} = \pi - 1.309 = 1.8326\,\text{rad}$$

Keeping the phase relationship among the current phasors as obtained

$$\phi_{Ai} = 0.9848 - 1.309 = -0.3242\text{rad}$$

$$\phi_{Bi} = -1.0782 - 1.309 = -2.3872\text{rad}$$

The three line current vectors can be computed as

$$\tilde{I}_{ABCLine} = \begin{bmatrix} |\tilde{I}_A|\{\cos(\phi_{Ai}) + j\sin(\phi_{Ai})\} \\ |\tilde{I}_B|\{\cos(\phi_{Bi}) + j\sin(\phi_{Bi})\} \\ |\tilde{I}_C|\{\cos(\phi_{Ci}) + j\sin(\phi_{Ci})\} \end{bmatrix} = \begin{bmatrix} 8.4729 - j\,2.8474 \\ -6.1592 - j5.7886 \\ -2.3140 + j\,8.6359 \end{bmatrix}$$

The sequence components of the line currents can be computed as

$$[\tilde{I}_{012Line}] = \frac{1}{3}[T][\tilde{I}_{ABCLine}] = \begin{bmatrix} 0.0000 - j\,0.0000 \\ 8.4005 - j\,2.5337 \\ 0.0725 - j0.3137 \end{bmatrix}$$

Also, in a star-connected system

$$[\tilde{I}_{012}] = [\tilde{I}_{ABCLine}]$$

Similarly, another two sets of line voltages and currents of the machine at the same operating condition have been considered as given below

$$|\tilde{V}_{AB1}| = 208.2003\text{V}, \quad |\tilde{V}_{BC1}| = 211.2016\text{V}, \quad |\tilde{V}_{CA1}| = 209.6178\text{V}$$

$$|\tilde{I}_{A1}| = 9.0069\text{A}, \quad |\tilde{I}_{B1}| = 8.5427\text{A}, \quad |\tilde{I}_{C1}| = 8.9879\text{A}$$

$$|\tilde{V}_{AB2}| = 208.0923\text{V}, \quad |\tilde{V}_{BC2}| = 211.2212\text{V}, \quad |\tilde{V}_{CA2}| = 209.6975\text{V}$$

$$|\tilde{I}_{A2}| = 9.0366\text{A}, \quad |\tilde{I}_{B2}| = 8.5514\text{A}, \quad |\tilde{I}_{C2}| = 9.0140\text{A}$$

Following the same procedure, the sequence components (per phase) pertaining to the other two sets of data have been determined as

$$[\tilde{V}_{012}]_1 = 100\begin{bmatrix} 0.0000 + j\,0.0000 \\ 1.0433 + j\,0.6139 \\ -0.0052 - j0.0085 \end{bmatrix}, \quad [\tilde{I}_{012}]_1 = \begin{bmatrix} 0.0000 + j\,0.0000 \\ 8.4705 - j\,2.5406 \\ 0.0800 - j\,0.2900 \end{bmatrix}$$

$$[\tilde{V}_{012}]_2 = 100\begin{bmatrix} 0.0000 + j\,0.0000 \\ 1.0431 + j1.0431 \\ -0.0050 - j0.0091 \end{bmatrix}, \quad [\tilde{I}_{012}]_2 = \begin{bmatrix} 0.0000 - j\,0.0000 \\ 8.4877 - j\,2.5572 \\ 0.0846 - j\,0.3019 \end{bmatrix}$$

Using (2.3) and the three sets of data, the constants $\tilde{K}_1$ and $\tilde{K}_2$ have been determined using least square method as given below:

$$\begin{bmatrix} \tilde{K}_1 \\ \tilde{K}_2 \end{bmatrix} = \begin{bmatrix} 0.0005 - j\,0.0004 \\ -0.2435 + j\,0.1387 \end{bmatrix}$$

Sample Calculation of $\tilde{K}_0$, $\tilde{K}_1$ and $\tilde{K}_2$

From the terminal measurement of the machine, we can read the magnitudes of the three phase voltages as given below:

$$\left|\tilde{V}_A\right| = 119.7591\text{V},\ \left|\tilde{V}_B\right| = 120.8197\text{V},\ \left|\tilde{V}_C\right| = 122.5302\text{V}$$

The phase angles of the phase voltages can be considered as

$$\phi_{Av} = 0\,\text{rad}$$

$$\phi_{Bv} = \frac{4\pi}{3}\,\text{rad}$$

$$\phi_{Cv} = \frac{2\pi}{3}\,\text{rad}$$

The three phase voltages vectors can be computed as

$$\tilde{V}_{ABC} = \begin{bmatrix} \left|\tilde{V}_A\right|\{\cos(\phi_{Av}) + j\sin(\phi_{Av})\} \\ \left|\tilde{V}_B\right|\{\cos(\phi_{Bv}) + j\sin(\phi_{Bv})\} \\ \left|\tilde{V}_C\right|\{\cos(\phi_{Cv}) + j\sin(\phi_{Cv})\} \end{bmatrix} = 100 \begin{bmatrix} 1.0165 + j1.8158 \\ 1.0792 - j1.8158 \\ -2.0956 + j0.0000 \end{bmatrix}$$

The sequence components of the phase voltages can be computed as

$$[\tilde{V}_{012}] = \frac{1}{3}[T][\tilde{V}_{ABC}] = 100 \begin{bmatrix} -0.0064 + j\,0.0049 \\ 1.2104 - j\ 0.0000 \\ -0.0064 - j\,0.0049 \end{bmatrix}$$

From the terminal measurement of the machine, we can read the magnitudes of the three phase currents as given below:

$$\left|\tilde{I}_A\right| = 8.9385\text{A},\ \left|\tilde{I}_B\right| = 8.4524\text{A},\ \left|\tilde{I}_C\right| = 8.9406\text{A}$$

The phase angles (not in reference to the line voltages) of the line currents can be obtained as

$$\phi_{Ai} = \cos^{-1}\left[\frac{\left|\tilde{I}_B\right|^2 - \left|\tilde{I}_A\right|^2 - \left|\tilde{I}_C\right|^2}{-2\left|\tilde{I}_A\right|\left|\tilde{I}_C\right|}\right] = 0.9848\,\text{rad}$$

$$\phi_{Bi} = \cos^{-1}\left[\frac{\left|\tilde{I}_A\right|^2 - \left|\tilde{I}_B\right|^2 - \left|\tilde{I}_C\right|^2}{-2\left|\tilde{I}_B\right|\left|\tilde{I}_C\right|}\right] = -1.0782\,\text{rad}$$

$$\phi_{Ci} = \pi\,\text{rad}$$

Considering the power factor = 0.707, power factor angle = 45 degrees = 0.7854 radian, the $\tilde{I}_A$ lags $\tilde{V}_A$ by 45 degrees = 0.7854 radian.

Hence,

$$\phi_{Ai} = 0.9848 - 0.9848 - 0.7854 = -0.7854\,\text{rad}$$

Keeping the phase relationship among the current phasors as obtained

$$\phi_{Bi} = -1.0782 - 0.9848 - 0.7854 = -2.8484\text{rad}$$

$$\phi_{Ci} = \pi - 0.9848 - 0.7854 = 1.3714\text{rad}$$

The three phase current vectors can be computed as

$$\tilde{I}_{ABCLine} = \begin{bmatrix} \left|\tilde{I}_A\right|\{\cos(\phi_{Ai}) + j\sin(\phi_{Ai})\} \\ \left|\tilde{I}_B\right|\{\cos(\phi_{Bi}) + j\sin(\phi_{Bi})\} \\ \left|\tilde{I}_C\right|\{\cos(\phi_{Ci}) + j\sin(\phi_{Ci})\} \end{bmatrix} = \begin{bmatrix} 6.3204 - j\,6.3205 \\ -8.0917 - j2.4429 \\ 1.7713 + j\,8.7634 \end{bmatrix}$$

The sequence components of the phase currents can be computed as

$$[\tilde{I}_{012Line}] = \frac{1}{3}[T][\tilde{I}_{ABCLine}] = \begin{bmatrix} 0.0000 - j\,0.0000 \\ 6.3952 - j\,6.0074 \\ -0.0748 - j0.3130 \end{bmatrix}$$

Similarly, another two sets of line voltages and currents of the machine at the same operating condition have been considered as given below

$$\left|\tilde{V}_{A1}\right| = 119.8194\text{V}, \quad \left|\tilde{V}_{B1}\right| = 120.8477\text{V}, \quad \left|\tilde{V}_{C1}\right| = 122.5215\text{V}$$

$$\left|\tilde{I}_{A1}\right| = 9.0069\text{A}, \quad \left|\tilde{I}_{B1}\right| = 8.5427\text{A}, \quad \left|\tilde{I}_{C1}\right| = 8.9879\text{A}$$

$$\left|\tilde{V}_{A2}\right| = 119.8061\text{V}, \quad \left|\tilde{V}_{B2}\right| = 120.8100\text{V}, \quad \left|\tilde{V}_{C2}\right| = 122.5672\text{V}$$

$$\left|\tilde{I}_{A2}\right| = 9.0366\text{A}, \quad \left|\tilde{I}_{B2}\right| = 8.5514\text{A}, \quad \left|\tilde{I}_{C2}\right| = 9.0140\text{A}$$

Following the same procedure, the sequence components (per phase) pertaining to the other two sets of data have been determined as

$$[\tilde{V}_{012}]_1 = 100\begin{bmatrix} -0.0062 + j\,0.0048 \\ 1.2106 - j\,0.0000 \\ -0.0062 - j0.0048 \end{bmatrix}, \quad [\tilde{I}_{012}]_1 = \begin{bmatrix} 0.0000 - j\,0.0000 \\ 6.4276 - j\,6.0738 \\ -0.0587 - j\,0.2951 \end{bmatrix}$$

$$[\tilde{V}_{012}]_2 = 100\begin{bmatrix} -0.0063 + j\,0.0051 \\ 1.2106 - j\,0.0000 \\ -0.0063 - j0.0051 \end{bmatrix}, \quad [\tilde{I}_{012}]_2 = \begin{bmatrix} 0.0000 + j\,0.0000 \\ 6.4491 - j\,6.0820 \\ -0.0593 - j\,0.3079 \end{bmatrix}$$

Using (2.5) and the three sets of data, the constants $\tilde{K}_0$, $\tilde{K}_1$ and $\tilde{K}_2$ have been determined using least square method as given below:

$$\begin{bmatrix} \tilde{K}_0 \\ \tilde{K}_1 \\ \tilde{K}_2 \end{bmatrix} = \begin{bmatrix} 0.0042 + j\,0.0032 \\ 0.7107 + j\,0.5453 \\ 0.3836 + j\,0.3074 \end{bmatrix}$$

Appendix C

Derivation of Stator Inductances and General Expressions for L_d & L_q

The mutual inductance between phase-A and phase-B of stator windings of the RSM can be obtained as follows with $p = 2$, $u = A$ & $v = B$;

$$L_{AB} = \mu_0 rl\left[\int_0^{2\pi} n_A(\phi) N_B(\phi) g^{-1}(\phi,\theta) d\phi\right] \tag{C1}$$

$$= \mu_0 rl \int_0^{2\pi} \left[\begin{pmatrix} a_{os} + \sum_{m=1,3,5,\ldots}^{\infty} a_{ms} \cos(2m\phi) \end{pmatrix} \begin{pmatrix} \sum_{m=1,3,5,\ldots}^{\infty} a_{ms} \cos\left\{2m\left(\phi - \frac{x}{2}\right)\right\} \end{pmatrix} \begin{pmatrix} a_{og} + \sum_{k=2,4,6,..}^{\infty} a_{kg} \cos\{2k(\phi-\theta)\} \end{pmatrix}\right] d\phi$$

$$= \mu_0 rl \int_0^{2\pi} \left[a_{og} \left(\sum_{m=1,3,5,\ldots}^{\infty} a_{ms} \cos(2m\phi) \right) \left(\sum_{m=1,3,5,\ldots}^{\infty} a_{ms} \cos\left\{ 2m\left(\phi - \frac{x}{2} \right) \right\} \right) \right] d\phi$$

$$+ \mu_0 rl \int_0^{2\pi} \left[\left(\sum_{m=1,3,5,\ldots}^{\infty} a_{ms} \cos(2m\phi) \right) \left(\sum_{m=1,3,5,\ldots}^{\infty} a_{ms} \cos\left\{ 2m\left(\phi - \frac{x}{2} \right) \right\} \right) \left(\sum_{k=2,4,6,..}^{\infty} a_{kg} \cos\{2k(\phi - \theta)\} \right) \right] d\phi$$

The other terms, upon integration, become zero. The mutual inductance between phase-A and phase-B can be given as

$$L_{AB} = \left[M_0 + \sum_{k=2,4,6,..}^{\infty} M_K \cos\left[pk\theta - \frac{kx}{2} \right] \right] \qquad \text{(C2)}$$

$$where \;\; M_k = 2\pi \mu_o rl(A_r + A_f) a_{kg}$$

$$M_0 = \frac{2\pi\,\mu_0 rla_{og}}{2}\left[\sum_{m=1,3,5,..}^{\infty}(a_{ms})^2\cos[mx]\right],\quad x=\frac{2\pi}{3}$$

$$A_f = \sum_{m=1,3,..}^{\infty}\frac{a_{ms}a_{(k+m)s}}{2}\cos\left[\left(\frac{k}{2}+m\right)x\right],\ A_r = \sum_{\substack{m=1,3,..\\(k-m)>0}}^{\infty}A_{ar},$$

$$A_{ar} = \frac{a_{ms}a_{(k-m)s}}{4},\qquad for\quad k=2m,$$

$$A_{ar} = \frac{a_{ms}a_{(k-m)s}}{2}\cos\left[\left(\frac{k}{2}-m\right)x\right],\qquad for\quad k\neq 2m,$$

Rewriting (C2) for $k = 2, 4$

$$L_{AB} = \left[M_0 + M_2\cos(4\theta - x) + M_4\cos(8\theta - 2x)\right] \tag{C3}$$

The mutual inductance between phase-A and phase-C can be obtained by substituting for 'x' by '$2x$' in (C3) and can be represented as

$$L_{AC} = \left[M_0 + M_2\cos(4\theta - 2x) + M_4\cos(8\theta - 4x)\right] \tag{C4}$$

The magnetizing inductance of phase-A can be obtained by substituting $x = 0$ in (C3) and can be represented as

$$L_{AA} = \left[L_0 + L_2\cos(4\theta) + L_4\cos(8\theta)\right] \tag{C5}$$

The net flux linkage per unit phase current at any rotor position can be obtained by using (2.18). Considering up to 2nd permeance harmonic and by substituting for L_{AA}, L_{AB} and L_{AC} from (C3)-(C5) in (2.18), we have

$$
\begin{aligned}
L = & \left\{L_0 + L_2\cos(4\theta) + L_4\cos(8\theta)\right\} \\
& - 0.5\begin{Bmatrix} M_0 + M_2\cos(4\theta - x) \\ + M_4\cos(8\theta - 2x) \end{Bmatrix} \\
& - 0.5\begin{Bmatrix} M_0 + M_2\cos(4\theta - 2x) \\ + M_4\cos(8\theta - 4x) \end{Bmatrix} + L_l
\end{aligned} \tag{C6}
$$

The maxima of 'L' occurs at $\theta = 0$ which corresponds to the inductance along direct axis (Ld) whereas minima of 'L' occurs at $\theta = \pi/4$ which corresponds to the inductance along quadrature axis (Lq). Hence Ld and Lq can be given as

$$L_d = L_0 - M_0 + L_2 + 0.5M_2 + L_4 + 0.5M_4 + L_l \tag{C7}$$

$$L_q = L_0 - M_0 - L_2 - 0.5M_2 + L_4 + 0.5M_4 + L_l \tag{C8}$$

By considering higher permeance harmonics, (2.19) and (2.20) can be obtained. (C7) and (C8) can be obtained by substituting m = 0, n = 0, 1, 2 and p = 1 in (2.19) and (2.20).

Appendix D

Validation of Inductances using Finite Element Method

Various inductances that are computed using WFA and MWFA have been compared with the corresponding inductances obtained using finite element method (FEM). Mostly the inductances seem to be matching but some discrepancies have been noticed. A possible reason for these differences is the effective pole arc reduction in the case of FEM results. An even larger difference in the case of SM with DC excitation is because of the shape of its rotor pole arc, which is not circular as shown in Figure 3.8. The FEM model includes the actual shape of the rotor pole. However it is not possible to accommodate the actual shape of pole arc in the WFA/MWFA based computations.

Table D1 Comparison of rotor loop Inductances of synchronous machines obtained using MWFA and FEM analysis

Machine	Self inductance of rotor loop1 (μH)		Mutual inductance between rotor loop1 and loop2 (μH)	
	MWFA	FEM	MWFA	FEM
RSM	1.35	1.1	0.11	0.15
SM With DC excitation	0.76	3.6	0.035	0.72

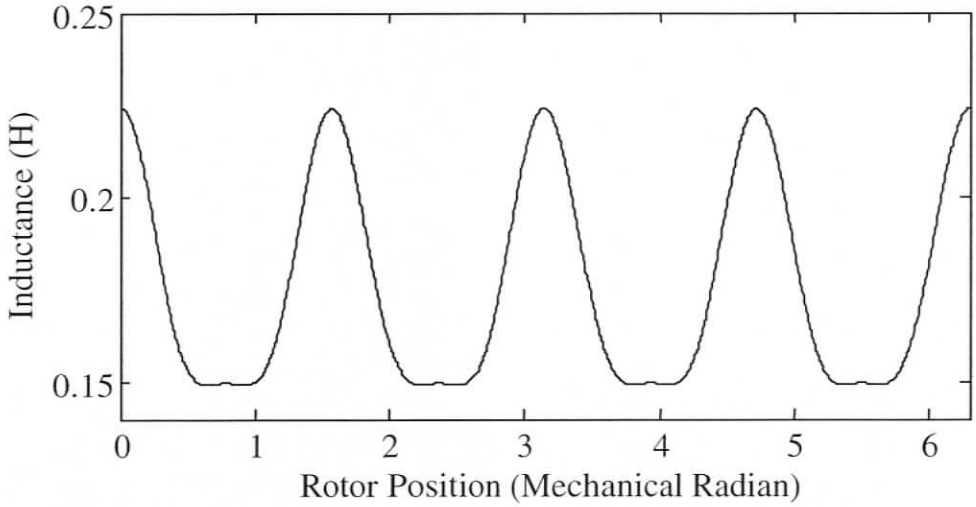

Figure D.1 Magnetizing inductance of stator phase-A of RSM using WFA

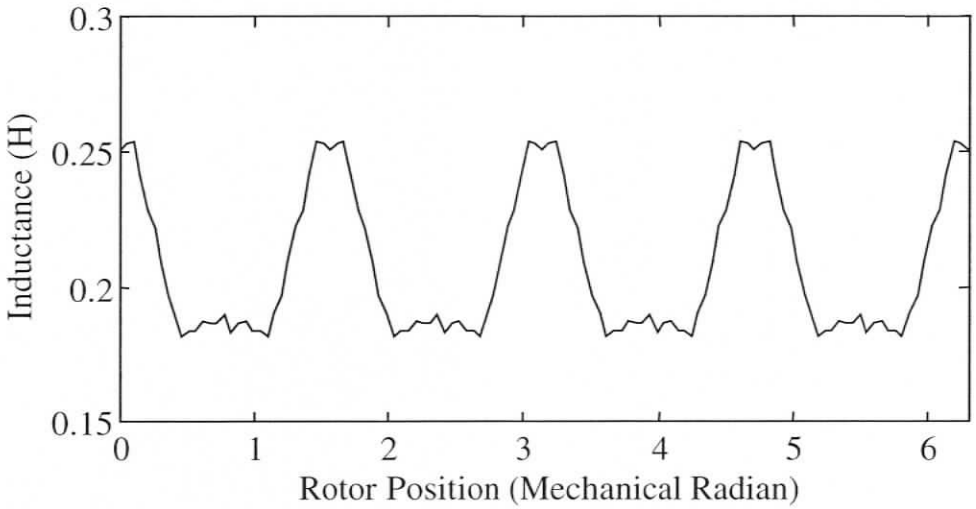

Figure D.2 Self-inductance of stator phase-A of RSM using FEM

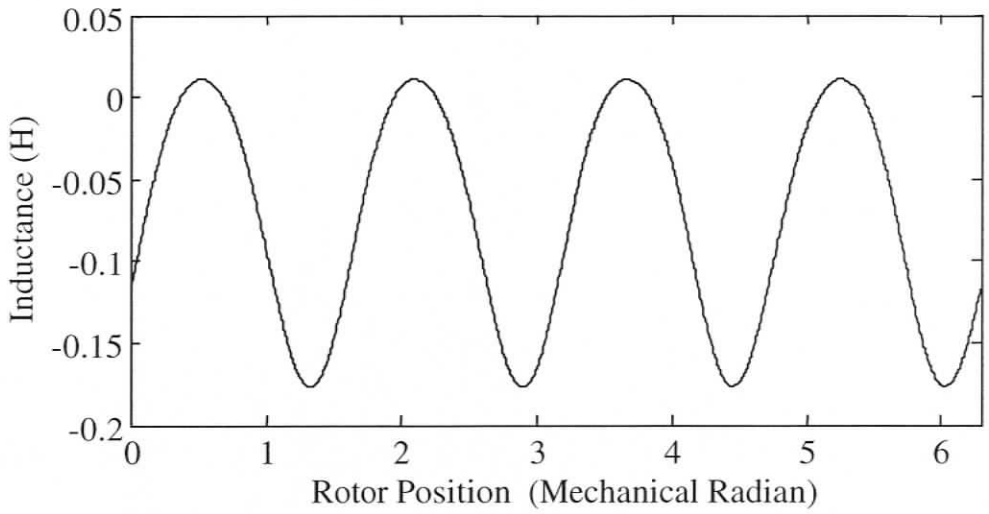

Figure D.3 Mutual inductance between stator phase-A and phase-B of RSM using WFA

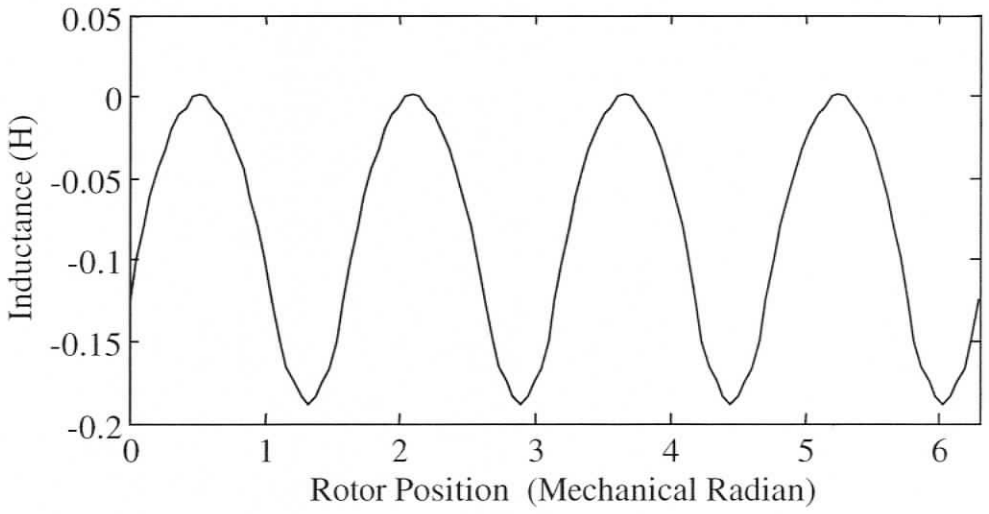

Figure D.4 Mutual inductance between stator phase-A and phase-B of RSM using FEM

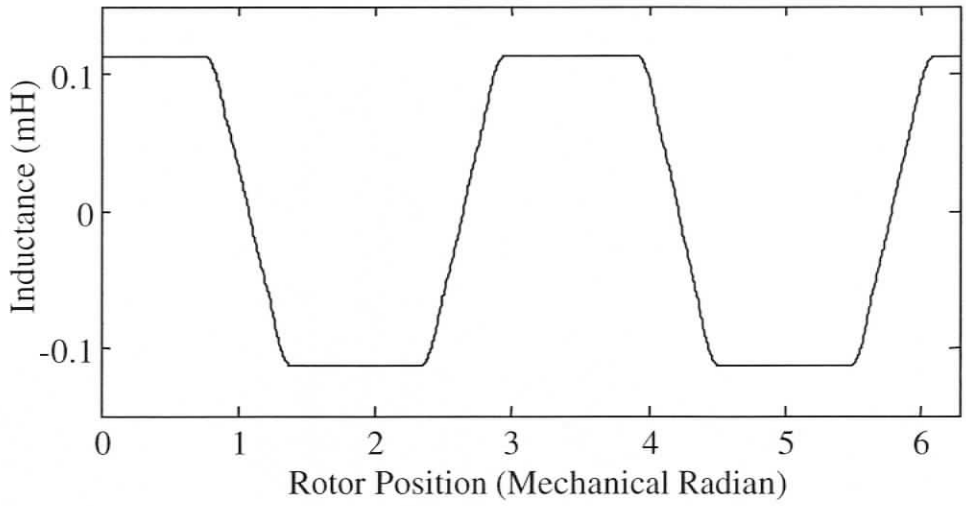

Figure D.5 Mutual inductance between stator phase-A and a typical rotor loop of RSM using WFA

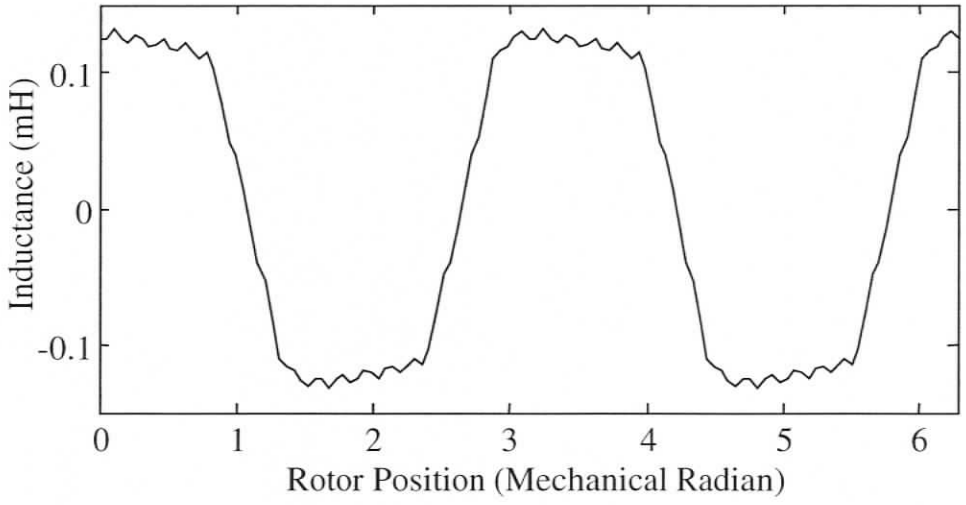

Figure D.6 Mutual inductance between stator phase-A and a typical rotor loop of RSM using FEM

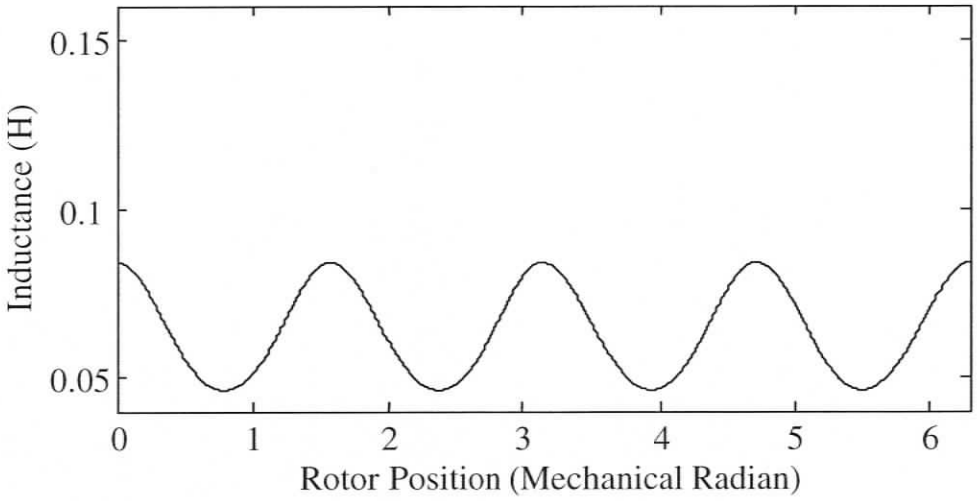

Figure D.7 Magnetizing inductance of stator phase-A of SM with DC excitation using WFA

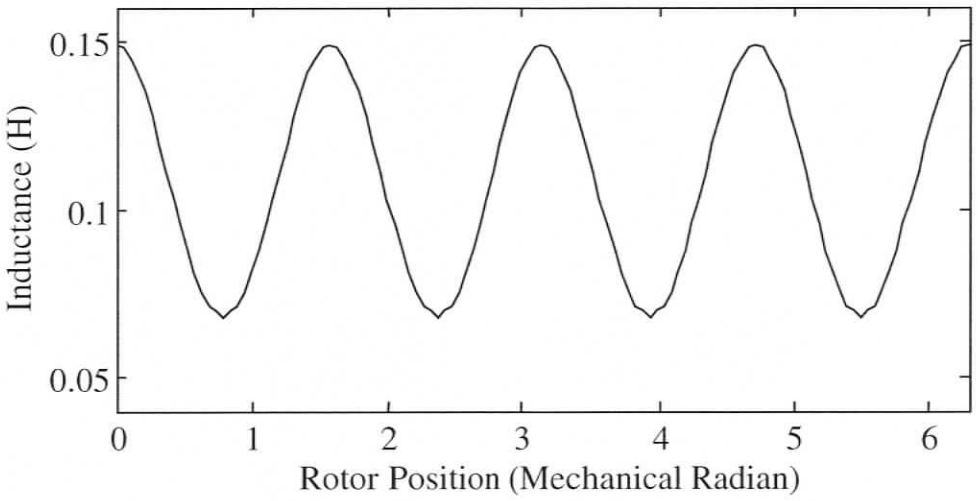

Figure D.8 Self-inductance of stator phase-A of SM with DC excitation using FEM

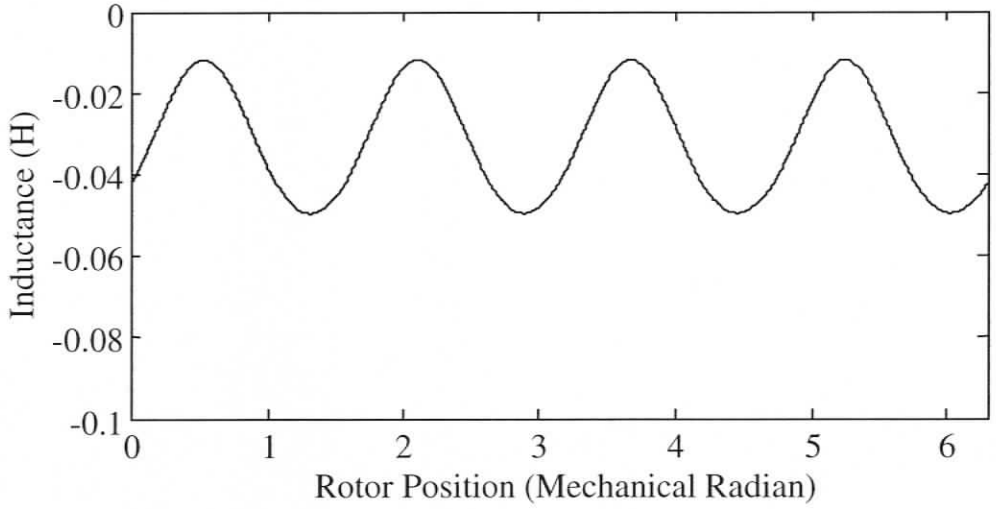

Figure D.9 Mutual inductance between stator phase-A and phase-B of SM with DC excitation using WFA

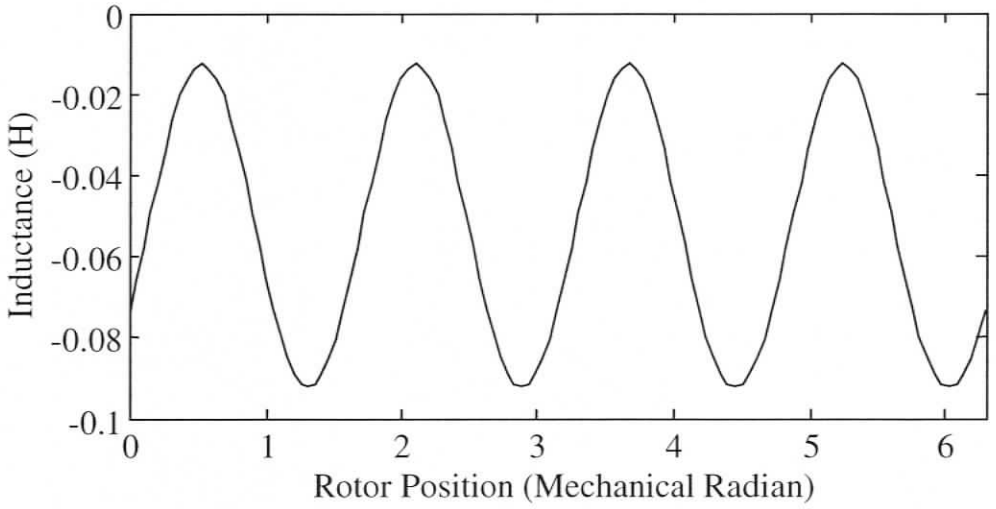

Figure D.10 Mutual inductance between stator phase-A and phase-B of SM with DC excitation using FEM

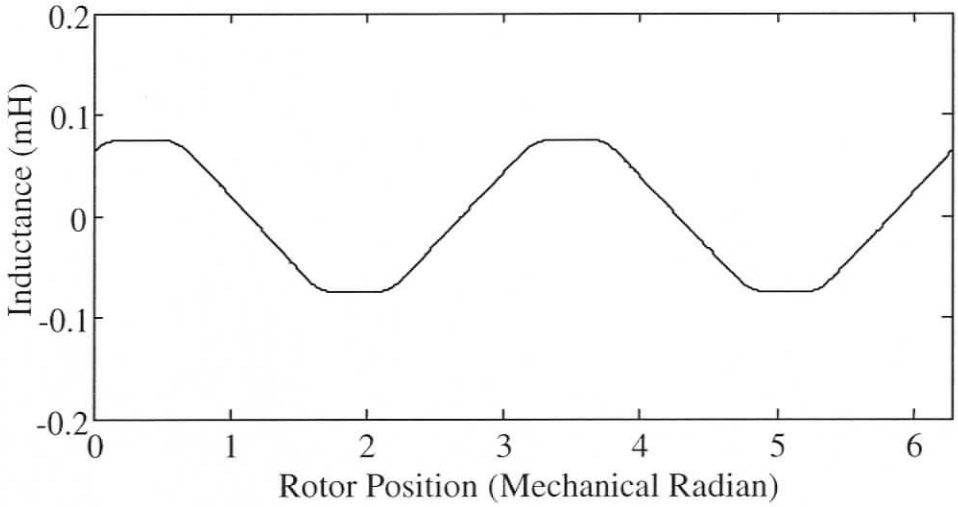

Figure D.11 Mutual inductance between stator phase-A and a typical rotor loop of SM with DC excitation using WFA

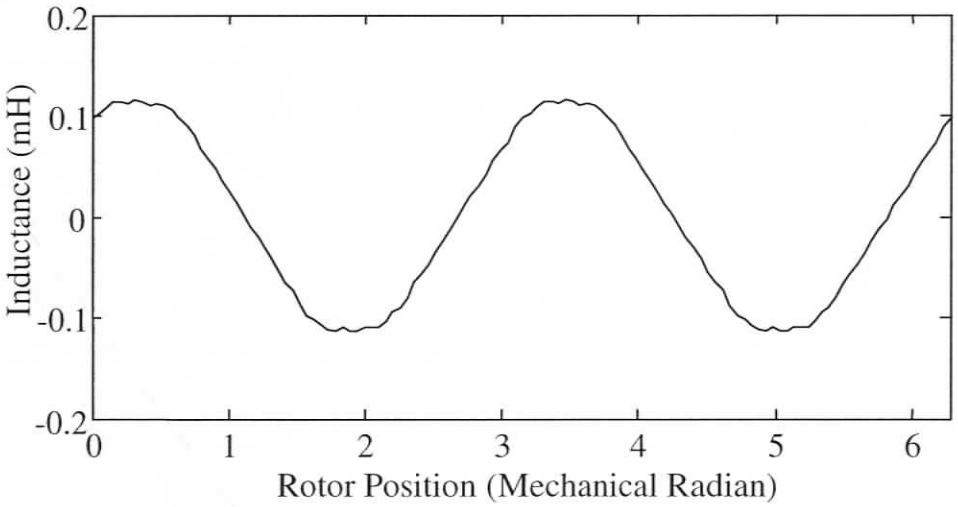

Figure D.12 Mutual inductance between stator phase-A and a typical rotor loop of SM with DC excitation using FEM

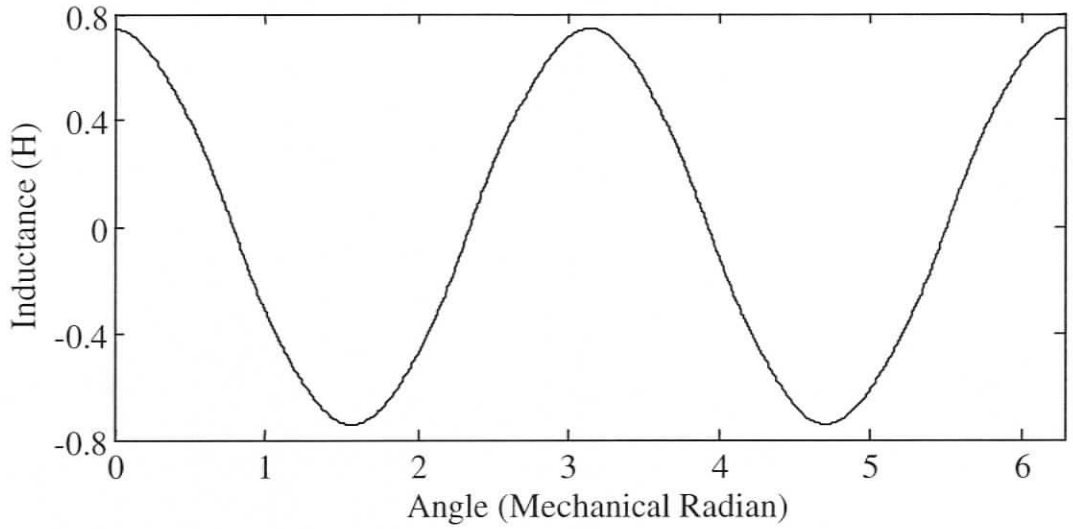

Figure D.13 Mutual inductance between stator phase-A and standard field winding of SM with DC excitation using WFA

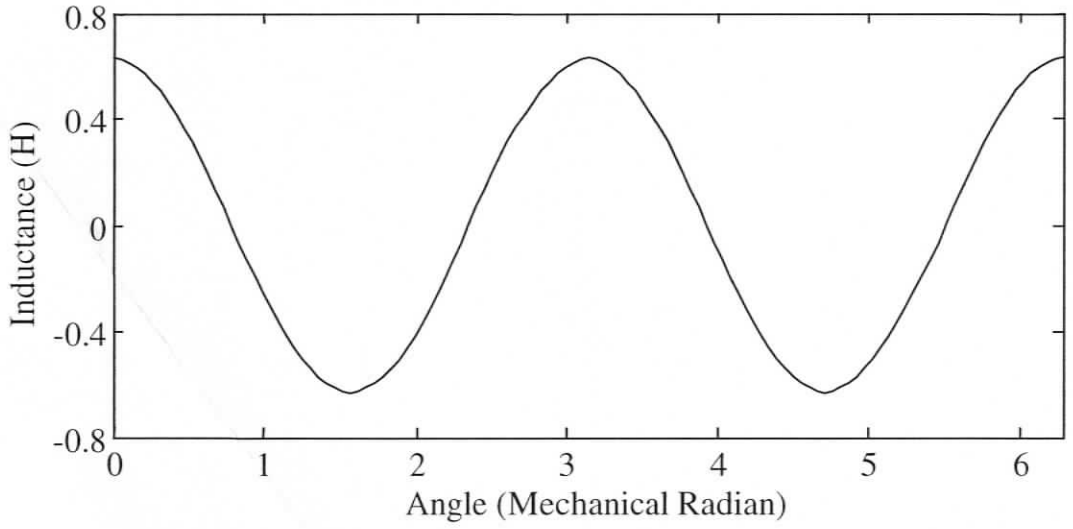

Figure D.14 Mutual inductance between stator phase-A and standard field winding of SM with DC excitation using FEM